ISSN 0042-8469
e-ISSN 2217-4753
UDC 623 + 355/359

Vol. 74, Issue 2
2026

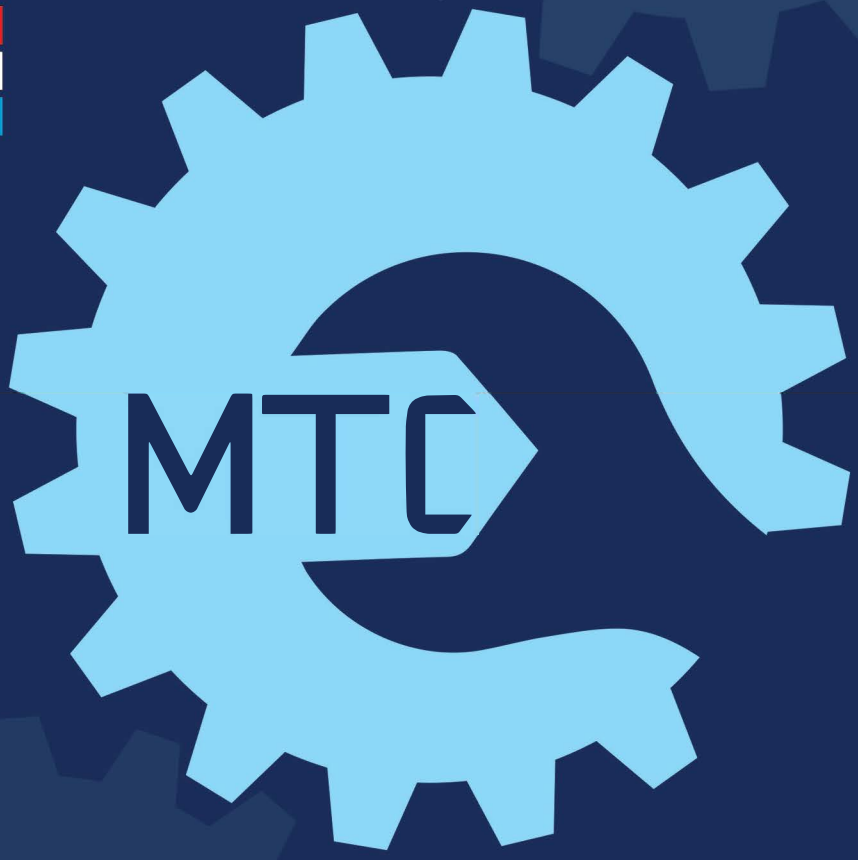

SCIENTIFIC JOURNAL OF THE MINISTRY OF DEFENCE AND THE SERBIAN ARMED FORCES

MILITARY TECHNICAL COURIER

MILITARY TECHNICAL COURIER 2 2026

www.vtg.mod.gov.rs

ISSN 0042-8469
e-ISSN 2217-4753
UDC 623 + 355/359

Vol. 74, Issue 2

2026

NAUČNI ČASOPIS MINISTARSTVA ODBRANE REPUBLIKE SRBIJE

VOJNOTEHNIČKI GLASNIK

www.vtg.mod.gov.rs

OWNERS:
Ministry of Defence and Serbian Armed Forces
PUBLISHER:
University of Defence in Belgrade, Military Academy
EDITORIAL TEAM (the pages of the Editorial Team's members in ORCID iD, Google Scholar, Web of Science ResearcherID, Scopus Author ID, and РИНЦ can be accessed at http://www.vtg.mod.gov.rs/editorial-team.html):
EDITOR IN CHIEF:
Dr. Dragan Trifković, University of Defence in Belgrade, Military Academy, Belgrade, Serbia,
e-mail: dragan.trifkovic@va.mod.gov.rs
EDITOR:
Dr. Vladan Anicijevic, University of Defence in Belgrade, Military Academy, Belgrade, Serbia,
e-mail: vojnotehnicki.glasnik@mod.gov.rs
Dr. Predrag Dobratic, University of Defence in Belgrade, Military Academy, Belgrade, Serbia,
e-mail: vojnotehnicki.glasnik@mod.gov.rs
Editor for Mathematics and Mechanics
Dr. Rale Nikolić, University of Defence in Belgrade, Military Academy, Belgrade, Serbia
Editor for Electronics, Telecommunications and Information Technology
Dr. Boban Bondžulić, University of Defence in Belgrade, Military Academy, Belgrade, Serbia
Editor for Mechanical Engineering
Dr. Branimir Krstić, University of Defence in Belgrade, Military Academy, Belgrade, Serbia
Editor for Materials and Chemical Technologies
Dr. Mihael Bučko, University of Defence in Belgrade, Military Academy, Belgrade, Serbia
EDITORIAL BOARD:
Dr. Gradimir Milovanović, Serbian Academy of Sciences and Arts, Belgrade, Serbia,
Dr. Ji-Huan He, Soochow University, College of Textile and Clothing Engineering, Soochow, China,
Dr. Madjid Tavana, La Salle University, Business Systems and Analytics Department, Philadelphia, USA,
Dr. Shankar Chakraborty, Jadavpur University, Department of Production Engineering, Kolkata, India,
Dr. Radu-Emil Precup, Politehnica University of Timisoara, Timisoara, Romania,
Dr. Jurgita Antuchevičienė, Vilnius Gediminas Technical University, Faculty of Civil Engineering, Vilnius, Lithuania,
Dr. Morteza Yazdani, ESIC Business and Marketing School, Madrid, Spain,
Dr. Prasenjit Chatterjee, MCKV Institute of Engineering, Department of Mechanical Engineering, Howrah, India,
Dr. Željko Stević, University of East Sarajevo, Faculty of Transportation, Doboj, Republic of Srpska, Bosnia and Herzegovina,
Dr. Hamed Fazlollahtabar, Damghan University, Department of Industrial Engineering, Damghan, Iran,
Dr. Jarosław Wątróbski, University of Szczecin, Faculty of Economics, Finance and Management, Szczecin, Poland,
Dr. Cristiano Fragassa, University of Bologna, Department of Industrial Engineering, Bologna, Italy,
Dr. Wojciech Sałabun, West Pomeranian University of Technology in Szczecin, Faculty of Computer Science and Information Technology, Szczecin, Poland,
Dr. Ieva Meidutė-Kavaliauskienė, General Jonas Žemaitis Military Academy of Lithuania, Research Group on Logistics and Defense Technology Management, Vilnius, Lithuania,
Dr. Šárka Mayerová, University of Defence in Brno, Department of Mathematics and Physics, Brno, Czech Republic,
Dr. Fatih Ecer, Afyon Kocatepe University, Faculty of Economics and Administrative Sciences, Afyonkarahisar, Turkey,
Dr. Ernesto D.R. Santibanez Gonzalez, Universidad de Talca, Talca, Chile,
Dr. Dragan Marinković, Technical University Berlin, Faculty of Mechanical and Transport Systems, Berlin, Germany,
Dr. Stefano Valvano, Kore University of Enna, Department of Aerospace Engineering, Enna, Italy,
Dr. Rafal Madonski, Jinan University, Energy Electricity Research Center, Guangzhou, China,
Dr. Milenko Andrić, University of Defence in Belgrade, Military Academy, Belgrade, Serbia,
Dr. Samarjit Kar, National Institute of Technology, Department of Mathematics, Durgapur, India,
Dr. Rosen Mitrev, Technical University of Sofia, Sofia, Bulgaria,
Dr. Bojan Milanović, University of Defence in Belgrade, Military Academy, Belgrade, Serbia,
Dr. Irik Mukhametzyanov, Ufa State Petroleum Technological University, Ufa, Russian Federation,
Dr. Pavel Otrisal, Palacký University, Olomouc, Czech Republic,
Dr. Radovan Radovanović, University of Criminal Investigation and Police Studies, Belgrade, Serbia,
Dr. Boško Rašuo, University of Belgrade, Faculty of Mechanical Engineering, Belgrade, Serbia,
Dr. Saad Aslam, Sunway University, Kuala Lumpu, Malaysia,
Dr. Nasreen Kausar, Yildiz Technical University, Istanbul, Turkey

VLASNICI:
Ministarstvo odbrane i Vojska Srbije
IZDAVAČ:
Univerzitet odbrane u Beogradu, Vojna akademija
UREDNIŠTVO (stranice članova uredništva u ORCID iD-u, Google Scholar-u, Web of Science ResearcherID-u, Scopus Author ID-u i RINC-u dostupni su na http://www.vtg.mod.gov.rs/urednistvo.html):
GLAVNI I ODGOVORNI UREDNIK:
Dr Dragan Trifković, Univerzitet odbrane u Beogradu, Vojna akademija, Beograd, Srbija,
e-mail: dragan.trifkovic@va.mod.gov.rs
UREDNIK:
Dr Vladan Anićijević, Univerzitet odbrane u Beogradu, Vojna akademija, Beograd, Srbija,
e-mail: vojnotehnicki.glasnik@mod.gov.rs
Dr Predrag Dobratić, Univerzitet odbrane u Beogradu, Vojna akademija, Beograd, Srbija,
e-mail: vojnotehnicki.glasnik@mod.gov.rs
Urednik za oblast matematike i mehanike
Dr Rale Nikolić, Univerzitet odbrane u Beogradu, Vojna akademija, Beograd, Srbija
Urednik za oblast elektronike, telekomunikacija i informacionih tehnologija
Dr Boban Bondžulić, Univerzitet odbrane u Beogradu, Vojna akademija, Beograd, Srbija
Urednik za oblast mašinstva
Dr Branimir Krstić, Univerzitet odbrane u Beogradu, Vojna akademija, Beograd, Srbija
Urednik za oblast materijala i hemijskih tehnologija
Dr Mihael Bučko, Univerzitet odbrane u Beogradu, Vojna akademija, Beograd, Srbija
UREĐIVAČKI ODBOR:
Dr Gradimir Milovanović, Srpska akademija nauka i umetnosti, Beograd, Srbija,
Dr Đi-Huan Hi, Univerzitet Sudžou, Fakultet za tekstilnu i odevnu tehniku, Sudžou, Kina,
Dr Mađid Tafana, Univerzitet La Sal, Odeljenje za poslovne sisteme i analitiku, Filadelfija, SAD,
Dr Šankar Čakraborti, Univerzitet Jadavpur, Odeljenje za proizvodno mašinstvo, Kalkuta, Indija,
Dr Radu-Emil Prekup, Univerzitet Politehnika u Temišvaru, Temišvar, Rumunija,
Dr Jurgita Antucheviči, Tehnički univerzitet Gediminas u Vilnjusu, Građevinski fakultet, Vilnjus, Litvanija,
Dr Srećko Joksimović, Univerzitet u Južnoj Australiji, Adelejd, Australija,
Dr Morteza Jazdani, Fakultet za biznis i marketing ESIC, Madrid, Španija,
Dr Prasendžit Čaterdži, Institut za inženjerstvo MCKV, Odeljenje za mašinstvo, Hovrah, Indija,
Dr Željko Stević, Univerzitet u Istočnom Sarajevu, Saobraćajni fakultet, Doboj, Republika Srpska, BiH,
Dr Hamed Fazlolahtabar, Univerzitet Damgan, Odeljenje za industrijsko inženjerstvo, Damgan, Iran,
Dr Jaroslav Vatrobski, Univerzitet u Ščećinu, Fakultet za ekonomiju, finansije i menadžment, Ščećin, Poljska,
Dr Kristiano Fragasa, Univerzitet u Bolonji, Odeljenje za industrijsko inženjerstvo, Bolonja, Italija,
Dr Vojčeh Salabun, Zapadnopomeranski tehnološki univerzitet u Ščećinu, Fakultet računarskih nauka i informacionih tehnologija, Ščećin, Poljska,
Dr Ieva Meidute-Kavaliauskiene, Vojna akademija Litvanije „General Jonas Žemaitis“, Viljnus, Litvanija,
Dr Šarka Majerova, Univerzitet odbrane u Brnu, Odeljenje za matematiku i fiziku, Brno, Češka Republika,
Dr Fatih Ecer, Univerzitet Afion Kođatepe, Fakultet za ekonomiju i administrativne nauke, Afionkarahisar, Turska,
Dr Ernesto D.R. Santibanez Gonzalez, Univerzitet u Talki, Talka, Čile,
Dr Dragan Marinković, Tehnički univerzitet u Berlinu, Fakultet za mašinske i transportne sisteme, Berlin, Nemačka,
Dr Stefano Valvano, Univerzitet Kore u Eni, Odeljenje za vazduhoplovni inženjering, Ena, Italija,
Dr Rafal Madonski, Univerzitet Đinan, Centar za istraživanje električne energije, Guangdžou, Kina,
Dr Milenko Andrić, Univerzitet odbrane u Beogradu, Vojna akademija, Beograd, Srbija,
Dr Samardžit Kar, Nacionalni institut za tehnologiju, Odeljenje za matematiku, Durgapur, Indija,
Dr Rosen Mitrev, Tehnički univerzitet u Sofiji, Sofija, Bugarska,
Dr Bojan Milanović, Univerzitet odbrane u Beogradu, Vojna akademija, Beograd, Srbija,
Dr Irik Muhamedzjanov, Državni naftni tehnološki univerzitet u Ufi, Ufa, Ruska Federacija,
Dr Pavel Otrisal, Univerzitet Palacki, Olomouc, Češka Republika,
Dr Radovan Radovanović, Kriminalističko-policijski univerzitet, Beograd, Srbija,
Dr Boško Rašuo, Univerzitet u Beogradu, Mašinski fakultet, Beograd, Srbija,
Dr Saad Aslam, Univerzitet Sunvai, Kuala Lumpur, Malezija,
Dr Nasrin Kausar, Tehnički univerzitet Jildiz, Fakultet umetnosti i nauke, Turska

C O N T E N T S / S A D R Ž A J

ORIGINAL SCIENTIFIC PAPERS / ORIGINALNI NAUČNI RADOVI

Helal Mohamed

Applications of the expanded Darbo's fixed point theorem to fractional differential equations with finite delay

Primene proširene Darboove teoreme o fiksnoj tački na frakcione diferencijalne jednačine sa konačnim kašnjenjem 269-282

Vladimir Milovanović, Aleksandar Aleksić, Snežana Nestić, Nikola Komatina, Vlada Sokolović, Marjan Milenkov

Multi-attribute approach for enhancing maintenance processes in maintenance depots under a type-2 fuzzy environment

Višeatributivni pristup za unapređenje procesa održavanja u remontnim zavodima u tip-2 fazi okruženju..... 283-308

Noureddine Mahmoudi, Mohammed Bentahar, Hachemi Nedir, Moulai Arbi Youcef

Fatigue crack propagation modeling in 2D structures using the CPCN-FEM node-based approach

Modeliranje širenja pukotine zamora u 2D strukturama primenom CPCN-FEM pristupa koji se zasniva na čvorovima..... 309-330

Xuan Son Bui, Van Gion Do, Duc Hung Pham

Design and analysis of an electro-mechanical impact sensor with an all-ways action mechanism and a Hall sensor

Projektovanje i analiza elektromehaničkog senzora udara sa mehanizmom dejstva u svim pravcima i Holovim senzorom 331-356

Maache Mouna, Brahmi Chihab Eddine, Belghar Nourredine, Kalfali Mahmoud

Natural convection and entropy generation inside porous square cavity with undulated vertical walls under four heating scenarios

Prirodna konvekcija i stvaranje entropije unutar porozne kvadratne šupljine sa neravnim vertikalnim zidovima u četiri režima zagrevanja..... 357-378

Rebai Billel, Tidjani Messas, Mustapha Meradjah, Mohammed Benali Amar

Free vibration analysis of porous functionally graded plates using a novel shape function

Analiza slobodnih vibracija poroznih funkcionalno gradiranih ploča primenom nove funkcije oblika..... 379-399

Viet Dung Bui, Martin Macko, Ba Ngoc Dang, Huu Nguyen Pham

Vibration of the weapon system on an unmanned ground vehicle during movement

Vibracije sistema naoružanja na

besposadnom kopnenom vozilu tokom kretanja 400-423

Asma Halimi, Amal Souad Bourokba,

Moulay Smaine Ghembaza, Abderlkader Hachichi

Improving silty sand performance with cement and fiber reinforcement: a study of mechanical behavior

Poboljšanje performansi muljevitog peska primenom

cementa i vlakanaste armature: studija mehaničkog ponašanja 424-452

Fadhila Ali Kouadri, Mohamed Salhi, Toufik Boubekeur,

Amar Benyahia, Alex Li, Boussad Abbès

Evaluation of the durability performance of roller-compacted

concrete incorporating recycled pavement materials

Procena trajnosti valjanog betona sa recikliranim

materijalima iz kolovoznih konstrukcija 453-476

Oualid Largueche, Mostefa Lallam,

Miloud Driss, Mohammed Amine Hamadouched

Fuzzy algorithms applied to the comparative evaluation of crossroad designs

Primena fazi algoritama u komparativnoj evaluaciji projektovanja raskrsnica 477-502

Lazar Lazarević, Nebojša Hristov, Damir Jerković, Darko Latinkić, Mihael Bučko

Experimental determination of surface emissivity for military

equipment components and comparison with reference data

Eksperimentalno određivanje površinske emisivnosti za

komponente vojne opreme i poređenje sa referentnim podacima 503-518

REVIEW PAPERS / PREGLEDNI RADOVI

Dragan R. Stojadinović, Snezana B. Jovanović,

Aleksandar S. Đurić, Aleksandar B. Bukvić, Sreten R. Perić

Experimental assessment of acoustic effects of cannon fire on crew

Eksperimentalna procena akustičnih uticaja topovske paljbe na posadu 519-530

CALL FOR PAPERS AND INSTRUCTIONS FOR

AUTHORS / POZIV I UPUTSTVO AUTORIMA 531-541

Applications of the expanded Darbo's fixed point theorem to fractional differential equations with finite delay

Mohamed Helal

Mustapha Stambouli University of Mascara, Science and Technology Faculty, B.P. 763, 29000, Mascara, Algeria,+
Djillali Liabes University of Sidi Bel-Abbès, Laboratory of Mathematics, B.P. 89, 22000, Sidi Bel-Abbès, Algeria,
e-mail: helalmohamed@univ-mascara.dz,
ORCID iD: https://orcid.org/0000-0002-7845-1018

https://doi.org/10.5937/vojtehg74-57904

FIELD: mathematics
ARTICLE TYPE: original scientific paper

Abstract:

Introduction/purpose: The aim of this paper is to study the existence of mild solutions to the initial value problem (IVP for short) of the Darboux problem for partial hyperbolic fractional differential equations via the Caputo derivative with finite delay in Fréchet spaces.

Methods: In our analysis, Darbo's fixed point theorem is employed together with the notion of measure of noncompactness to establish the existence of solutions by reducing the research to proving the existence and uniqueness of fixed points of appropriate operators.

Results: Under suitable conditions, existence of mild solutions to the considered fractional partial hyperbolic differential equations is proved. An illustrative example demonstrates the theoretical results applicability.

Conclusion: Throughout this paper, sufficient conditions were considered to establish the existence and uniqueness of solutions to the Darboux problem by applying Darbo's fixed point theorem on unbounded interval. The study provides a rigorous methodological framework for analyzing similar classes of problems and contributes to the broader understanding of mild solutions in fractional calculus and functional analysis. The results offer potential applications for researchers investigating fractional differential equations in infinite-dimensional spaces.

Key words: differential partial hyperbolic equation, fractional order derivative, mild solution, Fréchet space.

ACKNOWLEDGMENT: The author is grateful to the referees for their helpful remarks and suggestions, as well as to Grant PRFU: C00L03UN290120220002 from DGRSDT of Algeria.

Introduction

For many years, not only have mathematicians been interested in fractional calculus and fractional order differential equations, but physicists and engineers have been as well. In fact, there is a wide range of applications in the fields of porous media, electrochemistry, viscoelasticity, electromagnetism and rheology (Baleanu, et al.; Hilfer, 2000; Ortigueira, 2011; Tarasov, 2010). In recent years, ordinary and partial fractional differential equations have undergone significant development. For more details, see Abbas *et al.* (Abbas et al., 2012) and Podlubny (Podlubny, 1999), Abbas and Bechochra (Abbas and Benchohra, 2009, 2012), Benchohra *et al.* (Benchohra and Hellal, 2014a,b; Benchohra et al., 2017), Helal (Helal, 2020), Kilbas and Marzan (Kilbas and Marzan, 2005), Vityuk and Golushkov (Vityuk and Golushkov, 2004) and the references therein.

In 1930, Kuratowski (Kuratowski, 1930) first proposed the notion of a measure of noncompactness. This concept is a powerful tool in functional analysis, particularly in operator equation theory in Banach spaces and metric fixed point theory. The study of the existence of solutions for integral and integro-differential, ordinary and partial differential equations also makes use of this notion. We refer the reader to (Banaei, 2018; Banás et al., 2017; Banás and Mursaleen, 2014) for further information.

In this paper, we examine the existence of solutions to fractional order initial value problem (IVP for short). More precisely, we will consider the following problem:

$$({}^{c}D_0^{r}u)(t,x) = f(t,x,u_{(t,x)}), \text{ for a. a } (t,x) \in J, \tag{1}$$

$$u(t,x) = \phi(t,x), \quad if \ \ (t,x) \in \tilde{J}, \tag{2}$$

$$\begin{cases} u(t,0) = \varphi(t), \\ u(0,x) = \psi(x), \quad (t,x) \in J, \\ \varphi(0) = \psi(0), \end{cases} \tag{3}$$

where $J := [0,\infty) \times [0,\infty)$, $\tilde{J} := [-\alpha,\infty) \times [-\beta,\infty) \backslash [0,\infty) \times [0,\infty)$, ${}^{c}D_0^{r}$ is the standard Caputo's fractional derivative of order $r = (r_1, r_2) \in (0,1] \times (0,1]$, $f : J \times E \to E$ is a given function, $(E, ||\cdot||_E)$ is a (real or complex) Banach space, $\phi : \tilde{J} \to E$ is a given continuous function with $\phi(t,0) = \varphi(t)$, $\phi(0,x) = \psi(x)$ for each $(t,x) \in J$, φ, $\psi : [0,\infty) \to E$ are given absolutely continuous and $\varphi(t)$ and $\psi(x)$ are measurable for all $(t,x) \in J$.

We denote by $u_{(t,x)}$ the element of $C(\tilde{J}, E)$ defined by

$$u_{(t,x)}(s,\tau) = u(t+s, x+\tau); \quad (s,\tau) \in \tilde{J},$$

where $u_{(t,x)}(\cdot,\cdot)$ represents the history of the state u.

Inspired by other studies, we examine the existence of solutions for the problem (1)-(3). The existence of solutions for this problem will be found by using the expanded Darbo's fixed point theorem (Dudek, 2017; Dudek and Olszowy, 2015), and the notion of measure of noncompactness (Ayerbee Toledano et al., 1997) in Fréchet spaces. To the author's knowledge, there are few papers on fractional differential equations with delay in Fréchet spaces. This work aims to further continue this investigation.

The paper is organized as follows: we will go over some essential information in Section 2 that will be applied to the next sections. The main results are presented in Section 3, where we demonstrate that the problems (1)-(3) have mild solutions. In the last section, an example is given to justify the application of our results.

Background materials and preliminaries

In this section, we give some notations, essential definitions of fractional partial integrals and derivatives and preliminary facts to simplify the forthcoming analysis.

Let $J_0 = [0,n] \times [0,n]$; $n > 0$. A measurable function $u : J_0 \to E$ is Bochner integrable if and only if $||u||$ is Lebesgue integrable. For properties of the Bochner integral, see, for instance, Yosida (1980).

$C(J_0)$ is the Banach space of all continuous functions from J_0 into E with the norm

$$\|u\|_\infty = \sup_{(t,x)\in J_0} \|u(t,x)\|.$$

$AC(J_0)$ denotes the space of absolutely continuous functions from J_0 into E. $L^1(J_0)$ is the Banach space of measurable functions $u : J_0 \to E$ which are Bochner integrable and normed by

$$\|u\|_{L^1} = \int_0^n \int_0^n \|u(t,x)\|_E dt dx.$$

Now, we provide some basic overview of fractional calculus.

Definition 1. *(Vityuk and Golushkov, 2004) Let* $r = (r_1, r_2) \in (0,\infty) \times (0,\infty), \theta = (0,0)$ *and* $u \in L^1(J_0)$. *The left-sided mixed Riemann-Liouville integral of order* r *of* u *is defined by*

$$(I_\theta^r u)(t,x) = \frac{1}{\Gamma(r_1)\Gamma(r_2)} \int_0^t \int_0^x (t-s)^{r_1-1}(x-\tau)^{r_2-1} u(s,\tau)\, d\tau ds.$$

In particular,

$$(I_\theta^\theta u)(t,x) = u(t,x),\ (I_\theta^\sigma u)(t,x) = \int_0^t \int_0^x u(s,\tau)\, d\tau ds;$$

for almost all

$$(t,x) \in J_0,$$

where $\sigma = (1,1)$.
For instance, $I_\theta^r u$ exists for all $r_1, r_2 \in (0,\infty) \times (0,\infty)$, when $u \in L^1(J_0)$. Note also that when $u \in C(J_0)$, then $(I_\theta^r u) \in C(J_0)$. Moreover

$$(I_\theta^r u)(t,0) = (I_\theta^r u)(0,x) = 0;\ (t,x) \in J_0.$$

Example 1. Let $\lambda, \omega \in (-1,\infty)$ and $r = (r_1, r_2) \in (0,\infty) \times (0,\infty)$, then

$$I_\theta^r t^\lambda x^\omega = \frac{\Gamma(1+\lambda)\Gamma(1+\omega)}{\Gamma(1+\lambda+r_1)\Gamma(1+\omega+r_2)} t^{\lambda+r_1} x^{\omega+r_2},\ \text{for almost all } (t,x) \in J_0.$$

By $1-r$ we mean $(1-r_1, 1-r_2) \in (0,1] \times (0,1]$. Denoted by $D_{tx}^2 := \frac{\partial^2}{\partial t \partial x}$, the mixed second order partial derivative.

Definition 2. *Vityuk and Golushkov (2004) Let* $r \in (0,1] \times (0,1]$ *and* $u \in L^1(J_0)$. *The mixed fractional Riemann-Liouville derivative of order* r *of* u *is defined by the expression*

$$D_\theta^r u(t,x) = (D_{tx}^2 I_\theta^{1-r} u)(t,x)$$

and the Caputo fractional-order derivative of order r *of* u *is defined by the expression*

$$({}^c D_\theta^r u)(t,x) = \left(I_\theta^{1-r} \frac{\partial^2}{\partial t \partial x} u \right)(t,x).$$

The case $\sigma = (1,1)$ is included, thus we have

$$(D_\theta^\sigma u)(t,x) = ({}^c D_\theta^\sigma u)(t,x) = (D_{tx}^2 u)(t,x),\ \text{for almost all } (t,x) \in J_0.$$

Example 2. Let $\lambda, \omega \in (-1, \infty)$ and $r = (r_1, r_2) \in (0, 1] \times (0, 1]$, then

$$D_\theta^r t^\lambda x^\omega = \frac{\Gamma(1+\lambda)\Gamma(1+\omega)}{\Gamma(1+\lambda-r_1)\Gamma(1+\omega-r_2)} t^{\lambda-r_1} x^{\omega-r_2}, \text{ for almost all } (t, x) \in J_0.$$

We recall the definition of the concept of a sequence of measures of noncompactness, as given in Dudek (2017); Dudek and Olszowy (2015), as follows:

Definition 3. *Let $\mathcal{M}_X$ be the family of all nonempty and bounded subsets of a Fréchet space X. A family of functions α where $\alpha : \mathcal{M}_X \to [0, \infty)$ is said to be a family of measures of noncompactness in the real Fréchet space X if it satisfies the following conditions for all $B, B_1, B_2 \in \mathcal{M}_X$:*

(a) *α is full, that is: $\alpha(B) = 0$ if and only if B is precompact,*

(b) *$\alpha(B_1) \leq \alpha(B_2)$ for $B_1 \subset B_2$,*

(c) *$\alpha(ConvB) = \alpha(B)$,*

(d) *If $\{B_i\}_{i=1,\cdots}$ is a sequence of closed sets from $\mathcal{M}_X$ such that $B_{i+1} \subset B_i$; $i = 1, \cdots$ and if $\lim_{i\to 1} \alpha(B_i) = 0$, then the intersection set $B_\infty := \cap_{i=1}^{\infty} B_i$ is nonempty.*

Some Properties:

(e) *We call the family of measures of noncompactness α to be homogeneous if $\alpha(\lambda B) = |\lambda|\alpha(B)$, for $\lambda \in \mathbb{R}$.*

(f) *If the family α satisfies the condition $\alpha(B_1 \cup B_2) \leq \alpha(B_1) + \alpha(B_2)$, it is called subadditive.*

(g) *It is sublinear if both conditions (e) and (f) hold.*

(h) *We say that the family of measures α has the maximum property if $\alpha(B_1 \cup B_2) = \max\{\alpha(B_1), \alpha(B_2)\}$.*

(i) *The family of measures of noncompactness α is said to be regular if the conditions $(a), (g)$ and (h) hold; (full sublinear and has maximum property).*

For more details on measure of noncompactness and its properties see Appell (1981).

Lemma 1. *A nonempty subset $B \subset X$ is said to be bounded if*

$$\sup_{u \in X} ||u||_n < \infty, \qquad for\ n \in \mathbb{N}.$$

Lemma 2. *Bothe (1998) If Y is a bounded subset of Fréchet space X, then for each $\epsilon > 0$, there is a sequence $\{y_k\}_{k=1}^{\infty} \subset Y$ such that*

$$\alpha(Y) \leq 2\alpha(\{y_k\}_{k=1}^{\infty}) + \epsilon.$$

Lemma 3. **?** *If $\{u_k\}_{k=1}^{\infty} \subset L^1(J_0)$ is uniformly integrable, then $\alpha(\{u_k\}_{k=1}^{\infty})$ is measurable and for each $(t, x) \in J_0$,*

$$\alpha\left(\left\{\int_0^t \int_0^x u_k(s,\tau)d\tau ds\right\}_{k=1}^{\infty}\right) \leq 2\int_0^t \int_0^x \alpha(\{u_k(s,\tau)\}_{k=1}^{\infty})d\tau ds.$$

Definition 4. *Let Ω be a nonempty subset of a Fréchet space X, and let $A : \Omega \to X$ be a continuous operator which transforms bounded subsets. One says that A satisfies the Darbo condition with constants $(k_n)_{n\in\mathbb{N}}$ with respect to a family of measures of noncompactness α, if*

$$\alpha(A(B)) \leq k_n\alpha(B),$$

for each bounded set $B \subset \Omega$ and $n \in \mathbb{N}$.

If $k_n < 1,\ n \in \mathbb{N}$ then A is called a contraction with respect to α.

The following expanded Darbo's fixed point theorem for Fréchet spaces will be utilized in the sequel.

Theorem 1. *Dudek (2017); Dudek and Olszowy (2015) Let Ω be a nonempty, bounded, closed, and convex subset of a Fréchet space X and let $V : \Omega \longrightarrow \Omega$ be a continuous mapping. Suppose that V is a contraction with respect to a family of measures of noncompactness α. Then V has at least one fixed point in the set Ω.*

Existence and uniqueness of mild solutions

This section is devoted to the proof of the global existence of solutions for the problem (1)-(3).

For each $n \in \mathbb{N}$ we consider the following set,

$$C_n = C([-\alpha, n] \times [-\beta, n], E)$$

and we define in $C_0 := C([-\alpha, \infty) \times [-\beta, \infty), E)$ the semi-norms by:

$$\|u\|_n = \{\sup \|u(t,x)\| : -\alpha \leq t \leq n, -\beta \leq x \leq n\}.$$

Then C_0 is a Fréchet space with the family of semi-norms $\{\|u\|_n\}$.

Let us begin by explaining what we mean by a solution of the problem (1)-(3).

Definition 5. *A function $u \in C_0$ is said to be a solution of (1)-(3) if u satisfies the equations (1) and (3) on J and the condition (2) on $\tilde{J}$.*

We shall use the following lemma for the existence of solutions for the problem (1)-(3):

Lemma 4. *A function $u \in C_0$ is a solution of problem (1)-(3) if and only if u satisfies the equation*

$$u(t,x) = z(t,x) + \frac{1}{\Gamma(r_1)\Gamma(r_2)} \int_0^t \int_0^x (t-s)^{r_1-1}(x-\tau)^{r_2-1} f(s,\tau,u_{(s,\tau)})d\tau ds,$$

for all $(t,x) \in J$ and the condition (2) on $\tilde{J}$, where

$$z(t,x) = \varphi(t) + \psi(x) - \varphi(0).$$

we propose the following assumptions to prove our main results:

$(H1)$ The functions $\varphi(t)$ and $\psi(x)$ are measurable and bounded for a.e. $(t,x) \in J_0$,

$(H2)$ The function $(t,x) \to f(t,x,u)$ is measurable on J_0, and the function $u \to f(t,x,u)$ is continuous on E for a. e. $(t,x) \in J_0$.

$(H3)$ There exist functions $p_1, p_2 : J_0 \to [0,\infty)$ such that for each $(t,x) \in J_0$,

$$\|f(t,x,u)\|_E \leq p_1(t,x) + p_2(t,x)\|u\|_n, \qquad for\ all\ u \in E.$$

$(H4)$ For each $(t,x) \in J_0$, and any bounded $B \subset X$,

$$\alpha(f(t,x,B)) \leq p_2(t,x)\alpha(B),$$

where α is a measure of noncompactness on the Banach space E.

$(H5)$ There exists a positive real number R_n such that

$$z^* + \frac{[p_{1n}^* + p_{2n}^* R_n]n^{r_1+r_2}}{\Gamma(r_1+1)\Gamma(r_2+1)} \leq R_n,$$

where

$$z^* = \sup_{(t,x)\in J_0} \|z(t,x)\|_E, \qquad p_{in}^* = \sup_{(t,x)\in J_0} p_i(t,x), i = 1,2.$$

M. Helal, Applications of the expanded Darbo's fixed point theorem to fractional differential equations with finite delay, pp.269–282

Theorem 2. *Assuming that assumptions* $(H1)$-$(H5)$ *hold. If*

$$\ell_n := \frac{4p^*_{2n}n^{r_1+r_2}}{\Gamma(r_1+1)\Gamma(r_2+1)} < 1,$$

then the propsed problem (1)-(3) *has at least one mild solution.*

Proof. Define the operator $N : C_0 \to C_0$ by

$$(Nu)(t,x) = \begin{cases} \phi(t,x), & (t,x) \in \tilde{J}, \\ z(t,x) \\ +\dfrac{1}{\Gamma(r_1)\Gamma(r_2)}\displaystyle\int_0^t\int_0^x (t-s)^{r_1-1}(x-\tau)^{r_2-1} \\ \times f(s,\tau,u_{(s,\tau)})d\tau ds, & (t,x) \in J. \end{cases} \tag{4}$$

It is evident that the fixed points of the operator N are solutions of our problem (1)-(3).

We consider the ball $B_{R_n} = \{u \in C_0 : \|u\|_n \leq R_n\}$, then from $(H3)$, for any $u \in B_{R_n}$, we obtain

$$\|(Nu)(t,x)\|_E \leq$$

$$\begin{aligned}
&\leq \|z(t,x)\|_E + \int_0^t\int_0^x \frac{(t-s)^{r_1-1}(x-\tau)^{r_2-1}}{\Gamma(r_1)\Gamma(r_2)}\|f(s,\tau,u_{(s,\tau)})\|_E d\tau ds \\
&\leq \|z(t,x)\|_E + \frac{1}{\Gamma(r_1)\Gamma(r_2)}\int_0^t\int_0^x (t-s)^{r_1-1}(x-\tau)^{r_2-1}p_1(s,\tau)d\tau ds \\
&+\frac{1}{\Gamma(r_1)\Gamma(r_2)}\int_0^t\int_0^x (t-s)^{r_1-1}(x-\tau)^{r_2-1}p_2(s,\tau)\|u_{(s,\tau)}\|d\tau ds \\
&\leq z^*(w) + \frac{p^*_{1n}}{\Gamma(r_1)\Gamma(r_2)}\int_0^t\int_0^x (t-s)^{r_1-1}(x-\tau)^{r_2-1}d\tau ds \\
&+\frac{p^*_{2n}R_n}{\Gamma(r_1)\Gamma(r_2)}\int_0^t\int_0^x (t-s)^{r_1-1}(x-\tau)^{r_2-1}d\tau ds \\
&\leq z^* + \frac{[p^*_{1n}+p^*_{2n}R_n]n^{r_1+r_2}}{\Gamma(r_1+1)\Gamma(r_2+1)} \\
&\leq R_n.
\end{aligned}$$

This demonstrates that N transforms the ball B_{R_n} into itself.

We shall show that the operator $N : B_{R_n} \to B_{R_n}$ satisfies all the conditions of Theorem 1.

The proof will proceed in a sequence of steps.

Step 1: N is continuous.
Let $\{u_m\}_{m\in\mathbb{N}}$ be a sequence such that $u_m \to u$ in C_0. Then, for each $(t,x) \in J_0$, we have

$$\begin{aligned} & \|(Nu_m)(t,x) - (Nu)(t,x)\| \\ \leq & \frac{1}{\Gamma(r_1)\Gamma(r_2)} \int_0^t \int_0^x (t-s)^{r_1-1}(x-\tau)^{r_2-1} \|f(s,\tau,u_{m(s,\tau)}) - \\ - & f(s,\tau,u_{(s,\tau)})\| d\tau ds. \end{aligned}$$

Since $u_m \to u$ as $m \to \infty$, the Lebesgue dominated convergence theorem implies that

$$\|Nu_m - Nu\|_n \to 0 \text{ as } m \to \infty.$$

Step 2: $N(B_{R_n})$ is bounded.
Since $N(B_{R_n}) \subset B_{R_n}$ and B_{R_n} is bounded, then $N(B_{R_n})$ is bounded.

Step 3: For each bounded subset D of B_{R_n}, we have

$$\alpha(N(D)) \leq \ell_n \alpha(D).$$

From Lemmas 2 and 3, for any $D \subset B_{R_n}$ and any $\epsilon > 0$, there exists a sequence $\{u_m\}_{m=0}^{\infty} \subset D$, such that for all $(t,x) \in J_0$, we have

$$\begin{aligned} & \alpha((N(D))(t,x)) \\ & = \alpha\left(\left\{ z(t,x) + \int_0^t \int_0^x \frac{(t-s)^{r_1-1}(x-\tau)^{r_2-1}}{\Gamma(r_1)\Gamma(r_2)} f(s,\tau,u_{(s,\tau)}) d\tau ds;\ u \in D \right\}\right) \\ & \leq \left\{ \int_0^t \int_0^x \frac{(t-s)^{r_1-1}(x-\tau)^{r_2-1}}{\Gamma(r_1)\Gamma(r_2)} f(s,\tau,u_{m(s,\tau)}) d\tau ds \right\}_{m=1}^{\infty} + \epsilon \\ & \leq 4 \int_0^t \int_0^x \alpha\left(\left\{ \frac{(t-s)^{r_1-1}(x-\tau)^{r_2-1}}{\Gamma(r_1)\Gamma(r_2)} f(s,\tau,u_{m(s,\tau)}) \right\}_{m=1}^{\infty} \right) d\tau ds + \epsilon \\ & \leq 4 \int_0^t \int_0^x \frac{(t-s)^{r_1-1}(x-\tau)^{r_2-1}}{\Gamma(r_1)\Gamma(r_2)} \alpha\left(\{f(s,\tau,u_{m(s,\tau)})\}_{m=1}^{\infty} \right) d\tau ds + \epsilon \\ & \leq 4 \int_0^t \int_0^x \frac{(t-s)^{r_1-1}(x-\tau)^{r_2-1}}{\Gamma(r_1)\Gamma(r_2)} p_2(s,\tau) \alpha\left(\{u_{m(s,\tau)}\}_{m=1}^{\infty} \right) d\tau ds + \epsilon \\ & \leq \left(4 \int_0^t \int_0^x \frac{(t-s)^{r_1-1}(x-\tau)^{r_2-1}}{\Gamma(r_1)\Gamma(r_2)} p_2(s,\tau) d\tau ds \right) \alpha\left(\{u_m\}_{m=1}^{\infty} \right) + \epsilon \\ & \leq \left(4 \int_0^t \int_0^x \frac{(t-s)^{r_1-1}(x-\tau)^{r_2-1}}{\Gamma(r_1)\Gamma(r_2)} p_2(s,\tau) d\tau ds \right) \alpha(D) + \epsilon \end{aligned}$$

M. Helal, Applications of the expanded Darbo's fixed point theorem to fractional differential equations with finite delay, pp.269–282

$$\leq \left(\frac{4p_{2n}^{*}n^{r_1+r_2}}{\Gamma(r_1+1)\Gamma(r_2+1)}\right)\alpha(D)+\epsilon$$
$$=\ell_n\alpha(D)+\epsilon.$$

Since $\epsilon>0$ is arbitrary, then

$$\alpha(N(D))\leq \ell_n\alpha(D).$$

As a consequence of steps 1 to 3, together with Theorem 1, we can conclude that N has at least one fixed point in B_{R_n} which is a mild solution of problem (1)-(3).

Applications

Let us examine the following example as an application of our findings.

Example 3. *Let $E=\mathbb{R}$ be equipped with the usual σ-algebra consisting of Lebesgue measurable subsets of $(-\infty,0)$.*

$$({}^{c}D_0^{r}u)(t,x)=\frac{c_n}{e^{t+x+2}(1+|u(t-1,x-2)|)};\ \textit{if}\ (t,x)\in J:=[0,\infty)\times[0,\infty), \tag{5}$$

$$u(t,x)=t+x^2,\ (t,x)\in\tilde{J}:=[-1,\infty)\times[-2,\infty)\backslash[0,\infty)\times[0,\infty), \tag{6}$$

$$\begin{cases}u(t,0)=t,\\ u(0,x)=x^2,\end{cases}\quad (t,x)\in J, \tag{7}$$

Where

$$c_n=\frac{\Gamma(r_1+1)\Gamma(r_2+1)}{n^{r_1+r_2}};\quad n\in\mathbb{N}^{*}.$$

$$f(t,x,u_{(t,x)})=\frac{c_n}{e^{t+x+2}(1+|u(t-1,x-2)|)};\qquad (t,x)\in J.$$

The function $(t,x)\mapsto f(t,x,u)$ is jointly continuous for all $u\in C(J,E)$ and hence jointly measurable for all $u\in C(J,E)$. Also the map $u\mapsto f(t,x,u)$ is continuous for all $(t,x)\in J$. Thus, the function f is Carathéodory on $J\times E$. For each $u\in E,\ (t,x)\in J$, we have

$$|f(t,x,u)|\leq 1+\frac{c_n|u|}{e^3}.$$

Hence the condition $(H3)$ is satisfied with $p_{1n}^{*}=1,\ p_{2n}^{*}=c_ne^{-3}$.

Moreover, the condition $(H4)$ *is satisfied. We shall show that the condition* $\ell_n < 1$ *holds for each* $(r_1, r_2) \in (0;1] \times (0;1]$ *we obtain*

$$\begin{aligned} \ell_n &= \frac{4p^*_{2n} n^{r_1+r_2}}{\Gamma(r_1+1)\Gamma(r_2+1)} \\ &= \frac{4}{e^3} \\ &< 1. \end{aligned}$$

As a result, Theorem 2 *implies that our problem* (5)-(7) *has a fixed point* u *defined on* J *which is a solution of our problem* (5)-(7).

Conclusion

Fractional calculus is a broad topic that calls for a variety of techniques and sophisticated tools. In this paper, we have contributed to the study of various classes of Darboux problems for partial hyperbolic functional fractional differential equations via the Caputo derivative with finite delay in Fréchet spaces.

Throughout most of this paper, sufficient conditions were considered in order to obtain the existence and uniqueness of solutions for our problem by reducing the research to the existence and uniqueness of fixed points of suitable operators, using the expanded Darbo's fixed point theorem associated with the notion of measure of noncompactness. There are numerous directions in which the work presented here can be extended. To find existence results, one should examine the properties of the operators and the structure of the space. The presence of weighted continuous functions in the space, their uniqueness, the composition of the solution set, and the optimality of the conditions met by the operators are just a few of the numerous other topics and questions that can be investigated.

References

Baleanu, D., Diethelm, K., Scalas, E., and Trujillo, J. J. (2012). *Fractional Calculus Models and Numerical Methods*. World Scientific Publishing, New York. Available at: https://doi.org/10.1142/9789814355212

Abbas, S. and Benchohra, M. (2009). Darboux problem for perturbed partial differential equations of fractional order with finite delay. *Nonlinear Analysis: Hybrid Systems*, 3, 597-604. Available at: https://doi.org/10.1016/j.nahs.2009.01.001

Abbas, S. and Benchohra, M. (2012). Fractional order partial hyperbolic differential equations involving Caputo's derivative. *Studia Universitatis Babeş–Bolyai Mathematica*, 57(4), 469-479.

Abbas, S., Benchohra, M., and N'Guérékata, G. M. (2012). *Topics in Fractional Differential Equations*. Springer, New York. Available at: https://doi.org/10.1007/978-1-4614-4036-0

Appell, J. (1981). Implicit functions, nonlinear integral equations, and the measure of noncompactness of the superposition operator. *Journal of Mathematical Analysis and Applications*, 83, 251-263. Available at: https://doi.org/10.1016/0022-247X(81)90160-9

Ayerbee Toledano, J. M., Dominguez Benavides, T., and López Acedo, G. (1997). *Measures of noncompactness in metric fixed point theory*. Operator Theory: Advances and Applications, 99. Birkhäuser, Basel, Boston, Berlin. Available at: https://doi.org/10.1007/978-3-0348-8875-7

Banaei, Sh. (2018). Solvability of a system of integral equations of Volterra type in the Fréchet space $L^p_{loc}(\mathbb{R}^+)$ via measure of noncompactness. *Filomat*, 32, 5255-5263. Available at: https://doi.org/10.2298/FIL1813255B

Banás, J., Jleli, M., Mursaleen, M., and Samet, B. (2017). *Advances in Nonlinear Analysis via the Concept of Measure of Noncompactness*. Springer, Singapore. Available at: https://doi.org/10.1007/978-981-10-4565-8

Banás, J., and Mursaleen, M. (2014). *Sequence Spaces and Measures of Noncompactness with Applications to Differential and Integral Equations*. Springer, Berlin. Available at: https://doi.org/10.1007/978-3-319-01392-4

Benchohra, M., and Hellal, M. (2014). Global uniqueness result for fractional partial hyperbolic differential equations with state-dependent delay. *Annales Polonici Mathematici*, 110(3), 259-281. Available at: https://doi.org/10.4064/ap110-3-2

Benchohra, M., and Hellal, M. (2014). Perturbed partial fractional order functional differential equations with infinite delay in Fréchet spaces. *Nonlinear Dynamics and System Theory*, 14(3), 244-257. Available at: https://doi.org/10.1007/s11071-014-1491-5

Benchohra, M., Henderson, J., and Heris, A. (2017). Fractional partial random differential equations with delay. *PanAmerican Mathematical Journal*, 27(1), 29-40. Available at: https://doi.org/10.1007/s40815-017-0034-2

Bothe, D. (1998). Multivalued perturbation of m-accretive differential inclusions. *Israel Journal of Mathematics*, 108, 109-138. Available at: https://doi.org/10.1007/BF02777780

Dudek, S. (2017). Fixed point theorems in Fréchet Algebras and Fréchet spaces and applications to nonlinear integral equations. *Applied Analysis and Discrete Mathematics*, 11, 340-357. Available at: https://doi.org/10.2298/AADM170340D

Dudek, S., and Olszowy, L. (2015). Continuous dependence of the solutions of nonlinear integral quadratic Volterra equation on the parameter. *Journal of Function Spaces*, 2015, Article ID 471235, 9 pages. Available at: https://doi.org/10.1155/2015/471235

Helal, M. (2020). Perturbed Partial Functional Differential Equations on Unbounded Domains with Finite Delay. *Applied Mathematics E-Notes*, 20, 82-92. Available at: https://doi.org/10.2478/AMEN-2020-0010

Hilfer, R. (2000). *Applications of Fractional Calculus in Physics*. World Scientific, Singapore. Available at: https://doi.org/10.1142/9789812816223

Kilbas, A. A., and Marzan, S. A. (2005). Nonlinear differential equations with the Caputo fractional derivative in the space of continuously differentiable functions. *Differential Equations*, 41, 84-89. Available at: https://doi.org/10.1007/s10625-005-0010-4

Kuratowski, K. (1930). Sur les espaces complets. *Fundamenta Mathematicae*, 15, 301-309. Available at: https://doi.org/10.4064/fm-15-1-301-309

Ortigueira, M. D. (2011). *Fractional Calculus for Scientists and Engineers*. Lecture Notes in Electrical Engineering, 84. Springer, Dordrecht. Available at: https://doi.org/10.1007/978-94-007-0531-3

Podlubny, I. (1999). *Fractional Differential Equations*. Academic Press, San Diego. Available at: https://doi.org/10.1016/B978-0-12-558840-9.X5000-3

Tarasov, V. E. (2010). *Fractional Dynamics. Applications of Fractional Calculus to Dynamics of Particles, Fields and Media*. Springer, Heidelberg. Available at: https://doi.org/10.1007/978-3-642-11218-3

Vityuk, A. N., and Golushkov, A. V. (2004). Existence of solutions of systems of partial differential equations of fractional order. *Nonlinear Oscillations*, 7(3), 318-325. Available at: https://doi.org/10.1023/B:NONO.0000045252.92915.0f

Yosida, K. (1980). *Functional Analysis*, 6th edition. Springer-Verlag, Berlin. Available at: https://doi.org/10.1007/978-3-662-02410-7

Mönch, H. (1980). Boundary value problems for nonlinear ordinary differential equations of second order in Banach spaces. *Nonlinear Analysis: Theory, Methods and Applications*, 4, 985-999. Available at: https://doi.org/10.1016/0362-546X(80)90076-6

Primene proširene Darboove teoreme o fiksnoj tački na frakcione diferencijalne jednačine sa konačnim kašnjenjem

Mohamed Helal

Mustapha Stambouli University of Mascara, Science and Technology Faculty, B.P. 763, 29000, Mascara, Algeria,+
Djillali Liabes University of Sidi Bel-Abbès, Laboratory of Mathematics, B.P. 89, 22000, Sidi Bel-Abbès, Algeria

OBLAST: matematika
KATEGORIJA (TIP) ČLANKA: originalni naučni rad

Sažetak:

Uvod/cilj: Cilj rada je proučavanje postojanja blagih rešenja problema početne vrednosti Darbuovog problema za parcijalne hiperboličke frakcione diferencijalne jednačine pomoću Kaputovog izvoda sa konačnim kašnjenjem u Frešeovim prostorima.

Metode: U analizi se koriste Darboova teorema o fiksnoj tački sa pojmom mere nekompaktnosti kako bi se utvrdilo postojanje rešenja svođenjem istraživanja na dokazivanje postojanja i jedinstvenosti fiksnih tačaka odgovarajućih operatora.

Rezultati: Postojanje blagih rešenja posmatranih parcijalnih hiperboličkih frakcionih diferencijalnih jednačina je dokazano pod odgovarajućim uslovima. Primenljivost teorijskih rezultata je ilustrovana primerom.

Zaključak: U radu se razmatraju dovoljni uslovi za utvrđivanje postojanja i jedinstvenosti rešenja Darbuovog problema primenom Darboove teoreme o fiksnoj tački na neograničenom intervalu. Istraživanje pruža metodološki okvir za analizu sličnih problema i doprinosi širem razumevanju blagih rešenja u frakcionom računu i funkcionalnoj analizi. Dobijeni rezultati nude potencijalne primene za istraživače koji se bave frakcionim diferencijalnim jednačinama u beskonačno-dimenzionalnim prostorima.

Ključne reči: parcijalna hiperbolička diferencijalna jednačina, frakcioni izvod, blago rešenje, Frešeov prostor.

Paper received on: 11 April 2025.
Manuscript corrections submitted on: 11 February 2025.
Paper accepted for publishing on: 16 March 2026.

© 2026 The Authors. Published by Vojnotehnički glasnik / Military Technical Courier (http://vtg.mod.gov.rs). This article is an open access article distributed under the terms and conditions of the Creative Commons Attribution license (http://creativecommons.org/licenses/by/4.0/rs/).

Multi-attribute approach for enhancing maintenance processes in maintenance depots under a type-2 fuzzy environment

Vladimir Milovanović[a], *Aleksandar* Aleksić[b], *Snežana* Nestić[c], *Nikola* Komatina[d], *Vlada* Sokolović[e], *Marjan* Milenkov[f]

[a] University of Defence, Military Academy, Belgrade, Republic of Serbia,
e-mail: vladimir.milovanovic@va.mod.gov.rs,
ORCID iD: https://orcid.org/0000-0002-5109-4321

[b] University of Kragujevac, Faculty of Engineering, Kragujevac, Republic of Serbia,
e-mail: aaleksic@kg.ac.rs, **corresponding author**,
ORCID iD: https://orcid.org/0000-0002-7990-9123

[c] University of Kragujevac, Faculty of Engineering, Kragujevac, Republic of Serbia,
e-mail: s.nestic@kg.ac.rs,
ORCID iD: https://orcid.org/0000-0003-1461-9595

[d] University of Kragujevac, Faculty of Engineering, Kragujevac, Republic of Serbia,
e-mail: nkomatina@kg.ac.rs,
ORCID iD: https://orcid.org/0000-0001-6964-5673

[e] University of Defence, Military Academy, Belgrade, Republic of Serbia,
e-mail: vlada.sokolovic@va.mod.gov.rs,
ORCID iD: https://orcid.org/0000-0003-0782-0506

[f] University of Defence, Military Academy, Belgrade, Republic of Serbia,
e-mail: marjan.milenkov@va.mod.gov.rs,
ORCID iD: https://orcid.org/0000-0003-2054-0525

https://doi.org/10.5937/vojtehg74-58054

FIELD: mathematics, decision sciences, industrial engineering
ARTICLE TYPE: original scientific paper

Abstract:

Introduction/purpose: The purpose of this research is to determine the priority of Key Performance Indicators (KPIs) in a precise and structured manner. By applying the fuzzy multi-attribute decision-making model, operational management can identify and prioritize activities that will enhance maintenance process reliability in the shortest possible time while simultaneously reducing costs.

ACKNOWLEDGMENT: The work stemmed from the project Model of Logistics Support Planning Support System (VA-TT-1 / 20-25). The research was funded by the Ministry of Science, Technological Development and Innovation of the Republic of Serbia, contract number 451-03-136/2025-03/200107 (Faculty of Engineering, University of Kragujevac).

Methods: The relative importance of sub-processes and KPI values is represented using predefined linguistic terms modelled by interval type-2 fuzzy numbers (IT2FNs). *These assessments are formulated as a fuzzy group decision-making framework. The weight vector is determined using the fuzzy geometric mean, while the ranking of KPIs is obtained through the Taxonomy method combined with IT2FNs, which represents the main scientific contribution of this research.*

Results: Real-world data gathered from a maintenance depot were used to test the proposed model. The study effectively modelled uncertainty in KPI evaluations using seven predefined linguistic expressions mapped onto IT2FNs. A consistent weight vector was obtained using the fuzzy group decision-making approach. Effective KPI ranking was achieved through a combination of the Taxonomy method and IT2FNs, which helped pinpoint the most important areas for operational improvement. The method's ability to provide clear priorities to support reliability improvements while cutting costs was validated through its application.

Conclusion: The key contributions of this study are: (i) fuzzy algebra rules with IT2FNs are used to determine the group utility value, and (ii) the integration of the Taxonomy method with IT2FNs for an improved decision-making procedure.

Key words: key performance indicators, operational management, maintenance process reliability, interval type-2 fuzzy numbers, Taxonomy method, group decision-making.

Introduction

In recent decades, with the rapid advancement of technology, maintenance has become one of the key business processes in manufacturing companies, particularly within maintenance systems. The complexity of maintenance systems in terms of organization, technology, and resource diversity creates conditions for unforeseen losses, which are often invisible to management but directly impact the achievement of established goals.

Generally, the overhaul process can be defined as the restoration of resources through the application of approved technological procedures. It consists of complementary preventive and corrective maintenance processes. The overhaul process ensures the required reliability of assets in operation, ultimately achieving their expected operational readiness. At the same time, this process requires specialized verification and maintenance-related technical documentation.

Developing a model for measuring key performance indicators (KPIs) in the execution of core activities within complex maintenance

systems enables management to achieve target values more quickly and efficiently, which are of strategic importance for system functionality.

Research trends indicate that the relative importance of sub-processes and KPI values can be more precisely described using linguistic variables. The development of mathematical theories, such as type-2 fuzzy set theory (Zadeh, 1988), has enabled accurate quantification of these linguistic variables. One advantage of type-2 fuzzy sets over other kinds of fuzzy sets is that they offer more flexibility and freedom, enabling better handling of uncertainty (Mendel & John, 2002). The requirement for intricate and time-consuming computational processes is a major drawback of using type-2 fuzzy sets in real-world decision-making situations. Many authors recommend using interval type-2 fuzzy numbers, which are a special case of type-2 fuzzy sets, to overcome this limitation (Tadić & Komatina, 2025; Komatina et al., 2022; Celik, Yucesan, & Gul, 2021; Đurić et al., 2019; Aleksic et al., 2019; Zhong & Yao, 2017). The domain, granularity, and membership function are the primary features of fuzzy numbers. In the literature, interval type-2 triangular fuzzy numbers (IT2FNs) are most commonly used, as they effectively capture the imprecision inherent in natural language expressions. Granularity can be defined as the number of linguistic expressions used to describe the considered uncertainty. When determining granularity, decision-makers (DMs) must take into account the size of the problem. The domains of the used IT2FNs are defined on the real line, belonging to different intervals. In this research, existing uncertainties are described using seven linguistic expressions. The domains of IT2FNs, which model these uncertainties, are defined on the measurement scale [1-10].

Many authors suggest that the assessment of relative importance should be framed as a fuzzy group decision-making problem, as in (Komatina et al., 2025; Tadić et al., 2025; Tian, Wang, & Zhang, 2018). Additionally, many authors argue that when there are more attributes, as in this study, determining the weight vector is easier and more accurate through the application of subjective methods combined with fuzzy algebra rules (Komatina, 2025; Sudžum et al., 2024; Božanić et al., 2024; Xu et al., 2024; Komatina et al., 2023; Aleksić et al., 2023). In this paper, the fuzzy geometric mean operator is used to determine the unique assessment of the relative importance of sub-processes. The normalized weight vector is determined using a linear normalization procedure (Palczewski & Sałabun, 2019).

Ranking the KPIs, taking into account all sub-processes as well as their weights under a type-2 uncertain environment, can be considered a

MADM problem extended with IT2FNs, as in Aleksić & Tadić (2023), Celik et al. (2015), Mardani, Jusoh, & Zavadskas (2015). In many studies found in the literature (Keshavarz Ghorabaee et al., 2017), determining the values of the elements of the fuzzy decision matrix is treated as a fuzzy group decision-making problem (Oğuz, 2024; Toptancı et al., 2023), as in this research. In general, attributes can be either of the benefit or cost type. In such cases, it is necessary to construct a normalized fuzzy decision matrix to determine the values, thereby increasing the computational effort. To reduce the computational load, some authors have introduced the assumption that, when assessing the value of alternatives, decision-makers should consider the attribute type (Li et al., 2022; Đurić et al., 2019). There are also studies in which the authors formulate the problem in such a way that the attributes are of the same type (Petrović et al., 2022; Aleksic et al., 2019). In this research, the sub-processes are of the same type, so there is no need to apply the normalization process. After constructing the weighted fuzzy decision matrix, the developed MADM method can be applied to determine the ranking. It should be noted that the choice of the MADM method can be considered a separate problem.

In the literature, there are several papers where the Taxonomy method has been extended with different types of fuzzy numbers and applied to determine the ranking of alternatives in various research domains. In Centobelli, Cerchione, & Esposito (2018), the Taxonomy method is proposed for evaluating operational tools at the level of each macro area. The paper shows how enterprises can use this tool to understand which category they belong to and support decision-making for introducing changes that lead to improved alignment levels. The weight vector of macro perspectives is determined using the Delphi method. At the level of each macro-perspective, operational tools are defined. The values of the defined operational tools are described by predefined linguistic terms. The modeling of these linguistic expressions is done using trapezoidal fuzzy numbers of the first order. Based on the results obtained, decision-makers can identify measures to support the competitiveness of local systems by improving management processes.

Taxonomy with spherical fuzzy sets is proposed by Diao, Cai, & Wei (2022). The paper discusses the problem of selecting car rental companies according to various criteria. The criteria weights are determined using the entropy method. The values of the criteria are described by spherical fuzzy sets (Kutlu Gündoğdu & Kahraman, 2019). The spherical fuzzy composite distance matrix is calculated according to the procedure proposed by the conventional Taxonomy method and

fuzzy algebra rules with spherical fuzzy sets (Szmidt & Kacprzyk, 2000). The ranking of the considered companies is determined according to the conventional Taxonomy method. The problem of ranking companies according to technological innovations using the Taxonomy method with T-Spherical Fuzzy Numbers is proposed by Liu & Wang (2022). The elements of the fuzzy decision matrix are modeled by T-Spherical Fuzzy Numbers (Mahmood et al., 2019). These fuzzy numbers represent an extension of Pythagorean fuzzy numbers (Peng & Yang, 2016) and intuitionistic fuzzy numbers (Atanassov, 1999), which can depict a neutral attitude in human thinking with a considerably large expression range. In Wei et al. (2020), the authors propose a fuzzy two-stage multi-attribute decision model with Pythagorean fuzzy numbers. The proposed model is tested on an example involving rating and selecting tourist destinations. The values of the elements of the fuzzy decision matrix are determined by the Pythagorean fuzzy weighted average operator (Peng & Yang, 2016). The weight vector is determined using the procedure proposed in the entropy method and the normalized Hamming distance (Zhang & Xu, 2014). The ranking of the considered tourist destinations is obtained by the conventional Taxonomy method combined with fuzzy algebra rules with Pythagorean fuzzy numbers.

The broader objective of this research can be interpreted as the integration of the following approaches: (i) modeling existing uncertainties in the relative importance of sub-processes and KPI values using IT2FNs, (ii) determining the relative importance of sub-processes as a fuzzy group decision-making problem; the fuzzy weights vector is determined using the fuzzy geometric mean combined with a linear normalization procedure, (iii) ranking KPIs using the proposed Taxonomy method with IT2FNs, and (iv) implementing appropriate methods to improve KPI values, thus enhancing the effectiveness and reliability of the maintenance depot.

The rest of the paper is organized as follows: Section 2 describes the proposed two-stage fuzzy model. A case study with real-world data is presented in Section 3, while Section 4 provides the conclusion.

Methodology

This section provides a brief overview of the proposed two-stage fuzzy model. In the first stage, the weights of sub-processes are determined using a subjective approach. In the second stage, the ranking of the considered KPIs is established, enabling decision-makers to select the KPIs that need to be improved in order to increase the operational

efficiency of the maintenance depot. A simple graphical representation of the proposed model is presented in Figure 1.

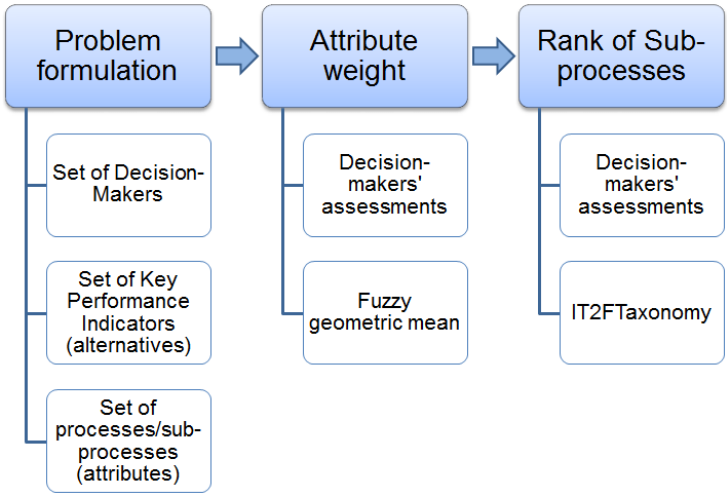

Figure 1 – The proposed model

In the following section, additional explanations of the proposed model are provided, along with detailed guidelines for applying this approach. The interval type-2 fuzzy algebra used is presented in the Appendix.

Defining the set of decision-makers

The assessment of the relative importance of the sub-processes and KPI values, as well as their evaluation, was conducted by ten DMs originating from the maintenance sector of six manufacturing companies, including the considered maintenance depot. In this case, a total of three maintenance managers, four maintenance engineers, and three maintenance operators participated.

The DMs were selected to ensure a balanced representation of all hierarchical levels within the maintenance sector, namely the managerial, engineering, and operational levels. Maintenance managers were selected from three of the six companies. They are responsible for strategic decisions within the maintenance department. Four maintenance engineers were chosen based on their practical experience, as well as three maintenance operators who are directly involved in the execution of daily maintenance activities. One of the key criteria for

selecting the decision-makers was that they possess a minimum of five years of work experience in the maintenance sector.

These DMs are formally represented by the set of indices $\{1, \dots, e, \dots, E\}$. The total number of DMs is denoted as E, and a DM index is represented as e, where $e, e = 1, \dots, E$.

In the case of KPI value assessment, the evaluation was conducted by five employees from the considered maintenance depot. The assessment team comprised the maintenance depot manager, two maintenance engineers, and two maintenance operators. In this case, the DMs are formally presented by the set of indices $\{1, \dots, j, \dots, J\}$. The total number of DMs is denoted as J, and a DM index is represented as j, where $j, j = 1, \dots, J$.

The presented two-step decision-making approach is aligned with the objectives of the study. In the first phase, DMs from six manufacturing companies participated in order to objectively assess the importance of sub-processes and minimize the impact of the specific situation and characteristics of just one organization. In the second phase, the evaluations were carried out exclusively by employees of the considered maintenance depot, as they were directly relevant to the considered case study.

Defining the set of alternatives

In the general case, DMs define a varying number of KPIs that are essential for monitoring the reliability of the maintenance process in the considered maintenance depot. The set of KPIs is represented by the index set $\{1, \dots, i, \dots, I\}$. The total number of KPIs is denoted as I, and the index of a KPI is represented as i, where $i = 1, \dots, I$.

In this study, the following KPIs are considered:

- Availability of protective equipment required in the maintenance process $(i = 1)$,
- Customer satisfaction with the maintenance service $(i = 2)$,
- Material supply of spare parts and consumables $(i = 3)$,
- Implementation level of occupational safety measures in the maintenance process $(i = 4)$,
- Availability of general and specialized tools and equipment $(i = 5)$,
- Required knowledge and skills level of experts $(i = 6)$,
- Coordination level with other units of the maintenance organization $(i = 7)$,
- Ability to follow modern maintenance trends $(i = 8)$,

- Compliance level of procedures ($i = 9$),
- Availability of experts ($i = 10$),
- Accessibility of technical documentation and literature ($i = 11$),
- Availability of workshop capacities ($i = 12$).

The term KPI is commonly used for quantitative and measurable indicators that directly affect system performance (e.g., downtime, effectiveness, efficiency, number of complaints, etc.). In this paper, it is important to note that the term is used in a broader sense. In this context, KPIs refer to all factors that have a significant impact on the performance of the maintenance sector, even if they are not necessarily part of performance metrics. Essentially, KPIs in this study include various factors and characteristics of the system. As previously mentioned, this interpretation and use of the term have been applied in relevant literature, and that approach was adopted in this research.

Defining the set of attributes

In this research, the considered attributes are sub-processes of the maintenance process in the maintenance depot. Generally, the set of considered sub-processes is represented by the index set $\{1, \dots, p, \dots, P\}$. The total number of sub-processes is denoted as $\boldsymbol{P}$, and the index of a sub-process is represented as p, where $p = 1, \dots, P$.

The selected sub-processes of the considered maintenance depot are (Milovanović et al., 2024):

- Defect detection in the assembled state ($p = 1$),
- Dismantling of assemblies, subassemblies, and components ($p = 2$),
- Regeneration of spare parts ($p = 3$),
- Assembly, adjustment, and partial testing ($p = 4$),
- Final inspections ($p = 5$),
- Painting of equipment ($p = 6$),
- Testing ($p = 7$),
- Verification of the maintenance process and documentation completion ($p = 8$),
- Identification and risk assessment ($p = 9$).

Defining a set of linguistic variables for describing uncertain data

In this research, uncertain data, such as the relative importance of sub-processes and KPI values, are adequately assessed using a seven-

point scale. Determining the attribute weights is formulated as a fuzzy group decision-making problem. These predefined linguistic expressions are modeled using IT2FNs:

- Very low importance/values (L1): $\left((1,1,2.5;1),(1,1,2;0.8)\right)$
- Low importance/values (L2): $\left((1,2.5,4;1),(1.5,2.5,3.5;0.8)\right)$
- Fairly medium-low importance/values (L3): $\left((2,3.5,5;1),(2.5,3.5,4.5;0.8)\right)$
- Medium importance/values (L4): $\left((4,5.5,7;1),(4.5,5.5,6.5;0.8)\right)$
- Fairly medium-high importance/values (L5): $\left((6,7.5,9;1),(6.5,7.5,8.5;0.8)\right)$
- High importance/values (L6): $\left((7,8.5,10;1),(7.5,8.5,9.5;0.8)\right)$
- Very high importance/values (L7): $\left((8.5,10,10;1),(9,10,10;0.8)\right)$

The domain values of the IT2FNs are defined within the interval [1-10]. A value of 1 indicates that the relative importance of sub-processes and KPI values have an almost negligible influence, whereas a value of 10 signifies a significantly strong influence in evaluating and selecting KPIs.

Determining the weight vector

In this research, determining the relative importance of the considered sub-processes of the maintenance process is formulated as a fuzzy group decision-making problem. It is assumed that all DMs have equal importance in assessing the relative importance of sub-processes. The procedure for determining the fuzzy weights vector is presented as follows:

Step 1. Each DM evaluates the relative importance of sub-process $p, p = 1,..,P$ using one of the predefined linguistic expressions, $\tilde{\tilde{W}}_p^e$.

Step 2. The aggregation of the DMs' assessments into a unique value, $\tilde{\tilde{W}}_p$ is obtained applying the fuzzy geometric mean operator, so that:

$$\tilde{\tilde{W}}_p = \sqrt[E]{\prod_{e=1}^{E} \tilde{\tilde{W}}_p^e} \tag{1}$$

Step 3. The normalized fuzzy weights vector is obtained by applying a linear normalization procedure (Palczewski & Sałabun, 2019):

$$\left[\tilde{\tilde{\omega}}_p\right]_{1xP}$$

Determining the rank of KPIs using Taxonomy method with IT2FNs

The rank of KPIs is determined using the proposed IT2FNs based Taxonomy method.

Step 1. Each DM evaluates the value of KPIs at the level of each sub-process using one of the predefined linguistic expressions, $\tilde{\tilde{x}}_{ip}^{j}$.

Step 2. The aggregated assessments of DMs, $\tilde{\tilde{x}}_{ip}$ are obtained by using the fuzzy geometric mean, so that:

$$\tilde{\tilde{x}}_{ip} = \sqrt[J]{\tilde{\tilde{x}}_{ip}^{j}} \tag{2}$$

The fuzzy decision matrix can be presented as:

$$\left[\tilde{\tilde{x}}_{ip}\right]_{IxP}$$

Step 3. Construct the weighted normalized decision matrix:

$$\left[\tilde{\tilde{y}}_{ip}\right]_{IxP}$$

where:

$$\tilde{\tilde{y}}_{ip} = \tilde{\tilde{\omega}}_{p} \cdot \tilde{\tilde{x}}_{ip} \tag{3}$$

Step 4. Construct the standardized decision matrix:

$$\left[z_{ip}\right]_{IxP}$$

where:

$$z_{ip} = \frac{d\left(\tilde{\tilde{y}}_{ip}, \tilde{\tilde{y}}_{p}\right)}{\sigma_{p}} \tag{4}$$

$\tilde{\tilde{y}}_{p}$is the average value of sub-process $p, p = 1, .., P$ and:

$$\tilde{\tilde{y}}_{p} = \frac{1}{I} \cdot \sum_{i=1,..,I} \tilde{\tilde{y}}_{ip} \tag{5}$$

The standard deviation is calculated as:

$$\sigma_{p} = \sqrt{\frac{1}{I-1} \cdot \sum_{i=1,..,I} \left(d\left(\tilde{\tilde{y}}_{ip}, \tilde{\tilde{y}}_{p}\right)\right)^{2}} \tag{6}$$

Step 5. Construct the compromise decision matrix:

$$\left[c_{ii'}\right]_{IxI}$$

where:

$$c_{ii'} = \sqrt{\sum_{p=1,..,P-1} \left(c_{ii'}^{p} - c_{ii'}^{p+1}\right)^2} \tag{7}$$

Step 6. Check the homogeneity of alternatives according to the following procedure:

$$O_i = \min_{i'=1,..,I} c_{ii'} \tag{8}$$

The homogeneity check for alternatives is computed using the expression:

$$O_i = \bar{O} \pm 2 \cdot \sigma_0 \tag{9}$$

where:

$$\bar{O} = \frac{1}{I} \cdot \sum\nolimits_{i=1,..,I} O_i \tag{10}$$

$$\sigma_0 = \sqrt{\frac{1}{I-1} \cdot (O_i - \bar{O})^2} \tag{11}$$

If all O_i values lie within a specific confidence interval, it can be considered that the alternatives are homogeneous.

Step 7. Development Model:

Determine the values of z_{0i} as:

$$z_{0i} = \max_{p=1,..,P} z_{ip} \tag{12}$$

The values of C_{i0} are calculated according to the formula:

$$C_{i0} = \sqrt{\sum_{p=1,..,P} \left(z_{ip} - z_{0i}\right)^2} \tag{13}$$

where:

The average value is denoted as $\bar{C}$, and the standard deviation is denoted as σ.

Determine:

$$C_0 = \bar{C} + 2 \cdot \sigma \tag{14}$$

Step 8. Determine the development attribute values, F_i:

$$F_i = \frac{C_{i0}}{C_0} \tag{15}$$

Step 9. Rank the values of F_i in descending order. The alternative with the highest F_i value will be ranked first and can be considered the best.

Case study

The proposed model is tested and verified on real-world data originating from the considered maintenance depot. The researchers organized an online panel discussion that lasted 30 minutes, during which ten DMs from a total of six manufacturing companies participated. During this panel discussion, the DMs were explained the problem under consideration and the procedure for providing their assessments. Afterward, the DMs had one week to submit their assessments via email.

KPI value assessment was carried out by five DMs from the considered maintenance depot. Also, these data were collected using the indirect survey method. The DMs submitted their evaluations of the KPI values to the researchers via email. They also had one week to provide their assessments. Furthermore, the proposed methodology is illustrated with data from the considered maintenance facility.

Determining the weights of sub-processes

The evaluation of the relative importance of sub-processes is performed by DMs and presented in Table 1.

Table 1 – The assessed relative importance of sub-processes

	$p=1$	$p=2$	$p=3$	$p=4$	$p=5$	$p=6$	$p=7$	$p=8$	$p=9$
$e=1$	*L6*	*L5*	*L4*	*L4*	*L7*	*L6*	*L5*	*L5*	*L1*
$e=2$	*L7*	*L4*	*L4*	*L6*	*L3*	*L2*	*L5*	*L5*	*L5*
$e=3$	*L6*	*L4*	*L5*	*L4*	*L3*	*L6*	*L6*	*L4*	*L5*
$e=4$	*L7*	*L4*	*L5*	*L5*	*L2*	*L4*	*L2*	*L4*	*L5*
$e=5$	*L6*	*L4*	*L4*	*L4*	*L4*	*L4*	*L5*	*L4*	*L6*
$e=6$	*L7*	*L3*	*L4*	*L5*	*L5*	*L2*	*L1*	*L6*	*L3*
$e=7$	*L2*	*L6*	*L6*	*L4*	*L7*	*L5*	*L6*	*L5*	*L6*
$e=8$	*L4*	*L5*	*L5*	*L6*	*L5*	*L1*	*L5*	*L3*	*L3*
$e=9$	*L6*	*L5*	*L5*	*L4*	*L4*	*L6*	*L5*	*L4*	*L5*
$e=10$	*L7*	*L4*	*L6*	*L2*	*L4*	*L5*	*L6*	*L3*	*L5*

The normalized weight vector of sub-processes is:

$$\tilde{\tilde{\omega}}_1 = \big((0.67,0.87,1;1),(0.74,0.87,0.96;0.8)\big)$$
$$\tilde{\tilde{\omega}}_2 = \big((0.43,0.58,0.71;1),(0.49,0.58,0.66;0.8)\big)$$
$$\tilde{\tilde{\omega}}_3 = \big((0.60,0.77,0.94;1),(0.68,0.77,0.89;0.8)\big)$$
$$\tilde{\tilde{\omega}}_4 = \big((0.48,0.67,0.85;1),(0.55,0.67,0.79;0.8)\big)$$
$$\tilde{\tilde{\omega}}_5 = \big((0.43,0.63,0.79;1),(0.50,0.63,0.74;0.8)\big)$$
$$\tilde{\tilde{\omega}}_6 = \big((0.26,0.49,0.73;1),(0.42,0.49,0.66;0.8)\big)$$
$$\tilde{\tilde{\omega}}_7 = \big((0.50,0.65,0.86;1),(0.55,0.65,0.79;0.8)\big)$$
$$\tilde{\tilde{\omega}}_8 = \big((0.47,0.65,0.83;1),(0.53,0.65,0.77;0.8)\big)$$
$$\tilde{\tilde{\omega}}_9 = \big((0.47,0.61,0.83;1),(0.52,0.61,0.80;0.8)\big)$$

The proposed Taxonomy method with IT2FNs

The estimated values of KPIs are presented in Table 2 (Step 1 of the proposed Algorithm).

Table 2 – The assessed KPI values

		$p=1$	$p=2$	$p=3$	$p=4$	$p=5$	$p=6$	$p=7$	$p=8$	$p=9$
$j=1$	$i=1$	L6	L7	L6	L7	L6	L7	L7	L6	L4
$j=2$		L7	L5	L6	L6	L6	L5	L7	L3	L6
$j=3$		L6	L4	L6	L4	L6	L6	L7	L7	L6
$j=4$		L7	L3	L5	L3	L7	L5	L7	L7	L2
$j=5$		L6	L6	L7	L5	L7	L5	L7	L6	L5
$j=1$	$i=2$	L6	L6	L7	L6	L6	L6	L7	L6	L6
$j=2$		L6	L6	L5	L7	L7	L7	L5	L6	L3
$j=3$		L7	L6	L4	L3	L6	L5	L5	L4	L2
$j=4$		L6	L4	L6	L4	L7	L7	L5	L4	L1
$j=5$		L7	L7	L7	L6	L2	L5	L5	L6	L7
$j=1$	$i=3$	L7	L7	L7	L4	L5	L5	L6	L7	L6
$j=2$		L7	L7	L7	L6	L6	L7	L5	L7	L6
$j=3$		L7	L7	L6	L7	L6	L5	L5	L7	L6
$j=4$		L7	L7	L6	L7	L6	L7	L5	L7	L6
$j=5$		L7	L7	L2	L5	L6	L6	L6	L6	L6
$j=1$	$i=4$	L7	L7	L5	L7	L6	L4	L6	L5	L6
$j=2$		L6	L4	L7	L7	L6	L7	L6	L6	L7
$j=3$		L7	L1	L5	L6	L6	L5	L6	L5	L5
$j=4$		L6	L7	L7	L5	L6	L6	L6	L6	L6
$j=5$		L3	L6	L6	L5	L6	L7	L6	L4	L5
$j=1$	$i=5$	L7	L7	L7	L7	L7	L6	L7	L7	L7
$j=2$		L5	L4	L5	L6	L7	L5	L7	L5	L4
$j=3$		L7	L6	L7	L7	L6	L5	L7	L7	L7
$j=4$		L5	L5	L6	L6	L7	L7	L7	L7	L6
$j=5$		L6	L4	L7	L5	L7	L4	L7	L5	L7
$j=1$	$i=6$	L6	L6	L5	L7	L6	L5	L7	L5	L6
$j=2$		L5	L7	L4	L6	L6	L7	L7	L5	L5
$j=3$		L6	L5	L7	L5	L6	L4	L7	L7	L7
$j=4$		L6	L7	L4	L7	L6	L5	L7	L5	L7
$j=5$		L7	L7	L7	L6	L4	L4	L7	L7	L5
$j=1$	$i=7$	L5	L6	L4	L7	L6	L6	L6	L6	L3
$j=2$		L6	L6	L4	L6	L6	L5	L6	L6	L4
$j=3$		L6	L4	L4	L6	L6	L7	L6	L6	L6
$j=4$		L6	L6	L4	L7	L6	L6	L6	L6	L6
$j=5$		L5	L4	L4	L7	L5	L5	L6	L6	L6
$j=1$	$i=8$	L6	L5	L7	L6	L4	L5	L6	L2	L5
$j=2$		L6	L7	L6	L6	L6	L6	L6	L6	L6
$j=3$		L5	L5	L6	L4	L5	L7	L6	L6	L4

		$p=1$	$p=2$	$p=3$	$p=4$	$p=5$	$p=6$	$p=7$	$p=8$	$p=9$
$j=4$		L6	L7	L7	L6	L6	L6	L6	L2	L5
$j=5$		L6	L5	L7	L5	L6	L4	L6	L6	L4
$j=1$	$i=9$	L7	L7	L6	L7	L7	L2	L5	L7	L6
$j=2$		L7	L6	L6	L6	L7	L7	L7	L6	L6
$j=3$		L7	L6	L6	L6	L7	L6	L7	L5	L6
$j=4$		L6	L6	L4	L6	L4	L7	L7	L4	L6
$j=5$		L6	L5	L6	L7	L5	L2	L7	L7	L6
$j=1$	$i=10$	L7	L7	L7	L5	L7	L2	L7	L7	L7
$j=2$		L7	L4	L7	L6	L6	L5	L5	L6	L6
$j=3$		L7	L6	L7	L6	L7	L7	L4	L5	L5
$j=4$		L7	L6	L7	L5	L4	L7	L7	L5	L4
$j=5$		L7	L7	L7	L6	L6	L6	L6	L5	L6
$j=1$	$i=11$	L6	L7	L7	L7	L6	L5	L5	L3	L7
$j=2$		L6	L5	L7	L5	L7	L7	L7	L3	L3
$j=3$		L6	L5	L7	L5	L5	L6	L7	L5	L2
$j=4$		L5	L7	L6	L7	L6	L7	L6	L3	L6
$j=5$		L6	L7	L7	L7	L7	L3	L7	L7	L7
$j=1$	$i=12$	L6	L7	L6	L7	L6	L6	L7	L5	L4
$j=2$		L7	L5	L7	L6	L5	L7	L5	L7	L5
$j=3$		L7	L4	L6	L4	L6	L6	L7	L7	L6
$j=4$		L7	L7	L5	L7	L7	L7	L7	L6	L7
$j=5$		L6	L6	L7	L5	L7	L7	L7	L7	L5

The weighted aggregated KPI values are obtained using the fuzzy geometric mean and are presented in Tables 3 to 5 (Step 2 to Step 3 of the proposed Algorithm).

Table 3 – The weighted aggregated KPI values and fuzzy arithmetic mean

	$p=1$	$p=2$	$p=3$
$i=1$	$\left(\begin{matrix}(5.07,7.89,10;1),\\(5.97,7.89,9.31;0.8)\end{matrix}\right)$	$\left(\begin{matrix}(2.11,3.81,5.64;1),\\(2.68,3.81,4.95;0.8)\end{matrix}\right)$	$\left(\begin{matrix}(4.23,6.59,9.20;1),\\(5.13,6.59,8.35;0.8)\end{matrix}\right)$
$i=2$	$\left(\begin{matrix}(5.07,7.89,10;1),\\(5.97,7.89,9.31;0.8)\end{matrix}\right)$	$\left(\begin{matrix}(2.80,4.67,6.61;1),\\(3.44,4.67,5.87;0.8)\end{matrix}\right)$	$\left(\begin{matrix}(3.94,6.24,8.57;1),\\(4.80,6.24,7.82;0.8)\end{matrix}\right)$
$i=3$	$\left(\begin{matrix}(5.69,8.70,10;1),\\(6.66,8.70,9.60;0.8)\end{matrix}\right)$	$\left(\begin{matrix}(3.65,5.80,7.10;1),\\(4.41,5.80,6.60;0.8)\end{matrix}\right)$	$\left(\begin{matrix}(3.08,5.47,7.83;1),\\(3.97,5.47,7.07;0.8)\end{matrix}\right)$
$i=4$	$\left(\begin{matrix}(3.94,6.61,8.71;1),\\(4.79,6.61,8.02;0.8)\end{matrix}\right)$	$\left(\begin{matrix}(1.97,4.98,7.94;1),\\(2.39,4.98,6.88;0.8)\end{matrix}\right)$	$\left(\begin{matrix}(4.27,6.64,9.01;1),\\(5.18,6.64,8.25;0.8)\end{matrix}\right)$
$i=5$	$\left(\begin{matrix}(4.77,7.51,9.59;1),\\(5.64,7.51,8.90;0.8)\end{matrix}\right)$	$\left(\begin{matrix}(2.43,4.17,6.03;1),\\(3.02,4.17,5.32;0.8)\end{matrix}\right)$	$\left(\begin{matrix}(4.58,7.04,9.20;1),\\(5.53,7.04,8.53;0.8)\end{matrix}\right)$
$i=6$	$\left(\begin{matrix}(3.94,6.61,8.71;1),\\(4.79,6.61,8.02;0.8)\end{matrix}\right)$	$\left(\begin{matrix}(3.28,5.30,6.95;1),\\(3.98,5.30,6.32;0.8)\end{matrix}\right)$	$\left(\begin{matrix}(4.58,7.04,9.20;1),\\(5.53,7.04,8.53;0.8)\end{matrix}\right)$
$i=7$	$\left(\begin{matrix}(4.41,7.03,9.59;1),\\(5.24,7.03,8.72;0.8)\end{matrix}\right)$	$\left(\begin{matrix}(2.69,4.52,6.61;1),\\(3.32,4.52,5.81;0.8)\end{matrix}\right)$	$\left(\begin{matrix}(2.40,4.23,6.58;1),\\(5.53,4.23,5.78;0.8)\end{matrix}\right)$

	$p = 1$	$p = 2$	$p = 3$
$i = 8$	((4.55,7.21,9.79; 1), (5.39,7.21,8.92; 0.8))	((2.97,4.88,6.67; 1), (4.01,4.88,5.99; 0.8))	((4.72,7.22,9.40; 1), (5.69,7.22,8.76; 0.8))
$i = 9$	((5.27,8.15,9.59; 1), (6.19,8.15,9.41; 0.8))	((3.03,4.97,6.95; 1), (3.70,4.97,6.19; 0.8))	((3.76,5.76,8.75; 1), (4.60,5.76,7.84; 0.8))
$i = 10$	((5.69,8.70,10; 1), (6.66,8.70,9.60; 0.8))	((2.91,4.82,6.61; 1), (3.57,4.82,5.93; 0.8))	((5.10,7.70,9.40; 1), (6.12,7.70,8.90; 0.8))
$i = 11$	((4.55,7.21,9.79; 1), (5.39,7.21,8.92; 0.8))	((3.18,5.17,6.81; 1), (3.87,5.17,6.18; 0.8))	((4.91,7.45,9.40; 1), (5.90,7.45,8.81; 0.8))
$i = 12$	((5.27,8.15,9.59; 1), (6.19,8.15,9.41; 0.8))	((2.82,4.70,6.47; 1), (3.47,4.70,5.80; 0.8))	((4.40,6.81,9.20; 1), (5.33,6.81,8.44; 0.8))
$\tilde{\tilde{y}}_p$	((4.85,7.64,9.61; 1), (5.73,7.64,9.01; 0.8))	((2.82,4.82,6.70; 1), (3.49,4.82,5.99; 0.8))	((4.16,6.52,8.81; 1), (5.78,6.52,8.09; 0.8))

Table 4 – The weighted aggregated KPI values and fuzzy arithmetic mean (continuations)

	$p = 4$	$p = 5$	$p = 6$
$i = 1$	((2.36,4.40,6.75; 1), (3.01,4.40,5.92; 0.8))	((3.25,5.71,7.90; 1), (4.03,5.71,7.18; 0.8))	((1.72,3.99,6.85; 1), (2.30,3.99,5.93; 0.8))
$i = 2$	((2.43,4.52,6.89; 1), (3.10,4.52,6.05; 0.8))	((2.20,4.47,6.58; 1), (2.92,4.47,5.88; 0.8))	((1.85,4.23,6.70; 1), (3.20,4.23,6.12; 0.8))
$i = 3$	((3.14,5.43,7.75; 1), (3.34,5.43,6.94; 0.8))	((2.92,5.22,7.74; 1), (3.64,5.22,6.88; 0.8))	((1.85,4.23,6.70; 1), (3.20,4.23,6.12; 0.8))
$i = 4$	((3.41,5.78,8.15; 1), (4.19,5.78,7.33; 0.8))	((3.01,5.35,7.90; 1), (3.75,5.35,7.03; 0.8))	((1.71,3.97,6.66; 1), (2.97,3.97,5.80; 0.8))
$i = 5$	((3.52,5.93,8.32; 1), (4.31,5.93,7.49; 0.8))	((3.52,6.10,7.90; 1), (4.34,6.10,7.32; 0.8))	((1.59,3.75,6.52; 1), (2.79,3.75,5.62; 0.8))
$i = 6$	((3.52,5.93,8.32; 1), (4.31,5.93,7.49; 0.8))	((2.69,4.91,7.36; 1), (3.39,4.91,6.52; 0.8))	((1.42,3.44,6.07; 1), (2.52,3.44,5.21; 0.8))
$i = 7$	((3.78,6.28,8.50; 1), (4.33,6.28,7.74; 0.8))	((2.92,5.22,7.74; 1), (3.64,5.22,6.88; 0.8))	((1.78,4.09,6.99; 1), (3.09,4.09,6.06; 0.8))
$i = 8$	((3.36,5.69,8.50; 1), (4.12,5.69,7.50; 0.8))	((2.61,4.79,7.20; 1), (3.29,4.79,6.37; 0.8))	((1.54,3.66,6.38; 1), (2.71,3.66,5.49; 0.8))
$i = 9$	((4.24,6.08,8.50; 1), (4.44,6.08,7.66; 0.8))	((2.93,5.28,7.20; 1), (3.67,5.28,6.57; 0.8))	((0.90,2.72,5.06; 1), (1.78,2.72,4.29; 0.8))
$i = 10$	((3.16,5.42,8.15; 1), (3.90,5.42,7.18; 0.8))	((2.91,5.24,7.36; 1), (3.64,5.24,6.65; 0.8))	((1.29,3.39,5.95; 1), (2.39,3.39,5.13; 0.8))
$i = 11$	((3.55,5.97,8.15; 1), (2.80,5.97,7.40; 0.8))	((3.15,5.57,7.74; 1), (3.92,5.57,7.02; 0.8))	((1.48,3.63,6.22; 1), (2.64,3.63,5.39; 0.8))
$i = 12$	((3.15,5.43,7.75; 1), (3.89,5.43,6.94; 0.8))	((3.15,5.57,7.74; 1), (3.92,5.57,7.02; 0.8))	((2.04,4.59,6.60; 1), (3.51,4.59,6.47; 0.8))
$\tilde{\tilde{y}}_p$	((3.30,5.61,7.98; 1), (4.04,5.61,7.14; 0.8))	((2.94,5.29,7.53; 1), (3.68,5.29,6.78; 0.8))	((1.60,3.81,6.39; 1), (2.76,3.81,5.64; 0.8))

Table 5 – The weighted aggregated KPI values and fuzzy arithmetic mean (continuations)

	$\boldsymbol{p=7}$	$\boldsymbol{p=8}$	$\boldsymbol{p=9}$
$i=1$	$\begin{pmatrix}(4.25,6.50,7.90;1),\\(4.95,6.50,7.90;0.8)\end{pmatrix}$	$\begin{pmatrix}(2.77,3.63,6.30;1),\\(2.48,3.63,6.43;0.8)\end{pmatrix}$	$\begin{pmatrix}(1.93,4.94,7.23;1),\\(3.04,4.94,5.64;0.8)\end{pmatrix}$
$i=2$	$\begin{pmatrix}(3.22,5.16,7.90;1),\\(3.82,5.16,6.94;0.8)\end{pmatrix}$	$\begin{pmatrix}(2.63,4.64,7.19;1),\\(3.24,4.64,6.28;0.8)\end{pmatrix}$	$\begin{pmatrix}(1.22,2.29,4.56;1),\\(1.57,2.29,3.97;0.8)\end{pmatrix}$
$i=3$	$\begin{pmatrix}(3.19,5.13,8.07;1),\\(3.79,5.13,7.02;0.8)\end{pmatrix}$	$\begin{pmatrix}(3.84,6.29,8.30;1),\\(4.60,6.29,7.62;0.8)\end{pmatrix}$	$\begin{pmatrix}(3.29,5.18,8.30;1),\\(3.90,5.18,7.60;0.8)\end{pmatrix}$
$i=4$	$\begin{pmatrix}(3.50,5.52,8.60;1),\\(4.12,5.52,7.51;0.8)\end{pmatrix}$	$\begin{pmatrix}(2.77,4.82,7.41;1),\\(3.39,4.82,6.49;0.8)\end{pmatrix}$	$\begin{pmatrix}(3.22,5.09,7.96;1),\\(3.82,5.09,7.34;0.8)\end{pmatrix}$
$i=5$	$\begin{pmatrix}(4.25,6.50,7.90;1),\\(4.95,6.50,7.90;0.8)\end{pmatrix}$	$\begin{pmatrix}(3.73,6.14,8.13;1),\\(4.47,6.14,7.45;0.8)\end{pmatrix}$	$\begin{pmatrix}(3.31,5.24,7.73;1),\\(3.15,5.24,7.19;0.8)\end{pmatrix}$
$i=6$	$\begin{pmatrix}(3.50,5.52,8.60;1),\\(4.12,5.52,7.51;0.8)\end{pmatrix}$	$\begin{pmatrix}(3.24,5.47,7.79;1),\\(3.92,5.47,6.98;0.8)\end{pmatrix}$	$\begin{pmatrix}(3.34,5.26,7.96;1),\\(3.96,5.26,7.42;0.8)\end{pmatrix}$
$i=7$	$\begin{pmatrix}(3.50,5.52,8.60;1),\\(4.12,5.52,7.51;0.8)\end{pmatrix}$	$\begin{pmatrix}(3.29,5.52,8.30;1),\\(3.97,5.52,7.31;0.8)\end{pmatrix}$	$\begin{pmatrix}(2.29,3.98,6.73;1),\\(2.83,3.98,6.07;0.8)\end{pmatrix}$
$i=8$	$\begin{pmatrix}(3.50,5.52,8.60;1),\\(4.12,5.52,7.51;0.8)\end{pmatrix}$	$\begin{pmatrix}(1.51,3.39,5.75;1),\\(2.09,3.39,4.91;0.8)\end{pmatrix}$	$\begin{pmatrix}(2.47,4.14,6.90;1),\\(3.00,4.14,6.25;0.8)\end{pmatrix}$
$i=9$	$\begin{pmatrix}(3.96,6.14,8.42;1),\\(4.64,6.14,7.65;0.8)\end{pmatrix}$	$\begin{pmatrix}(3.08,5.27,7.57;1),\\(3.75,5.27,6.77;0.8)\end{pmatrix}$	$\begin{pmatrix}(3.29,5.18,8.30;1),\\(3.90,5.18,7.60;0.8)\end{pmatrix}$
$i=10$	$\begin{pmatrix}(3.28,5.27,7.95;1),\\(3.89,5.27,6.94;0.8)\end{pmatrix}$	$\begin{pmatrix}(3.12,5.29,7.79;1),\\(3.78,5.29,6.91;0.8)\end{pmatrix}$	$\begin{pmatrix}(2.97,4.79,7.57;1),\\(3.55,4.79,6.96;0.8)\end{pmatrix}$
$i=11$	$\begin{pmatrix}(3.81,5.94,8.42;1),\\(4.47,5.94,7.57;0.8)\end{pmatrix}$	$\begin{pmatrix}(1.56,3.27,5.36;1),\\(2.07,3.27,4.62;0.8)\end{pmatrix}$	$\begin{pmatrix}(1.88,3.63,6.02;1),\\(2.44,3.63,5.47;0.8)\end{pmatrix}$
$i=12$	$\begin{pmatrix}(3.96,6.14,8.42;1),\\(4.64,6.14,7.64;0.8)\end{pmatrix}$	$\begin{pmatrix}(3.58,5.94,8.13;1),\\(4.31,5.94,7.38;0.8)\end{pmatrix}$	$\begin{pmatrix}(2.88,4.67,7.41;1),\\(3.45,4.67,6.81;0.8)\end{pmatrix}$
$\tilde{\tilde{y}}_p$	$\begin{pmatrix}(3.66,5.74,8.03;1),\\(4.29,5.74,7.47;0.8)\end{pmatrix}$	$\begin{pmatrix}(2.93,4.98,7.33;1),\\(3.51,4.98,6.59;0.8)\end{pmatrix}$	$\begin{pmatrix}(2.67,4.53,7.22;1),\\(3.22,4.53,6.53;0.8)\end{pmatrix}$

According to the proposed procedure (Step 4 of the proposed Algorithm), the obtained results are presented in Table 6.

Table 6 – The standard deviation

	$p=1$	$p=2$	$p=3$	$p=4$	$p=5$	$p=6$	$p=7$	$p=8$	$p=9$
σ_p	0.801	0.498	0.852	0.577	0.391	0.475	0.420	0.953	0.885

The standardized decision matrix (Step 5 of the proposed Algorithm) is presented in Table 7.

Table 7 – The standardized decision matrix

	$p=1$	$p=2$	$p=3$	$p=4$	$p=5$	$p=6$	$p=7$	$p=8$	$p=9$
z_{1p}	0.336	1.922	0.242	2.007	0.387	0.539	1.442	1.020	0.488
z_{2p}	0.336	0.291	0.415	1.809	2.120	0.832	1.157	0.312	2.441
z_{3p}	1.091	1.675	1.333	0.496	0.207	0.832	1.160	1.212	0.854
z_{4p}	2.116	1.185	0.228	0.463	0.320	0.366	0.540	0.144	0.697
z_{5p}	0.127	1.205	0.525	0.532	1.724	0.114	1.442	1.056	0.667
z_{6p}	1.226	0.865	0.525	0.532	0.795	0.697	0.540	0.463	0.842
z_{7p}	0.574	0.444	2.305	0.912	0.207	0.697	0.540	0.613	0.554
z_{8p}	0.411	0.235	0.691	0.315	1.105	0.229	0.540	1.634	0.364
z_{9p}	0.521	0.325	0.723	0.719	0.192	2.295	0.838	0.258	0.854
z_{10p}	1.091	0.080	1.086	0.674	0.182	0.872	1.164	0.325	0.346
z_{11p}	0.411	0.612	0.865	0.636	0.645	0.362	0.481	1.783	1.050
z_{12p}	0.521	0.231	0.380	0.591	0.645	1.408	0.836	0.805	0.208

The remaining elements of the compromise decision matrix are calculated in the same way (Step 6 of the proposed Algorithm) so that:

$$\begin{bmatrix} - & 3.196 & 2.115 & 2.785 & 2.194 & 2.368 & 2.956 & 2.781 & 2.945 & 2.681 & 2.431 & 2.496 \\ 3.196 & - & 3.145 & 3.567 & 2.641 & 2.738 & 3.489 & 3.186 & 3.130 & 3.240 & 2.939 & 3.069 \\ 2.115 & 3.145 & - & 2.072 & 2.182 & 1.624 & 1.937 & 2.226 & 2.392 & 1.919 & 1.752 & 2.130 \\ 2.785 & 3.567 & 2.072 & - & 2.780 & 1.202 & 2.794 & 2.648 & 2.731 & 1.968 & 2.567 & 2.334 \\ 2.194 & 2.641 & 2.182 & 2.780 & - & 1.929 & 2.785 & 1.653 & 3.023 & 2.489 & 1.839 & 2.147 \\ 2.368 & 2.738 & 1.624 & 1.202 & 1.929 & - & 2.089 & 1.747 & 1.978 & 1.350 & 1.667 & 1.435 \\ 2.956 & 3.489 & 1.937 & 2.794 & 2.785 & 2.089 & - & 2.266 & 2.327 & 1.578 & 2.032 & 2.191 \\ 2.781 & 3.186 & 2.226 & 2.648 & 1.653 & 1.747 & 2.266 & - & 2.740 & 2.035 & 1.001 & 1.608 \\ 2.945 & 3.130 & 2.392 & 2.731 & 3.023 & 1.978 & 2.327 & 2.740 & - & 1.707 & 2.560 & 1.361 \\ 2.681 & 3.240 & 1.919 & 1.968 & 2.489 & 1.350 & 1.578 & 2.035 & 1.707 & - & 2.088 & 1.308 \\ 2.431 & 2.939 & 1.752 & 2.567 & 1.839 & 1.667 & 2.032 & 1.001 & 2.560 & 2.088 & - & 1.811 \\ 2.496 & 3.069 & 2.130 & 2.334 & 2.147 & 1.435 & 2.191 & 1.608 & 1.361 & 1.308 & 1.811 & - \end{bmatrix}$$

$O_1 = 2.115$ $O_2 = 2.641$ $O_3 = 1.624$ $O_4 = 1.968$ $O_5 = 1.653$ $O_6 = 1.435$
$O_7 = 1.578$ $O_8 = 1.001$ $O_9 = 1.361$ $O_{10} = 1.308$ $O_{11} = 1.001$ $O_{12} = 1.308$

Let us check the homogeneity of the alternatives:

$$O_i = 1.583 \pm 2 \cdot 0.473 \in [0.637 - 2.529]$$

It can be concluded that all KPIs, except for $(i = 2)$, are homogeneous, meaning they are mutually independent. However, the value of the second KPI does not deviate significantly from the prescribed homogeneity boundaries, so we can further accept that all KPIs are considered mutually independent.

According to the proposed Algorithm (Step 7), the development model is constructed:

$z_{01} = 2.007$ $z_{02} = 2.441$ $z_{03} = 1.675$ $z_{04} = 2.116$ $z_{05} = 1.724$ $z_{06} = 1.226$
$z_{07} = 2.305$ $z_{08} = 1.634$ $z_{09} = 2.295$ $z_{010} = 1.164$ $z_{011} = 1.783$ $z_{012} = 1.408$

The values C_{i0} are:

$C_{01} = 3.871$ $C_{02} = 4.736$ $C_{03} = 2.422$ $C_{04} = 4.673$ $C_{05} = 3.148$ $C_{06} = 1.664$
$C_{07} = 4.943$ $C_{08} = 3.338$ $C_{09} = 4.975$ $C_{010} = 1.962$ $C_{011} = 3.310$ $C_{012} = 2.571$

$$C_0 = 3.711 + 2 \cdot 1.282 = 6.275$$

The values of the development attribute, F_i and the ranked KPIs are presented in Table 8.

Table 8 – Rank of KPIs

	F_i	Rank		F_i	Rank
$i = 1$	0.603	5	$i = 7$	0.788	2
$i = 2$	0.755	3	$i = 8$	0.532	6
$i = 3$	0.386	10	$i = 9$	0.793	1
$i = 4$	0.745	4	$i = 10$	0.313	11
$i = 5$	0.502	8	$i = 11$	0.528	7
$i = 6$	0.265	12	$i = 12$	0.410	9

In the general case, maintenance process improvement can be achieved by taking management actions aimed at improving all KPIs. However, in practice, this process cannot be realized due to limited time and financial resources, as well as the availability of workers. Based on the obtained results, DMs determine the set of KPIs that need to be improved. In this way, costs and downtime are significantly reduced, which leads to an increase in the effectiveness of the maintenance process. It can be concluded that it is necessary to improve the KPI in the last position. In this case, it is KPI $(i = 6)$ – Required knowledge and skills level of experts. To improve the value of this KPI, it is necessary to have knowledge of equipment, fault detection, component disassembly and assembly. Furthermore, improving this KPI requires increasing worker training for the maintenance of newer equipment. One of the recommended management actions is to organize continuous worker training over time.

Many researchers suggest that management actions should target two or three KPIs simultaneously. In this case, based on good practice experience, it is assumed that three KPIs in the last three positions in the ranking should be improved simultaneously. Therefore, in addition to the aforementioned KPI, the following KPIs need to be improved: (i) KPI ($i =$

10) – Availability of experts. The shortage of experts is present in most companies due to various factors (planned and natural departures, migrations, moves to better positions, retraining for other positions, etc.), inability to replace personnel in case of absence, and the entry of younger and less experienced individuals into the technological process. To improve this KPI, it is necessary to follow one of the basic principles of business known as employee stability; (ii) KPI ($i = 3$) – Material supply of spare parts and consumables. Global issues in the world market can affect the production of spare parts, resulting in delivery delays, supply of smaller quantities than required, and reduced reliability of delivered parts due to frequent failures after repairs. Improving the procurement of reliable spare parts and consumables leads to an improvement in this KPI.

It should be noted that the results obtained in this study closely align with those reported in (Milovanović et al., 2024).

Conclusion

This research proposes a fuzzy MADM model that provides a framework for ranking KPIs under an interval type-2 fuzzy environment and helps define management actions aimed at improving the reliability of the maintenance process. The proposed model has been tested and validated using real-world data from a maintenance depot. The DMs base their assessments on both their experience and the available evidence.

The main contributions of the presented research are: (1) Modeling of existing uncertainties in the relative importance of sub-processes and KPI values, based on IT2FNs; (2) Formulating the assessment of existing uncertainties as a fuzzy group decision-making problem; (3) Determining the weights vector of sub-processes using the fuzzy geometric mean, which offers practical advantages for industrial applications; (4) Ranking the KPIs using the proposed IT2FNs based Taxonomy.

The practical implications of the proposed methodology are directed towards operations managers, who need to prioritize actions to address identified failures. The methodology identifies failures requiring immediate attention, considering the potential costs that may arise if the manufacturing process is interrupted.

The key advantage of the proposed fuzzy MADM model is its ability to precisely identify the set of KPIs that need improvement through targeted management actions. This model can be extended to analyze other production enterprises.

The main limitations of the proposed fuzzy MADM model are: (1) the subjectivity in obtaining input data for the model, and (2) the increased

computational complexity compared to traditional decision-making methods. Future research should focus on developing user-friendly software tools to facilitate the practical application of the proposed fuzzy MADM model in real-world scenarios.

Appendix

In this section, fundamental definitions concerning the fuzzy algebra rules of IT2FNs are introduced (Mendel, 2017).

Definition 1. A type-2 fuzzy set, $\widetilde{\widetilde{A}}$ in the universe of discourse X can be represented by a type-2 membership function $\mu_{\widetilde{\widetilde{A}}}$ shown as follows:

$$\widetilde{\widetilde{A}} = \left\{(x,u), \mu_{\widetilde{\widetilde{A}}}(x,u) | \forall x \in X, \forall u \in J_x \subseteq (0,1), 0 \leq \mu_{\widetilde{\widetilde{A}}}(x,u) \leq 1\right\}$$

Definition 2. If X is a set of real numbers, then a type-2 fuzzy set and an interval type-2 fuzzy set in X are referred to as a type-2 fuzzy number and an interval type-2 fuzzy number, respectively.

Definition 3. If the upper and lower membership functions of $\widetilde{\widetilde{A}}$ are two triangular type-1 fuzzy numbers, then $\widetilde{\widetilde{A}}$ is called a triangular interval type-2 fuzzy number and is denoted as: $\widetilde{\widetilde{A}} = \left(\widetilde{A}^U, \widetilde{A}^L\right)$ so that:

$$\widetilde{\widetilde{A}} = \left(\widetilde{A}^U, \widetilde{A}^L\right) = \left(\left(a_1^U, a_2^U, a_3^U;\ \alpha\right), \left(a_1^L, a_2^L, a_3^L;\ \beta\right)\right)$$

where: 1) a_1^U and a_3^U represent the lower and upper bounds in the domain, respectively; 2) a_1^L and a_3^L represent the lower and upper bounds of the lower membership function, respectively; 3) a_2^U and a_2^L are the modal values of the upper and lower membership functions, respectively; 4) The values of the membership function are defined as $(\alpha, \beta) \in [0,1]$.

Definition 4. Let $\widetilde{\widetilde{A}}$, and $\widetilde{\widetilde{B}}$ be two IT2FNs:

$$\widetilde{\widetilde{A}} = \left(\left(a_1^U, a_2^U, a_3^U;\ \alpha_1\right), \left(a_1^L, a_2^L, a_3^L;\ \beta_1\right)\right)$$

$$\widetilde{\widetilde{B}} = \left(\left(b_1^U, b_2^U, b_3^U;\ \alpha_2\right), \left(b_1^L, b_2^L, b_3^L;\ \beta_2\right)\right)$$

The arithmetic operations are defined as follows:

- Addition:

$$\widetilde{\widetilde{A}} + \widetilde{\widetilde{B}} = \begin{pmatrix} \left(a_1^U + b_1^U, a_2^U + b_2^U, a_3^U + b_3^U ; \min(\alpha_1, \alpha_2), \min(\beta_1, \beta_2)\right) \\ \left(a_1^L + b_1^L, a_2^L + b_2^L, a_3^L + b_3^L; \min(\alpha_1, \alpha_2), \min(\beta_1, \beta_2)\right) \end{pmatrix} \quad \text{(A1)}$$

- Subtraction:

$$\widetilde{\widetilde{A}} - \widetilde{\widetilde{B}} = \begin{pmatrix} \left(a_1^U - b_3^U, a_2^U - b_2^U, a_3^U - b_1^U; \min(\alpha_1, \alpha_2), \min(\beta_1, \beta_2)\right) \\ \left(a_1^L - b_3^L, a_2^L - b_2^L, a_3^L - b_1^L; \min(\alpha_1, \alpha_2), \min(\beta_1, \beta_2)\right) \end{pmatrix} \quad \text{(A2)}$$

- Multiplication:

$$\tilde{\tilde{\mathrm{A}}} \cdot \tilde{\tilde{\mathrm{B}}} = \begin{pmatrix} \left(\mathrm{a}_1^{\mathrm{U}} \cdot \mathrm{b}_1^{\mathrm{U}}, \mathrm{a}_2^{\mathrm{U}} \cdot \mathrm{b}_2^{\mathrm{U}}, \mathrm{a}_3^{\mathrm{U}} \cdot \mathrm{b}_3^{\mathrm{U}}; \min(\alpha_1, \alpha_2), \min(\beta_1, \beta_2)\right) \\ \left(\mathrm{a}_1^{\mathrm{L}} \cdot \mathrm{b}_1^{\mathrm{L}}, \mathrm{a}_2^{\mathrm{L}} \cdot \mathrm{b}_2^{\mathrm{L}}, \mathrm{a}_3^{\mathrm{L}} \cdot \mathrm{b}_3^{\mathrm{L}}; \min(\alpha_1, \alpha_2), \min(\beta_1, \beta_2)\right) \end{pmatrix} \quad \text{(A3)}$$

- Division:

$$\tilde{\tilde{\mathrm{A}}} : \tilde{\tilde{\mathrm{B}}} = \begin{pmatrix} \left(\mathrm{a}_1^{\mathrm{U}} : \mathrm{b}_3^{\mathrm{U}}, \mathrm{a}_2^{\mathrm{U}} : \mathrm{b}_2^{\mathrm{U}}, \mathrm{a}_3^{\mathrm{U}} : \mathrm{b}_1^{\mathrm{U}}; \min(\alpha_1, \alpha_2), \min(\beta_1, \beta_2)\right) \\ \left(\mathrm{a}_1^{\mathrm{L}} : \mathrm{b}_3^{\mathrm{L}}, \mathrm{a}_2^{\mathrm{L}} : \mathrm{b}_2^{\mathrm{L}}, \mathrm{a}_3^{\mathrm{L}} : \mathrm{b}_1^{\mathrm{L}}; \min(\alpha_1, \alpha_2), \min(\beta_1, \beta_2)\right) \end{pmatrix} \quad \text{(A4)}$$

Definition 5. Let $\tilde{\tilde{\mathrm{A}}}$ be a triangular interval type-2 fuzzy number and let k be a crisp value:

$$\mathrm{k} \cdot \tilde{\tilde{\mathrm{A}}} = \tilde{\tilde{\mathrm{A}}} = \left(\left(k \cdot \mathrm{a}_1^{\mathrm{U}}, \mathrm{k} \cdot \mathrm{a}_2^{\mathrm{U}}, \mathrm{k} \cdot \mathrm{a}_3^{\mathrm{U}}; \alpha\right), \left(\mathrm{k} \cdot \mathrm{a}_1^{\mathrm{L}}, \mathrm{k} \cdot \mathrm{a}_2^{\mathrm{L}}, \mathrm{k} \cdot \mathrm{a}_3^{\mathrm{L}};\ \beta\right)\right) \quad \text{(A5)}$$

$$\left(\tilde{\tilde{\mathrm{A}}}\right)^{-1} = \left(\left(\frac{1}{a_3^U}, \frac{1}{a_2^U}, \frac{1}{a_1^U}; \alpha\right), \left(\frac{1}{a_3^L}, \frac{1}{a_2^L}, \frac{1}{a_1^L}; \beta\right)\right) \quad \text{(A6)}$$

Definition 6. The Hamming distance between $\tilde{\tilde{A}}$ and $\tilde{\tilde{B}}$ is determined according to the following expression (Nehi & Keikha, 2016; Heidarzade, Mahdavi, & Mahdavi-Amiri, 2016):

$$d_H\left(\tilde{\tilde{A}}, \tilde{\tilde{B}}\right) = \frac{d_H^U + d_H^L}{2} \quad \text{(A7)}$$

$$d_H^U = \left\{\frac{1}{4}\left[\left|a_1^U - b_1^U\right| + 2 \cdot \left|a_2^U - b_2^U\right| + \left|a_3^U - b_3^U\right| + \ |\alpha_1 - \alpha_2|\right]\right\} \quad \text{(A8)}$$

$$d_H^L = \left\{\frac{1}{4}\left[\left|a_1^L - b_1^L\right| + 2 \cdot \left|a_2^L - b_2^L\right| + \left|a_3^L - b_3^L\right| + |\beta_1 - \beta_2|\right]\right\} \quad \text{(A9)}$$

Definition 7. Let there be n interval type-2 triangular fuzzy numbers:

$$\tilde{\tilde{A}}_1 = \left(\left(\mathrm{a}_{11}^{\mathrm{U}}, \mathrm{a}_{21}^{\mathrm{U}}, \mathrm{a}_{31}^{\mathrm{U}};\ \alpha_1\right), \left(\mathrm{a}_{11}^{\mathrm{L}}, \mathrm{a}_{21}^{\mathrm{L}}, \mathrm{a}_{31}^{\mathrm{L}};\ \beta_1\right)\right), \ldots, \tilde{\tilde{A}}_i$$
$$= \left(\left(\mathrm{a}_{1\mathrm{i}}^{\mathrm{U}}, \mathrm{a}_{2\mathrm{i}}^{\mathrm{U}}, \mathrm{a}_{3\mathrm{i}}^{\mathrm{U}};\ \alpha_i\right), \left(\mathrm{a}_{1\mathrm{i}}^{\mathrm{L}}, \mathrm{a}_{2\mathrm{i}}^{\mathrm{L}}, \mathrm{a}_{3\mathrm{i}}^{\mathrm{L}};\ \beta_i\right)\right), \ldots$$
$$\tilde{\tilde{A}}_n = \left(\left(\mathrm{a}_{1\mathrm{n}}^{\mathrm{U}}, \mathrm{a}_{2\mathrm{n}}^{\mathrm{U}}, \mathrm{a}_{3\mathrm{n}}^{\mathrm{U}};\ \alpha_n\right), \left(\mathrm{a}_{1\mathrm{n}}^{\mathrm{L}}, \mathrm{a}_{2\mathrm{n}}^{\mathrm{L}}, \mathrm{a}_{3\mathrm{n}}^{\mathrm{L}};\ \beta_n\right)\right)$$

The normalized values of these IT2FNs are calculated as follows, $\tilde{\tilde{r}}_i$ (Palczewski & Sałabun, 2019):

a) benefit-type:

$$\tilde{\tilde{r}}_i = \left(\left(\frac{a_{1i}^U}{u^*}, \frac{a_{2i}^U}{u^*}, \frac{a_{3i}^U}{u^*}; \alpha_i\right), \left(\frac{a_{1i}^L}{u^*}, \frac{a_{2i}^L}{u^*}, \frac{a_{3i}^L}{u^*}; \beta_i\right)\right) \quad \text{(A10)}$$

b) cost-type:

$$\tilde{\tilde{r}}_i = \left(\left(\frac{l^*}{a_{3i}^U}, \frac{l^*}{a_{2i}^U}, \frac{l^*}{a_{1i}^U}; \alpha_i\right), \left(\frac{l^*}{a_{3i}^L}, \frac{l^*}{a_{2i}^L}, \frac{l^*}{a_{1i}^L}; \beta_i\right)\right) \quad \text{(A11)}$$

where:

$$u^* = \max_{i=1,..,n} a_{3i}^U,\ l^* = \min_{i=1,..,n} a_{1i}^U$$

References

Aleksić, A., Milanović, D.D., Komatina, N. and Tadić, D., 2023. Evaluation and ranking of failures in manufacturing process by combining best-worst method and VIKOR under type-2 fuzzy environment.*Expert Systems*, 40(2), p.e13148. Available at: https://doi.org/10.1111/exsy.13148

Aleksic, A., Runic Ristic, M., Komatina, N. and Tadic, D., 2019. Advanced risk assessment in reverse supply chain processes: A case study in Republic of Serbia. *Advances in Production Engineering & Management*, 14(4), pp.421–434. Available at: https://doi.org/10.14743/apem2019.4.338

Aleksić, A. and Tadić, D., 2023. Industrial and Management Applications of Type-2 Multi-Attribute Decision-Making Techniques Extended with Type-2 Fuzzy Sets from 2013 to 2022. *Mathematics*, 11(10), p.2249. Available at: https://doi.org/10.3390/math11102249

Atanassov, K.T., 1999. Intuitionistic Fuzzy Sets. In: *Intuitionistic Fuzzy Sets*, Studies in Fuzziness and Soft Computing. [online] Heidelberg: Physica-Verlag HD. pp.1–137. Available at: https://doi.org/10.1007/978-3-7908-1870-3_1

Božanić, D., Epler, I., Puška, A., Biswas, S., Marinković, D. and Koprivica, S., 2024. Application of the DIBR II – rough MABAC decision-making model for ranking methods and techniques of lean organization systems management in the process of technical maintenance.*FactaUniversitatis, Series: Mechanical Engineering*, 22(1), Available at: p.101. https://doi.org/10.22190/FUME230614026B

Celik, E., Gul, M., Aydin, N., Gumus, A.T. and Guneri, A.F., 2015. A comprehensive review of multi criteria decision making approaches based on interval type-2 fuzzy sets. *Knowledge-Based Systems*, 85, pp.329–341. Available at: https://doi.org/10.1016/j.knosys.2015.06.004

Celik, E., Yucesan, M. and Gul, M., 2021. Green supplier selection for textile industry: a case study using BWM-TODIM integration under interval type-2 fuzzy sets. *Environmental Science and Pollution Research*, 28(45), pp.64793–64817. Available at: https://doi.org/10.1007/s11356-021-13832-7

Centobelli, P., Cerchione, R. and Esposito, E., 2018. How to deal with knowledge management misalignment: a taxonomy based on a 3D fuzzy methodology. *Journal of Knowledge Management*, 22(3), pp.538–566. Available at: https://doi.org/10.1108/JKM-10-2016-0456

Diao, F., Cai, Q. and Wei, G., 2022. Taxonomy Method for Multiple Attribute Group Decision Making Under the Spherical Fuzzy

Environment.*Informatica*, pp.713–729. Available at: https://doi.org/10.15388/22-INFOR497

Đurić, G., Mitrović, Č., Komatina, N., Tadić, D. and Vorotović, G., 2019. The hybrid MCDM model with the interval Type-2 fuzzy sets for the software failure analysis. *Journal of Intelligent & Fuzzy Systems*, 37(6), pp.7747–7759. Available at: https://doi.org/10.3233/JIFS-182541

Heidarzade, A., Mahdavi, I. and Mahdavi-Amiri, N., 2016. Supplier selection using a clustering method based on a new distance for interval type-2 fuzzy sets: A case study. *Applied Soft Computing*, 38, pp.213–231. Available at: https://doi.org/10.1016/j.asoc.2015.09.029

KeshavarzGhorabaee, M., Amiri, M., Zavadskas, E.K., Turskis, Z. and Antucheviciene, J., 2017. A new multi-criteria model based on interval type-2 fuzzy sets and EDAS method for supplier evaluation and order allocation with environmental considerations. *Computers & Industrial Engineering*, 112, pp.156–174. Available at: https://doi.org/10.1016/j.cie.2017.08.017

Komatina, N., 2025. A Novel BWM-RADAR Approach for Multi-Attribute Selection of Equipment in the Automotive Industry.*Spectrum of Mechanical Engineering and Operational Research*, 2(1), pp.104–120. Available at: https://doi.org/10.31181/smeor21202531

Komatina, N., Marinković, D., Tadić, D. and Pamučar, D., 2025. Advancing PFMEA Decision-Making: FRADAR Based Prioritization of Failure Modes Using AP, RPN, and Multi-Attribute Assessment in the Automotive Industry. *Tehničkiglasnik/Technical Journal*, 19(3), p.accepted for publication. Available at: https://doi.org/10.31803/tg-20250221185213

Komatina, N., Tadić, D., Aleksić, A. and Banduka, N., 2022. The integrated PFMEA approach with interval type-2 fuzzy sets and FBWM: A case study in the automotive industry. *Proceedings of the Institution of Mechanical Engineers, Part D: Journal of Automobile Engineering*, 236(6), pp.1201–1212. Available at: https://doi.org/10.1177/09544070211034799

Komatina, N., Tadić, D., Aleksić, A. and Jovanović, A.D., 2023. The assessment and selection of suppliers using AHP and MABAC with type-2 fuzzy numbers in automotive industry.*Proceedings of the Institution of Mechanical Engineers, Part O: Journal of Risk and Reliability*, 237(4), pp.836–852. Available at: https://doi.org/10.1177/1748006X221095359

KutluGündoğdu, F. and Kahraman, C., 2019.Spherical fuzzy sets and spherical fuzzy TOPSIS method.*Journal of Intelligent & Fuzzy Systems*, 36(1), pp.337–352. Available at: https://doi.org/10.3233/JIFS-181401

Li, H., Guo, Y., Li, F., Cao, Y., Wang, L. and Ma, Y., 2022. Assessment of operation safety risk for South-to-North Water Diversion Project: a fuzzy VIKOR-FMEA approach. *Water Supply*, 22(4), pp.3685–3701. Available at: https://doi.org/10.2166/ws.2022.009

Liu, P. and Wang, D., 2022. An Extended Taxonomy Method Based on Normal T-Spherical Fuzzy Numbers for Multiple-Attribute Decision-Making.*International Journal of Fuzzy Systems*, 24(1), pp.73–90. Available at: https://doi.org/10.1007/s40815-021-01109-7

Mahmood, T., Ullah, K., Khan, Q. and Jan, N., 2019.An approach toward decision-making and medical diagnosis problems using the concept of spherical fuzzy sets.*Neural Computing and Applications*, 31(11), pp.7041–7053. Available at: https://doi.org/10.1007/s00521-018-3521-2

Mardani, A., Jusoh, A. and Zavadskas, E.K., 2015. Fuzzy multiple criteria decision-making techniques and applications – Two decades review from 1994 to 2014. *Expert Systems with Applications*, 42(8), pp.4126–4148. Available at: https://doi.org/10.1016/j.eswa.2015.01.003

Mendel, J.M., 2017. *Uncertain Rule-Based Fuzzy Systems: Introduction and New Directions, 2nd Edition*. [online] Cham: Springer International Publishing. Available at: https://doi.org/10.1007/978-3-319-51370-6

Mendel, J.M. and John, R.I.B., 2002. Type-2 fuzzy sets made simple. *IEEE Transactions on Fuzzy Systems*, 10(2), pp.117–127. Available at: https://doi.org/10.1109/91.995115

Milovanović, V., Aleksić, A., Milenkov, M. and Sokolović, V., 2024. Ranking of asset maintenance process KPIs using Fermatean fuzzy Delphi and Fermatean fuzzy ELECTRE method. *Journal of Intelligent & Fuzzy Systems*, pp.1–17. Available at: https://doi.org/10.3233/JIFS-238907

Nehi, H.M. and Keikha, A., 2016. TOPSIS and Choquet integral hybrid technique for solving MAGDM problems with interval type-2 fuzzy numbers.*Journal of Intelligent & Fuzzy Systems*, 30(3), pp.1301–1310. Available at: https://doi.org/10.3233/IFS-152044

Oğuz, A., 2024. Drone Selection for Agricultural Enterprises with Interval Type-2 Fuzzy COPRAS Method. *Journal of Research in Business*, 9(2), pp.395–421. Available at: https://doi.org/10.54452/jrb.1447602

Palczewski, K. and Sałabun, W., 2019.The fuzzy TOPSIS applications in the last decade.*Procedia Computer Science*, 159, pp.2294–2303. Available at: https://doi.org/10.1016/j.procs.2019.09.404

Peng, X. and Yang, Y., 2016. Fundamental Properties of Interval-Valued Pythagorean Fuzzy Aggregation Operators: Interval-Valued Pythagorean Fuzzy Aggregation Operations. *International Journal of Intelligent Systems*, 31(5), pp.444–487. Available at: https://doi.org/10.1002/int.21790

Petrović, T., Vesić Vasović, J., Komatina, N., Tadić, D., Klipa, Đ. and Đurić, G., 2022.A Two-Stage Model Based on EFQM, FBWM, and FMOORA for Business Excellence Evaluation in the Process of Manufacturing.*Axioms*, 11(12), p.704. Available at: https://doi.org/10.3390/axioms11120704

Sudžum, R., Nestić, S., Komatina, N. and Kraišnik, M., 2024. An Intuitionistic Fuzzy Multi-Criteria Approach for Prioritizing Failures That Cause Overproduction: A Case Study in Process Manufacturing. *Axioms*, 13(6), p.357. Available at: https://doi.org/10.3390/axioms13060357

Szmidt, E. and Kacprzyk, J., 2000. Distances between intuitionistic fuzzy sets.*Fuzzy Sets and Systems*, 114(3), pp.505–518. Available at: https://doi.org/10.1016/S0165-0114(98)00244-9

Tadić, D. and Komatina, N., 2025. A Hybrid Interval Type-2 Fuzzy DEMATEL-MABAC Approach for Strategic Failure Management in Automotive

Manufacturing.*Journal of Engineering Management and Systems Engineering*, 4(1), pp.21–38. Available at: https://doi.org/10.56578/jemse040102

Tadić, D., Lukić, J., Komatina, N., Marinković, D. and Pamučar, D., 2025. A Fuzzy Decision-Making Approach to Electric Vehicle Evaluation and Ranking.*Tehnickivjesnik/Technical Gazette*, 4(32), pp.1066–1075. Available at: https://doi.org/10.17559/TV-20250223002410

Tian, Z., Wang, J. and Zhang, H., 2018. An integrated approach for failure mode and effects analysis based on fuzzy best-worst, relative entropy, and VIKOR methods. Available at: *Applied Soft Computing*, 72, pp.636–646. https://doi.org/10.1016/j.asoc.2018.03.037

Toptancı, Ş., Gündoğdu, H.G., Korucuk, S., Aytekin, A. and Stević, Ž., 2023. Corporate sustainability strategy selection for a metropolitan municipality using a trapezoidal interval type-2 fuzzy SWARA–COPRAS framework. *Soft Computing*. [online first], Available at: https://doi.org/10.1007/s00500-023-08800-x

Wei, G., Tang, Y., Zhao, M., Lin, R. and Wu, J., 2020.Selecting the Low-Carbon Tourism Destination: Based on Pythagorean Fuzzy Taxonomy Method. *Mathematics*, 8(5), p.832. Available at: https://doi.org/10.3390/math8050832

Xu, D.-Y., Cui, H.-Q., Wang, T.-Y., Fu, J.-W.and Zhu, G.-B., 2024. Interactions and influences on coal miners' safety attention: An evaluation using an improved DEMATEL-ISM approach. *Facta Universitatis, Series: Mechanical Engineering*, 22(1), p.139. Available at: https://doi.org/10.22190/FUME230726042X

Zadeh, L.A., 1988. Fuzzy logic. *Computer*, 21(4), pp.83–93. Available at: https://doi.org/10.1109/2.53

Zhang, X. and Xu, Z., 2014. Extension of TOPSIS to Multiple Criteria Decision Making with Pythagorean Fuzzy Sets: Extension of TOPSIS to Multiple Criteria Decision Making. *International Journal of Intelligent Systems*, 29(12), pp.1061–1078. Available at: https://doi.org/10.1002/int.21676

Zhong, L. and Yao, L., 2017. An ELECTRE I-based multi-criteria group decision making method with interval type-2 fuzzy numbers and its application to supplier selection. *Applied Soft Computing*, 57, pp.556–576. Available at: https://doi.org/10.1016/j.asoc.2017.04.001

Višeatributivni pristup za unapređenje procesa održavanja u remontnim zavodima u fazi okruženju tip-2

Vladimir Milovanović[a], *Aleksandar* Aleksić[b], **autor za prepisku**, *Snežana* Nestić[b], *Nikola* Komatina[b], *Vlada* Sokolović[a], *Marjan* Milenkov[a]
[a] University of Defence, Military Academy, Belgrade, Republic of Serbia
[b] University of Kragujevac, Faculty of Engineering, Kragujevac, Republic of Serbia

OBLAST: matematika, nauke o odlučivanju, industrijsko inženjerstvo
KATEGORIJA (TIP) ČLANKA: originalni naučni rad

Sažetak:

Uvod/cilj: Cilj ovog istraživanja je određivanje prioriteta ključnih indikatora performansi (eng. KPI) na precizan i strukturiran način. Primenom modela odlučivanja koji se zasniva na višeatributivnoj fazi logici, operativni menadžment može identifikovati i prioritetno tretirati aktivnosti koje će u najkraćem mogućem roku poboljšati pouzdanost procesa održavanja, uz istovremeno smanjenje troškova.

Metode: Relativna važnost potprocesa i vrednosti KPI procenjivana je korišćenjem unapred definisanih lingvističkih iskaza modelovanih pomoću intervalnih fazi brojeva tipa-2 (eng. IT2FNs). Ove procene su formulisane kroz okvir grupnog odlučivanja u fazi okruženju. Vektori težina određeni su pomoću fazi geometrijske sredine, dok je rangiranje KPI izvršeno primenom metode Taksonomije u kombinaciji sa IT2FNs, što predstavlja glavni naučni doprinos ovog istraživanja.

Rezultati: Realni podaci prikupljeni iz jednog remontnog zavoda korišćeni su za testiranje predloženog modela. U istraživanju je uspešno modelovana neizvesnost u oceni KPI korišćenjem sedam unapred definisanih lingvističkih izraza mapiranih pomoću IT2FNs. Konzistentan vektor težina dobijen je kroz pristup fazi grupnog odlučivanja. Efikasno rangiranje KPI postignuto je kombinovanjem metode Taksonomije i IT2FNs, što je omogućilo identifikaciju najvažnijih oblasti za operativno unapređenje. Validacijom primene potvrđena je sposobnost metode da pruži jasne prioritete za unapređenje pouzdanosti uz smanjenje troškova.

Zaključak: Ključni doprinosi ove studije su: (i) upotreba pravila fazi algebre sa IT2FNs za određivanje grupne korisnosti, i (ii) integracija metode Taksonomije sa IT2FNs u cilju unapređenja procesa odlučivanja.

Ključne reči: ključni indikatori performansi, operativni menadžment, pouzdanost procesa održavanja, intervalni fazi brojevi tipa-2, metoda Taksonomije, grupno odlučivanje.

Paper received on: 8 April 2025.
Manuscript corrections submitted on: 22 May 2025.
Paper accepted for publishing on: 4 June 2025.

© 2026 The Authors. Published by Vojnotehnički glasnik / Military Technical Courier (www.vtg.mod.gov.rs).This article is an open access article distributed under the terms and conditions of the Creative Commons Attribution license (http://creativecommons.org/licenses/by/4.0/rs/

Fatigue crack propagation modeling in 2D structures using the CPCN-FEM node-based approach

Mohammed Bentahar[a], *Noureddine* Mahmoudi[b], *Nedir* Hachemi[c], *Youcef* Moulai Arbi[d]

[a] Universiy of Saida Dr. Moulay Tahar, Faculty of Technology, Department of Civil Engineering and Hydraulics, Saida, People's Democratic Republic of Algeria,
e-mail: bentahae@yahoo.fr, **corresponding author**,
ORCID ID: https://orcid.org/0000-0002-2166-678X

[b] University of Saida Dr. Moulay Tahar, Faculty of Technology, Department of Civil Engineering and Hydraulics, Saida, People's Democratic Republic of Algeria,
e-mail: mahmoudi.noureddine@yahoo.fr,
ORCID ID: https://orcid.org/0000-0002-9740-0857

[c] University of Mustapha Stambouli, Mascara, People's Democratic Republic of Algeria,
e-mail: nedirhachemidz@gmail.com,
ORCID ID: https://orcid.org/0009-0008-2211-0776

[d] University of Mustapha Stambouli, Laboratory of Quantum Physics of Matter and Mathematical Modeling (LPQ3M), Mascara, People's Democratic Republic of Algeria,
e-mail: youcef.moulaiarbi@univ-mascara.dz,
ORCID ID: https://orcid.org/0000-0002-6534-8820

https://doi.org/10.5937/vojtehg74-59257

FIELD: mechanical engineering, materials
ARTICLE TYPE: original scientific paper

Abstract:

Introduction/purpose: The study aims to model fatigue-related crack propagation by introducing a numerical method, CPCN-FEM (Crack Propagation by Coordinates of Nodes – Finite Element Method), which predicts crack trajectories through the systematic generation of nodal coordinates around the crack front.

Methods: The approach defines four principal nodes to control the propagation direction and computes the stress intensity factors (K I) and (KII), along with the crack inclination angle (β). The method was implemented in FORTRAN to automate node tracking, coordinate updating, and stepwise crack advance in a two-dimensional elastic isotropic model. Simulations were conducted and compared with analytical crack-path solutions, using the Richard criterion to determine crack orientation.

Results: The numerical model reproduced expected crack trajectories with high agreement with analytical predictions and demonstrated stable displacement behavior across multiple propagation cases. Mesh integrity was preserved during all propagation steps, and no remeshing was required.

Conclusion: The findings show that CPCN-FEM provides an accurate, efficient, and mesh-preserving technique for modeling crack growth under fatigue, offering reliable predictions of crack path evolution in fracture mechanics.

Keywords: crack propagation, Stress Intensity Factor (SIF), finite element method, CPCN-FEM, node coordinates, fracture mechanics.

Introduction

Fracture mechanics is a relatively modern branch of solid mechanics, having seen its primary theoretical growth during the twentieth century. In parallel, the phenomenon of material fatigue attracted growing attention from researchers as early as the beginning of the 1900s. Both fields share a common objective: enabling engineers to anticipate the behavior of structures up to their eventual failure (Elguedj et al., 2006).

In this context, Kocańda et al. (2009) introduced a deterministic methodology to forecast fatigue crack growth in components subjected to variable-amplitude loading, including overload and underload cycles. More recently, Niu et al. (2023) investigated how the length of steel fibers affects fatigue crack propagation in ultra-high-performance concrete (UHPC) exposed to cyclic bending, employing both Paris' law and the J-integral, in addition to a theoretical model of multiple crack growth.

Other approaches, such as that proposed by Mehmet et al., focus on predicting fatigue life and crack propagation by incorporating cycle counting and stress ratio calculations. Ricardo et al. (2018) studied the influence of propagation speed on crack opening and closing stresses through finite element modeling of ASTM-type specimens. Ilie and Ince et al. (2022) developed a systematic 3D FEM-based model to simulate crack growth behavior.

Several innovative strategies for crack propagation analysis have also been introduced in recent literature. For example, Wysmulski et al. (2023) applied both numerical and experimental methods to analyze crack formation in a carbon-epoxy composite plate featuring a central hole. In a similar vein, Nie et al. (2025) proposed a fatigue-based model aimed at capturing the complexity of small-scale crack networks.

Borges et al. (2022) explored fatigue crack growth in aluminum alloy 2024-T351 using the plastic CTOD (Crack Tip Opening Displacement)

technique to examine strain rate effects. Complementarily, Robles et al. (2023) applied various evaluation methods to characterize crack progression in AA2024-T315, with a focus on improving data reliability.

Crusat et al. (2021) contributed a numerical model for crack propagation in two-dimensional semi-brittle structures using zero-thickness interface elements, integrated within a finite element framework and grounded in constitutive mechanics principles. Moreover, several researchers, including Zhang et al. (2023), Si et al. (2024), and Zhang et al. (2024) investigated crack nucleation processes in brittle materials through both experimental and numerical approaches.

Pramana et al. (2024) carried out a study combining experimental and computational analyses to understand crack propagation in Al 2024, with a focus on developing loading spectra based on the Paris equation. Numerous studies have also sought to determine and quantify stress intensity factors (SIFs). For example, Montasser et al. (2023) applied isometric analysis techniques for crack control, while Sadek et al. (2024) used both the J-integral and CTOD methods to calculate SIFs in various structural geometries.

Alshoaibi and Fageehi (2023) introduced the "split-knot" method in fracture simulations to enhance crack path prediction through successive linear segment growth. Bentahar et al. (2023) used the Extended Finite Element Method (XFEM) to analyze inclined cracks and to evaluate energy dissipation (ALLDMD) and deformation energy (ALLSE) during fatigue crack progression.

Furthermore, Sedmak et al. (2024) demonstrated the effectiveness of XFEM for simulating fatigue crack growth in welded joints, providing reliable estimates of cycles to failure. A complementary study by Sedmak et al. (2023) reinforced the value of XFEM for evaluating fatigue life through comprehensive case studies. In another development, Alshoaibi and Ariffin (2015) used a two-dimensional modeling approach to trace crack trajectories and evaluate the lifespan of structural components in the context of damage tolerance.

Finally, Rahman et al. (2024) examined crack development using finite element techniques, focusing on self-healing materials where fracture mechanics is coupled with oxidation kinetics.

The objective of the present work is to implement a novel computational approach, CPCN-FEM (Crack Propagation via Coordinates of Nodes – Finite Element Method), which allows for the accurate construction of four key nodes along the crack front. This framework enables not only the evaluation of stress intensity factors (K_I and K_{II}), but also the calculation of the crack orientation angle β. The methodology is

applied to the crack propagation problem in an isotropic elastic material, enabling detailed modeling of the crack trajectory through a step-by-step numerical process.

Fracture mechanics

Criterion of Richard 2D

Richard's criterion, which is based on K_V, is superior to the toughness K_{IC}. Therefore, irregular crack growth occurs, as indicated by equation (1).

$$K_V = \frac{K_I}{2} + \frac{1}{2}\sqrt{K_I^2 + 5.366K_{II}^2} = K_{IC} \tag{1}$$

where K_V is influenced by the stress intensity factors (K_I and K_{II}).

The Richard criterion provides excellent approximations for the ultimate fracture surface, compared to the maximum tangential stress criterion by Erdogan and Sih (1963). Equation (2) allows determining the crack inclination angle (β):

$$\beta = \mp\left[140^\circ \frac{|K_{II}|}{|K_I| + |K_{II}|} - 70^\circ\left(\frac{|K_{II}|}{|K_I| + |K_{II}|}\right)^2\right] \tag{2}$$

where KI and KII are the stress intensity factors corresponding to Mode I and Mode II.

For K_{II} greater than zero, angle β is less than zero and vice versa as long as K_I remains above zero.

Nuismer's criterion

The energy release rate indicator developed by Nuismer et al. (1975) is based on the assumption of a short-duration curved crack (Figure 1). Therefore, there are other parameters, such as the criterion by Amestoy et al. (1980) which relies on the energy release rate and depicts crack propagation in the context of 2D mixed-mode loading. The conclusions for the crack deflection angles and the fracture limit curve correspond to those of the maximum tangential stress criterion (Richard et al, 2004). Bilby and Cardew (1975) address this criterion.

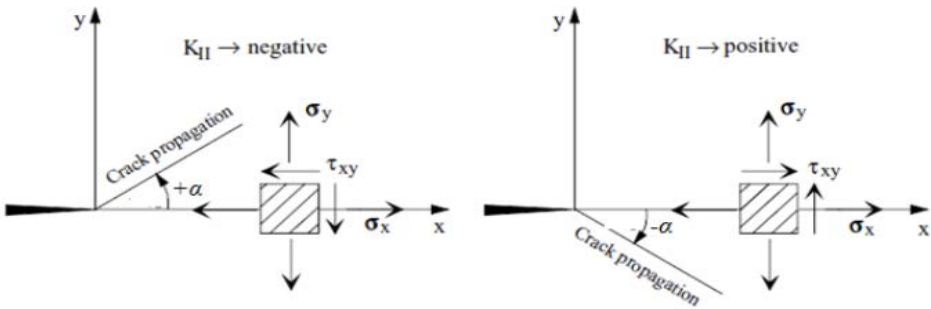

Figure 1 - Illustration of crack propagation using Richard's criterion [31]

Stress field

For the coordinates r and θ, Tada et al. (2000) provided the equation of the two-dimensional stress field close to the fracture tip, which is described by the stress intensity factor K.

$$\sigma_{i,j}^{I,II}(r,\theta) = \frac{K_{I,II}}{\sqrt{2\pi r}} f(\theta) \tag{3}$$

$K_{I, II}$ is the SIF in Mode I and II,

$\sigma_{i,j}^{I,II}$ is the stress field associated with Mode I and II.

Consequently, singular elements must be constructed to precisely characterize the singularity field at the crack front. Since the leading front method generates triangular elements from boundary faces, the area surrounding the crack front must be separated before generating singular elements (Zienkiewicz et al, 2005). First, nodes are created around the crack tip in a rosette manner, then the node at the crack front and the associated edge segments are extracted. The rosette elements are then constructed by forming triangles as shown in Figure 2.

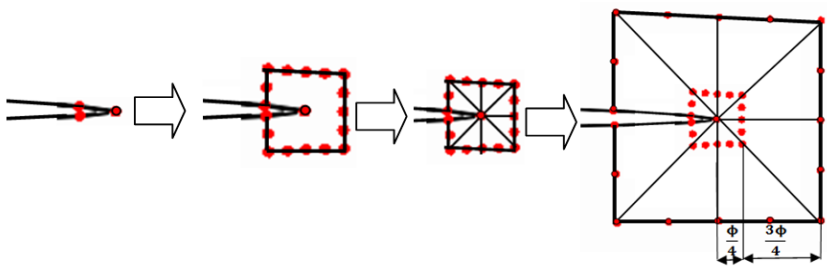

Figure 2 - Special finite elements quarter point around the crack front

Bentahar, M. et al, Fatigue crack propagation modeling in 2D structures using the CPCN-FEM node-based approach, pp.309-330

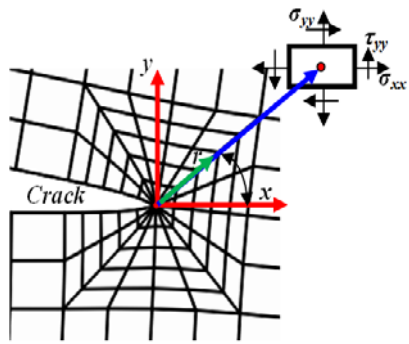

Figure 3 - Stress field around the crack front

$$\sigma_{xx} = \frac{K_I}{\sqrt{2\pi r}}\cos\frac{\theta}{2}\left(1-\sin\frac{\theta}{2}\sin\frac{3\theta}{2}\right)$$
$$\sigma_{yy} = \frac{K_I}{\sqrt{2\pi r}}\cos\frac{\theta}{2}\left(1+\sin\frac{\theta}{2}\sin\frac{3\theta}{2}\right) \quad (4)$$
$$\tau_{xy} = \frac{K_I}{\sqrt{2\pi r}}\sin\frac{\theta}{2}\cos\frac{\theta}{2}\cos\frac{3\theta}{2}$$

Stress Intensity Factor

Saverio et al. (2024) defined the stress intensity factor K as a parameter which makes it possible to determine the state of stress and strain at any point in the vicinity of the crack.

$$K_I = R\sigma\sqrt{a\pi} \quad (5)$$

where R is the geometric correction factor of the model used.

$$R = 1.12 - 0.23\left(\frac{a}{L}\right) + 10.6\left(\frac{a}{L}\right)^2$$
$$-21.7\left(\frac{a}{L}\right)^3 + 30.4\left(\frac{a}{L}\right)^4$$

where a is the crack length [mm] and L is the length of the structure.

The stress intensity factor KII is given by the relation

$$K_I \sin\theta + K_{II}(3\sin\theta - 1) = 0 \qquad (7)$$

Numerical model

We consider an elastic material structure of isotropic behavior, as shown in Figure 4. The structure has a height B = 20 mm and a length L = 18 mm, and 4 node elements were used in this analysis. The structure is subjected to a tensile stress applied to the upper surface of σ = 110 MPa, and the lower part is subjected to a fixed boundary condition. The mechanical properties of the material (Aluminum Alloy, AA) are E = 72,400 MPa and Poisson's ratio *v* is 0.3.

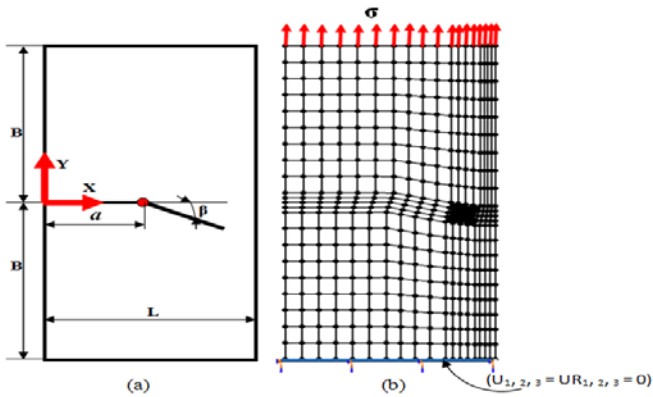

Figure 4 - CPCN-FEM model

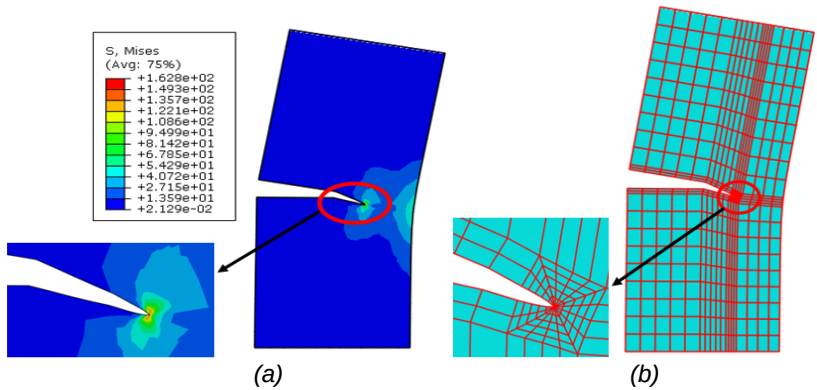

Figure 5 - a) stress field and b) crack propagation on the CPCN-FEM model

Figure 5 illustrates the crack propagation trajectory for different crack inclination angles using the CPCN-FEM approach. Furthermore, Figure 5a

illustrates the stress field in the vicinity of the crack front, and Figure 5b shows the different contours around the crack front.

Strategy of the CPCN-FEM method

Creation of node coordinates by the Finite Element Method (CPCN-FEM) at the crack front of each crack propagation stage comprises the following steps:

Creation of the node coordinates for the first propagation, Fig. 6a;
Creation of the node coordinates for the second propagation, Fig. 6b;
Creation of the node coordinates for the third propagation Fig. 6c;
Creation of the node coordinates for the fourth propagation Fig. 6d;
Creation of the node coordinates for the fifth propagation Fig. 6e;
Creation of the node coordinates for the sixth propagation Fig. 6f.

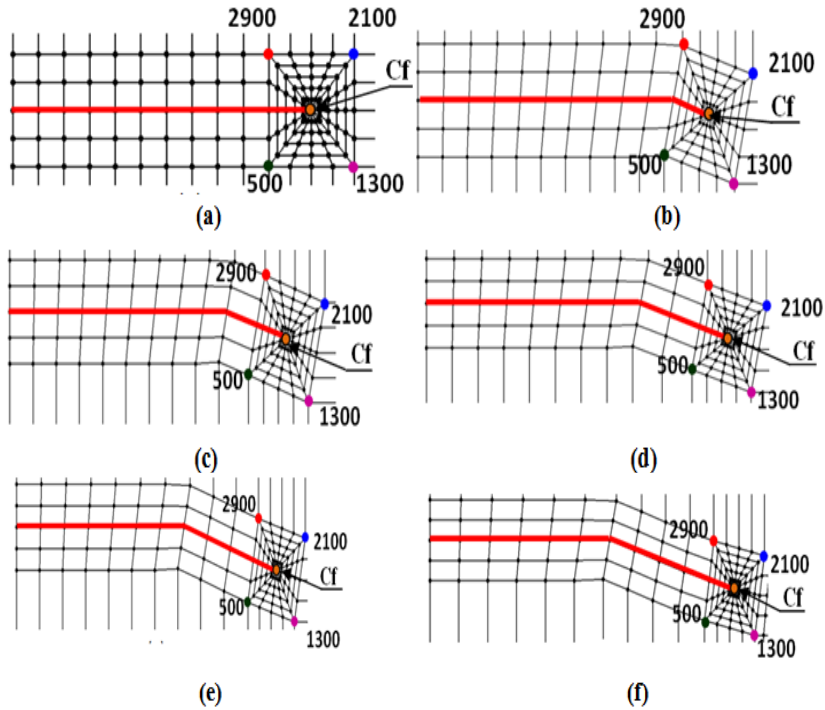

Figure 6 - Strategy of the CPCN-FEM method: a) 1st propagation, b) 2nd propagation, c) 3rd propagation, d) 4th propagation, e) 5th propagation and f) 6th propagation

Coordinates of the nodes

Initial crack

Table 1 - Coordinates of the nodes on the initial crack front

Nodes	Coordinates	
	X	Y
2900	a -ϕ/2	+ϕ /2
2100	a +ϕ /2	+ϕ /2
1300	a -ϕ /2	-ϕ /2
500	a +ϕ /2	-ϕ /2

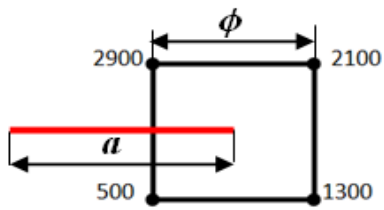

Figure 7 - Initial crack with length a with node numbering

The coordinates of the four nodes for the initial crack are given by equation (8):

$$X_i = a - S\frac{\phi}{2}$$
$$Y_i = S\frac{\phi}{2} \quad (8)$$

where i=2900, 2100,1300 and 500 with S=1 for the X coordinate of 2900 and 500 and the Y coordinate of 2900 and 2100, and S= -1, for the X coordinate of 2100 and 1300 and the Y coordinate of 500 and 1300. Moreover, a is the crack length [mm], measured from the centerline of the structure, ϕ is the total crack front length [mm], i.e., the span of the crack opening in the Y-direction at the crack front, and S is a directional scaling factor used to distribute the nodes symmetrically around the crack front. Its values are S=±1, depending on the node location, to simplify the expressions for X and Y coordinates in the crack plane.

The role of S is purely geometric: it ensures the correct sign for each coordinate, so that nodes are placed in all four quadrants surrounding the crack tip.

The four nodes of the crack front

The second part of the study presents the crack propagation coordinates of the nodes, obtained by the CPCN-FEM Finite Element Method and explained using different equations based on the two axes (X and Y).

Consequently, for node 2900, we obtain equations (9) and (10) as follows:

$$X(2900) = a + \frac{\phi}{2}\left[\sum_{q=1}^{i-1} cos \sum_{j=1}^{q}(\beta_j)(-1)^i sin \sum_{j=1}^{i}(\beta_j)\right] \tag{9}$$

a is crack length, ϕ is crack front length and β is the angle of crack inclination.

$$Y(2900) = \frac{\phi}{2}\left[\sum_{q=1}^{i-1} sin \sum_{j=1}^{q}(\beta_j) + cos\left(\sum_{j=1}^{i}(\beta_j)\right)\right] \tag{10}$$

with i=1, ..,6.

Equations (11) and (12) describe the coordinates of node 2100.

$$X(2100) = a + \frac{\phi}{2}\left[\sum_{q=1}^{i-1} cos \sum_{j=1}^{q}(\beta_j)(-1)^i sin\left(\sum_{j=1}^{i}(\beta_j)\right) + cos\left(\sum_{j=1}^{i}(\beta_j)\right)\right] \tag{11}$$

with i=1, ..,6.

$$Y(2100) = \frac{\phi}{2}\left[cos \sum_{j=1}^{i}(\beta_j) + \sum_{q=1}^{i} sin \sum_{j=1}^{q}(\beta_j) + sin\left(\sum_{j=1}^{i}(\beta_j)\right)\right] \tag{12}$$

with i=1, ..,6.

Node 1300 is defined during crack propagation by the coordinate obtained by equations (13) and (14).

$$X(1300) = a + \frac{\phi}{2}\left[\sum_{q=1}^{i} cos \sum_{j=1}^{q}(\beta_j) + cos \sum_{j=1}^{i}(\beta_j) + sin \sum_{j=1}^{i}(\beta_j)\right] \tag{13}$$

with i=1, ..,6.

$$Y(1300) = \frac{\phi}{2}\left[\sum_{q=1}^{i} sin \sum_{j=1}^{q}(\beta_j) + sin \sum_{j=1}^{i}(\beta_j) - cos \sum_{j=1}^{i}(\beta_j)\right] \quad (14)$$

with i=1, ..,6.

For the different stages of crack propagation concerning node 500, we have the coordinates (15) and (16):

$$X(500) = a + \frac{\phi}{2}\left[\sum_{q=1}^{i} cos \sum_{j=1}^{q}(\beta_j) + sin \sum_{j=1}^{i}(\beta_j)\right] \quad (15)$$

with i=1, ..,6.

$$Y(500) = \frac{\phi}{2}\left[\sum_{q=1}^{i} sin \sum_{j=1}^{q}(\beta_j) - cos \sum_{j=1}^{i}(\beta_j)\right] \quad (16)$$

with i=1, ..,6.

Results and discussion

Numerical validation and mesh convergence

To ensure the robustness of the numerical results, a convergence study was carried out using different mesh densities around the crack front. Several refined meshes were tested, including configurations with:

- Coarse mesh: average element size ≈ 0.5 mm,
- Medium mesh: ≈ 0.2 mm,
- Fine mesh: ≈ 0.1 mm around the crack tip.

The stress intensity factor (SIF) K_I was computed for each configuration. Results showed that the relative variation of K_I was below 2% between the medium and fine meshes, indicating that the solution is mesh-independent at the chosen resolution.

In addition, the numerical results were validated against analytical solutions for initial crack cases. The CPCN-FEM results showed excellent agreement, with an average relative error below 5% in the linear elastic fracture mechanics (LEFM) regime.

Computation time remained acceptable (less than 1 min per propagation step) due to the localized refinement strategy and the use of FORTRAN routines for node updates without global remeshing. We show the different extents of the initial crack front, for the four nodes that form the crack front. The nodes are numbered using the FORTRAN program,

and the four nodes are plotted using equation (8) concerning the two coordinates (X and Y), for the different crack lengths a = 1, 2, 3, 3.5 mm.

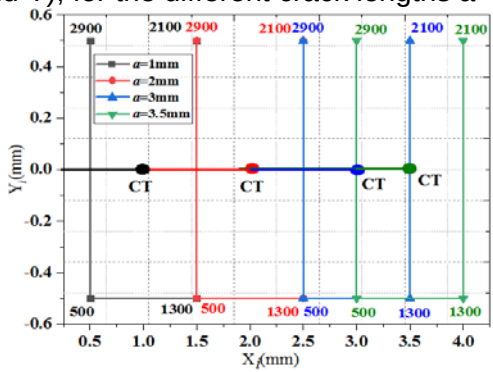

Figure 8 - Node coordinates by CPCN-FEM method with i= 2900, 2100, 1300 and 500 regarding crack length a=1, 2, 3, and 3.5mm

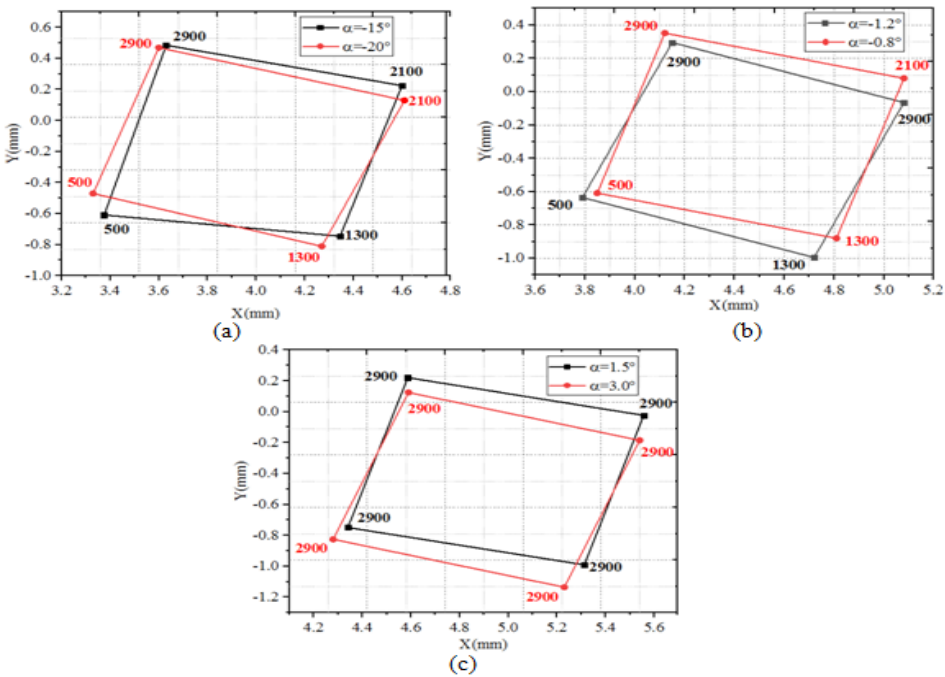

Figure 9 - Variation of different crack front nodes for different crack angles: a) β=-15°, -20°; b) β=-1.2°, -0.8° and c) β=1.5°, 3.0°

Figure 9 presents the variation of node positions in the X, Y plane, based on the application of equations (9) to (16) for different crack inclination angles: (a) β = –15° and –20°; (b) β = –1.2° and –0.8°; and (c)

β = 1.5° and 3.0°. Each configuration reveals that the nodes undergo a shift along both the X and Y axes, with the displacement interval in the X-direction depending significantly on the angle β. For instance, when β = –20°, the X-coordinate varies between approximately 3.33 mm and 4.61 mm, while for β = –15°, it ranges from 3.375 mm to 4.6 mm. These results indicate that as the crack propagates, the inclination angle tends to increase, influencing the deformation of the surrounding nodes. These variations can be attributed to the redistribution of stress fields around the crack tip, which becomes more anisotropic with increasing β. This anisotropy leads to directional displacement patterns in the material, especially in heterogeneous media, where crack paths are highly sensitive to local mechanical contrasts. Such behavior aligns with recent studies in fracture mechanics, which highlight that crack propagation often follows directions of maximum energy release or stress intensity (Worthington et al, 2023). The CPCN-FEM approach used here effectively captures these complex interactions between crack orientation and mechanical response, demonstrating its reliability for modeling advanced crack growth scenarios.

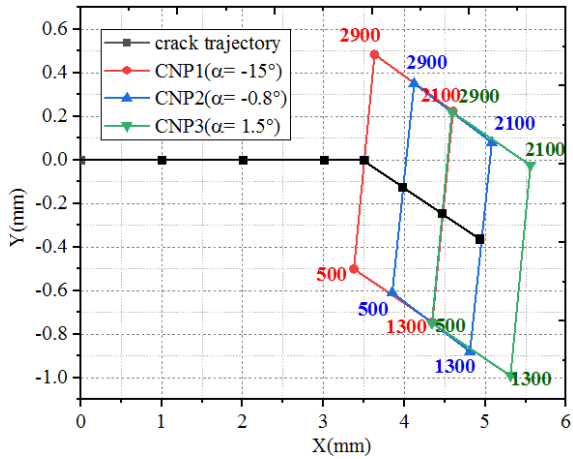

Figure 10 - Comparison between three propagations by the CPCN-FEM method concerning the three angles: β=-15°, -0.8° and β=1.5°

Figure 10 illustrates a comparison between three crack propagation scenarios, each inclined by a different angle: β = –15°, –0.8°, and 1.5°, as modeled using the CPCN-FEM approach. The crack trajectory, which extends up to a propagation length of a = 3.5 mm, is described by equation (8), while the propagation of each configuration is governed by equations (9) through (16). The figure clearly demonstrates that the CPCN-FEM method accurately captures the step-by-step evolution of the crack front

for various inclination angles without requiring any modification of the global mesh. This highlights one of the method's key advantages: the ability to model complex crack paths in a continuous domain with high precision. Physically, the observed differences in crack advancement for the three inclination angles can be attributed to the redistribution of local stress fields and the directional dependency of crack growth mechanisms. As the angle increases, the deviation of the crack front becomes more evident, reflecting the influence of anisotropy and the material's fracture resistance along different paths. These results are consistent with the findings of recent studies that emphasize the importance of incorporating orientation-dependent criteria in predictive fracture models (e.g., Guizhong et al, 2024). Overall, the CPCN-FEM method proves to be a robust and efficient tool for simulating realistic crack propagation without compromising mesh integrity.

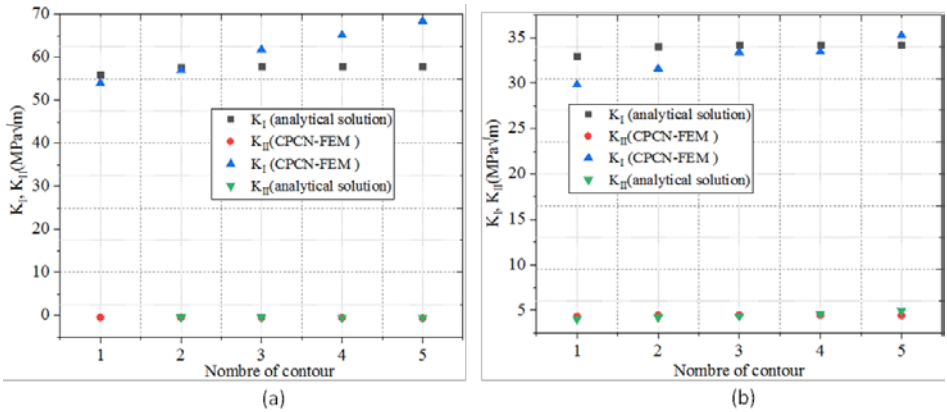

Figure 11 - Evolution of stress intensity factors by the CPCN-FEM method: a) first propagation and b) second propagation

Figure 11 illustrates the variation of the stress intensity factors K_I and K_{II} as a function of the number of contours, computed using the CPCN-FEM method. This analysis highlights the effectiveness of the numerical approach in accurately characterizing the stress field near the crack front.

In the first configuration (Figure 11a), which corresponds to a straight crack with an inclination angle $\beta = 0°$, K_I increases gradually with the number of contours, while K_{II} remains nearly constant and close to zero. This behavior indicates that the loading is predominantly Mode I, as expected for a straight crack subjected to symmetric conditions. The stability of K_{II} suggests that the stress field is well-resolved and that the numerical formulation successfully isolates the mode components. The

strong agreement between the CPCN-FEM results and the analytical solution confirm the reliability of the method in modeling initial straight crack propagation.

Figure 11b presents the case of an inclined crack at β = 15°, which introduces a mixed-mode loading condition. Here, K_I shows a similar trend to the previous case, increasing with the number of contours. However, K_{II} remains constant at a non-negligible value, indicating the contribution of shear stresses due to the inclined crack front. Equations (8), (9), and (10) were used to simulate the crack extension along appropriate directions, accounting for the nodal positions along the crack front in both propagation scenarios.

These results demonstrate that increasing the number of contours improves the accuracy of K_I estimation, while K_{II}, though sensitive to the crack orientation, remains relatively unaffected by this parameter. This observation is consistent with the findings of Keprate et al. (2019), who emphasized the role of contour selection and mesh refinement in the accurate evaluation of stress intensity factors. Furthermore, recent studies (Gdoutos et al., 2012; Fayed et al., 2017) have shown that combining mode decomposition techniques with multi-contour integration enhances the fidelity of numerical predictions, particularly in mixed-mode fracture problems involving anisotropic or composite materials.

The good agreement between the CPCN-FEM results and the analytical solutions across both cases reinforces the validity of the numerical method. The approach proves to be robust for simulating crack propagation in both straight and inclined configurations, accurately capturing the relative contributions of Modes I and II.

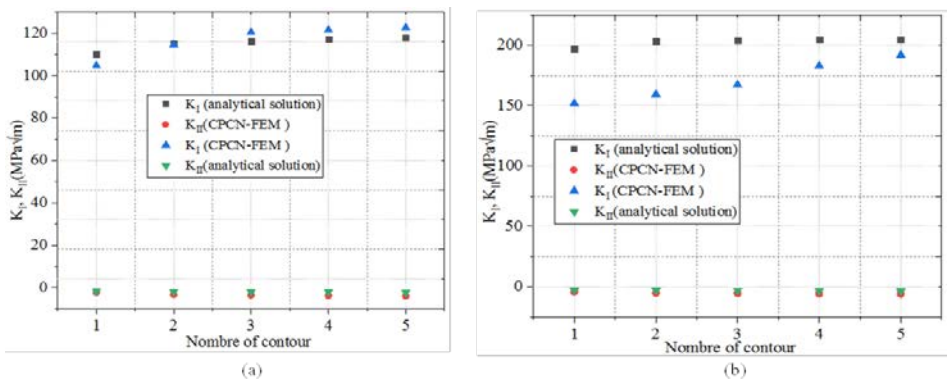

Figure 12 - Evolution of stress intensity factors by the CPCN-FEM method; a) third propagation and b) fourth propagation

Figure 12 shows the variation of the stress intensity factors K_I and K_{II} as a function of the number of contours for the third (Figure 12a) and fourth (Figure 12b) crack propagation scenarios, using the CPCN-FEM method. These cases correspond to more advanced stages of crack growth, where the geometry and the stress field become increasingly complex.

In the third propagation case (Figure 12a), the values of K_I increase significantly with the number of contours, stabilizing around 120 MPa$\sqrt{m}$. This trend indicates a clear sensitivity of the stress intensity factor to the extent of crack growth. The increase in $K_I$is consistent with the physical expectation that a longer or more evolved crack experiences a higher stress concentration at its tip. Meanwhile, K_{II} remains low and nearly constant, suggesting that Mode I still dominates and that the numerical approach is effective in capturing the crack tip singularity in this configuration.

In the fourth propagation case (Figure 12b), the values of K_I are even higher, reaching up to approximately 200 MPa$\sqrt{m}$, which aligns with the progression of the crack and the corresponding increase in energy release rate. This rise in K_I reflects the cumulative effect of crack length and propagation angle, both of which contribute to intensified stress conditions at the crack front. As in the previous case, K_{II} remains stable across all contours, further confirming that the CPCN-FEM method reliably separates the contributions of each fracture mode.

These results support the theoretical understanding that the stress intensity factor K_I increases with crack length and propagation, as confirmed in studies such as those by Fayed et al. (2017) and Kumar et al. (2016), which highlight the dependency of fracture parameters on crack geometry and material configuration. Furthermore, the consistent results across multiple contours reflect the robustness of the CPCN-FEM technique, especially in modeling cracks under complex, multi-stage propagation paths. This is in agreement with findings from recent numerical investigations (Chang et al, 2014), where multi-contour techniques significantly improved accuracy in evaluating mixed-mode fracture parameters.

Overall, the comparison with analytical solutions demonstrates that the CPCN-FEM method remains accurate and effective, even in advanced crack propagation cases involving large stress gradients. The results underline its potential for reliable use in structural integrity assessments and fracture mechanics simulations of complex geometries.

Conclusion

In this study, a novel numerical approach, CPCN-FEM (Crack Propagation via Coordinates of Nodes - Finite Element Method), was developed and applied to simulate the progressive propagation of a crack in an elastic, isotropic material. The method centers on the strategic generation of four key nodes around the crack front to guide its directional growth at each propagation stage. This approach enabled accurate tracking of crack path geometry while maintaining a stable mesh configuration, thanks to the FORTRAN-based node-updating algorithm.

One of the major contributions of this work lies in the ability of CPCN-FEM to compute the stress intensity factors (SIFs) in Modes I and II (K_I and K_{II}), as well as to estimate the crack inclination angle (β), with high consistency across multiple propagation stages. The method's validity was confirmed through comparative analysis with classical analytical solutions, showing excellent agreement in both crack trajectory and SIF values. Additionally, the study demonstrated that changes in the crack angle result in measurable and predictable variations in the positions of the key nodes, reflecting the sensitivity and robustness of the proposed model.

By avoiding the need for full remeshing during crack growth, CPCN-FEM offers a highly efficient solution suitable for large-scale simulations or real-time fracture analysis. Its simplicity in node control, combined with its compatibility with standard finite element frameworks, makes it an attractive tool for researchers and engineers working in fracture mechanics, fatigue analysis, and damage tolerance assessment.

Looking forward, this method can be further extended to account for nonlinear material behavior, anisotropic properties, and thermal or environmental effects. It also holds potential for integration with experimental crack tracking data, enabling hybrid approaches for validating simulation accuracy. Moreover, coupling the CPCN-FEM model with adaptive meshing strategies and 3D implementations would significantly enhance its applicability to more complex real-world structures and loading conditions.

In conclusion, the CPCN-FEM method provides a reliable, computationally efficient, and theoretically sound framework for analyzing crack propagation in 2D elastic structures, paving the way for future advancements in digital fracture mechanics.

References

Abdulnaser Alshoaibi and Ahmad Kamal Ariffin. 2015. Finite Element Modeling of Fatigue Crack Propagation Using a Self Adaptive Mesh Strategy, *International Review of Aerospace Engineering (IREASE)*, 8(6):209, Available at: https://doi.org/10.15866/irease.v8i6.8823

AlshoaibI, A. M. and Fageehi, Y. A. 2023. A Computational Framework for 2D Crack Growth Based on the Adaptive Finite. Element Method, *Appl. Sci,* v. 13, n. 1, 2023. 284, https:// doi.org/10.3390/app13010284

Amestoy, M. Bui, H.D. and Dang Van K. 1980. [In:] *International Advances in Fracture Research,* Fran¸cois D. et al. (Eds.), Oxford, pp. 107-113.

Bentahar M. 2023. ALLDMD Dissipation Energy Analysis by the Method Extended Finite Elements of a 2D Cracked Structure of an Elastic Linear Isotropic Homogeneous Material. *Journal of Electronics, Computer Networking and Applied Mathematics,* v. 3, n. 2, pp. 1-8, 2023. Available at: https://doi.org/10.55529/jecnam.32.1.8

Bentahar, M. 2023. Fatigue Analysis of an Inclined Crack Propagation Problem by the X-FEM Method. *International Journal of Applied and Structural Mechanics (IJASM),* v. 3, n. 4, pp. 23–31, Available at: https://doi.org/10.55529/ijasm.34.23.31

Bentahar, M. Benzaama, H. and Mahmoudi, N. 2021. Numerical modeling of the evolution of the strain energy ALLSE of the crack propagation by the X-FEM method. *Revue des matériaux et énergies renouvelables*, v. 5, n. 2, pp. 24-31, Available at : https://asjp.cerist.dz/en/article/167392

Bilby, B. A., and Cardew, G. E. 1975. The crack with a kinked tip. *International Journal of Fracture,* 11, pp. 708-712. Available at: https://doi.org/10.1007/BF00116380

Borges, M. F. Lopez-Crespo, P. Antunes, F.V. Moreno, B. Prates, P. Camas, D. and Neto, D.M. 2021. Fatigue crack propagation analysis in 2024-T351 aluminium alloy using nonlinear parameters, *International Journal of Fatigue,* V153, 106478, Available at: https://doi.org/10.1016/j.ijfatigue.2021.106478.

Chang, J. H., & Jiang, J. Y. 2014. Modified Contour Integrals for Calculation of Stress Intensity Factors for Cracks in Anisotropic FGMs. *Applied Mechanics and Materials*, 627, 129-133. Available at: https://doi.org/10.4028/www.scientific.net/AMM.627.129

Crusat, L. Carol, I. and Garolera, D. 2021. Application of configurational mechanics to crack propagation in quasi-brittle materials*, Engineering Fracture Mechanics*, V 241, 107349, Available at: https://doi.org/10.1016/j.engfracmech.2020.107349

Elguedj, T. 2006. Simulation numérique de la propagation de fissure en fatigue par la méthode des éléments finis étendus : thèse prise en compte de la plasticité et du contact-frottement*, lamcos - umr cnrs* 5514 - INSA de Lyon 20, avenue Albert Einstein, 69621 Villeurbanne Cedex (FRANCE).

Erdogan, F. and Sih G.C. 1963. On the crack extension in plates under plane loading and shear, *Journal of Basic Engineering*, 85, 4, pp. 519-527. Available at: https://doi.org/10.1115/1.3656897

Fayed, A. S. 2017. Numerical analysis of mixed mode I/II stress intensity factors of edge slant cracked plates*. Engineering Solid Mechanics*, 5(1), 61-70. Available at: https://doi.org/10.5267/j.esm.2016.8.001

Gdoutos, E. E. 2012. Problems of mixed mode crack propagation (Vol. 2). *Springer Science & Business Media*.

Guizhong, X. I. E., Chongmao, Z. H. A. O., Hao, L. I., Jun, L. I. U., Wenliao, D. U., Jiahe, L. V., & Chao, W. U. 2024. An adaptive extended finite element based crack propagation analysis method. *Mechanics,* 30(1), 74-82. Available at: https://doi.org/10.5755/j02.mech.33301

Ilie, P. and Ince, A. 2022. Three-dimensional fatigue crack growth simulation and fatigue life assessment based on finite element analysis*, Fatigue & Fracture of Engineering Materials & Structures*, v.45, n.11, pp. 3251-3266, Available at: https://doi.org/10.1111/ffe.13815

Keprate, A., Chandima Ratnayake, R. M., & Sankararaman, S. 2019. Experimental validation of the adaptive Gaussian process regression model used for prediction of stress intensity factor as an alternative to finite element method. *Journal of Offshore Mechanics and Arctic Engineering*, 141(2), 021606. Available at: https://doi.org/10.1115/1.4041457

Kocańda, D. and Torzewski, J. 2009. Deterministic approach to predicting the fatigue crack growth in the 2024-t3 aluminum alloy under variable amplitude loading *, Fatigue of Aircraft Structures,* Vol. 1, pp.102-115, Available at: https://doi.org/10.2478/v10164-010-0010-1

Kumar, D., Roy, R., Kweon, J. H., & Choi, J. H. 2016. Numerical modeling of combined matrix cracking and delamination in composite laminates using cohesive elements. *Applied Composite Materials*, 23, 397-419. , Available at: doi.org/10.1007/s10443-015-9465-0

Mehmet, F. Yaren, M. F. Ayhan, A. O. 2024. A new method for prediction of fatigue crack propagation life under variable amplitude spectrum loading, *Theoretical and Applied Fracture Mechanics,* Volume 131, 104355, , Available at: https://doi.org/10.1016/j.tafmec.2024.104355

Montassir, S. Moustabchir, H. and Elkhalfi, A. 2023. Application of NURBS in the Fracture Mechanics Framework to Study the Stress Intensity Factor. Statistics, *Optimization and Information Computing*, v. 11, n. 1, pp. 106–115. Available at: https://doi.org/10.19139/soic-2310-5070-1553

Nie, Y. Wang, X. Wu, B. Zhang, G. Gamage, R. P. Li, Shiyuan. and Zhang, L. 2025. Influences of the stress ratio and local micro mineral aggregates on small fatigue crack propagation in the shale containing bedding planes, *International Journal of Rock Mechanics and Mining Sciences,* V185, 105980, Available at: https://doi.org/10.1016/j.ijrmms.2024.105980

Niu, Y. Fan, J. Shi, X. Wei, J. Jiao, C. and Hu, J. 2023. Application of the J-Integral and Digital Image Correlation (DIC) to Determination of Multiple Crack

Propagation Law of UHPC under Flexural Cyclic Loading. *Materials,* v. 6, p. 1296, Available at: https://doi.org/10.3390/ma16010296

Nuismer, R.J. 1975. An energy release rate criterion for mixed mode fracture, *International Journal of Fracture*, 11, 2, pp. 245-250. Available at: https://doi.org/10.1007/BF00038891

Pramana, N. et al. 2024.Experimental and numerical analysis of crack propagation material Al 2024 under spectrum load. *AIP Conference Proceedings.* Vol. 3003. No. 1. AIP Publishing LLC, Available at: https://doi.org/10.1063/5.0186423

Rahman, M. Maeda, T. Osada, T. and Ozaki, S. 2024. Finite element analysis of crack propagation, crack-gap-filling, and recovery behavior of mechanical properties in oxidation-induced self-healing ceramics, *International Journal of Solids and Structures*, v. 306, n.3, 113104, Available at: https://doi.org/10.1016/j.ijsolstr.2024.113104

Ricardo, L.C.H. 2018. Crack Propagation by Finite Element Method, *Frattura edIntegrità Strutturale*, v. 12, n. 43, pp. 57-78. , Available at: : https://doi.org/10.3221/IGF-ESIS.43.04

Richard, H. A. 2004. Fulland, M and Sander, M. Theoretical crack path prediction Publishing Ltd. *Fatigue Fract Engng Mater Struct* 28, pp. 3-12. Available at : https://doi.org/10.1111/j.1460-2695.2004.00855.x

Richard, H.A. 1985. Bruchvorhersagen bei überlagerter Normal- und Schubbeanspruchung von Rissen.*VDI-Forschungsheft* 631. VDI-Verlag, Düsseldorf. ISBN: 3188506317

Robles, J .M. Vasco-Olmo, J.M. Cruces, A.S. Diaz, F.A. James, M.N. and Lopez-Crespo, P. 2023. Fatigue crack characterisation in 2024-T351 aluminium alloy through SEM observation combined with the CJP model, *International Journal of Fatigue*Volume 166, 107279, Available at: https://doi.org/10.1016/j.ijfatigue.2022.107279

Sadek, M. Bergström, J. and Hallbäck, N. 2024. Computing the stress intensity factor range for fatigue crack growth testing at 20 kHz. *Engineering Reports*. 6(6):e12792. Available at: https://doi.org/10.1002/eng2.12792

Saverio, F. 2014. Modélisation tridimensionnelle de la fermeture induite par plasticité lors de la propagation d'une fissure de fatigue dans l'acier 304L. Thèse (Doctorat) – *L'Ecole Nationale Supérieure de Mécanique* et *D'Aérotechnique.* Soutenue le 24/11/2014. https://theses.hal.science/tel01129079

Sedmak, A. 2023. Fatigue crack growth simulation by extended finite element method: A review of case studies. Fatigue Fract. Eng. *Mater. Struct*. c, 47, pp. 1819–1855. Available at: https://doi.org/10.1111/ffe.14277

Sedmak, A. Grbović, A. Gubeljak, N. Sedmak, S. and Budimir, N. 2024 Numerical Simulation of Fatigue Crack Growth and Fracture in Welded Joints Using XFEM—A Review of Case Studies. *Materials* , 17, 5531. Available at: https://doi.org/10.3390/ma17225531

Si, Z. Yu, T. Fang, W. Natarajan, S. 2024. An adaptive multi-patch isogeometric phase-field model for fatigue fracture. *Int. J. Mech*. Sci.2024, 271, 109146. Available at: https://doi.org/10.1016/j.ijmecsci.2024.109146

Tada H.P., Paris P.C. and Irwin G.R. 2000. The Stress Analysis of Cracks Handbook, *American Society of Mechanical Engineering.* Available at: https://doi.org/10.1115/1.801535

Worthington, M., & Chew, H. B. 2023. Crack path predictions in heterogeneous media by machine learning. *Journal of the Mechanics and Physics of Solids,* 172, 105188. Available at : https://doi.org/10.1016/j.jmps.2022.105188

Wysmulski, P. 2023. Numerical and Experimental Study of Crack Propagation in the Tensile Composite Plate with the Open Hole , *Adv. Sci. Technol. Res. J.* v. 17, n.4, pp. 249-261, Available at: https://doi.org/10.12913/22998624/169970

Yaren, M. F. Ayhan, A. O. 2024. A new method for prediction of fatigue crack propagation life under variable amplitude spectrum loading, *Theoretical and Applied Fracture Mechanics*, Volume 131, 104355,Available at: https://doi.org/10.1016/j.tafmec.2024.104355

Zhang, T. Yu, T. Ding, J. and Natarajan, S. 2024. Low-cycle fatigue crack growth in brittle materials: Adaptive phase-field modeling withvariable-node elements*. Comput. Methods Appl. Mech*. Eng. 2024, 425, 116917.Available at : https://doi.org/10.1016/j.cma.2024.116917

Zhang, T. Yu, T. Li, Y. Bui, T.Q. 2023. Crack growth in anisotropic brittle and polycrystalline materials by adaptive phase field modelusing variable-node elements*. Finite Elem. Anal.* Des. 217, 103909. Available at : https://doi.org/10.1016/j.finel.2023.103909

Zienkiewicz, O.C. Taylor, R.L. and Zhu, J.Z. 2005.The Finite Element Method: Its Basis and Fundamentals*; Elsevier:* Amsterdam, The Netherlands. ISBN: 9780080472775

Modeliranje širenja pukotine zamora u 2D strukturama primenom CPCN-FEM pristupa koji se zasniva na čvorovima

Mohammed Bentahar[a], **autor za prepisku**, *Noureddine* Mahmoudi[a], *Nedir* Hachemi[b], *Youcef* Moulai Arbi[c]

[a] Universiy of Saida Dr. Moulay Tahar, Faculty of Technology, Department of Civil Engineering and Hydraulics, Saida, People's Democratic Republic of Algeria

[b] University of Mustapha Stambouli, Mascara,People's Democratic Republic of Algeria

[c] University of Mustapha Stambouli, Laboratory of Quantum Physics of Matter and Mathematical Modeling (LPQ3M), Mascara, People's Democratic Republic of Algeria

OBLAST: mašinstvo, materijali
KATEGORIJA (TIP) ČLANKA: originalni naučni rad

Sažetak:

Uvod/cilj: Cilj ovog rada je modeliranje širenja pukotina nastalih usled zamora uvođenjem numeričke metode CPCN-FEM (eng. Crack Propagation by Coordinates of Nodes – Finite Element Method) koja predviđa putanje pukotina sistematskim generisanjem koordinata čvorova oko fronta pukotine.

Metode: Pristup definiše četiri glavna čvora za kontrolu pravca širenja i izračunava faktore intenziteta napona (K I) i (K II), kao i ugao nagiba pukotine (β). Metoda je implementirana u FORTRAN-u radi automatizacije praćenja čvorova, ažuriranja koordinata i postepenog napredovanja pukotine u dvodimenzionalnom elastičnom izotropnom modelu. Simulacije se sprovode i upoređuju sa analitičkim rešenjima putanje pukotine koristeći Ričardov kriterijum za određivanje orijentacije pukotine.

Rezultati: Numerički model je reprodukovao očekivane putanje pukotina uz visoko podudaranje sa analitičkim predviđanjima i pokazao stabilno ponašanje pomeranja kroz više slučajeva širenja. Integritet mreže je očuvan tokom svih koraka širenja.

Zaključak: Rezultati pokazuju da metoda CPCN-FEM predstavlja tačnu, efikasnu i mrežno stabilnu tehniku za modeliranje širenja pukotina nastalih usled zamora koja pruža pouzdana predviđanja evolucije putanje pukotine u mehanici loma.

Ključne reči: širenje pukotina, faktor intenziteta napona (SIF), metoda konačnih elemenata, CPCN-FEM, koordinate čvorova, mehanika loma.

Paper received on: 4 June 2025.
Manuscript corrections submitted on: 28 November 2025.
Paper accepted for publishing on: 21 November 2025.

© 2026 The Authors. Published by Vojnotehnički glasnik / Military Technical Courier (www.vtg.mod.gov.rs).This article is an open access article distributed under the terms and conditions of the Creative Commons Attribution license (http://creativecommons.org/licenses/by/4.0/rs/

Design and analysis of an electro-mechanical impact sensor with an all-ways action mechanism and a Hall sensor

Xuan Son Bui[a], *Van Gion* Do[b], *Duc Hung* Pham[c]

Le Quy Don Technical University, Faculty of Special Equipment, Hanoi, Socialist Republic of Vietnam

[a] e-mail: buixuanson@lqdtu.edu.vn,
ORCID iD: https://orcid.org/0000-0003-4520-5168

[b] e-mail: dovangion@lqdtu.edu.vn, **corresponding author**,
ORCID iD: https://orcid.org/0000-0001-8719-4984

[c] e-mail: hungthoi75@gmail.com,
ORCID iD: https://orcid.org/0009-0008-5645-5596

https://doi.org/10.5937/vojtehg74-59737

FIELD: mechanical engineering
ARTICLE TYPE: original scientific paper

Abstract:

Introduction/purpose: The paper proposes an electro-mechanical impact sensor for grenade detonation using an all-ways action mechanism with permanent magnets and a Hall sensor. After experimental validation, a mathematical model assesses how structural parameters, such as activation threshold, inertial mass, and Hall sensor placement, affect the fuse's sensitivity. The study provides recommendations for optimal sensor design to ensure reliable activation at all impact angles.

Methods: The study used a combined approach to address the problem. Dynamic equations of the all-ways action mechanism were solved using the Runge-Kutta method, the magnetic field was simulated with FEMM 4.2 software, and the Hall voltage variation over time was analyzed to assess the fuse's sensitivity under grenade impact conditions.

Results: The results show that an activation threshold below 80 mV ensures reliable operation at any impact angle with an impact velocity not greater than 2.5 m.s^{-1}. The mass of the inertial object has a significant impact on the sensitivity, more than the mass of the magnet, and the location of the Hall sensor is critical, with some locations providing stable sensitivity and others resulting in poor performance.

Conclusion: The hybrid method presented in this paper effectively studies the signal from an electro-mechanical impact sensor combining an all-ways action mechanism, permanent magnets, and a Hall sensor. The research results are useful contributions to the design of impact sensors in grenade fuses.

Key words: electro-mechanical impact sensor, all-ways action mechanism, Hall effect sensor.

Introduction

Contact with the target is the simplest and affords the most direct solution to the fuzing problem (Headquaters of United States Army Materiel Command, 1969). Nowadays, electro-mechanical sensors have become a common trend, as these alternatives allow for a more compact explosive chain, enhanced control capabilities, and flexible parameter adjustments before use, reducing the size and mass of the fuse. Therefore, they have been applied in many types of ammunition, including grenade fuses.

This paper proposes an electro-mechanical impact sensor for a grenade fuse that consists of an all-ways action mechanism that carries ring permanent magnets and an analog signal Hall sensor, as shown in Figure 1. Each inertial body is equipped with a ring-shaped permanent magnet that moves relative to the fuse body and closer to each other when inertial force acts on the pair of inertial bodies. A Hall sensor is mounted at fixed positions on the fuse body.

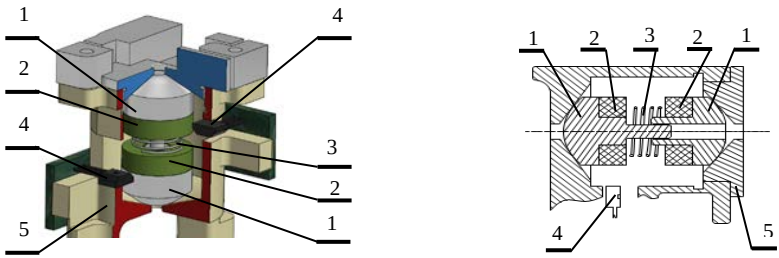

Figure 1 - The structure diagram of the electro-mechanical impact fuse used for hand grenade: *1. The inertial body; 2. Ring permanent magnet; 3. Spring; 4. Hall sensor; 5. fuse body*

With such a structure, when the grenade collides with the media, the inertial bodies move under the action of inertial forces caused by the reaction force of the media and, simultaneously, move the magnets and cause the Hall voltage to change. If the change in the Hall voltage exceeds the activation threshold set in the drive program, the microprocessor will send a signal to detonate the fuse.

To further study the working characteristics of the proposed sensor, the paper incorporates magnetic interaction force into the dynamic model of the all-ways action mechanism. The program for solving the dynamic model for the All-ways action mechanism is linked with the FEMM 4.2 program to simulate the impact sensor signal during grenade operation. The accuracy of the impact sensor signal simulation program is validated through experimental testing. Then, the simulation program is used to

evaluate the influence of some structural parameters on the sensitivity of the proposed impact sensor.

Establishing the program to calculate the output signal of the impact sensor

The Hall voltage calculation program was developed in three steps: (1) establishing the dynamic model of the mechanism, (2) incorporating the magnetic force of the ring magnets, and (3) simulating the magnetic field and calculating the Hall voltage.

The dynamics model of the all-ways action mechanism

The structure and some dimensions of the inertial bodies of the all-ways action mechanism in the proposed electro-mechanical impact sensor are shown in Figure 2.

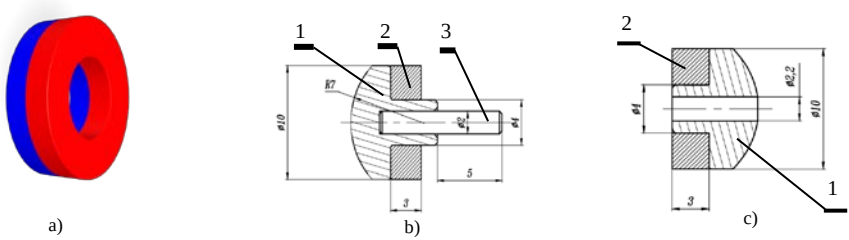

Figure 2 - Type of ring magnet and some dimensions of inertial bodies of the all-ways action mechanism in impact sensor: *a) The magnetic pole of the ring magnet; b) the inertial body 1; c) the inertial body 2*
1. Inertial body; 2. Ring magnet; 3. Guide pillar

The method for establishing the dynamic model of this mechanism is the same as that of the all-ways action mechanism in the URG-86 grenade fuse, as shown in Xuan Son Bui et al. (2021). The forces acting on all the bodies of the mechanism in the general case are shown in Figure 3 and Figure 4.

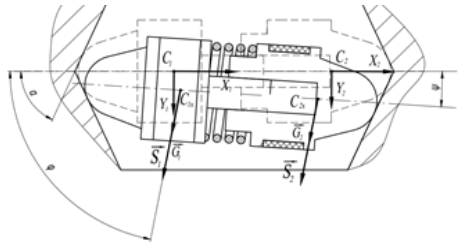

Figure 3 – Some geometric symbols and forces acting on all the bodies of all-ways action mechanism during impact in the general case

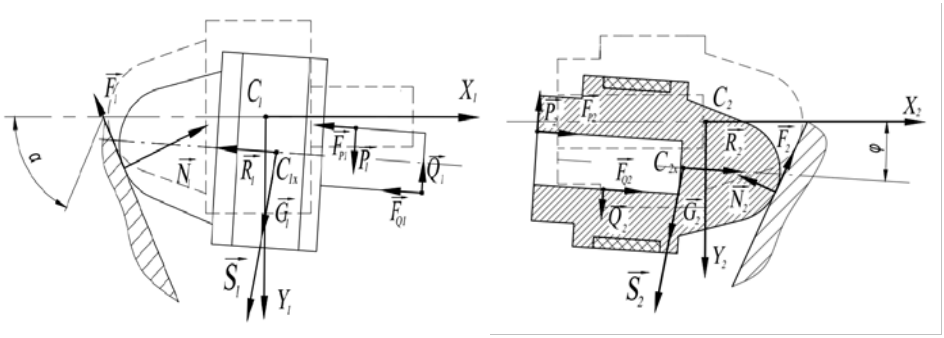

Figure 4 - Forces acting on each body of the all-ways action mechanism during impact in the general case

The dynamic equilibrium equations of all inertial bodies are:

$$\begin{cases} m_1 \dfrac{d\vec{v}_1}{dt} = \vec{S}_1 + \vec{G}_1 + \vec{N}_1 + \vec{F}_1 + \vec{R}_1 + \vec{P}_1 + \vec{Q}_1 + \vec{F}_{P1} + \vec{F}_{Q1} \\ B_1 \dfrac{d^2\psi_1}{dt^2} = \sum_{(i)} M_{1i} \\ m_2 \dfrac{d\vec{v}_2}{dt} = \vec{S}_2 + \vec{G}_2 + \vec{N}_2 + \vec{F}_2 + \vec{R}_2 + \vec{P}_2 + \vec{Q}_2 + \vec{F}_{P2} + \vec{F}_{Q2} \\ B_2 \dfrac{d^2\psi_2}{dt^2} = \sum_{(i)} M_{2i} \end{cases}, \quad (1)$$

where m_1, m_2 $\dfrac{d\vec{v}_2}{dt}$ and $\dfrac{d\vec{v}_1}{dt}$ are the mass and the acceleration of the inertial bodies 1 and 2, respectively. With $i = (1, 2)$, $\vec{S}_i$ and $\vec{G}_i$ are the inertial forces and gravitational forces; $\vec{N}_i$ are the reaction normal forces of the driving face on the body; $\vec{F}_i$ are friction forces; $\vec{R}_i$ are elastic forces of the springs acting on inertial bodies 1 and 2, respectively; $\vec{P}_i$, $\vec{Q}_i$ and $\vec{F}_{Pi}$, $\vec{F}_{Qi}$ are internal forces between the two bodies; ψ_i are the rotations of the corresponding body 1 or 2; B_i are the moments of inertia about the axis passing through the center of gravity and perpendicular to the motion plane of the inertial bodies 1 and 2. M_{1i} and M_{2i} are moments of the forces acting on each inertial bodies 1 and 2 about the axis passing through the

center of gravity and perpendicular to the motion plane of the inertial body 1 or 2.

These equations have more variables than the number of equations, so we need to add some constraint equations before solving. The constraint equations are:

$$\Delta_x = C_1C_2 - C_{1x}C_{2x} = C_1C_2 - \frac{C_1C_2 - x_1 + x_2}{\cos\psi}, \quad (2)$$

$$\psi_1 = \psi_2 = \psi, \quad (3)$$

$$\tan\psi = \frac{y_2 - y_1}{C_1C_2 - x_1 + x_2}, \quad (4)$$

$$y_1 = \left(x_1 + O_1C_1 - O_1C_1\cos\psi\right)\tan\alpha + O_1C_1\sin\psi, \quad (5)$$

$$y_2 = \left(O_1C_1 - O_1C_1\cos\psi - x_2\right)\tan\alpha - O_1C_1\sin\psi, \quad (6)$$

where, x_1, x_2, y_1 and y_2 are the displacements of the center of gravity of the inertial bodies 1 and 2 along the axes of the coordinate system. C_1C_2 and $C_{1x}C_{2x}$ are the distances between the gravity centers of the two bodies at the initial time and the considered time of the impact process, whereas O_1C_1 and O_2C_2 are the distances between the center of gravity and the center of the hemisphere in the two bodies, respectively. Some characteristic points and geometric parameters of the all-ways action mechanism in the proposed sensor used in constraint equations are shown in Figure 5.

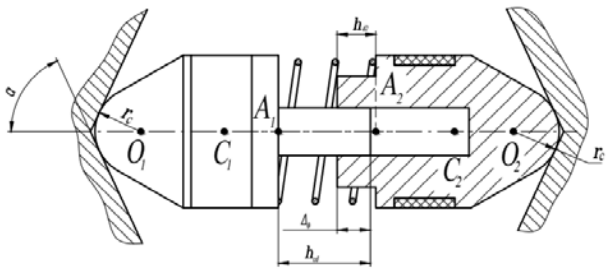

Figure 5 – Some Characteristic points and geometric parameters used in constraint equations

After eliminating all internal forces, we obtain the equations:

$$\begin{cases} \ddot{x}_1 = K_{six1}.\ddot{\psi} - K_{y1x1}.\ddot{y}_1 - K_{y2x1}.\ddot{y}_2 + K_{s2x1}.(S_2 + G_2) + K_{s1x1}.(S_1 + G_1) + K_{rx1}.R \\ \ddot{y}_1 = \tan\alpha.\ddot{x}_1 + O_1C_1.\tan\alpha.\left(\sin\psi.\ddot{\psi} + \cos\psi.\dot{\psi}^2\right) + O_1C_1.\left(\cos\psi.\ddot{\psi} - \sin\psi.\dot{\psi}^2\right) \\ \ddot{x}_2 = K_{six2}\ddot{\psi} + K_{y1x2}\ddot{y}_1 + K_{y2x2}\ddot{y}_2 - K_{s2x2}(S_2 + G_2) - K_{s1x2}(S_1 + G_1) + K_{rx2}R \\ \ddot{y}_2 = -\tan\alpha.\ddot{x}_2 + O_2C_2.\tan\alpha.\left(\sin\psi.\ddot{\psi} + \cos\psi.\dot{\psi}^2\right) - O_2C_2.\left(\cos\psi.\ddot{\psi} - \sin\psi.\dot{\psi}^2\right), \\ \ddot{\psi} = \cos^2\psi.\left\{\dfrac{\ddot{y}_2 - \ddot{y}_1}{C_1C_2 - x_1 + x_2} + \dfrac{(\ddot{x}_1 - \ddot{x}_2)(y_2 - y_1) + 2(\dot{x}_1 - \dot{x}_2)(\dot{y}_2 - \dot{y}_1)}{(C_1C_2 - x_1 + x_2)^2}\right\} \\ + \dfrac{2.(\dot{x}_1 - \dot{x}_2).(\dot{x}_1 - \dot{x}_2).(y_2 - y_1)}{(C_1C_2 - x_1 + x_2)^4}.\cos^2\psi - \dfrac{2\sin\psi.\dot{\psi}^2}{\cos\psi} \end{cases} \quad (7)$$

where, K_{xy} (x=[x_1, y_1, x_2, y_2, ψ, S_1, S_2, R], y=[x_1, y_1, x_2, y_2, ψ], $x \neq y$) are reduction coefficients.

Using the same method for these cases, as shown in Figure 6, we apply the dynamic model for the all-ways action mechanism in all impact angles.

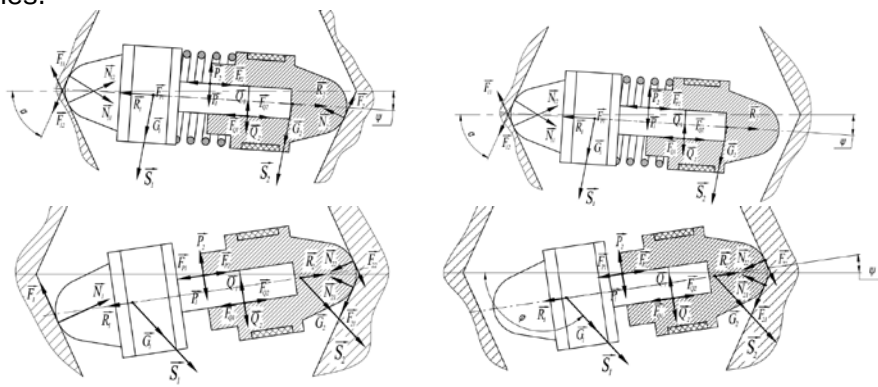

Figure 6 - All other working cases of the all-ways action mechanism

The elastic force $\vec{R}$ can be calculated using the following formula:

$$R = k.(\lambda_0 + \Delta_x), \quad (8)$$

where, R is the spring elastic force, k is the stiffness of the spring, λ0 is the initial compression of the spring, and Δ_x is the relative displacement between the two inertial bodies, calculated by equation (2).

The inertial force acting on each inertial body is:

$$S_i = m_i.\frac{dV(t)}{dt}, \quad (9)$$

where *V(t)* is the velocity function of the grenade over time upon impact.

The paper concentrates on analyzing the operation of the impact sensor in a grenade during impact with the concrete ground. The authors conducted a drop test examining the impact of a grenade on concrete, utilizing the method presented in Martin Macko et al. (2024). The tests were performed with initial velocities below 5 m.s^{-1}, and the velocity of the grenade during impact was recorded using a high-speed camera. Several time-based regression functions were used to approximate the grenade's velocity from the test results. After evaluating the various options, the most accurate approximation of the grenade's velocity upon impact was found to be represented by a specific expression:

$$V(t) = \frac{1}{2}(1-\beta_{con})V_i + \frac{1}{2}(1+\beta_{con})V_i \cos(\Omega_{con}t), \quad (10)$$

The coefficients for this expression were determined based on the initial impact velocity using polynomial functions:

$$\beta_{con} = 0,0053V_i^2 - 0,1113V_i - 2,3094, \quad (11)$$

$$\Omega_{con} = 14,082V_i^2 - 356,56V_i + 4446,1, \quad (12)$$

If the initial grenade impact velocity is higher than 5 m.s^{-1}, the velocity function proposed by D.M.Komarov is used as used in Xuan Son Bui et al. (2021) and K. Phanthavong et al. (2023). In the case of impact with concrete media, the coefficient $\beta = 0.45$ and the frequency Ω are calculated using the following formula:

$$\Omega = \frac{\pi}{t_V}, \quad (13)$$

where t_V is the total impact time calculated from the ratio $\frac{V_V}{t_V} = 6.10^3$.

Adding the magnetic force of the pair of ring magnets in the dynamic model of the all-ways action mechanism

In the proposed impact sensor, the two magnets are positioned so that their like poles point toward each other, and the magnetic force between them is repulsive. This repulsive force is calculated using the surface electric method, as demonstrated in K. Yuan et al. (2019). Figure 7 illustrates the model of the pair of magnets.

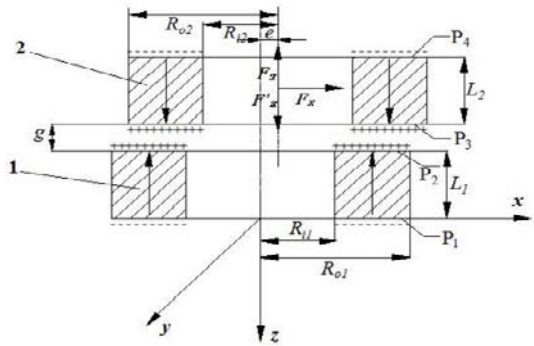

Figure 7 - Model of the interaction force between the pair of ring magnets

The magnetic forces between the faces are calculated using the following equations (K. Yuan et al, 2019):

$$F_{14,z} = \frac{B_r^2}{4\pi\mu_0} \int_0^{2\pi}\int_0^{2\pi}\int_{R_{i1}}^{R_{o1}}\int_{R_{i2}}^{R_{o2}} \frac{(L_1+g+L_2).r_1.r_4 dr_1 dr_4 d\alpha d\beta}{\left[(L_1+g+L_2)^2+(r_1\cos\alpha - r_4\cos\beta - e)^2+(r_1\sin\alpha - r_4\sin\beta)^2\right]^{3/2}} \quad (14)$$

$$F_{13,z} = \frac{B_r^2}{4\pi\mu_0} \int_0^{2\pi}\int_0^{2\pi}\int_{R_{i1}}^{R_{o1}}\int_{R_{i2}}^{R_{o2}} \frac{(L_1+g).r_1.r_3 dr_1 dr_3 d\alpha d\beta}{\left[(L_1+g)^2+(r_1\cos\alpha - r_3\cos\beta - e)^2+(r_1\sin\alpha - r_3\sin\beta)^2\right]^{3/2}} \quad (15)$$

$$F_{23,z} = \frac{B_r^2}{4\pi\mu_0} \int_0^{2\pi}\int_0^{2\pi}\int_{R_{i1}}^{R_{o1}}\int_{R_{i2}}^{R_{o2}} \frac{(g).r_2.r_3 dr_2 dr_3 d\alpha d\beta}{\left[(g)^2+(r_2\cos\alpha - r_3\cos\beta - e)^2+(r_2\sin\alpha - r_3\sin\beta)^2\right]^{3/2}} \quad (16)$$

$$F_{24,z} = \frac{B_r^2}{4\pi\mu_0} \int_0^{2\pi}\int_0^{2\pi}\int_{R_{i1}}^{R_{o1}}\int_{R_{i2}}^{R_{o2}} \frac{(L_2+g).r_2.r_4 dr_2 dr_4 d\alpha d\beta}{\left[(L_2+g)^2+(r_2\cos\alpha - r_4\cos\beta - e)^2+(r_2\sin\alpha - r_4\sin\beta)^2\right]^{3/2}} \quad (17)$$

The summary repulsive force acting on each magnet can be calculated by the equation:

$$F_z = F_{14,z} - F_{13,z} + F_{23,z} - F_{24,z} \quad (18)$$

The impact sensor uses magnets made from N35-NdFeB. The magnetic parameters of this magnetic material are shown in Table 1 (Arnold magnetic technologies, 2021).

Table 1 - Magnetic parameters of NdFeB magnetic material N35

Parameter	Symbol	Unit	Value
Residual induction	B_r	T	1.12
Coercivity	H_{cb}	kA/m	836
Intrinsic coercivity	H_c	kA/m	955
Maximum energy product	$(BH)_{max}$	K.J/m^3	239

The change in the magnetic interaction force of the pair of ring magnets is shown in Figure 8.

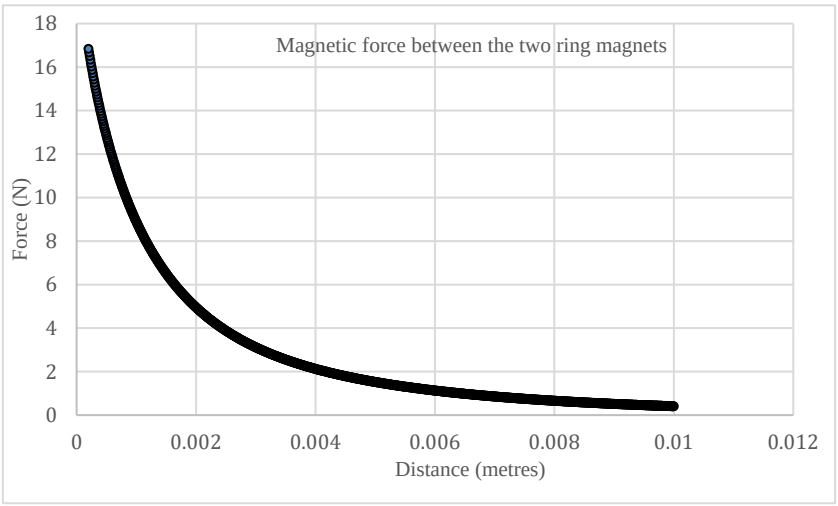

Figure 8 - The magnetic interaction force of the pair of ring magnets in the impact sensor depending on the distance

When adding the magnetic interaction force between the two magnets, we obtain the equations in the general case as shown:

$$\begin{cases} \ddot{x}_1 = K_{six1}\ddot{\psi} - K_{y1x1}\ddot{y}_1 - K_{y2x1}\ddot{y}_2 + K_{s2x1}(S_2+G_2) + K_{s1x1}(S_1+G_1) + K_{rx1}(R+\boldsymbol{F_{mg}}) \\ \ddot{y}_1 = \tan\alpha.\ddot{x}_1 + O_1C_1\tan\alpha\left(\sin\psi.\ddot{\psi} + \cos\psi.\dot{\psi}^2\right) + O_1C_1.\left(\cos\psi.\ddot{\psi} - \sin\psi.\dot{\psi}^2\right) \\ \ddot{x}_2 = K_{six2}\ddot{\psi} + K_{y1x2}\ddot{y}_1 + K_{y2x2}\ddot{y}_2 - K_{s2x2}(S_2+G_2) - K_{s1x2}(S_1+G_1) + K_{rx2}(R+\boldsymbol{F_{mg}}) \\ \ddot{y}_2 = -\tan\alpha.\ddot{x}_2 + O_2C_2\tan\alpha\left(\sin\psi.\ddot{\psi} + \cos\psi.\dot{\psi}^2\right) - O_2C_2.\left(\cos\psi.\ddot{\psi} - \sin\psi.\dot{\psi}^2\right) \\ \ddot{\psi} = \cos^2\psi.\left\{\dfrac{\ddot{y}_2-\ddot{y}_1}{C_1C_2-x_1+x_2} + \dfrac{(\ddot{x}_1-\ddot{x}_2)(y_2-y_1)+2(\dot{x}_1-\dot{x}_2)(\dot{y}_2-\dot{y}_1)}{(C_1C_2-x_1+x_2)^2}\right\} \\ \quad + \dfrac{2.(\dot{x}_1-\dot{x}_2)(\dot{x}_1-\dot{x}_2)(y_2-y_1)}{(C_1C_2-x_1+x_2)^4}.\cos^2\psi - \dfrac{2\sin\psi.\dot{\psi}^2}{\cos\psi} \end{cases} \quad (19)$$

where $\boldsymbol{F_{mag}}$ is the magnetic interaction force calculated using equation (18).

Doing the same for all other cases, the dynamic model of the all-ways action mechanism in the electro-mechanical impact sensor is established. This dynamic model can be solved using the ODE45 function in MATLAB software, and the output results are the kinematic parameters of the two inertial bodies, such as displacements, velocities, and accelerations, depending on the impact angle and collision velocity conditions.

Calculating the impact sensor output signal using the dynamic model of the all-ways action mechanism and the FEMM 4.2 program

The program to solve the all-ways action mechanism's dynamic model is combined with FEMM 4.2 software to build a model of the pair of magnets and determine the magnetic flux density. From that, the output signal of the impact sensor can be calculated. The model and simulation results for the impact sensor at one specific time step are illustrated in Figure 9.

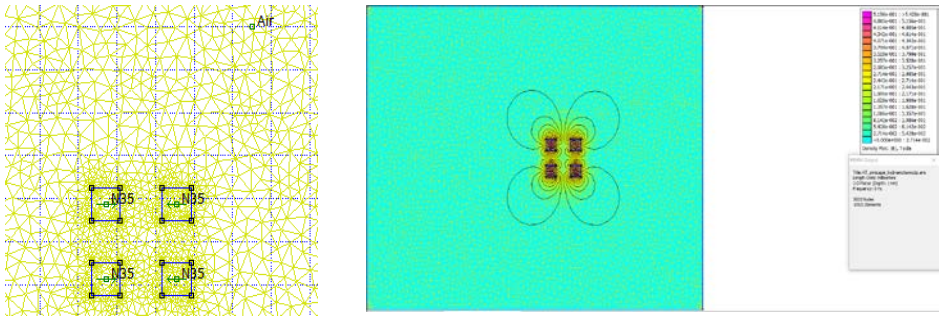

Figure 9 - The model and the magnetic field of the pair of magnets in FEMM 4.2

Figure 10 displays the variation in magnetic flux density and the output of the Hall voltage from the sensor during a grenade impact scenario.

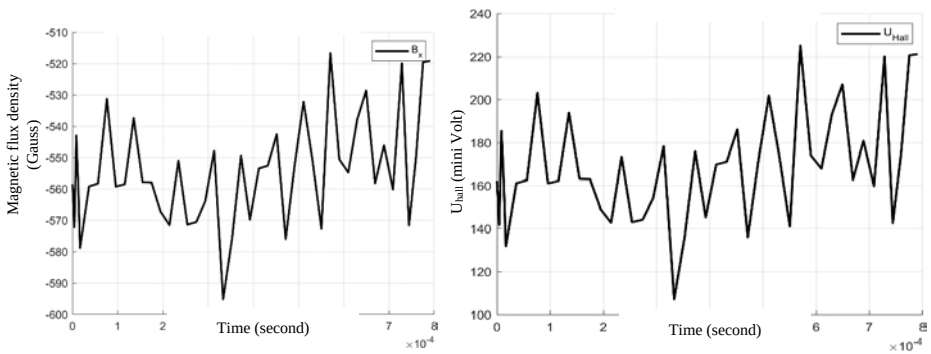

Figure 10 - Change of magnetic flux density and the Hall voltage of proposed sensor

Testing to evaluate the accuracy of the results obtained from the established program

An experiment was carried out to assess the accuracy of the developed mathematical model for the impact sensor to measure the sensor's output signal, as shown in Figure 11.

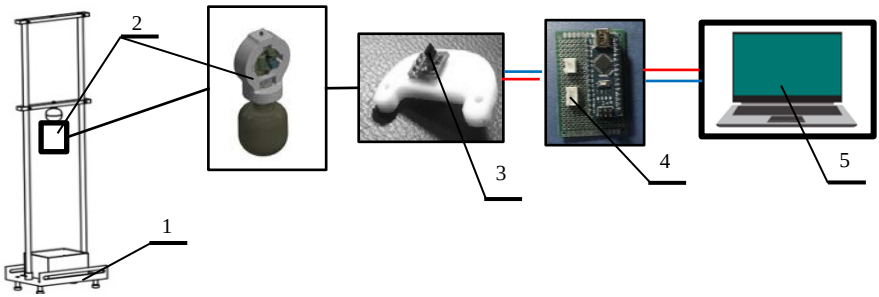

Figure 11 - Assembly of equipment to measure the Hall voltage of the impact sensor during the grenade impact on concrete: *1. The frame; 2. The grenade body with the impact sensor; 3. Circuit with the Hall sensor; 4. The measuring and signal conversion circuit; 5. The computer*

Some dimensions of the inertial bodies are illustrated in Figure 2, and three samples of the proposed impact sensor were fabricated. The mass of the inertial bodies for each sample is presented in Table 2.

Table 2 - Mass of three different samples for the test of math model accuracy

	Mass of the inertial body 1 (gram)	Mass of the inertial body 2 (gram)
Sample 1	1.92	1.57
Sample 2	1.95	1.58
Sample 3	1.87	1.56

The grenade body was released from a height of 0.87 m, resulting in an initial impact velocity of 4.1 $m.s^{-1}$ upon striking a concrete block. A test impact sensor was positioned on an angle-adjustable mechanism to align with the impact angle of the all-ways action mechanism during the test. Figure 12 illustrates the setup and the measured data from one test angle.

Figure 12 - Set up and measured data of one test case

The Hall sensor used in this impact sensor has code AH49E, and the change of Hall voltage conforms to the change of magnetic flux density when the input voltage is 5 volt, as shown in Figure 13 (Honeywell Inc., 1998; BCD Semiconductor Manufacturing Limited, 2010).

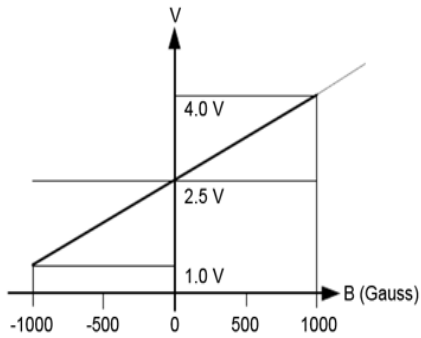

Figure 13 - The change of th Hall voltage as the change of magnetic flux density when input voltage is 5 volts

Figure 14 shows the change of the Hall voltage as a function of the impact time in one experiment.

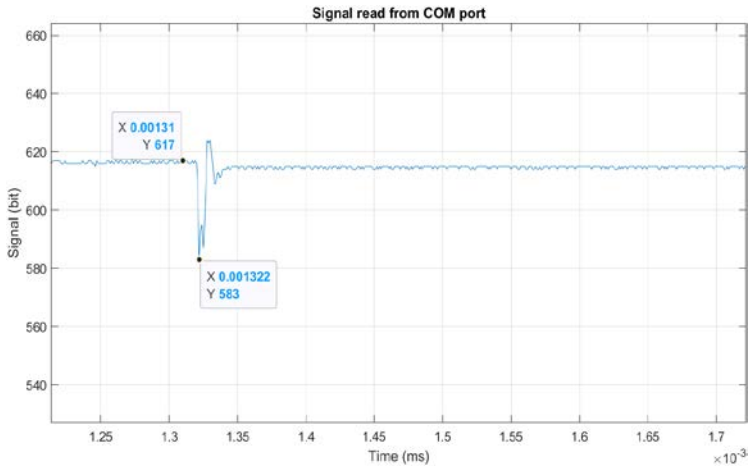

Figure 14 - The change of impact sensor signal over time in one measurement case

The experimental results and the calculation results obtained from the developed program simulate the output signal of the impact sensor in the given setup, as shown in Figure 15.

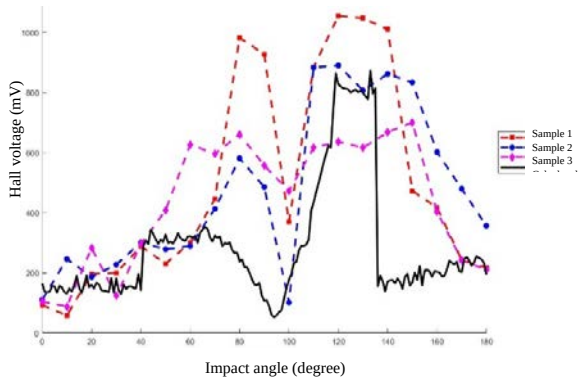

Figure 15 - Comparing the Hall voltage measured in the experiment and the theoretical calculation results for the impact sensor

The results show that the program for determining the signal of the electro-mechanical impact sensor in the grenade fuse is relatively accurate. The program can be used to study the operation of the proposed impact sensor in the grenade fuse.

Evaluation of the influence of the magnetic force of the pair of ring magnets on the dynamic characteristics of the all-ways action mechanism

Figure 16 and Figure 17 compare the maximum relative displacement between the inertial bodies and the maximum rotation angle of the mechanism at various impact angles in the range from 0° to 180° and velocities, both with and without the magnetic force.

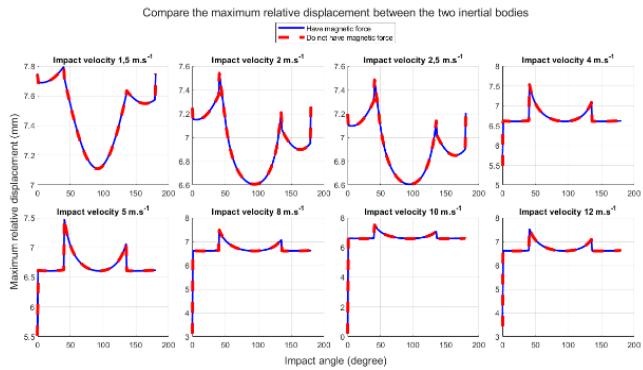

Figure 16 – Comparison of the maximum relative displacement of the two inertial bodies with and without the magnetic force at some cases of impact velocities

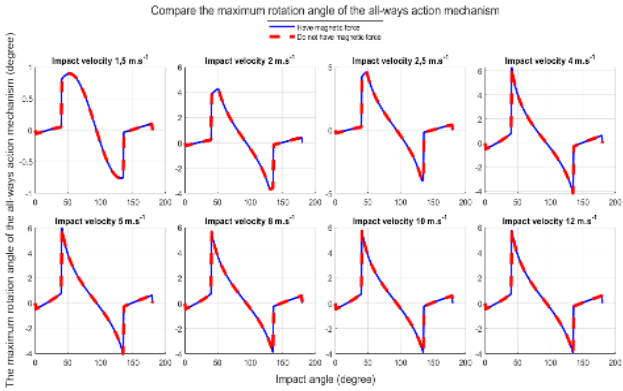

Figure 17 - Comparison of the maximum rotation angle of the all-ways action mechanism with and without the magnetic force at some cases of impact velocities

The comparison results show that the magnetic interaction force between the two magnets mounted on the two inertial bodies has very little effect on the kinematics of the inertial blocks. This is becaise the value of this interaction force is relatively small, being smaller than the elastic force of the compression spring in the all-ways action mechanism of the impact grenade fuse. Meanwhile, the effect of the elastic force of the compression spring on the kinematics of the inertial bodies is not very large (Xuan Son Bui et al, 2021), so the effect of the magnetic interaction force on the kinematics of the inertial bodies is also negligible.

The change of the impact sensor signal when the all-ways action mechanism works with the impact process of the grenade

The Hall sensor works with a magnetic field perpendicular to the surface of the Hall plate, corresponding to the OX direction of the coordinate system in the dynamic model setup of the all-ways action impact mechanism. To evaluate the influence of the kinematics of inertial masses on the change of electro-mechanical sensor signals, this paper compares the change in the maximum value of the Hall voltage deviation generated by the sensor at different contact angles with the change in the initial velocity of the grenade when it impacts the concrete media. The calculation results are shown in Figure 18.

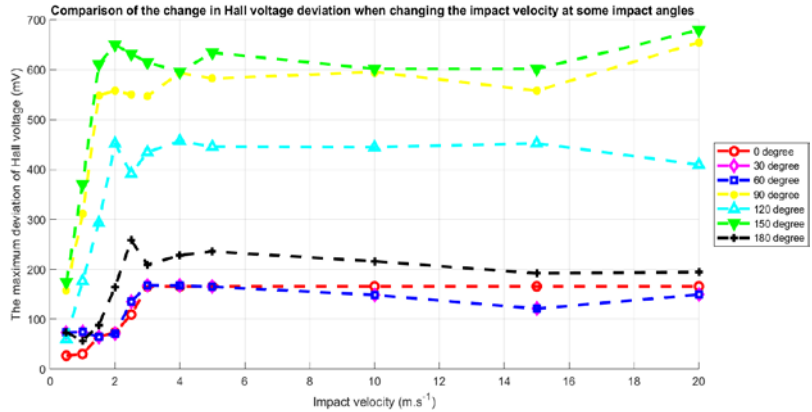

Figure 18 - Comparison of the change of the Hall voltage at an impact angle while changing the impact velocity

The calculated results show that the change level in the Hall voltage deviation at different impact angles is different and depends greatly on the impact velocity. However, it can be seen that in the impact velocity region below 4 $m.s^{-1}$, the Hall voltage deviation increases sharply when the impact velocity of the grenade with the ground increases. However, when the impact velocity is greater than 4 $m.s^{-1}$, the Hall voltage deviation changes little with increasing impact velocity.

Investigation of the influence of some structural parameters on the sensitivity of the electro-mechanical impact sensor

In this part, the paper uses the program developed above to calculate the electro-mechanical impact sensor signal and evaluate the effect of the following parameters: the setting threshold of the control program, the mass of the inertial bodies, and the position of the Hall sensor on the sensitivity of the impact sensor.

Setting the threshold of the control program

To determine a suitable threshold for the control program and ensure the required sensitivity of the grenade fuse, this paper investigates how the threshold value affects sensor sensitivity. All sensor parameters are kept constant except for the threshold. Sensitivity is compared based on the minimum impact velocity, at each angle from 0° to 180°, that produces a Hall voltage equal to or greater than the set threshold. The sensor is considered suitably sensitive if the required impact velocity at all angles remains below 2.5 $m.s^{-1}$. Figure 19 and Figure 20 show the sensitivity

diagrams of the electro-mechanical impact sensor with thresholds ranging from 70 mV to 150 mV.

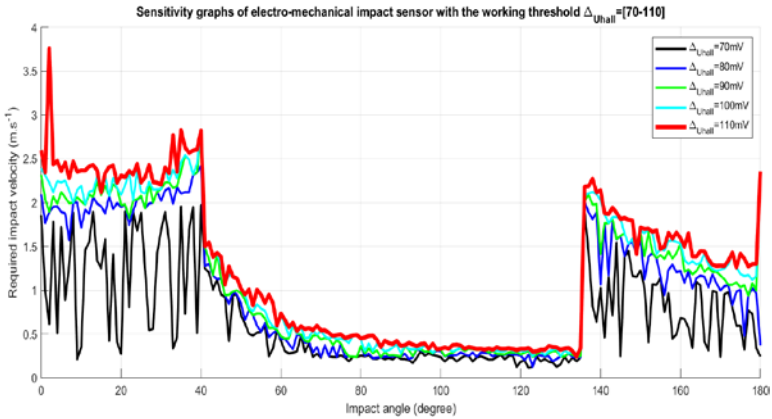

Figure 19 - Sensitivity graphs for cases where the threshold changes from 70 mV to 110 mV

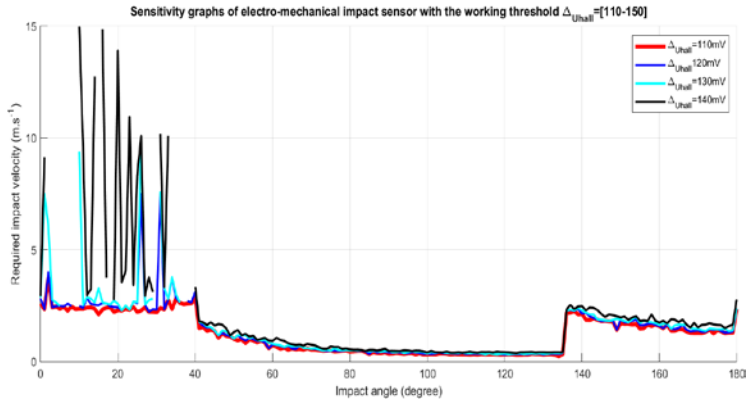

Figure 20 - Sensitivity graphs for cases where the threshold changes from 110 mV to 150 mV

The sensitivity graphs show that with activation thresholds between 70 mV and 110 mV, the sensor can operate at any impact angle with velocities below 4 $m.s^{-1}$. At thresholds of 120 mV to 150 mV, some angles still show high sensitivity at velocities under 1 $m.s^{-1}$, but sensitivity is very low for impact angles below 45^0. At 130 mV or higher, some angles require impact velocities above 15 $m.s^{-1}$. Figure 21 compares the ratio of impact angles at which the sensor can operate over a range of initial impact velocities of the grenade.

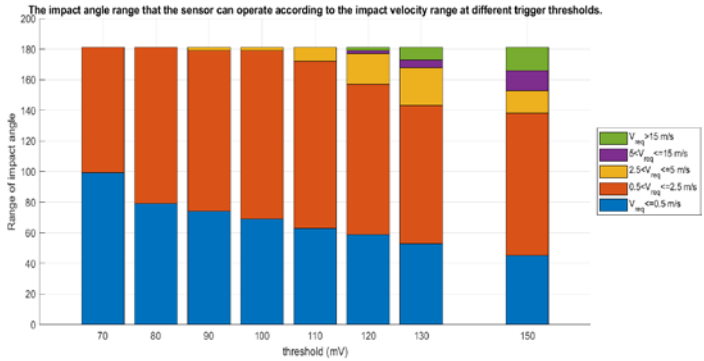

Figure 21 – Comparison of the range of impact angles at which the impact sensor can operate for different impact velocity ranges and activation thresholds

The chart shows that when the activation threshold is below 80 mV, the sensor works at 100% of impact angles with velocities under 2.5 $m.s^{-1}$. At a 70 mV threshold, 55.8% of impact angles work below 0.5 $m.s^{-1}$, while at 80 mV, it drops to 43.6%. For activation thresholds of 90 mV and 100 mV, the figures are 40.9% and 38.1%, respectively, with a small proportion (about 1.1%) requiring velocities between 2.5 $m.s^{-1}$ and 5 $m.s^{-1}$. At 110 mV, this increases to 5%, and at 120 mV or higher, some angles require velocities over 15 $m.s^{-1}$.

In conclusion, activation thresholds below 80 mV are recommended to ensure that the sensor meets the sensitivity requirements of an impact grenade. Thresholds of 90 mV and 100 mV still offer acceptable sensitivity, with only a few angles requiring impact velocities higher than 2.5 $m.s^{-1}$. This study selects 90 mV as the sensor's activation threshold, as it closely matches the required sensitivity across most impact angles.

Mass of the inertial bodies

To study the effect of the mass of these components on the sensor sensitivity, the paper analyzes changes in sensor sensitivity when using different materials. The materials used are listed in Table 3 and Table 4.

Table 3 - Test of the case changes the magnet's material of the two inertial bodies

Test number	1	2	3	4	5
The density of the magnetic material ($g.cm^{-3}$)	4,8	5,0	6,5	6,9	7,55
The density of the inertial body's material ($g.cm^{-3}$)	1,03	1,03	1,03	1,03	1,03
Mass of the first inertial body (gram)	1,46	1,5	1,79	1,87	2,0
Mass of the second inertial body (gram)	1,38	1,42	1,71	1,79	1,92

Table 4 - Test of the case changes the main body's material of the two inertial bodies.

Test number	1	2	3	4	5	6
The density of the magnetic material ($g.cm^{-3}$)	7,55	7,55	7,55	7,55	7,55	7,55
The density of the inertial body's material ($g.cm^{-3}$)	1,03	1,637	2,7	4,73	8,0	8,73
Mass of the first inertial body (gram)	2,002	2,143	2,391	2,812	3,623	3,794
Mass of the second inertial body (gram)	1,922	2,174	2,616	3,37	4,82	5,12

Sensitivity diagrams of the impact sensor for changes in the density of the magnet materialare shown in Figure 22.

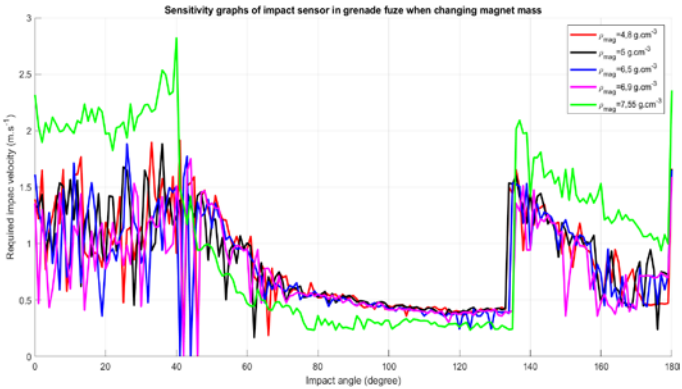

Figure 22 - The sensitivity graphs of the electro-mechanical impact sensor in grenade fuse when changing the mass of magnets.

From the diagram, we can see that when the ring magnet uses a material with a density of less than 6.9 $g.cm^{-3}$, the effect of changes in the magnet mass on the sensitivity of the electro-mechanical impact sensor is insignificant. The sensor can work with a required impact velocity of less than 2 $m.s^{-1}$ in all tested cases. However, when the sensor uses a magnet with a density of up to 7.55 $g.cm^{-3}$, its sensitivity changes significantly and is not uniform. When the density of the magnet block is 7.55 $g.cm^{-3}$, in the impact angle areas below 40^0 and above 136^0, the sensitivity of the impact sensor decreases, the required impact velocity of this range of impact angle increases, and some impact angles require an impact velocity of nearly 3 $m.s^{-1}$. In the impact angle area greater than 41^0 and below 135^0, the sensitivity of the electro-mechanical impact sensor increases when the required impact velocity is smaller than that of the sensor using a magnet with a density of less than 6.9 $g.cm^{-3}$.

By comparing the operating angle range at various impact velocities from 0 to 15 $m.s^{-1}$, we obtain the graph shown in Figure 23.

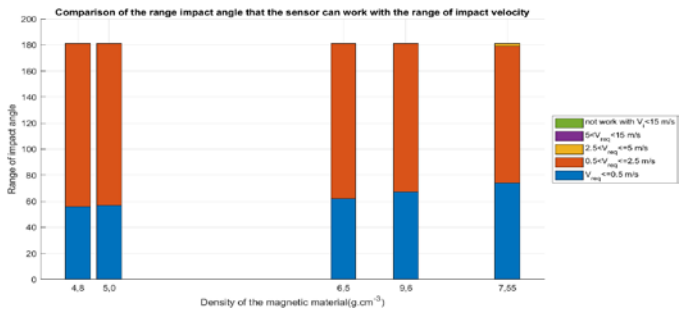

Figure 23 - Comparison of the range of impact angles at which the sensor can operate with the range of impact velocities

While the magnet material has a density of less than 6.9 g.cm^{-3}, approximately 30% of the impact angles allow the impact sensor to operate with an impact velocity of less than 0.5 m.s^{-1}. However, when the density of the magnet changes to 7.55 g.cm^{-3}, the required impact velocity of less than 0.5 m.s^{-1} increases and reaches 40.9%, 58% of the impact angles work with an impact velocity of less than 2.5 m.s^{-1}, but at the same time, some impact angles accounting for about 1% of the total impact angles require an impact velocity of more than 2.5 m.s^{-1} to work reliably.

The change in sensor sensitivity when changing the density of the magnet material is explained by the change in the inertial properties of the inertial masses. When the density of the magnet ring is below 6.9 g.cm^{-3}, the mass of the magnet still accounts for a small proportion of the inertial mass, so the kinematic properties of the sensor are less affected. However, when the density of the magnet ring material is 7.55 g.cm^{-3}, the mass of the magnet accounts for a large proportion of the inertial mass. It changes the kinematic properties of the sensor when colliding, thus significantly reducing its sensitivity.

When changing the main body's material, the impact sensor's sensitivity graphs are shown in Figure 24.

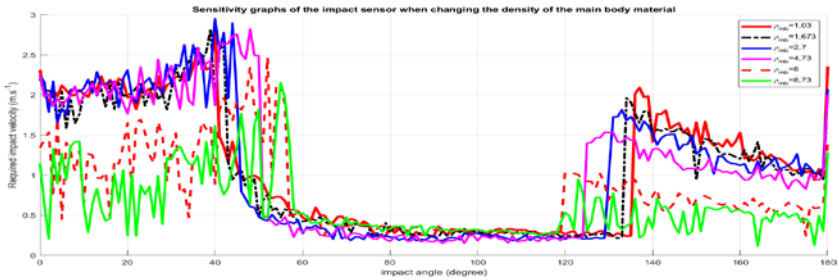

Figure 24 - The sensitivity graphs of the impact sensor when changing the density of the main body of the inertial masses

The sensitivity graphs show that the mass of the main body has a greater impact on sensor sensitivity than the magnet's mass. Increasing the main body's density from 1.03 g.cm^{-3} to 4.73 g.cm^{-3} slightly improves sensitivity, requiring about 3 m.s^{-1} impact velocity for activation at all angles. At 8 g.cm^{-3}, sensitivity significantly improves, lowering the required velocity to 2.5 m.s^{-1}, and at 8.73 g.cm^{-3}, to 2.2 m.s^{-1}.

Density changes also shift sensitivity ranges. At 1.03 g.cm^{-3}, the sensor is less sensitive below 40°, with minimum activation velocity above 1.8 m.s^{-1}. It performs best between 40° and 136°, needing less than 0.25 m.s^{-1} at some angles. Above 137°, sensitivity drops, requiring at least 1 m.s^{-1}. As density increases to 2.7, 4.73, and 8.73 g.cm^{-3}, the high-sensitivity angle range narrows from 43°–134° to 58°–120°.

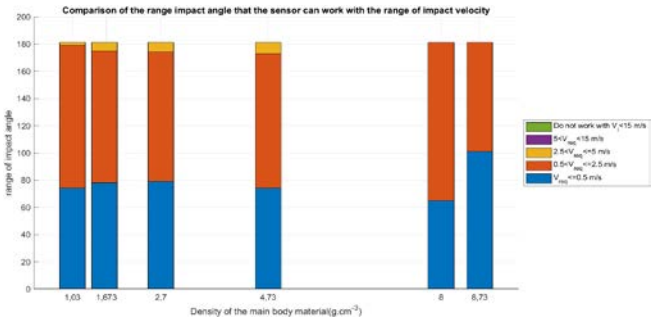

Figure 25 - Comparison of the range of impact angles at which the sensor can operate with the range of impact velocities when changing the material density of the main body

Position of the Hall sensor

To evaluate the influence of the Hall sensor placement on the sensitivity of the electro-mechanical impact sensor, the input parameters for the program were kept constant, including the geometric parameters of the all-ways action mechanism, the activation threshold was 90 mV, the magnet type was NdFeB N35, and the inertial main body's material was plastic with a density of 1.03 g.cm^{-3}. The Hall sensor placement was varied according to several options, as shown in the diagram in Figure 26.

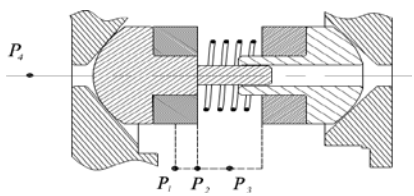

Figure 26 - Diagram of the locations in the study of the influence of Hall sensor placement on the sensitivity of electro-mechanical impact sensor

All study positions are located on the moving plane of the all-ways action mechanism. Position P_1 is on the magnet ring's cross-sectional symmetry axis, P_2 is on the lower edge of the magnet ring near the guide pin, P_3 is on the symmetry axis of two magnets, and P_4 is on the center axis of a magnet pair. At each position, the Hall sensor is placed at specific distances from a reference point. For P_1 to P_3, the reference point is where the study axis intersects the mechanism's symmetry axis. For P_4, it is where the symmetry axis meets the boundary of the magnet head near the guide pin. Distances are listed in Table 5.

Table 5 - Distance from the points where the Hall sensor is placed to the reference point at each sampling position

Point number / Study position	**1**	**2**	**3**	**4**	**5**
P_1	8,5	9,0	9,5	10	12
P_2	8,5	9,0	9,5	10	12
P_3	8,5	9,0	9,5	10	12
P_4	8,0	8,5	9,5	10	12

The sensitivity diagram of the electro-mechanical impact sensor when placing the Hall sensor at the study position P_1 is shown in Figure 27.

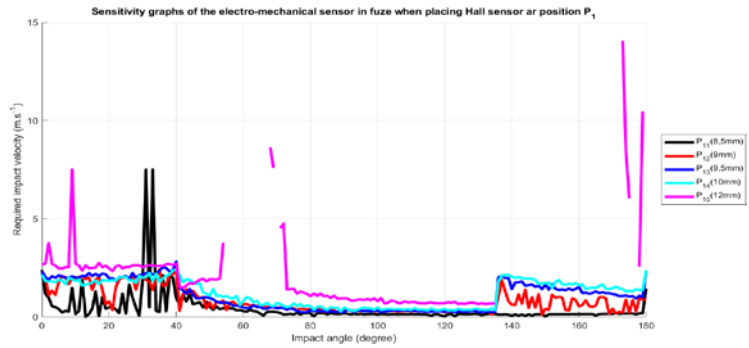

Figure 27- Sensitivity graphs of the impact sensor when placing the Hall sensor at position P_1

The analysis shows that when the Hall sensor is placed at position P_1, the impact sensor has low sensitivity at angles below 60°, where the first inertial body is mostly stationary or rotating, and the second moves toward it. Between 60° and 135°, where both inertial bodies move, the sensor is most sensitive and requires the lowest impact velocities. Above 135°, sensitivity decreases but remains better than below 60°.

At position P_{11}, the sensor shows very high sensitivity, needing less than 1 $m.s^{-1}$ impact velocity at almost all angles, except between 31° and 33°, where over 7 $m.s^{-1}$ is required. At P_{12} and P_{13}, sensitivity is more balanced—slightly lower where both bodies move, but higher in other ranges. At P_{14}, sensor sensitivity drops significantly, with some angles requiring more than 15 $m.s^{-1}$ for activation.

When comparing the required impact velocities in the maximum, minimum, and average values for the working impact angle ranges with impact velocities below 15 $m.s^{-1}$, we obtain the graph shown in Figure 28.

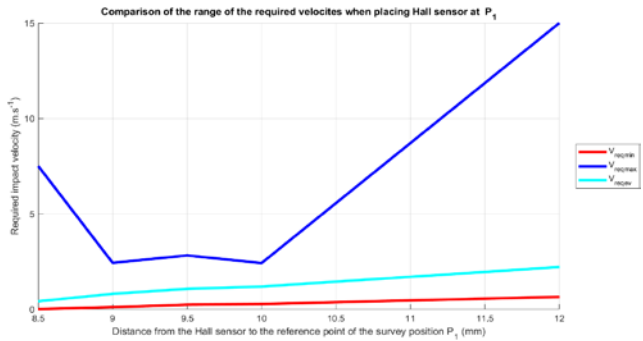

Figure 28 - Comparison of the range of required impact velocities when placing the Hall sensor at position P_1

When the Hall sensor is set at P_{11}, the minimum required impact velocity is very low, but the maximum required impact velocity is as high as 7.5 $m.s^{-1}$. When the Hall sensor is set at any P_{12}, P_{13}, or P_{14}, all require contact velocities less than 3.5 $m.s^{-1}$. If the Hall sensor is set at P_{15}, many impact angles require impact velocities close to 15 $m.s^{-1}$ to function.

The sensitivity graphs and the graph to compare the impact angles of the impact velocity range of the impact sensor when placing the Hall sensor at the sampling points of position P_2 are shown in Figure 29.

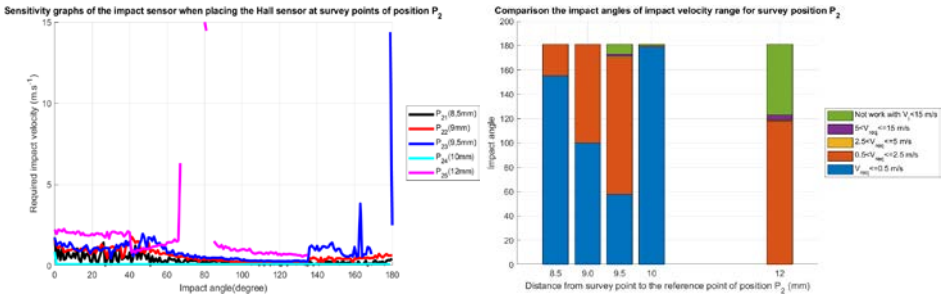

Figure 29 - The sensitivity graphs and comparison of the range of impact angles with different impact velocities when placing the Hall sensor at the position P_2

The sensor sensitivity diagram shows that when the Hall sensor is placed at P_{21} and P_{22}, the impact sensor has a very high sensitivity as it only needs an impact velocity of 1.79 $m.s^{-1}$ to operate at any impact angle. When the Hall sensor is placed at P_{23}, the sensitivity of the impact sensor decreases as the electro-mechanical impact sensor cannot operate at an impact velocity below 15 $m.s^{-1}$ in the impact angle range from 169^0 to 179^0 and within the impact angle range where the sensor can operate at an impact velocity below 15 $m.s^{-1}$, many impact angles require an impact velocity of up to 14.3 $m.s^{-1}$. When the Hall sensor is placed at P_{24}, the impact sensor has a high sensitivity as it can operate at any impact angle with an impact velocity of only 0.85 $m.s^{-1}$. When the Hall sensor is placed 12 mm from the symmetry axis of the all-ways action mechanism, the sensitivity of the impact sensor is very poor because many impact angle regions cannot operate at impact velocities below 15 $m.s^{-1}$.

The P_2 position also provides the sensor with high sensitivity and can operate in the entire contact angle area, but it is unstable and has large fluctuations. To ensure the working ability of the sensor, the Hall sensor must be placed at a position no more than 10 mm from the symmetry axis of the all-ways action mechanism, but there are still some points with low sensitivity within this range.

Figure 30 shows the sensitivity graphs of the impact sensor when placing the Hall sensor at position P_3's sampling points.

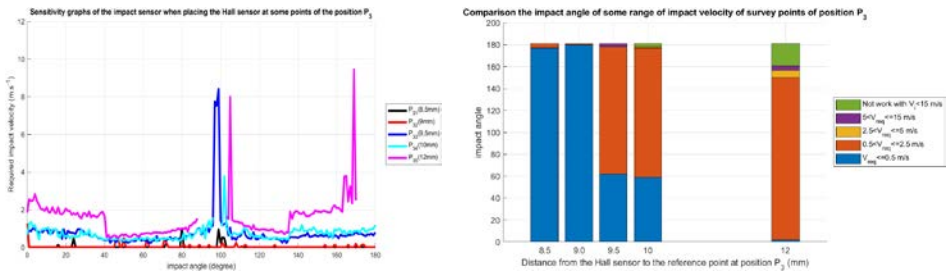

Figure 30 - The sensitivity graphs and comparison of the range of impact angles with different impact velocities when placing the Hall sensor at the position P_3

The sensitivity graphs show that when placing the Hall sensor at points P_{31} and P_{32} corresponding to distances of 8.5 mm and 9 mm from the symmetry axis of the all-ways action mechanism, the impact sensor has very high sensitivity, requiring an impact velocity of 1 $m.s^{-1}$, and it can operate at any impact angle. When placing the Hall sensor 9.5 mm away from the symmetry axis of the all-ways action mechanism, most of the impact angles still ensure good sensitivity when only needing an impact velocity of less than 2 $m.s^{-1}$ to be able to operate. However, there is a

range of impact angles from 96^0 to 100^0; the sensor has low sensitivity when needing an impact velocity of approximately 8 $m.s^{-1}$ to be able to work. Especially when the Hall is placed 10 mm from the all-ways action mechanism symmetry axis, in the impact angle range from 96^0 to 100^0, the sensor cannot work with impact velocity below 15 $m.s^{-1}$. When the distance between the Hall sensor and the all-ways action mechanism symmetry axis is 12 mm, there are two ranges of impact angle where the sensor cannot work with impact velocity below 15 $m.s^{-1}$, which are from 88^0 to 103^0 and from 170^0 to 180^0.

Figure 31 shows the sensitivity graphs of the impact sensor when placing the Hall sensor at position P_4's sampling points.

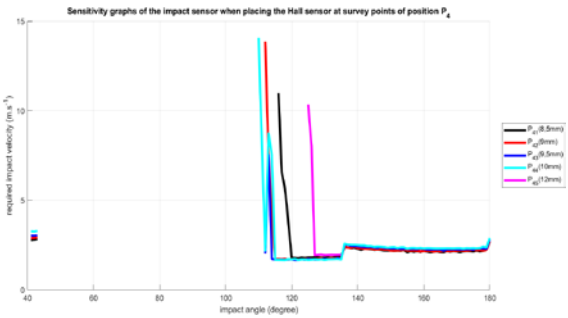

Figure 31 - Sensitivity graphs of the impact sensor when placing the Hall sensor at sampling points of position P_4

The sensitivity diagrams show that the P_4 sensor has poor sensitivity when there is a large range of impact angles at which it cannot operate, regardless of the position of the Hall sensor at the sampling points. The impact sensor can only operate in a very small area of impact angle from 41^0 to 43^0, and the area of impact angle from 110^0 to 180^0.

Study results show that positions P_2 and P_4 are unsuitable for placing the Hall sensor due to unstable sensitivity. The optimal position is P_3, located between the two inertial bodies and equidistant from the magnets, providing reliable performance within 10 mm of the mechanism's symmetry axis. Although P_1 offers lower sensitivity than P_3, it provides stable performance and can also be used. For the ring-shaped magnets in this design, the Hall sensor should be positioned 9–10 mm from the symmetry axis at P_1 or P_3 to meet sensitivity standards for the grenade fuse.

Conclusion

The paper presents a dynamic model of an all-ways action mechanism, incorporating magnetic interactions from ring magnets used

in an electro-mechanical impact sensor for grenade fuses. A combined simulation using this model and FEMM 4.2 software accurately calculates the sensor's output signal based on structural, magnetic, and velocity input parameters. The program is used to analyze how the activation threshold, inertial mass, and Hall sensor position affect sensor sensitivity. Results indicate that the activation threshold is critical, with an optimal range of 70–80 mV. The magnet's mass has minimal effect unless its density exceeds 7.55 $g.cm^{-3}$. The Hall sensor's location significantly impacts sensitivity, with positions P1 and P3 offering high and stable performance. It should be placed at one of these positions, within 9.5 mm of the mechanism's symmetry axis.

References

Xuan Son Bui, Duc Hung Pham, Van Gion Do, Van Bien Vo. Analysing the Sensitivity of the All-Ways Action Mechanism upon Impact on Target. 2021 International Conference on Military Technologies (ICMT), 2021 Brno. 1-5. Available at: https://doi.org/10.1109/ICMT52455.2021.9502816

Headquaters of United States Army Materiel Command 1969. *Engineering design handbook,* Washington DC, Headquaters of United statess army materiel command. Available at: https://apps.dtic.mil/sti/tr/pdf/AD0889245.pdf

Honeywell Inc. 1998. *Hall effect sensing and application*, Honeywell Inc. Available at: http://denethor.wlu.ca/pc300/projects/sensors/hallbook.pdf

BCD Semiconductor Manufacturing Limited 2010. Linear Hall-effect IC AH49E. Zi Xing Road, Shanghai ZiZhu Science-based Industrial Park, China. Available at: https://www.alldatasheet.com/datasheet-pdf/download/608101/DIODES/AH49E.html

Martin Macko, Xuan Son Bui, Kongsathit Phanthavong, Duc Hung Pham, Van Gion Do, Van Minh Do, Jiri Skala 2024. Velocity equation for grenades while impacting on dry sand media. *Defence Technology,* 35**,** 168-173. Available at: https://doi.org/10.1016/j.dt.2023.09.007

K. Phanthavong, Duc Hung Pham, Xuan Son Bui, Van Gion Do, M. Macko, Dinh Dung Tran. Analysis of Influence of Parameters on the Sensitivity of Semi-Allways Action Mechanism Using Taguchi's Method. 2023 International Conference on Military Technologies (ICMT), 23-26 May 2023 2023. 1-6. Available at: https://doi.org/10.1109/ICMT58149.2023.10171251

Arnold magnetic technologies 2021. N35-151021. *Sintered Neodymium-Iron-Boron Magnet.* Newyork: Arnold magnetic technologies. Available at: https://www.arnoldmagnetics.com/wp-content/uploads/2017/11/N35-151021.pdf

K. Yuan, G. Zhang, C. Xie, X. Song 2019. Integral definition method to solve magnetic force of axial permanent magnetic bearing. *IOP Conference Series: Materials Science and Engineering,* 504**,** 012064. Available at: https://doi.org/10.1088/1757-899X/504/1/012064

Projektovanje i analiza elektromehaničkog senzora udara sa mehanizmom dejstva u svim pravcima i Holovim senzorom

Xuan Son Bui, *Van Gion* Do, **autor za prepisku**, *Duc Hung* Pham
Le Quy Don Technical University, Faculty of Special Equipment, Hanoi, Socialist Republic of Vietnam

OBLAST: mašinstvo
KATEGORIJA (TIP) ČLANKA: originalni naučni rad

Sažetak:

Uvod/cilj: U radu se predlaže elektromehanički senzor udara za detonaciju granate koristeći mehanizam dejstva u svim pravcima u kombinaciji sa trajnim magnetima i Holovim senzorom. Nakon eksperimentalne verifikacije, koristi se matematički model za procenu uticaja strukturalnih parametara kao što su prag aktivacije, inercijalna masa i pozicija Holovog senzora na osetljivost upaljača. Studija pruža preporuke za optimalan dizajn senzora u cilju pouzdane aktivacije pod svim uglovima udara.

Metode: U studiji se koristi kombinovani pristup za rešavanje zadataka. Dinamičke jednačine mehanizma dejstva u svim pravcima rešavaju se metodom Runge-Kuta, magnetno polje se simulira softverom FEMM 4.2, a promena Holovog napona tokom vremena se analizira u cilju procene osetljivosti upaljača u uslovima udara granate.

Rezultati: Rezultati pokazuju da prag aktivacije ispod 80 mV pruža pouzdano funkcionisanje pod svim uglovima udara, sa brzinom udara koja nije već od 2,5 m/s. Masa inercijalnog tela ima značajan uticaj na osetljivost, više nego masa magneta, a pozicija Holovog senzora je ključna, jer neke pozicije pružaju stabilnu osetljivost, dok druge rezultiraju lošim performansama.

Zaključak: Hibridna metoda predstavljena u ovom radu efikasno proučava signal elektromehaničkog senzora udara koji kombinuje mehanizam dejstva u svim pravcima, trajne magnete i Holov senzor. Rezultati istraživanja predstavljaju koristan doprinos dizajnu senzora udara u upaljačima granata.

Ključne reči: elektromehanički senzor udara, mehanizam dejstva u svim pravcima, Holov sensor.

Paper received on: 25 June 2025.
Manuscript corrections submitted on: 3 October 2025.
Paper accepted for publishing on: 28 October 2025.

© 2026 The Authors. Published by Vojnotehnički glasnik / Military Technical Courier (www.vtg.mod.gov.rs).This article is an open access article distributed under the terms and conditions of the Creative Commons Attribution license (http://creativecommons.org/licenses/by/4.0/rs/

Natural convection and entropy generation inside porous square cavity with undulated vertical walls under four heating scenarios

Mouna Maache[a], *Chihab* Eddine Brahmi[b], *Nourredine* Belghar[c], *Mahmoud* Kalfali[d]

Faculty of Science and Technology, Department of Mechanical Engineering, Abbes Laghrour University, Khenchela, Algeria

[a] e-mail: mouna.maache@univ-khenchela.dz, **corresponding author**, ORCID iD: https://orcid.org/0000-0002-6466-1719

[b] e-mail: brahmi.chihabeddine@univ-khenchela.dz, ORCID iD: https://orcid.org/0009-0003-3578-8440

[c] e-mail: belghar.nourredine@univ-khenchela.dz, ORCID iD: https://orcid.org/0000-0002-7772-5101

[d] e-mail: kalfali.mahmoud@univ-khenchela.dz, ORCID iD: https://orcid.org/0009-0002-6183-7800

https://doi.org/10.5937/vojtehg74-58738

FIELD: mechanics, mechanical engineering
ARTICLE TYPE: original scientific paper

Abstract:

Introduction/purpose: This work studies natural convection within a porous cavity with undulated vertical walls focusing on investigating the effects of various heating scenarios. The model consists of a square cavity with sinusoidal undulations on its vertical walls. The cavity is characterized by a square cross-section, and the undulations are described by a sinusoidal wave function with a specific amplitude and wavelength. The left vertical wall of the cavity is maintained at a constant cold temperature, while the bottom wall is subjected to various heating profiles, including linear heating, constant heating, parabolic heating, and sinusoidal heating. The choice of these different heating scenarios is intended to explore how the heat transfer behavior changes under each condition. The top and right walls are assumed to be adiabatic.

Methods: The effects of heating methods and Darcy number on fluid flow and heat transfer in the cavity under a high Rayleigh number are numerically analyzed.

Results: Results show that all heating profiles create distinct thermal gradients, influencing the vortex strength and flow complexity. The study also investigates the irreversibilities within the system, focusing on entropy generation due to both heat transfer and fluid friction, to evaluate the thermodynamic efficiency of the cavity.

Conclusion: The study aims to provide a comprehensive understanding of how heating conditions, permeability variations and high Rayleigh number convection affect the thermal and fluid dynamics in porous cavities, with implications for improving the performance of thermal management systems in practical engineering applications.

Key words: cavity, porous medium, free convection, entropy generation, porosity, permeability.

Introduction

Heat transfer in porous media is a fundamental physical phenomenon that has developed over time. Whether in geothermal energy systems (Böttcher et al, 2016), agricultural soil management (Abed Gatea Al-Shammary et al, 2020), building insulation (Kumar et al, 2020; Pichler et al, 2012) or underground thermal storage (Bloemendal et al, 2014), heat movement plays a critical role in determining energy efficiency, environmental sustainability, and overall system performance. Heat transfer typically occurs through a variety of mechanisms. In complex systems such as porous media, these mechanisms often interact in complex ways, posing significant challenges for accurate modeling and prediction.

Heat transfer and fluid flow in porous media are governed by several factors, such as local thermal equilibrium or non-equilibrium (Gao et al, 2013), time, porosity, tortuosity and permeability, and other properties (Massoud Kaviany, 2011). The complexity is further enhanced by the interplay of thermal conduction, convection, and sometimes radiation within the porous matrix.

Recent advances in heat transfer research increasingly focus on understanding entropy generation mechanisms in porous enclosures under diverse thermal and geometric configurations. Basak et al. (2011), Kaluri & Basak (2011), Brahmi et al. (2024), and Dutta et al. (2021) investigate natural convection and entropy generation in various porous enclosures under different thermal boundary conditions, geometries, and heating methods. Key findings highlight that entropy generation is mainly influenced by heat transfer irreversibility at low Darcy numbers, while fluid friction becomes dominant at higher Darcy and Rayleigh numbers. Factors such as cavity shape, wall undulations, and non-uniform heating with phase shifts significantly affect heat transfer efficiency and entropy production, with optimal configurations minimizing irreversibility.

Extending these insights, Tasmin et al. (2021) incorporate nanofluids and non-Newtonian effects in a wavy porous cavity, demonstrating that lower power-law indices and higher nanoparticle concentrations enhance

heat transfer, with heat transfer irreversibility remaining dominant. Similarly, Al-Waaly et al. (2024) show that optimizing the heated segment length in triangular porous cavities improves thermal performance and reduces entropy generation. In contrast, Rashad et al. (2024) examine magneto-convective effects in nanofluid-filled inclined porous cavities, revealing that magnetic field strength and nanoparticle concentration can diminish heat transfer, highlighting the importance of strategic heat source and sink placement to control entropy generation.

However, despite these advances, limited attention has been given to the combined influence of high Rayleigh number convection, wall undulations, and different heating modes in porous cavities. Most existing studies have considered either simple geometries or uniform heating conditions, while the interplay between sinusoidal boundary geometries and non-uniform heating scenarios under varying permeability remains insufficiently explored.

This study numerically investigates the thermal and fluid flow behavior in a porous square cavity with sinusoidal vertical walls, each having four undulations. The cavity is cooled by a constant cold temperature Tc on the left vertical wall, while the bottom wall is subjected to varying heating scenarios, including linear, constant, parabolic, and sinusoidal heating, while the other walls are maintained insulated. This analysis is conducted under a high Rayleigh number condition ($Ra = 10^6$), which promotes natural convection, and focuses on the impact of different permeability levels, characterized by three values of Darcy numbers ($Da = 10^{-5}$, 10^{-3} and 10^{-1}). The study aims to understand how the combination of porous medium properties and heating conditions influences heat transfer within the cavity at high Rayleigh number. Specifically, the study seeks to explore the effects of different heating types on temperature distribution and flow patterns, examine the role of permeability variations in shaping convective heat transfer, and analyses the resulting flow and thermal fields using isotherms and streamlines. Furthermore, the performance of the system is assessed by calculating both local and average Nusselt numbers to quantify the convective heat transfer efficiency. The study also investigates the irreversibilities within the system, focusing on entropy generation due to both heat transfer and fluid friction, to evaluate the thermodynamic efficiency of the cavity. Ultimately, the study aims to provide a comprehensive understanding of how heating conditions, permeability variations, and high Rayleigh number convection affect the thermal and fluid dynamics in porous cavities, with implications for improving the performance of thermal management systems in practical engineering applications.

Problem description

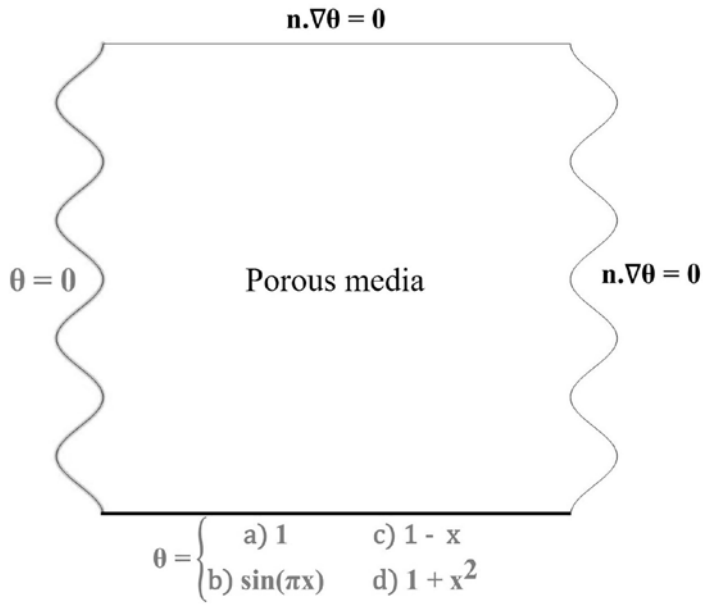

Figure 1 – Schematic of the undulated square porous cavity with four undulations on the vertical walls

Simplifying assumptions

- Fluid is a Newtonian, incompressible, steady, laminar, and two-dimensional.
- All properties are constant, except density, which varies based on the Boussinesq approximation.
- The extended Darcy–Brinkman–Forchheimer model governs the entire domain for momentum transfer.
- Local thermal equilibrium (LTE) is assumed between fluid and solid phases.
- Viscous dissipation is neglected.
- The entire domain of the physical model consists of a porous medium with irregular vertical walls.

Equations in dimensionless form

Based on the simplifying assumptions, the governing equations (Chen et al. 2008) for flow and heat transfer, applicable to the geometries illustrated in Figure 1, are expressed below using a Cartesian coordinate system:

Continuity equation

This equation ensures mass conservation in the fluid:

$$\frac{\partial U}{\partial X}+\frac{\partial V}{\partial Y}=0 \tag{1}$$

Momentum equations

The Extended Darcy–Brinkman–Forchheimer model is used to account for momentum transfer in the porous media:

- It includes Darcy drag to account for flow resistance due to the porous matrix.
- Incorporates Brinkman viscous effects, which describe velocity gradients in the porous medium.
- Accounts for Forchheimer inertial resistance to represent non-linear drag effects at higher velocities.

Momentum formulation along the x-axis

$$\frac{\partial}{\partial X}\left(\frac{UU}{\varepsilon}\right)+\frac{\partial}{\partial Y}\left(\frac{VU}{\varepsilon}\right)=-\frac{\partial P}{\partial X}+Pr\left(\frac{\partial^2 U}{\partial X^2}+\frac{\partial^2 U}{\partial Y^2}\right)-U\,\varepsilon\,\frac{Pr}{Da}-\frac{1.75}{\sqrt{150}}\,\frac{U\sqrt{(U^2+V^2)}}{\sqrt{Da\cdot\varepsilon}} \tag{2}$$

Momentum formulation along the y-axis

$$\frac{\partial}{\partial X}\left(\frac{UV}{\varepsilon}\right)+\frac{\partial}{\partial Y}\left(\frac{VV}{\varepsilon}\right)=-\frac{\partial P}{\partial Y}+Pr\left(\frac{\partial^2 V}{\partial X^2}+\frac{\partial^2 V}{\partial Y^2}\right)-$$

$$V\,\varepsilon\,\frac{Pr}{Da}+Ra\,Pr\;\varepsilon\;\theta-\frac{1.75}{\sqrt{150}}\,\frac{U\sqrt{(U^2+V^2)}}{\sqrt{Da\cdot\varepsilon}} \tag{3}$$

Energy equation

In the porous region:

$$U\,\frac{\partial\theta}{\partial X}+V\,\frac{\partial\theta}{\partial Y}=R_k\left(\frac{\partial^2\theta}{\partial X^2}+\frac{\partial^2\theta}{\partial Y^2}\right) \tag{4}$$

In the fluid region:

$$U\,\frac{\partial\theta}{\partial X}+V\,\frac{\partial\theta}{\partial Y}=\frac{\partial^2\theta}{\partial X^2}+\frac{\partial^2\theta}{\partial Y^2} \tag{5}$$

Stream function

The Stream function, denoted by the symbol ψ, offers a visual representation of fluid motion within the cavities. For two-dimensional flows, it is defined as below:

$$\frac{\partial^2\psi}{\partial X^2}+\frac{\partial^2\psi}{\partial Y^2}=\frac{\partial U}{\partial Y}-\frac{\partial V}{\partial X} \tag{6}$$

Boundary conditions

Bottom boundary (various heating conditions):

$$U = V = 0. \qquad \theta = \begin{pmatrix} 1 \\ 1-x \\ 1+x^2 \\ sin(\pi\, x) \end{pmatrix}$$

Top boundary (adiabatic):

$$U = V = 0. \qquad \partial\theta/\partial n \; = 0$$

Side walls:

$$U = V = 0.$$

At the left wall: $\theta = 0$ At the right wall: $\partial\theta/\partial n \; = 0$

Nusselt number

The local Nusselt number is calculated from the temperature gradient to assess the heat transfer along the cavity boundaries. It is calculated as follows:

$$Nu_L = -\frac{\partial\theta}{\partial n} \tag{7}$$

where $\frac{\partial}{\partial \mathrm{n}}$ represents the dimensionless derivative taken in the direction of the outward normal to the surface under consideration.

The average Nusselt number is the mean of the local Nusselt number along a wall and it is defined by Bhardwaj et al. (2015) as:

$$Nu_{avg} = \frac{1}{L}\int_0^L Nu_L \, dl \tag{8}$$

Heat transfer irreversibility

This type of irreversibility occurs due to non-uniform temperature distributions, leading to entropy generation. It is symbolized as S_{hti}. This irreversibility is formulated by Bejan, A. (1979) as:

$$S_{hti} = \left[\left(\frac{\partial\theta}{\partial X}\right)^2 + \left(\frac{\partial\theta}{\partial Y}\right)^2\right] \tag{9}$$

Fluid friction irreversibility

This irreversibility arises from viscous effects and velocity gradients within the fluid, contributing to entropy generation. It is denoted as $\mathrm{S_{ffi}}$. The formulation for this irreversibility is:

$$S_{ffi} = \xi\left[(U^2+V^2) + Da\left\{2\left(\left(\frac{\partial U}{\partial X}\right)^2 + \left(\frac{\partial V}{\partial Y}\right)^2\right) + \left(\frac{\partial U}{\partial Y} + \frac{\partial V}{\partial X}\right)^2\right\}\right] \tag{10}$$

Here, ξ is the irreversibility distribution ratio, defined as:

$$\xi = \frac{\mu T_0}{K}\left(\frac{\alpha}{\sqrt{K}\Delta T}\right)^2 \quad (11)$$

The entropy generation rate resulting from the combined contributions of these sources is denoted by S. This is expressed by the equation:

$$S = S_{hti} + S_{ffi} \quad (12)$$

S_T is the total entropy generation within these porous cavities can be derived as:

$$S_T = S_{hti_{total}} + S_{ffi_{total}} \quad (13)$$

where:

$$S_{hti_{total}} = \int_{\Omega} S_{hti}\, d\Omega \quad (14)$$

To assess the irreversibility distribution, the Bejan number (Be) represents the ratio of heat transfer irreversibility to the sum of the two contributors of entropy generation. Through analyzing the distribution of local entropy generation, the Bejan number is derived as follows:

$$Be = \frac{S_{hti}}{S_{hti}+S_{ffi}} \quad (15)$$

Then, average Bejan number is given by:

$$Be_{avg} = \frac{S_{hti_{total}}}{S_{hti_{total}}+S_{ffi_{total}}} \quad (16)$$

The value of Be_{avg} ranges between [0, 1]. When $Be_{avg} < 0.5$, heat transfer irreversibility is the dominant contributor to entropy generation. Conversely, when $Be_{avg} > 0.5$, fluid friction irreversibility becomes the primary source of entropy generation.

The numerical simulations software

The numerical simulations were carried out using the finite element method (FEM) implemented through the COMSOL Multiphysics® software. FEM is a well-established technique for solving partial differential equations over complex geometries, making it particularly suitable for modelling heat transfer in porous media. This method divides the computational domain into smaller subdomains (elements), ensuring accurate spatial resolution and efficient handling of irregular boundaries.

COMSOL Multiphysics® was selected for its robust FEM-based solver and its ability to couple various physics phenomena. Its user friendly interface and built-in modules allow for rapid prototyping and reliable

simulation of coupled thermal and flow processes in porous cavities. These features make COMSOL Multiphysics® a versatile tool for this study.

Findings and interpretation

Mesh consistency analysis

A mesh independence analysis was conducted to ensure the reliability and accuracy of the numerical results. Simulations were performed using varying mesh densities, and the results were compared to evaluate convergence. For this study, the computational domain employs a non-orthogonal grid tailored to accommodate the geometric irregularities of the enclosure's undulated side walls.

The convergence test focused on assessing natural convection within a 2D porous cavity with sinusoidal heating applied to the bottom wall, a cold left wall, and adiabatic (insulated) conditions on the remaining walls. The analysis was performed using specific parameters: porosity $(\varepsilon = 0.9)$, $(Pr = 0.71)$, $(Ra = 10^6)$ and $(Da = 10^{-2})$.

The mean Nusselt number along the heated bottom wall served as the evaluation metric for convergence. A range of mesh configurations, with discretization levels of 80, 120, 160, 200, 240, 280, 300, and 320 elements per side was tested to ensure consistency and precision in the numerical results.

The analysis demonstrated, as shown in Table 1, that a mesh consisting of approximately 90000 (300×300) elements yields a converged solution, ensuring both accuracy and computational efficiency.

Table 1 – Comparison of the Nu_{avg} along heated bottom boundary for various grid sizes

Mesh	80×80	120×120	160×160	200×200	240×240	280×280	300×300	320×320
Nu_{avg}	8.816	9.088	9.264	9.399	9.478	9.601	9.642	9.648

Validation

To ensure the accuracy of the numerical results, a validation study was performed by comparing the findings with benchmark data from a two-dimensional porous triangular cavity. The cavity featured undulated vertical left walls, which were cooled, a sinusoidally heated bottom boundary, and adiabatic inclined side walls. The validation was conducted using a structured grid with 10 000 elements and through a parametric analysis under the conditions of Darcy number $(Da = 10^{-2})$, Prandtl number $(Pr = 0.71)$, and varying Rayleigh numbers. The local Nusselt

number distribution along the heated bottom boundary was compared with the results reported by Bhardwaj et al. (2015).

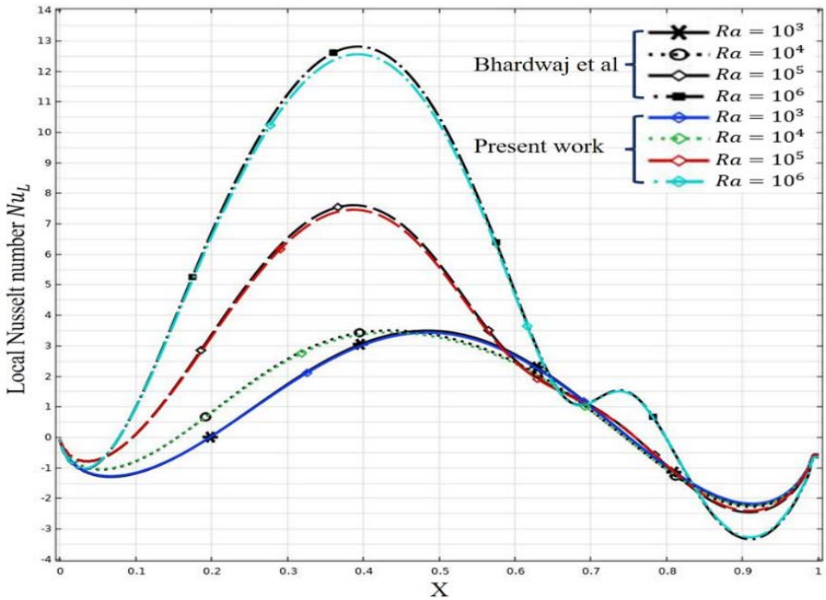

Figure 2 – Comparison between the current numerical simulation and those of Bhardwaj et al. (2015)

Isotherms and streamlines

The thermal and flow behavior within the side-wall undulated square cavity is significantly influenced by the heating conditions applied at the bottom wall. By analyzing the isotherms (Figure 3) and streamlines (Figure 4) for different permeability levels, characterized by Darcy numbers (Da = 10^{-5}, 10^{-3}, 10^{-1}), we can identify key trends in heat transfer and fluid motion across the four heating scenarios: constant heating, linear heating, parabolic heating, and sinusoidal heating.

Under constant heating ($\theta = 1$), where the bottom wall is maintained at a uniform hot temperature, the isotherms radiate outward from the lower-left corner at low permeability (Da = 10^{-5}). This pattern results from the high thermal gradient at the intersection of the hot and cold boundaries, leading to an unbounded heat flux at this singular point. As permeability increases, heat transfer transitions from conduction-dominated behavior to convective heat transfer, causing the isotherms to become more compact near the thermal boundaries.

The corresponding streamlines illustrate weak vortices at low permeability, indicating a suppression of convective motion due to the high resistance of the porous medium. However, as the permeability increases (Da = 10^{-1}), buoyancy-driven flow becomes more pronounced, strengthening the counterclockwise circulation within the cavity. This highlights the shift from conduction-dominated heat transfer at low permeability to convection-dominated transport at higher permeability.

In the case of linear heating ($\theta = 1 - x$), where the temperature decreases along the bottom wall from left to right, the isotherms reveal a concentrated high-temperature region at the left side of the cavity. This localized heating effect drives fluid motion, creating two circulation cells: a smaller clockwise rotating vortex in the right region and a larger counterclockwise vortex in the left region.

At low permeability (Da = 10^{-5}), the streamlines indicate minimal fluid motion due to high flow resistance. However, as the permeability increases (Da = 10^{-1}), the buoyancy force strengthens, leading to a more dynamic circulation pattern. The intensity of the vortices rises from 17 at (Da = 10^{-3}) to nearly 49.94 at (Da = 10^{-1}), demonstrating that convective transport becomes increasingly dominant with higher permeability.

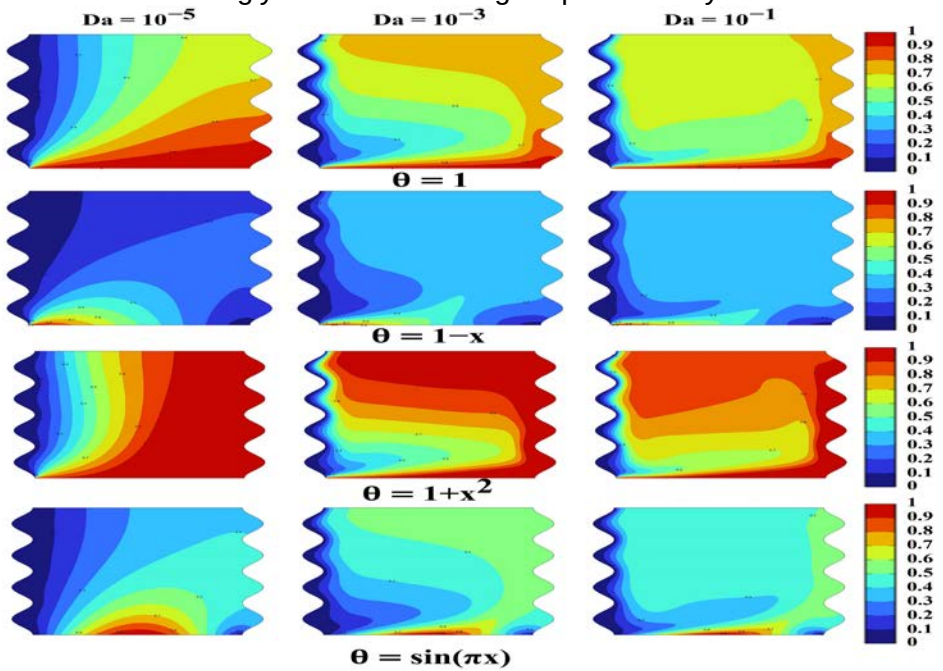

Figure 3 – Isothermal distributions under different heating conditions within the undulated square cavity filled by porous medium at Ra = 10^6

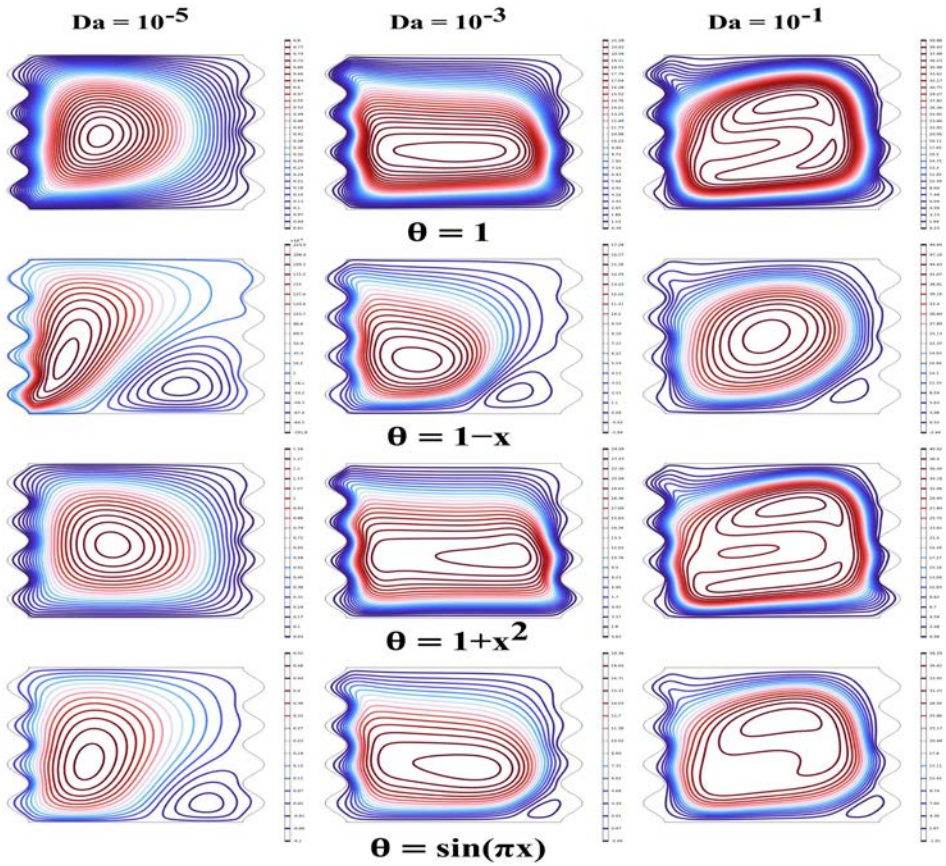

Figure 4 – Streamlines distributions under different heating conditions within the undulated square cavity filled by porous medium at Ra = 10^6

When a parabolic heating profile ($\theta = 1 + x^2$) is applied, the temperature gradient is steeper on the right side of the cavity, where heat accumulation is more pronounced. At low permeability (Da = 10^{-5}), limited fluid mobility results in localized thermal gradients, with conduction being the primary mode of heat transfer. As permeability increases (Da = 10^{-3}), stronger convective effects emerge, facilitating a counterclockwise circulation that redistributes thermal energy more efficiently.

At maximum permeability (Da = 10^{-1}), buoyancy forces are significantly enhanced, leading to a well-defined counterclockwise flow that ensures more uniform temperature distribution within the cavity. Compared to the other heating conditions, the parabolic heating case demonstrates a more localized thermal gradient, particularly in the right region, which governs the convective flow structure.

Under sinusoidal heating ($\boldsymbol{\theta}$ = Sin(πx)), where the bottom wall is subjected to a periodic temperature profile, the isotherms exhibit a distribution similar to that observed in the linear heating case. However, the key difference lies in the heat concentration, which is centered around the middle of the bottom wall rather than the left-hand side. This periodic heating results in alternating high and low-temperature zones, influencing the buoyancy-driven flow patterns.

The streamlines for sinusoidal and linear heating both display two counter-rotating vortices, one clockwise and one counterclockwise, driven by buoyancy forces. However, due to the periodic heating input, the sinusoidal case produces a more complex and oscillatory flow structure. Unlike linear heating, where the temperature gradient remains consistent along the heated surface, sinusoidal heating introduces fluctuations that create more intricate temperature zones and localized variations in fluid motion.

Nusselt number

Figure 5 presents the distributions of the local Nusselt number (Nu_L) for four heating scenarios, illustrating variations along (a) the hot bottom wall and (b) the cold left wall of the cavity for different Darcy numbers (Da = 10^{-5}, 10^{-3}, and 10^{-1}).

In subplots (a), Nu_L along the bottom wall generally decreases with increasing horizontal position (x) for all cases except when the heating profile follows (θ=sin(πx)).

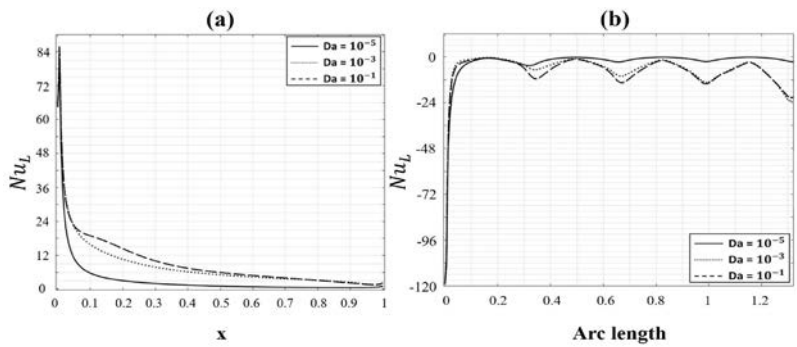

Case 1: $\theta = 1$

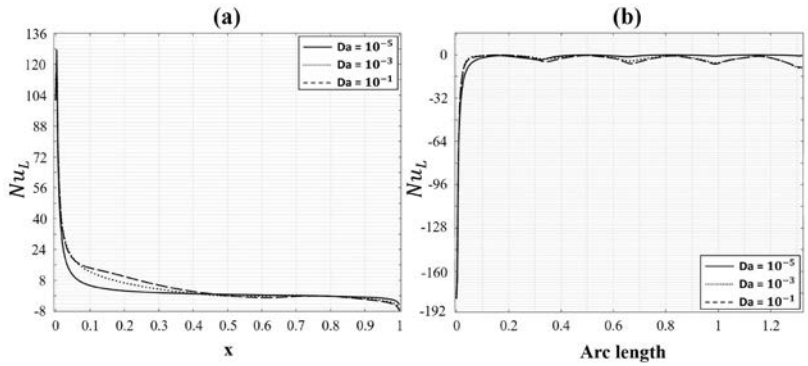

Case 2: $\theta = 1 - X$

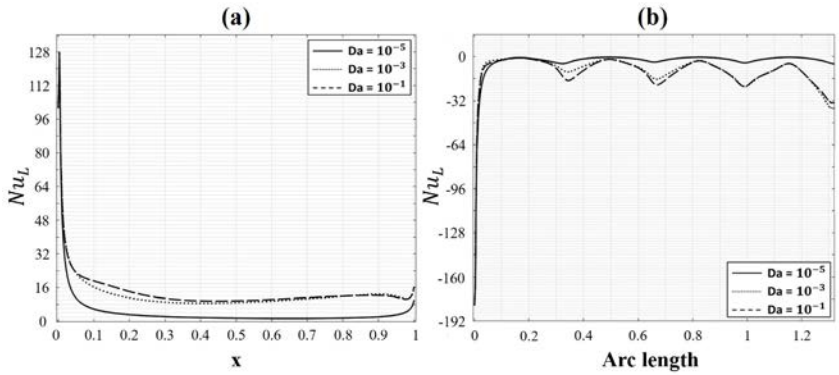

Case 3: $\theta = 1 + X^2$

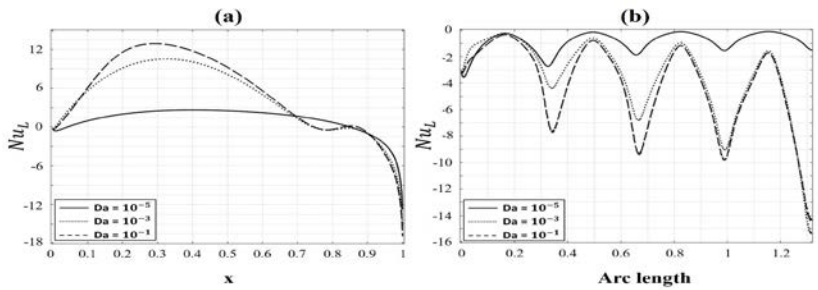

Case 4: $\theta = \sin(\pi X)$

Figure 5 – Nu_L distributions under different heating conditions along the bottom (a) and left (b) walls at Ra = 10^6

In this case, Nu_L initially increases on the left side before decreasing toward the right. This behavior directly corresponds to the oscillatory heating profile, where heat flux peaks coincide with the sinusoidal temperature maxima, producing alternating zones of enhanced and reduced heat transfer. Subplot (b) shows the Nu_L distribution along the cold left wall, where an oscillatory pattern is observed across all heating scenarios and Darcy numbers. Physically, these oscillations arise from the undulated geometry of the cold wall, which alternately accelerates and decelerates heat transfer by modifying local boundary layer thickness. As Da increases, the amplitude of these oscillations grows due to the influence of the undulated cold wall. A sharp decline in Nu_L near the bottom edges is likely caused by overlapping heating and cooling effects. Additionally, a higher Da reduces the sharp drop in Nu_L by enhancing buoyancy-driven convection, which facilitates heat transfer. The negative Nu_L values indicate a reversal in heat transfer direction, signifying that heat flows from the fluid to the cold wall rather than the reverse. This effect is driven by the cooling impact of the wall and buoyancy forces. Among the tested heating scenarios, the sinusoidal heating case results in the least pronounced Nu_L distribution along the cold wall, since the periodic input smooths out extreme gradients, distributing heat more evenly compared to localized heating cases.

Average Nusselt number

At a high Rayleigh number of 10^6, the two graphs present distinct yet complementary thermal behaviors, (a) along the heated bottom wall and (b) on the undulated cold vertical wall of the porous cavity under varying permeability and heating scenarios. Along the bottom boundary, the average Nusselt number is positive, indicating net heat release into the fluid, and its magnitude increases with permeability as higher Darcy numbers reduce flow resistance, intensify buoyancy-driven circulation, and thin the thermal boundary layer. Conversely, along the cold vertical wall, the Nusselt number is negative, reflecting heat absorption from the fluid, with its absolute value likewise growing with permeability due to stronger impingement of hot plumes. In both cases, the heating mode significantly influences convective performance: parabolic heating produces the strongest enhancement, followed by constant heating, while linear and sinusoidal distributions yield comparatively weaker transfer rates. The wall undulation further augments heat exchange by enlarging the effective surface area and generating local recirculation zones, particularly under high permeability. Overall, the comparison reveals that both boundaries

exhibit analogous trends governed by the same convective mechanisms, with opposite heat flux directions, and that parabolic heating consistently maximizes global heat transfer efficiency. These observations are in good agreement with the streamline and isothermal contour distributions, which clearly demonstrate intensified circulation cells and sharper thermal gradients under higher permeability and parabolic heating conditions.

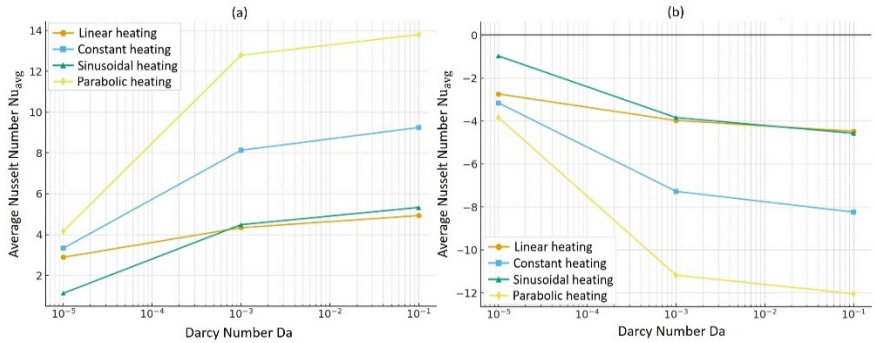

Figure 6 – Nu_{avg} distributions under different heating conditions along the bottom (a) and left (b) walls at Ra = 10^6

Entropy generation

This analysis examines the Bejan number for the four different heating conditions, with varying Rayleigh numbers ($Ra = 10^3$ *and* $Ra = 10^6$), and Darcy numbers ($Da = 10^{-1}, 10^{-3}$ *and* 10^{-5}).

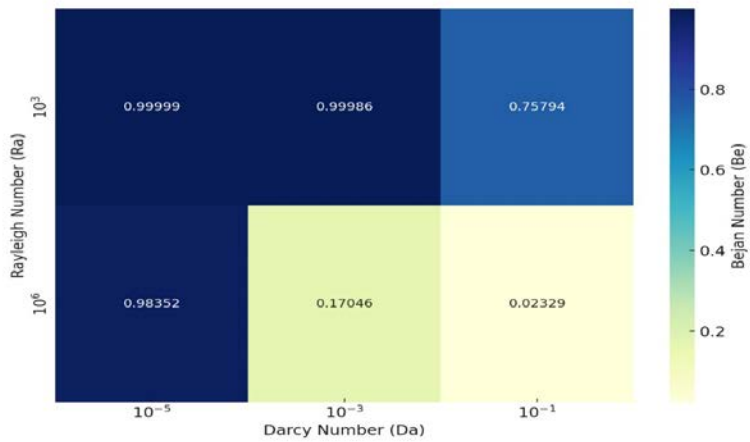

Figure 7 – Heat map of Be number depicting the influence of Ra and Da in case of constant heating from below

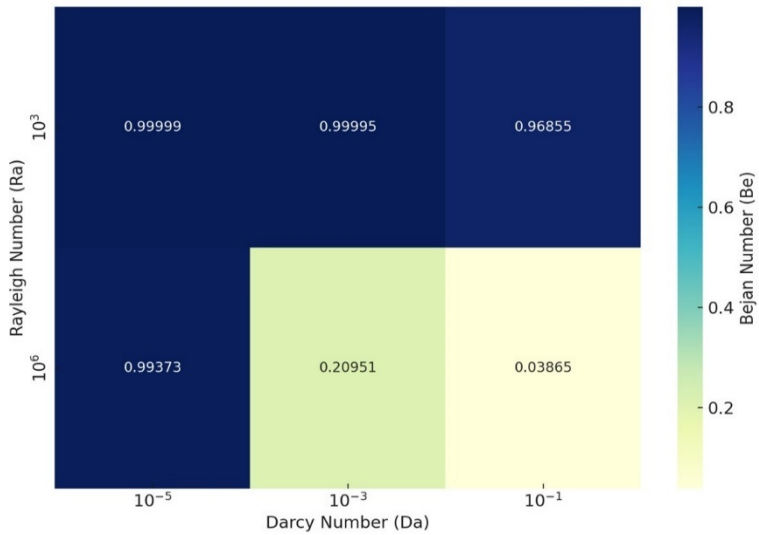

Figure 8 – Heat map of Be number depicting the influence of Ra and Da in case of linear heating from below

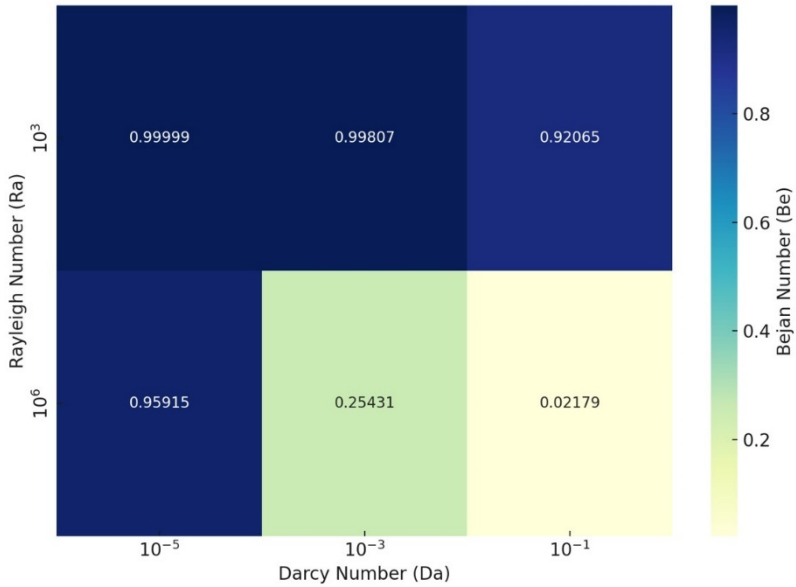

Figure 9 – Heat map of Be number depicting the influence of Ra and Da in case of quatratic heating from below

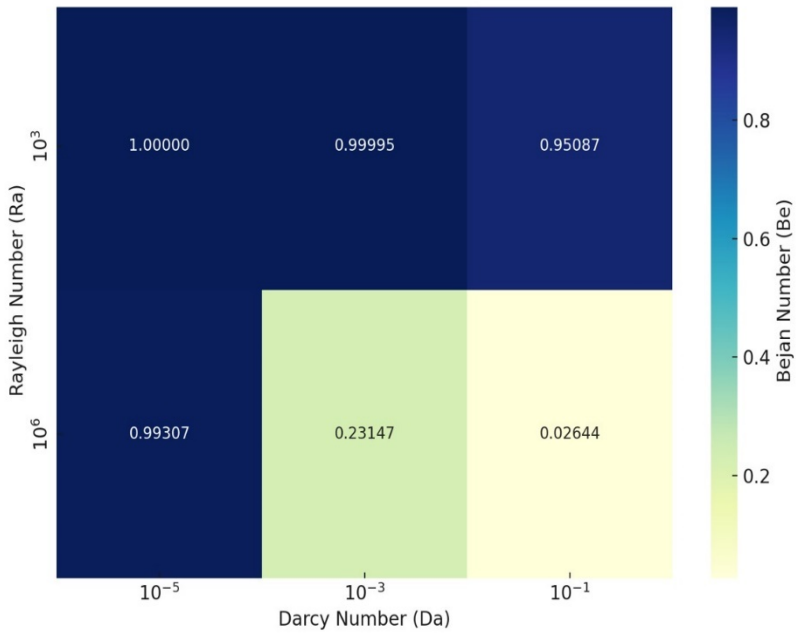

Figure 10 – Heat map of Be number depicting the influence of Ra and Da in case of sinusoidal heating from below

Across all four heating cases, thermal irreversibility dominates at low Rayleigh numbers $Ra = 10^3$, with the Bejan number remaining close to 1 for all Darcy numbers. This trend is consistent in linear, parabolic, sinusoidal, and constant heating cases, where fluid friction has a minimal effect. In contrast, for a Rayleigh number 10^6, the behavior shifts significantly. At high Rayleigh numbers and high permeability, fluid friction irreversibility dominates, particularly in the linear, parabolic, sinusoidal, and constant heating cases, with the Bejan number indicating strong convection effects. However, as the Darcy number decreases, the permeability decreases as well, and thermal irreversibility begins to take over. The Bejan number gradually increases towards 1, reflecting the increasing importance of thermal effects due to the suppression of convection and the rise in flow resistance. While the general trend of fluid friction dominance at higher Rayleigh numbers and lower permeability dominance at lower Rayleigh numbers holds true across all cases, the specific behavior of the Bejan number varies slightly based on the heating mode, with sinusoidal heating showing a more gradual transition compared to the others.

Practical applications

Although this study primarily focuses on numerical simulations, the insights gained have direct implications for real-world thermal systems. The influence of heating profiles and permeability on convective heat transfer is particularly relevant to cooling technologies such as electronic devices, heat exchangers, and energy storage systems, where efficient thermal management is crucial. Likewise, the balance between conduction and convection observed in porous cavities offers guidance for designing insulation materials in both construction and industry, especially under low-permeability conditions that minimize convective losses. In the biomedical field, porous media models are widely applied to tissue cooling, drug delivery, and cryopreservation; here, the demonstrated effects of sinusoidal and parabolic heating could support more effective localized thermal treatments and scaffold designs. Finally, the results also extend to renewable energy systems, including solar collectors and geothermal technologies, where the interplay between buoyancy-driven flow and porous structures governs overall thermal efficiency.

Table 2 – Nomenclature

Be	Bejan number
Be_{avg}	Average Bejan number
Da	Darcy number
g	Gravitational acceleration, ($m.s^{-2}$)
H	Height of the enclosure, (m)
k	Thermal conductivity, ($W.m^{-1}.\mathrm{K}^{-1}$)
K	Permeability, (m^2)
L	Length of the enclosure, (m)
Nu_L	Local Nusselt number
Nu_{avg}	Average Nusselt number
p	Pressure (Nm^{-2}))
P	Dimensionless pressure
Pr	Prandtl number
Ra	Rayleigh number
S	Dimensionless total entropy
S_T	Total entropy
S_{hti}	Dimensionless entropy generation due to heat transfer
S_{ffi}	Dimensionless entropy generation due to fluid friction
T	Temperature (K)
T_0	Bulk temperature $\frac{T_h+T_c}{2}$ (K)
u, v	Cartesian velocity components (m/s)

U, V	Dimensionless velocity components
X, Y	Dimensionless Cartesian coordinates
Greek symbols	
α	Thermal diffusivity, ($m^2 s^{-1}$)
β	Volumetric expansion coefficient, (K^{-1})
θ	Dimensionless temperature
μ	Dynamic viscosity, ($kg.m^{-1}.s^{-1}$)
λ	Wave amplitude
ν	Kinematic viscosity, ($m^2 s^{-1}$)
ε	Porosity
ξ	Irreversibility distribution ratio
ψ	Stream function
Subscripts	
avg	Average
c	Cold wall
h	Hot wall
max	Maximum
min	Minimum

Conclusion

This study comprehensively investigated the effects of heating methods and Darcy numbers ($Da = 10^{-5}, 10^{-3}$ and 10^{-1}) on fluid flow and heat transfer in a porous square cavity with sinusoidal vertical walls under a high Rayleigh number ($Ra = 10^6$). The results revealed that permeability and heating conditions significantly influence isotherm distribution, fluid circulation patterns and Nu_L variations. At low permeability $Da = 10^{-5}$, heat transfer is predominantly conductive, while at high permeability $Da = 10^{-1}$, convection becomes dominant. Different heating methods introduce distinct thermal and flow behaviors, but the overall trends remain consistent across the cavity. The key obtained findings are:

Increasing the Darcy number intensifies fluid circulation, with stronger vortices forming at higher permeability levels.

Linear, parabolic, sinusoidal, and constant heating profiles create distinct thermal gradients, influencing vortex strength and flow complexity.

Sinusoidal heating shows oscillatory trends in local Nusselt number, while permeability strongly affects heat flux distribution along the cavity walls.

At low Rayleigh numbers $Ra = 10^3$, thermal irreversibility dominates across all Darcy numbers. At high Rayleigh numbers $Ra = 10^6$, fluid friction irreversibility prevails at high Darcy numbers but shifts to thermal irreversibility as Darcy numbers decrease.

At low Rayleigh numbers $Ra = 10^3$, all heating methods show dominance of thermal irreversibility.

At high Rayleigh numbers $Ra = 10^6$, linear and parabolic heating exhibit stronger fluid friction irreversibility at higher Darcy numbers $Da = 10^{-1}$.

References

Böttcher, N., Watanebe, N., Görke, U. J., and Kolditz, O., 2016. Geoenergy Modeling I : Geothermal Processes in Factured Porous Media (Computational Modeling of Energy Systems). *Springer International Publishing*.

DOI:10.1007/978-3-319-31335-1

Abed Gatea Al-Shammary, A., Kouzani, A., Gyasi-Agyei, Y., Gates, W., and Rodrigo-Comino, J., 2020. Effects of solarisation on soil thermal-physical properties under different soil treatments: A review, *Geoderma,* 363, pp. 110038

https://doi.org/10.1016/j.geoderma.2019.114137

Kumar, D., Alam, M., Zou, P. X. W., Sanjayan, J. G., and Memon, R. A. 2020. Comparative analysis of building insulation material properties and performance, *Renewable and sustainable energy reviews,* 131, pp. 110038.

https://doi.org/10.1016/j.rser.2020.110038

Picher, C., Metzler, G., Niederegger, C., and Lacker, R. 2012. Thermo-mechanical optimization of porous building materials based on micromechanical concepts : Application to load-carring insulation materials.

https://doi.org/10.1016/j.compositesb.2011.09.013

Bloemendal, M., Olsthoom, T., and Boons, F., 2014. How to achieve optimal and sustainable use of the subsurface for Aquifer Thermal Energy Storage. *Energy Policy*, 66, pp 104-114

https://doi.org/10.1016/j.enpol.2013.11.034

Gao, D., Chen, Z., and Chen, L., 2014. A thermal lattice Bottzmann model for natural convection in porous media under local thermal non-equilibrium conditions. *International Journal of Heat and Mass Transfer*, 70, pp. 979-989.

https://doi.org/10.1016/j.ijheatmasstransfer.2013.11.050

Kaviany, M., 2011. Principles of heat transfer in porous media. *Mechanical Engineering Series*. Spring-Verlag New York Inc.

https://doi.org/10.1007/978-1-4612-4254-3

Basak, T., Kaluri, R.S. and Balakrishnan, A.R. 2011. Effects of Thermal Boundary Conditions on Entropy Generation during Natural Convection. *Numerical heat transfer. Part A. Applications.* 59(5), pp.372–402.

https://doi.org/10.1080/10407782.2011.549075

Kaluri, R.S. and Basak, T. 2011. Entropy generation due to natural convection in discretely heated porous square cavities. *Energy*, 36(8), pp. 5065–5080.
https://doi.org/10.1016/j.energy.2011.06.001
Brahmi, C.E., Maache, M., Belghar, N., Kalfali, M. and Bessaih, R. 2024. Free convection and entropy generation inside porous cavities with irregular vertical walls nonuniformly heated from below*. Numerical heat transfer. Part A. Applications.* pp.1–27.
https://doi.org/10.1080/10407782.2024.2359046
Dutta, S., Goswami, N., Pati, S. and Biswas, A.K. 2020. Natural convection heat transfer and entropy generation in a porous rhombic enclosure: influence of non-uniform heating. *Journal of Thermal Analysis and Calorimetry*, 144(4), pp.1493–1515.
https://doi.org/10.1007/s10973-020-09634-7
Tasmin, M., Nag, P., Hoque, Z.T. and Molla, Md. M. 2021. Non-Newtonian effect on heat transfer and entropy generation of natural convection nanofluid flow inside a vertical wavy porous cavity. *SN applied sciences*, 3(299).
https://doi.org/10.1007/s42452-021-04157-8
Al Waaly, A., Tumpa, S.A., Nag, P., Paul, A.R., Saha, G. and Saha, S.C. 2024. Entropy generation associated with natural convection within a triangular porous cavity containing equidistant cold domains. *Frontiers in Energy Research*, 12:1422256.
https://doi.org/10.3389/fenrg.2024.1422256
Rashad, A.M., Armaghani, T., Chamkha, A.J. and Mansour, M.A. 2018. Entropy generation and MHD natural convection of a nanofluid in an inclined square porous cavity: Effects of a heat sink and source size and location. *Chinese Journal of Physics*. 56(1), pp.193–211.
https://doi.org/10.1016/j.cjph.2017.11.026
Chen, X. B., Yu, P., Sui, Y., Winoto, S. H., and Low, H. T., 2008. Natural Convection in a Cavity Filled with Porous Layers on the Top and Bottom Walls. *Transport in Porous Media*.78(2), pp. 259-276.
https://doi.org/10.1007/s11242-008-9300-2
Bejan, A., 1979. A Study of Entropy Generation in Fundamental Convective Heat Transfer. *Journal of Heat Transfer*, 101(4) pp. 718-725.
https://doi.org/10.1115/1.3451063
Bhardwaj, S., Dalal, A., and Pati, S., 2015. Influence of wavy wall and non-uniform heating on natural convection heat transfer and entropy generation inside porous complex enclosure. *Energy.* 79 pp. 467-481.
https://doi.org/10.1016/j.energy.2014.11.036

Prirodna konvekcija i stvaranje entropije unutar porozne kvadratne šupljine sa neravnim vertikalnim zidovima u četiri režima zagrevanja

Mouna Maache, **autor za prepisku**, *Chihab* Eddine Brahmi, *Nourredine* Belghar, *Mahmoud* Kalfali
Faculty of Science and Technology, Department of Mechanical Engineering, Abbes Laghrour University, Khenchela, Algeria

OBLAST: mehanika, mašinstvo
TIP ČLANKA: originalni naučni rad

Sažetak:

Uvod/cilj: Ovaj rad proučava prirodnu konvekciju unutar porozne šupljine sa neravnim vertikalnim zidovima, sa težištem na ispitivanju uticaja različitih režima zagrevanja. Model se sastoji od kvadratne šupljine sa sinusoidnim neravninama na vertikalnim zidovima. Šupljina ima kvadratni poprečni presek, a neravnine su opisane sinusoidnom talasnom funkcijom sa određenom amplitudom i talasnom dužinom. Levi vertikalni zid šupljine održava se na konstantnoj niskoj temperaturi, dok je donji zid podvrgnut različitim profilima zagrevanja, uključujući linearno, konstantno, parabolično i sinusoidno zagrevanje. Izbor ovih različitih režima zagrevanja ima za cilj da ispita kako se ponašanje prenosa toplote menja u svakom režimu. Gornji i desni zid se smatraju adijabatskim.

Metode: Uticaj metoda zagrevanja i Darsijevog broja na strujanje fluida i prenos toplote pri visokom Rejnoldsovom broju analizira se numerički.

Rezultati: Rezultati pokazuju da svi profili zagrevanja stvaraju različite termičke gradijente koji utiču na jačinu vrtloga i složenost strujanja. U radu se ispituje i nepovratno ponašanje sistema sa fokusom na stvaranje entropije usled prenosa toplote i viskoznog trenja, a radi procene termodinamičke efikasnosti šupljine.

Zaključak: Cilj studije je da pruži sveobuhvatno razumevanje kako uslovi zagrevanja, promena permeabilnosti i konvekcija pri visokom Rejnoldsovom broju utiču na termičku i fluidnu dinamiku u poroznim šupljinama, kao i implikacije za unapređenje performansi sistema za upravljanje toplotom u praktičnim inženjerskim primenama.

Ključne reči: šupljina, porozna sredina, prirodna konvekcija, generisanje entropije, poroznost, permeabilnost.

Paper received on: 2 July 2025.
Manuscript corrections submitted on: 30 November 2025.
Paper accepted for publishing on: 22 January 2026.

© 2026 The Authors. Published by Vojnotehnički glasnik / Military Technical Courier (www.vtg.mod.gov.rs).This article is an open access article distributed under the terms and conditions of the Creative Commons Attribution license (http://creativecommons.org/licenses/by/4.0/rs/)

Free vibration analysis of porous functionally graded plates using a novel shape function

Billel Rebai[a], *Tidjani* Messas[b], *Mustapha* Meradjah[c], *Mohammed* Benali Amar[d]

[a] Faculty of Sciences & Technology, Civil Eng Department, University Abbes Laghrour, Khenchela, Algeria,
e-mail: billel.rebai@univ-khenchela.dz, **corresponding author**,
ORCID iD: https://orcid.org/0000-0003-3739-2784

[b] Faculty of Sciences & Technology, Civil Eng Department, University Abbes Laghrour, Khenchela, Algeria,
e-mail: messas_tidjani@univ-khenchela.dz,
ORCID iD: https://orcid.org/0000-0002-0399-3541

[c] Civil Eng Department, Faculty of Technology, University of Sidi Bel Abbes, Algeria +
Joint Research Team "Nano-Biomaterials and Digital Engineering for Pharmaceutical Applications", Thematic Agency for Research in Science and Technology (ATRST), Algeria,
e-mail: meradjahmustapha@gmail.com,
ORCID iD: https://orcid.org/0000-0002-5988-6120

[d] Civil Eng Department, Faculty of Technology,University of Sidi Bel Abbes, Algeria,
e-mail: mohabenali12@gmail.com,
ORCID iD: https://orcid.org/0000-0002-5988-4567

https://doi.org/10.5937/vojtehg74-59377

FIELD: mechanics, materials, mechanical engineering
ARTICLE TYPE: original scientific paper

Abstract:

Introduction/purpose: This study introduces a novel analytical framework to comprehensively investigate the natural vibration characteristics of porous functionally graded (FG) plates. The research aims to combine an innovative shape function methodology with a sophisticated porosity model within an advanced higher-order shear deformation theory (HSDT).

Methods: Material properties follow power-law distributions across the thickness, with voids incorporated via a refined porosity formulation. The governing equations for simply supported plates are solved analytically

ACKNOWLEDGMENT: The authors express their gratitude for the financial support provided by the University Research and Training Projects (PRFU) under the code A01L02UN220120200004, which plays a vital role in supporting doctoral training in higher education institutions in Algeria.

using the Navier technique. A parametric study examines the effects of power-law index, geometric ratios, and porosity distribution.

Results: Results show exceptional agreement with established theories, revealing significant relationships in which both the power-law index and porosity distribution critically influence natural frequencies. New insights are provided into their coupled effects on vibrational behavior.

Conclusion: This work offers fundamental understanding for optimizing porous FG plate design in advanced engineering applications such as aerospace and structural systems, where weight reduction and vibration control are crucial. It delivers practical guidelines for engineering design and material selection.

Key words: functionally graded plates, porosity, natural vibration, shape function, Hamilton's principle, analytical solution.

Introduction

Functionally graded materials (FGMs) have gained significant attention in recent years due to their unique properties that vary gradually through the thickness. Numerous studies have investigated the vibration behavior of FGM plates and shells using different theories and methods. Zhang & Zhou (2008) presented a theoretical analysis of FGM thin plates based on the physical neutral surface, which simplifies the governing equations compared to classical laminated plate theory. Vel & Batra (2004) developed a three-dimensional exact solution for vibrations of FGM rectangular plates, valid for both thick and thin plates with arbitrary material property variations. Several researchers have employed various plate theories to analyze FGM plates. Zenkour (2005) and Messas et al. (2023) used a sinusoidal shear deformation theory to study buckling and free vibration of FGM sandwich plates. Matsunaga (2008) applied a 2-D higher-order deformation theory to analyze natural frequencies and buckling stresses of FGM plates, considering transverse shear and normal deformations.

The inclusion of porosity effects in FGM plates has been a focus of recent studies. Rezaei & Saidi (2015) and Chitour et al. (2024) presented an exact solution for free vibration of thick rectangular porous plates saturated by inviscid fluid. Rebai (2023) investigated the impact of three homogenization models (Reuss, LRVE, Tamura) on the axial and shear stress of sandwich functionally graded plates (Ti-6A1-4V/ZrO2) subjected to linear and nonlinear thermal loads. Gupta & Talha (2018) examined the influence of porosities on flexural and free vibration responses of FGM plates in thermal environments. Various numerical methods have been employed

to analyze FGM structures. Sharma et al. (2022) used polynomial neural networks for stochastic frequency analysis of laminated composite plates with curvilinear fibers. Swain et al. (2020) and Boutrid et al. (2024) applied perturbation techniques and polynomial neural networks for aeroelastic analysis of laminated composite plates with material uncertainty. Degenerated shell elements have been utilized for vibration analysis of plates and shells. Lee & Han (2001) developed a nine-node assumed natural degenerated shell element for free vibration analysis of plates and shells. Tiwari et al. (2019) used 3D degenerated elements to analyze free vibration of delaminated composite plates. The same authors also formulated an 8-noded degenerated shell finite element for modeling and analysis of laminated composite shell structures (Tiwari et al., 2020). Recent studies have focused on advanced theories and methods for analysing FGM plates with porosities. Rezai et al. (2017) investigated natural frequencies of FGM plates with porosities using a simple four-variable plate theory. Zhao et al. (2009) applied the element-free kp-Ritz method for free vibration analysis of FGM plates. Adhikari & Singh (2019) employed a quasi-3D theory to study the dynamic response of FGM plates on elastic foundations. Several researchers have investigated the effects of piezoelectric layers and various porosity distributions on FGM plates. Van Long et al. (2016) developed a new eight-unknown shear deformation theory for bending and free vibration analysis of FGM plates. Choudhary et al. (2023) studied free vibration response of FGM porous metallic plates embedded with piezoelectric layers. Berkia et al. (2023) explored the free vibration behavior of functionally graded (FG) nano-beams using four homogenization schemes. Kurpa & Shmatko (2024) used the Ritz method combined with R-functions theory to analyze vibrations of porous FGM shallow shells with complex platforms. Shmatko et al. (2023) studied nonlinear free vibrations of FGM porous sandwich plates with complex shapes using R-functions theory and variational methods. Cho (2022) employed a 2D natural element method to analyze static bending and free vibration of FG porous plates, considering various porosity distributions. Vasara et al. (2022) used the differential quadrature method to analyze free vibration of FG porous circular and annular plates with different porosity distributions. Recent studies have also explored the effects of reinforcements in FGM plates. Lazar et al. (2023) investigated free vibration analysis of FGM plates reinforced with carbon nanotubes using an exponential distribution law. Huang et al. (2022) pre-

sented a nonlinear vibration analysis of functionally graded porous plates reinforced by graphene platelets on nonlinear elastic foundations.

This study aims to investigate the natural vibration behavior of porous functionally graded (FG) plates through the application of a novel shape function. Utilizing higher-order shear deformation theory (HSDT), the research examines material property variations across the plate thickness using power-law forms. The introduction of a porosity model allows for the analysis of the effects of void content on the plate's mechanical characteristics. The Navier solution technique is employed to obtain analytical solutions for simply supported FG plates. Key parameters, including the power-law index, side-to-thickness ratio, aspect ratio, and porosity, are examined for their influence on the natural frequencies of FG plates. The findings confirm the efficacy of the new shape function in accurately capturing the vibrational behavior of porous FG plates. This comprehensive analysis offers valuable insights for engineers and designers working with these advanced materials, providing a deeper understanding of how various parameters affect the vibrational properties of porous FG plates in practical applications.

Theoretical formulation

Figure 1 illustrates a functionally graded (FG) plate with dimensions h (thickness), a (length), and b (width). This FG plate is composed of a ceramic-metal mixture, where the material properties vary continuously through the thickness. This variation is governed by the volume fractions of the ceramic and metal constituents, leading to a smooth transition in material composition from the top to the bottom surface.

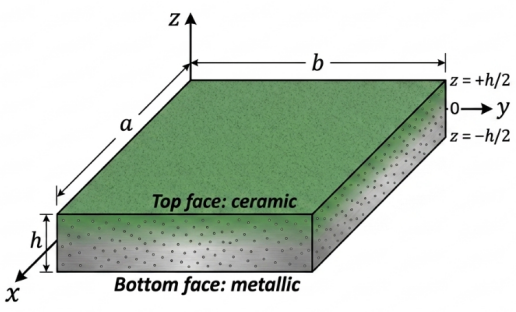

Figure 1 – Geometry of a functionally graded plate

Material property distribution

The homogenization scheme with a power-law distribution is employed to estimate material properties through the thickness. The effective material properties of FG plates are expressed as:

$$P(z) = (P_c - P_m)V_c + P_m \tag{1}$$

where P_c and P_m denote the Young's moduli (E), Poisson's ratios (ν), and mass densities (ρ) of the ceramic and metal materials located at the top and bottom surfaces, respectively. The volume fraction of ceramic material V_c is given by:

$$V_c(z) = \left(\frac{2z+h}{2h}\right)^p \tag{2}$$

where p is the power-law index (positive value) and $z \in [-h/2, h/2]$.

Homogeneous porosity model

Porosity distributions in FG plates can be modeled using various mathematical approaches. This study assumes a homogeneous (even) distribution of porosity throughout the thickness of the FG plate. The presence of porosity reduces the volume fraction of constituent materials as described by:

$$P_{\text{even}} = \frac{\alpha}{2} \tag{3}$$

where α is the porosity coefficient.

Material properties with porosity

The material properties of the porous FG plate vary only in the thickness direction. Using a power-law distribution, the equivalent properties (P) incorporating porosity effects are expressed as:

$$E(z) = (E_c - E_m)V_c(z) + E_m - \frac{\alpha}{2}(E_c + E_m) \tag{4}$$

$$\rho(z) = (\rho_c - \rho_m)V_c(z) + \rho_m - \frac{\alpha}{2}(\rho_c + \rho_m) \tag{5}$$

Rebai, B. et al., Free vibration analysis of porous functionally graded plates using a novel shape function, pp.379–399

Limitations of the porosity model

Analysis of Young's modulus and density as functions of porosity coefficient α and material index p reveals critical behavioral thresholds. Minimum values occur when $z \approx -h/2$, p is large, and α is significant. Specifically:

- $E(z) \to 0$ when $\alpha \approx 0.288$ at $z = -h/2$, becoming negative for $\alpha > 0.288$
- $\rho(z) \to 0$ when $\alpha \approx 0.831$ at $z = -h/2$, becoming negative for $\alpha > 0.831$

The findings necessitate limiting α in practical applications to maintain physical validity and structural integrity. The influence of p on property distributions and the significant effect of α on E and ρ values underscore the complex parameter interactions in functionally graded composites.

Kinematics and strains

The displacement field within the higher-order shear deformation theory (HSDT) is expressed as:

$$u(x,y,z) = u_0(x,y) - z\frac{\partial w_0}{\partial x} - f(z)\frac{\partial \phi}{\partial x} \tag{6}$$

$$v(x,y,z) = v_0(x,y) - z\frac{\partial w_0}{\partial y} - f(z)\frac{\partial \phi}{\partial y} \tag{7}$$

$$w(x,y,z) = w_0(x,y) \tag{8}$$

This investigation introduces a novel shape function that satisfies essential continuity conditions and improves analytical accuracy:

$$f(z) = 4.7z\left((z)^{\pi/5} - 0.79\right) \tag{9}$$

The associated strain field is derived from the displacement field as:

$$\boldsymbol{\epsilon} = \boldsymbol{\epsilon}^0 + z\boldsymbol{\kappa}^b + f(z)\boldsymbol{\kappa}^s \tag{10}$$

$$\boldsymbol{\gamma} = g(z)\begin{Bmatrix}\gamma_{xz}^0 \\ \gamma_{yz}^0\end{Bmatrix} = g(z)\begin{Bmatrix}\frac{\partial \phi}{\partial x} \\ \frac{\partial \phi}{\partial y}\end{Bmatrix} \tag{11}$$

where $\boldsymbol{\kappa}^b$, $\boldsymbol{\kappa}^s$, and $\boldsymbol{\gamma}^0$ represent bending curvatures, shear curvatures, and transverse shear strains, respectively, with $g(z) = -\frac{df}{dz}$. The strain compo-

nents are defined as:

$$\boldsymbol{\epsilon}^0 = \begin{Bmatrix} \frac{\partial u_0}{\partial x} \\ \frac{\partial v_0}{\partial y} \\ \frac{\partial u_0}{\partial y} + \frac{\partial v_0}{\partial x} \end{Bmatrix} \tag{12}$$

$$\boldsymbol{\kappa}^b = \begin{Bmatrix} -\frac{\partial^2 w_0}{\partial x^2} \\ -\frac{\partial^2 w_0}{\partial y^2} \\ -2\frac{\partial^2 w_0}{\partial x \partial y} \end{Bmatrix} \tag{13}$$

$$\boldsymbol{\kappa}^s = \begin{Bmatrix} -\frac{\partial^2 \phi}{\partial x^2} \\ -\frac{\partial^2 \phi}{\partial y^2} \\ -2\frac{\partial^2 \phi}{\partial x \partial y} \end{Bmatrix} \tag{14}$$

Constitutive relations

The linear constitutive relations for the FG plate are:

$$\begin{Bmatrix} \sigma_{xx} \\ \sigma_{yy} \\ \sigma_{xy} \end{Bmatrix} = \begin{bmatrix} C_{11} & C_{12} & 0 \\ C_{12} & C_{22} & 0 \\ 0 & 0 & C_{66} \end{bmatrix} \begin{Bmatrix} \epsilon_{xx} \\ \epsilon_{yy} \\ \gamma_{xy} \end{Bmatrix} \tag{15}$$

$$\begin{Bmatrix} \sigma_{xz} \\ \sigma_{yz} \end{Bmatrix} = \begin{bmatrix} C_{55} & 0 \\ 0 & C_{44} \end{bmatrix} \begin{Bmatrix} \gamma_{xz} \\ \gamma_{yz} \end{Bmatrix} \tag{16}$$

where the stiffness coefficients are:

$$C_{11}(z) = C_{22}(z) = \frac{E(z)}{1-\nu(z)^2} \tag{17}$$

$$C_{12}(z) = \nu(z) C_{11}(z) \tag{18}$$

$$C_{44}(z) = C_{55}(z) = C_{66}(z) = \frac{E(z)}{2(1+\nu(z))} \tag{19}$$

Equations of motion

Hamilton's principle is employed to derive the equations of motion:

$$\int_0^T (\delta U + \delta K) dt = 0 \tag{20}$$

Rebai, B. et al., Free vibration analysis of porous functionally graded plates using a novel shape function, pp.379–399

where δU and δK represent the variations of strain energy and kinetic energy, respectively. The variation of strain energy is:

$$\delta U = \int_A \begin{bmatrix} N_{xx}\dfrac{\partial \delta u_0}{\partial x} - M^b_{xx}\dfrac{\partial^2 \delta w_0}{\partial x^2} - M^s_{xx}\dfrac{\partial^2 \delta \phi}{\partial x^2} \\ +N_{yy}\dfrac{\partial \delta v_0}{\partial y} - M^b_{yy}\dfrac{\partial^2 \delta w_0}{\partial y^2} - M^s_{yy}\dfrac{\partial^2 \delta \phi}{\partial y^2} \\ +N_{xy}\left(\dfrac{\partial \delta u_0}{\partial y} + \dfrac{\partial \delta v_0}{\partial x}\right) - 2M^b_{xy}\dfrac{\partial^2 \delta w_0}{\partial x \partial y} \end{bmatrix} dA \tag{21}$$

with stress resultants defined as:

$$(N_{xx}, N_{yy}, N_{xy}) = \int_{-h/2}^{h/2} (\sigma_{xx}, \sigma_{yy}, \sigma_{xy}) dz \tag{22}$$

$$(M^b_{xx}, M^b_{yy}, M^b_{xy}) = \int_{-h/2}^{h/2} z(\sigma_{xx}, \sigma_{yy}, \sigma_{xy}) dz \tag{23}$$

$$(M^s_{xx}, M^s_{yy}, M^s_{xy}) = \int_{-h/2}^{h/2} f(z)(\sigma_{xx}, \sigma_{yy}, \sigma_{xy}) dz \tag{24}$$

$$(Q_x, Q_y) = \int_{-h/2}^{h/2} g(z)(\sigma_{xz}, \sigma_{yz}) dz \tag{25}$$

The variation of kinetic energy is given by:

$$\delta K = \int_A \begin{bmatrix} I_0(\dot{u}_0 \delta \dot{u}_0 + \dot{v}_0 \delta \dot{v}_0 + \dot{w}_0 \delta \dot{w}_0) \\ -I_1\left(\dot{u}_0\dfrac{\partial \delta \dot{w}_0}{\partial x} + \dfrac{\partial \dot{w}_0}{\partial x}\delta \dot{u}_0 + \dot{v}_0\dfrac{\partial \delta \dot{w}_0}{\partial y} + \dfrac{\partial \dot{w}_0}{\partial y}\delta \dot{v}_0\right) \\ +I_2\left(\dfrac{\partial \dot{w}_0}{\partial x}\dfrac{\partial \delta \dot{w}_0}{\partial x} + \dfrac{\partial \dot{w}_0}{\partial y}\dfrac{\partial \delta \dot{w}_0}{\partial y}\right) \\ -J_1\left(\dot{u}_0\dfrac{\partial \delta \dot{\phi}}{\partial x} + \dfrac{\partial \dot{\phi}}{\partial x}\delta \dot{u}_0 + \dot{v}_0\dfrac{\partial \delta \dot{\phi}}{\partial y} + \dfrac{\partial \dot{\phi}}{\partial y}\delta \dot{v}_0\right) \\ +K_2\left(\dfrac{\partial \dot{\phi}}{\partial x}\dfrac{\partial \delta \dot{\phi}}{\partial x} + \dfrac{\partial \dot{\phi}}{\partial y}\dfrac{\partial \delta \dot{\phi}}{\partial y}\right) \\ +J_2\left(\dfrac{\partial \dot{w}_0}{\partial x}\dfrac{\partial \delta \dot{\phi}}{\partial x} + \dfrac{\partial \dot{\phi}}{\partial x}\dfrac{\partial \delta \dot{w}_0}{\partial x} + \dfrac{\partial \dot{w}_0}{\partial y}\dfrac{\partial \delta \dot{\phi}}{\partial y} + \dfrac{\partial \dot{\phi}}{\partial y}\dfrac{\partial \delta \dot{w}_0}{\partial y}\right) \end{bmatrix} dA \tag{26}$$

where the inertia terms are:

$$(I_0, I_1, I_2) = \int_{-h/2}^{h/2} (1, z, z^2)\rho(z)dz \tag{27}$$

$$(J_1, J_2, K_2) = \int_{-h/2}^{h/2} (f(z), zf(z), f^2(z))\rho(z)dz \tag{28}$$

Applying integration by parts and collecting coefficients, the equations of motion are obtained:

$$\delta u_0 : \quad \frac{\partial N_{xx}}{\partial x} + \frac{\partial N_{xy}}{\partial y} = I_0\ddot{u}_0 - I_1\frac{\partial \ddot{w}_0}{\partial x} - J_1\frac{\partial \ddot{\phi}}{\partial x} \tag{29}$$

$$\delta v_0 : \quad \frac{\partial N_{xy}}{\partial x} + \frac{\partial N_{yy}}{\partial y} = I_0\ddot{v}_0 - I_1\frac{\partial \ddot{w}_0}{\partial y} - J_1\frac{\partial \ddot{\phi}}{\partial y} \tag{30}$$

$$\begin{aligned}\delta w_0 : \quad & \frac{\partial^2 M^b_{xx}}{\partial x^2} + 2\frac{\partial^2 M^b_{xy}}{\partial x \partial y} + \frac{\partial^2 M^b_{yy}}{\partial y^2} \\ & = I_0\ddot{w}_0 + I_1\left(\frac{\partial \ddot{u}_0}{\partial x} + \frac{\partial \ddot{v}_0}{\partial y}\right) - I_2\nabla^2\ddot{w}_0 - J_2\nabla^2\ddot{\phi}\end{aligned} \tag{31}$$

$$\begin{aligned}\delta \phi : \quad & \frac{\partial^2 M^s_{xx}}{\partial x^2} + 2\frac{\partial^2 M^s_{xy}}{\partial x \partial y} + \frac{\partial^2 M^s_{yy}}{\partial y^2} + \frac{\partial Q_x}{\partial x} + \frac{\partial Q_y}{\partial y} \\ & = J_1\left(\frac{\partial \ddot{u}_0}{\partial x} + \frac{\partial \ddot{v}_0}{\partial y}\right) - J_2\nabla^2\ddot{w}_0 - K_2\nabla^2\ddot{\phi}\end{aligned} \tag{32}$$

where $\nabla^2 = \frac{\partial^2}{\partial x^2} + \frac{\partial^2}{\partial y^2}$ is the Laplacian operator. The stress resultants are expressed in terms of strains as:

$$\begin{Bmatrix} \mathbf{N} \\ \mathbf{M}^b \\ \mathbf{M}^s \end{Bmatrix} = \begin{bmatrix} \mathbf{A} & \mathbf{B} & \mathbf{B}^s \\ \mathbf{B} & \mathbf{D} & \mathbf{D}^s \\ \mathbf{B}^s & \mathbf{D}^s & \mathbf{H}^s \end{bmatrix} \begin{Bmatrix} \boldsymbol{\epsilon}^0 \\ \boldsymbol{\kappa}^b \\ \boldsymbol{\kappa}^s \end{Bmatrix} \tag{33}$$

with stiffness coefficients:

$$(\mathbf{A}, \mathbf{B}, \mathbf{D}, \mathbf{B}^s, \mathbf{D}^s, \mathbf{H}^s) = \int_{-h/2}^{h/2} (1, z, z^2, f(z), zf(z), f^2(z))\mathbf{C}(z)dz \tag{34}$$

The transverse shear forces are:

$$\begin{Bmatrix} Q_x \\ Q_y \end{Bmatrix} = \begin{bmatrix} A^s_{55} & 0 \\ 0 & A^s_{44} \end{bmatrix} \begin{Bmatrix} \gamma^0_{xz} \\ \gamma^0_{yz} \end{Bmatrix} \tag{35}$$

where the shear stiffness components are:

$$A_{44}^s = A_{55}^s = \int_{-h/2}^{h/2} g^2(z) C_{44}(z) dz \tag{36}$$

Analytical solution for simply-supported FG plates

The Navier solution technique is employed to obtain analytical solutions for simply-supported boundary conditions. The displacement functions are expressed as:

$$u_0(x,y,t) = \sum_{m=1}^{\infty}\sum_{n=1}^{\infty} u_{mn}^0 \cos\lambda x \sin\mu y e^{i\omega t} \tag{37}$$

$$v_0(x,y,t) = \sum_{m=1}^{\infty}\sum_{n=1}^{\infty} v_{mn}^0 \sin\lambda x \cos\mu y e^{i\omega t} \tag{38}$$

$$w_0(x,y,t) = \sum_{m=1}^{\infty}\sum_{n=1}^{\infty} w_{mn}^0 \sin\lambda x \sin\mu y e^{i\omega t} \tag{39}$$

$$\phi(x,y,t) = \sum_{m=1}^{\infty}\sum_{n=1}^{\infty} \phi_{mn}^0 \sin\lambda x \sin\mu y e^{i\omega t} \tag{40}$$

where $\lambda = m\pi/a$, $\mu = n\pi/b$, ω is the natural frequency, and $i = \sqrt{-1}$. Substituting these into the equations of motion yields the eigenvalue problem:

$$\left(\begin{bmatrix} k_{11} & k_{12} & k_{13} & k_{14} \\ k_{12} & k_{22} & k_{23} & k_{24} \\ k_{13} & k_{23} & k_{33}+\alpha & k_{34} \\ k_{14} & k_{24} & k_{34} & k_{44} \end{bmatrix} - \omega^2 \begin{bmatrix} m_{11} & 0 & m_{13} & m_{14} \\ 0 & m_{22} & m_{23} & m_{24} \\ m_{13} & m_{23} & m_{33} & m_{34} \\ m_{14} & m_{24} & m_{34} & m_{44} \end{bmatrix} \right) \begin{Bmatrix} u_{mn}^0 \\ v_{mn}^0 \\ w_{mn}^0 \\ \phi_{mn}^0 \end{Bmatrix} = \begin{Bmatrix} 0 \\ 0 \\ 0 \\ 0 \end{Bmatrix} \tag{41}$$

where the stiffness and mass matrix components are defined as:

$$\begin{aligned} k_{11} &= A_{11}\lambda^2 + A_{66}\mu^2 \\ k_{12} &= (A_{12} + A_{66})\lambda\mu \\ k_{13} &= -B_{11}\lambda^3 - (B_{12} + 2B_{66})\lambda\mu^2 \\ k_{14} &= -B_{11}^s\lambda^3 - (B_{12}^s + 2B_{66}^s)\lambda\mu^2 \\ k_{22} &= A_{66}\lambda^2 + A_{22}\mu^2 \\ k_{23} &= -B_{22}\mu^3 - (B_{12} + 2B_{66})\lambda^2\mu \end{aligned}$$

$$
\begin{aligned}
k_{24} &= -B_{22}^s\mu^3 - (B_{12}^s + 2B_{66}^s)\lambda^2\mu \\
k_{33} &= D_{11}\lambda^4 + 2(D_{12} + 2D_{66})\lambda^2\mu^2 + D_{22}\mu^4 \\
k_{44} &= H_{11}^s\lambda^4 + 2(H_{12}^s + 2H_{66}^s)\lambda^2\mu^2 + A_{55}^s\lambda^2 + A_{44}^s\mu^2 + H_{22}^s\mu^4 \\
m_{11} &= m_{22} = I_0 \\
m_{13} &= -\lambda I_1 \\
m_{14} &= -\lambda J_1 \\
m_{23} &= -\mu I_1 \\
m_{24} &= -\mu J_1 \\
m_{33} &= I_0 + I_2(\lambda^2 + \mu^2) \\
m_{34} &= J_2(\lambda^2 + \mu^2) \\
m_{44} &= K_2(\lambda^2 + \mu^2) \\
\alpha &= -N_0(\lambda^2 + \gamma\mu^2)
\end{aligned}
$$

Numerical results and discussion

Comparisons and validation

This study examines a simply supported functionally graded (FG) rectangular plate with dimensions a (length) and b (width). Two material combinations are investigated: Al/Al_2O_3 and Al/ZrO_2, with their properties detailed in Table 1.

Table 1 – Material properties of metal and ceramic constituents

Material	Young's modulus (GPa)	Mass density (kg/m^3)	Poisson's ratio
Aluminum (Al)	70	2,702	0.3
Zirconia (ZrO_2)	151	3,000	0.3
Alumina (Al_2O_3)	380	3,800	0.3

The research presents numerical validation and explores how the power-law index (p) and side-to-thickness ratio (a/h) influence the natural frequencies of FG plates. Non-dimensional frequency parameters are employed throughout:

$$\overline{\omega} = \frac{\omega a^2}{h}\sqrt{\frac{\rho_c}{E_c}} \tag{42}$$

$$\overline{\beta} = \frac{\omega ab}{\pi^2 h}\sqrt{\frac{12(1-\nu_c^2)\rho_c}{E_c}} \tag{43}$$

Tables 2 and 3 present comparative analyses of non-dimensional frequencies for FG square plates. Table 2 focuses on Al/Al_2O_3 plates, while Table 3 examines Al/ZrO_2 plates, both showcasing results for various power-law indices (p) and aspect ratios.

Table 2 – Non-dimensional natural frequencies ($\overline{\omega}$) of Al/Al_2O_3 square plates

l/h	Mode (m,n)	Theory	p					
			0	0.5	1	2	5	10
5	(1,1)	Nguyen (2015)	5.2932	4.5258	4.0860	3.6859	3.3919	3.2574
		Present	5.2817	4.5248	4.0932	3.7023	3.4088	3.9730
	(1,2)	Nguyen (2015)	11.6113	10.0109	9.0538	8.1181	7.2951	6.9568
		Present	11.5590	9.9833	9.0404	8.1226	7.3120	9.8089
	(2,2)	Nguyen (2015)	16.8351	14.5888	13.2140	11.8101	10.4647	9.9360
		Present	16.7275	14.5031	13.1210	11.7231	10.4234	9.8591
10	(1,1)	Nguyen (2015)	5.7731	4.9031	4.4216	4.0105	3.7671	3.6388
		Present	5.7695	4.9209	4.4629	4.0743	3.8198	3.6644
	(1,2)	Nguyen (2015)	13.7855	11.7519	10.6036	9.5884	8.9042	8.5729
		Present	13.7656	11.7807	10.6840	9.7180	9.0138	8.6192
	(2,2)	Nguyen (2015)	21.1728	18.1033	16.3438	14.7435	13.5677	13.0296
		Present	21.1270	18.0995	16.3728	14.8092	13.6354	13.0383
20	(1,1)	Nguyen (2015)	5.9209	5.0176	4.5234	4.1104	3.8880	3.7629
		Present	5.9198	5.0490	4.5923	4.2145	3.9730	3.8075
	(1,2)	Nguyen (2015)	14.6131	12.3983	11.1785	10.1482	9.5645	9.2471
		Present	14.6073	12.4863	11.3767	10.4479	9.8089	9.3740
	(2,2)	Nguyen (2015)	23.0925	19.6126	17.6865	16.0419	15.0685	14.5550
		Present	23.0781	19.6839	17.8519	16.2972	15.2792	14.6576

Table 3 – Comparison of non-dimensional fundamental frequency ($\overline{\beta}$) of Al/ZrO_2 square plates

l/h	Theory	p							
		0	0.1	0.2	0.5	1	2	5	10
5	Present	1.7684	1.7218	1.6827	1.5984	1.5226	1.4617	1.4067	1.3695
	Nguyen (2015)	1.7723	1.7241	1.6850	1.6003	1.5245	1.4629	1.4084	1.3726
	Sekkal (et al.)	1.7723	1.7256	1.6866	1.6040	1.5297	1.4691	1.4121	1.3743
10	Present	1.9317	1.8787	1.8347	1.7420	1.6623	1.6034	1.5522	1.5096
	Nguyen (2015)	1.9330	1.8783	1.8342	1.7402	1.6593	1.5994	1.5500	1.5095
	Sekkal (et al.)	1.9330	1.8799	1.8361	1.7445	1.6657	1.6071	1.5548	1.5116
20	Present	1.9820	1.9270	1.8815	1.7868	1.7069	1.6493	1.5991	1.5542
	Nguyen (2015)	1.9824	1.9257	1.8799	1.7830	1.7006	1.6417	1.5945	1.5524
	Sekkal (et al.)	1.9824	1.9273	1.8819	1.7875	1.7075	1.6500	1.5996	1.5547
50	Present	1.9970	1.9414	1.8957	1.8008	1.7215	1.6646	1.6142	1.5680
	Nguyen (2015)	1.9971	1.9398	1.8935	1.7957	1.7129	1.6544	1.6079	1.5653
	Sekkal (et al.)	1.9971	1.9414	1.8955	1.8002	1.7199	1.6628	1.6131	1.5676
100	Present	1.9992	1.9435	1.8978	1.8032	1.7241	1.6675	1.6168	1.5702
	Nguyen (2015)	1.9993	1.9418	1.8955	1.7975	1.7147	1.6562	1.6098	1.5671
	Sekkal (et al.)	1.9993	1.9434	1.8974	1.8021	1.7216	1.6646	1.6150	1.5694

The results demonstrate excellent agreement with established theories by Nguyen (2015) and Sekkal et al. (2017), validating the accuracy of the

novel shape function approach. This analysis confirms the method's reliability and its ability to capture the effects of geometric ratios and material gradation on FG plate vibration characteristics.

Parametric study

Effect of side-to-thickness ratio (a/h) and porosity (α)

Figure 2 illustrates the significant impact of side-to-thickness ratio (a/h) and porosity (α) on the frequencies of square plates. As a/h increases, both natural ($\overline{\omega}$) and fundamental ($\overline{\beta}$) frequencies rise, with the effect being more pronounced at lower ratios. For instance, as a/h increases from 5 to 100, $\overline{\omega}$ increases from 3.70 to 4.29 for non-porous plates.

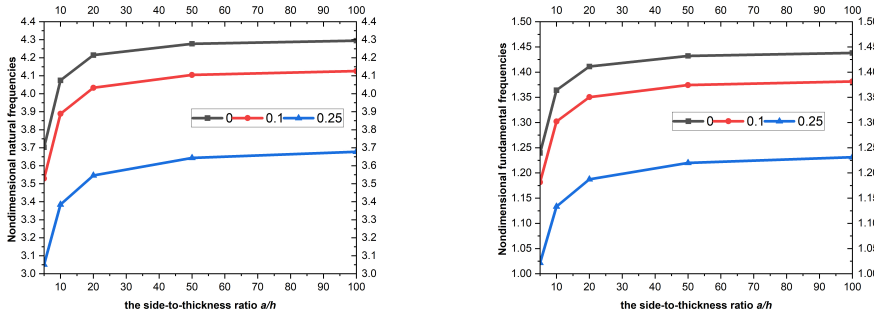

(a) Natural frequency ($\overline{\omega}$) *(b) Fundamental frequency ($\overline{\beta}$)*

Figure 2 – Effect of a/h and α on frequencies of Al/Al$_2$O$_3$ plates ($p = 2$)

Porosity reduces both frequency types consistently across all a/h ratios. At $a/h = 5$, $\overline{\omega}$ decreases from 3.70 to 3.05 as α increases from 0 to 0.25. The combined effect shows that while higher a/h ratios maintain higher frequencies, increased porosity mitigates this effect.

Effect of aspect ratio (a/b) and porosity (α)

Figure 3 demonstrates the influence of aspect ratio (a/b) and porosity on frequencies. As a/b increases, both frequency types rise substantially. When a/b increases from 1 to 10, $\overline{\omega}$ increases from 4.07 to 107.15 for non-porous plates.

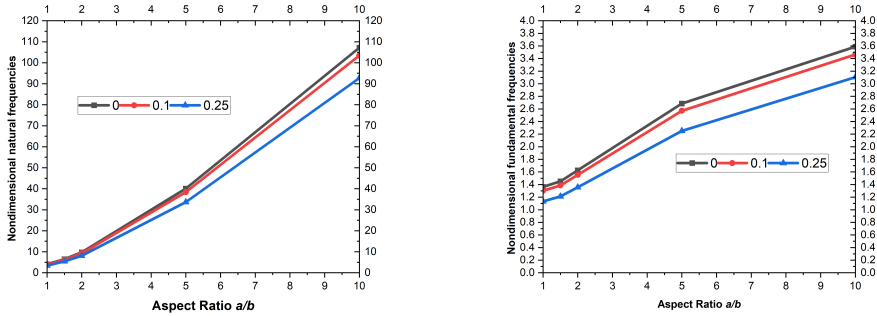

(a) Natural frequency ($\overline{\omega}$) *(b) Fundamental frequency ($\overline{\beta}$)*

Figure 3 – Effect of a/b and α on frequencies of Al/Al$_2$O$_3$ plates ($p = 2$)

Figure 4 provides a three-dimensional visualization of the aspect ratio and porosity effects. The nonlinear increase in $\overline{\omega}$ is particularly evident at higher aspect ratios. Porosity consistently reduces frequencies across all aspect ratios, with $\overline{\omega}$ decreasing from 4.07 to 3.38 at $a/b = 1$ as α increases from 0 to 0.25.

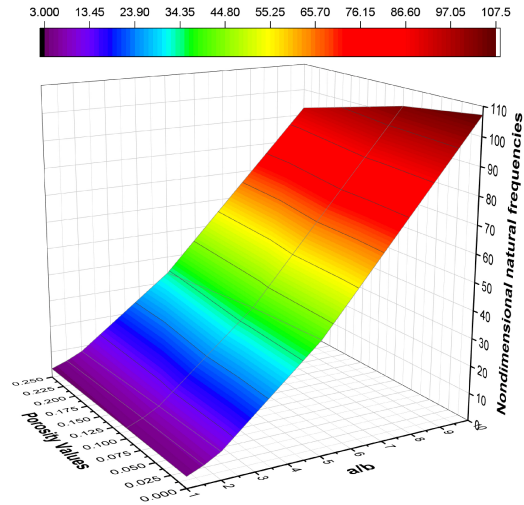

Figure 4 – 3D visualization of the effect of a/b and α on the natural frequency $\overline{\omega}$ for Al/Al$_2$O$_3$ plates ($p = 2$)

Effect of power-law index (p) and porosity (α)

Figure 5 shows the influence of power-law index (p) and porosity on frequencies. As p increases, both frequency types decrease. With $\alpha = 0$, $\overline{\omega}$ decreases from 5.77 at $p = 0$ to 3.22 at $p = 50$.

The rate of decline is most pronounced at lower p values. Porosity consistently reduces frequencies across all p values, with the most significant reductions occurring at higher p values. The combined effect shows a compounded frequency decrease, with the lowest $\overline{\omega} = 2.09$ occurring at $p = 50$ and $\alpha = 0.25$.

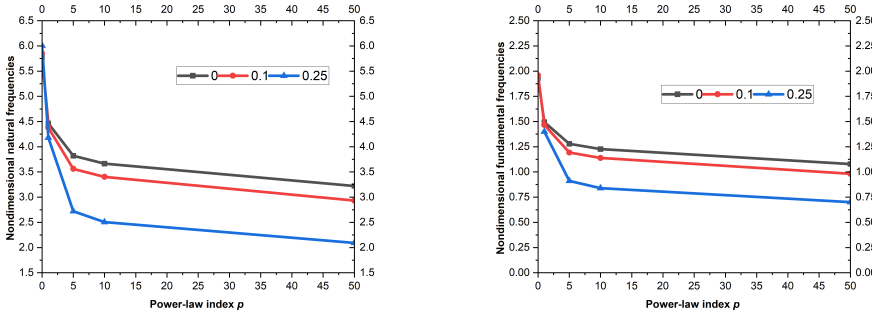

(a) Natural frequency ($\overline{\omega}$) *(b) Fundamental frequency ($\overline{\beta}$)*

Figure 5 – Effect of p and α on frequencies of Al/Al$_2$O$_3$ plates

Effect of mode shapes (m, n) and porosity (α)

Figure 6 illustrates the impact of mode shapes and porosity on natural frequency. As mode numbers increase, $\overline{\omega}$ rises substantially. With $\alpha = 0$, $\overline{\omega}$ increases from 4.46 for (1,1) to 31.50 for (4,1). Porosity reduces $\overline{\omega}$ uniformly across all modes. For mode (2,1), $\overline{\omega}$ decreases from 10.61 at $\alpha = 0$ to 9.89 at $\alpha = 0.25$. The reduction is more significant in absolute terms for higher modes, though the relative reduction remains consistent across modes.

These findings emphasize the need for balanced design approaches that optimize both geometric parameters (a/h, a/b), material composition (p), and porosity (α) to achieve desired vibrational characteristics in engineering applications.

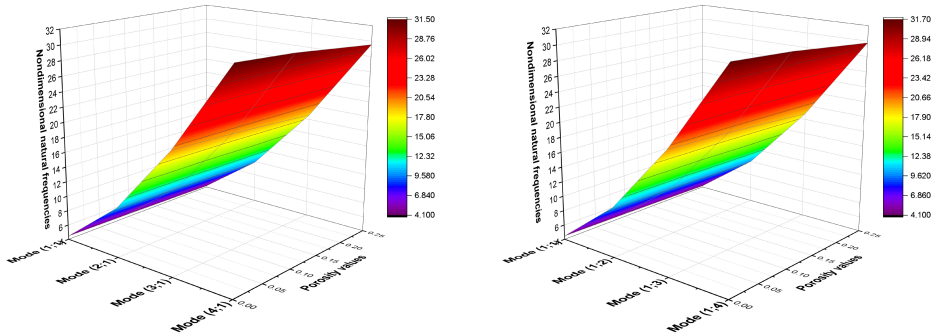

(a) Mode (1,1) to (4,1) *(b) Mode (1,1) to (1,4)*

Figure 6 – Effect of mode shapes and α on $\overline{\omega}$ (Al/Al$_2$O$_3$ plates)

Conclusion

In this study, the natural vibration behavior of porous functionally graded (FG) plates was thoroughly investigated using a novel shape function. A higher-order shear deformation theory (HSDT) was adopted to capture the variation of material properties through the plate thickness using a power-law distribution. Additionally, the inclusion of a porosity model allowed for the assessment of how void content affects the mechanical performance of the plates.

By applying the Navier solution technique, analytical solutions were obtained for simply supported FG plates. A comprehensive parametric study was conducted, considering the effects of power-law index, side-to-thickness ratio, aspect ratio, and porosity on the natural frequencies. The proposed shape function proved effective in precisely modeling the dynamic behavior of porous FG plates.

The results demonstrated that both material gradation and porosity significantly influence the vibrational response of FG structures. These findings provide valuable insights for engineers and researchers in optimizing the design and performance of FG plates in advanced structural applications. The proposed methodology serves as a reliable analytical tool for predicting the dynamic response of such advanced composite systems.

References

Adhikari, B. & Singh, B.N. 2019. Dynamic response of functionally graded plates resting on two-parameter-based elastic foundation model using a quasi-3D theory. *Mechanics Based Design of Structures and Machines*, 47(4), pp.399–429. Available at: https://doi.org/10.1080/15397734.2018.1555965

Berkia, A., Rebai, B., Litouche, B., Abbas, S. & Mansouri, K. 2023. Investigating parametric homogenization models for natural frequency of FGM nano beams. *AIMS Materials Science*, 10(5). Available at: https://doi.org/10.3934/matersci.2023048

Boutrid, A., Rebai, B., Mamen, B., Bouhadra, A. & Tounsi, A. 2024. Combined effect of temperature dependent material properties and boundary conditions on non-linear thermal stability of porous FG beams. *Acta Mechanica*, 235(5), pp.2867–2887. Available at: https://doi.org/10.1007/s00707-024-03860-y

Chitour, M., Khadraoui, F., Mansouri, K., Rebai, B., Menasria, A., Zemmouri, A., ... & Boumediri, H. 2024. A novel high order theory for static bending of functionally graded (FG) beams subjected to various mechanical loads. *Research on Engineering Structures and Materials*, 10. Available at: http://dx.doi.org/10.17515/resm2024.141me0104rs

Choudhary, P.K., Kumar, R. & Kumar, S. 2023. Free Vibration Response of Functionally Graded Porous Metallic Plates Embedded with Piezoelectric Layers. *Journal of Mines, Metals & Fuels*, 71(10). Available at: http://dx.doi.org/10.18311/jmmf/2023/35867

Cho, J.R. 2022. Natural Element Static and Free Vibration Analysis of Functionally Graded Porous Composite Plates. *Applied Sciences*, 12(22), 11648. Available at: https://doi.org/10.3390/app122211648

Gupta, A. & Talha, M. 2018. Influence of porosity on the flexural and free vibration responses of functionally graded plates in thermal environment. *International Journal of Structural Stability and Dynamics*, 18(01), 1850013. Available at: https://doi.org/10.1142/S021945541850013X

Huang, X., Wang, C., Wang, J. & Wei, N. 2022. Nonlinear vibration analysis of functionally graded porous plates reinforced by graphene platelets on nonlinear elastic foundations. *Strojniški vestnik-Journal of Mechanical Engineering*, 68(9), pp.571-582. Available at: https://doi.org/10.5545/sv-jme.2022.274

Kurpa, L. & Shmatko, T. 2024. Research of Vibration Behavior of Porous FGM Panels by the Ritz Method. In *Selected Problems of Solid Mechanics and Solving Methods* (pp. 325-338). Cham: Springer Nature Switzerland. Available at: https://doi.org/10.1007/978-3-031-54063-9_22

Lazar, M.E., Ezzraimi, M., Tiberkak, R., Chiker, Y., Bachene, M. & Rechak, S. 2023. Vibration analysis of composite plates reinforced CNTs using an exponential function approach. *Materials Science and Technology*, 39(17), pp.2680-2689. Available at: https://doi.org/10.1080/02670836.2023.2213975

Lee, S.J. & Han, S.E. 2001. Free-vibration analysis of plates and shells with a nine-node assumed natural degenerated shell element. *Journal of Sound and Vibration*, 241(4), pp.605-633. Available at: https://doi.org/10.1006/jsvi.2000.3313

Matsunaga, H. 2008. Free vibration and stability of functionally graded shallow shells according to a 2D higher-order deformation theory. *Composite structures*, 84(2), pp.132-146. Available at: https://doi.org/10.1016/j.compstruct.2007.07.006

Messas, T., Rebai, B., Mansouri, K., Chitour, M., Berkia, A. & Litouche, B. 2023. Analyzing vibration behavior of Nano FGM (Si_3N_4/SUS304) plates: Impact of homogenization models and nano parameters. *Journal of Nano- and Electronic Physics*, 15(6), 06018. Available at: https://doi.org/10.21272/jnep.15(6).06018

Nguyen, T.K. 2015. A higher-order hyperbolic shear deformation plate model for analysis of functionally graded materials. *International Journal of Mechanics and Materials in Design*, 11(2), pp.203-219. Available at: https://doi.org/10.1007/s10999-014-9260-3

Rebai, B. 2023. Contribution to study the effect of (Reuss, LRVE, Tamura) models on the axial and shear stress of sandwich FGM plate (Ti-6A1-4V/ZrO_2) subjected on linear and nonlinear thermal loads. *AIMS Materials Science*, 10(1). Available at: https://doi.org/10.3934/matersci.2023002

Rebai, B., Mansouri, K., Chitour, M., Berkia, A., Messas, T., Khadraoui, F. & Litouche, B. 2023. Effect of idealization models on deflection of functionally graded material (FGM) plate. *Journal of Nano- and Electronic Physics*, 15(1), 01022. Available at: https://doi.org/10.21272/jnep.15(1).01022

Rezaei, A.S. & Saidi, A.R. 2015. Exact solution for free vibration of thick rectangular plates made of porous materials. *Composite Structures*, 134, pp.1051-1060. Available at: https://doi.org/10.1016/j.compstruct.2015.08.125

Rezaei, A.S., Saidi, A.R., Abrishamdari, M. & Mohammadi, M.P. 2017. Natural frequencies of functionally graded plates with porosities via a simple four variable plate theory: an analytical approach. *Thin-Walled Structures*, 120, pp.366-377. Available at: https://doi.org/10.1016/j.tws.2017.08.003

Sekkal, M., Tounsi, A., Fahsi, B. & Mahmoud, S.R. 2017. A novel and simple higher order shear deformation theory for stability and vibration of functionally graded sandwich plate. *Steel and Composite Structures*, 25(4), pp.389-401. Available at: https://doi.org/10.12989/scs.2017.25.4.389

Sharma, N., Swain, P.K., Maiti, D.K. & Singh, B.N. 2022. Stochastic frequency analysis of laminated composite plate with curvilinear fiber. *Mechanics of Advanced Materials and Structures*, 29(6), pp.933-948. Available at: https://doi.org/10.1080/15376494.2020.1800152

Shmatko, T., Kurpa, L. & Lacarbonara, W. 2023. Nonlinear Free Vibrations of Functionally Graded Porous Sandwich Plates with Complex Shape. In *International Conference on Nonlinear Dynamics and Applications* (pp. 203-215). Cham: Springer Nature Switzerland. Available at: https://doi.org/10.1007/978-3-031-50631-4_18

Swain, P.K., Sharma, N., Maiti, D.K. & Singh, B.N. 2020. Aeroelastic analysis of laminated composite plate with material uncertainty. *Journal of Aerospace Engineering*, 33(1), 04019111. Available at: https://doi.org/10.1061/(ASCE)AS.1943-5525.0001110?

Tiwari, P., Barman, S.K., Maiti, D.K. & Maity, D. 2019. Free vibration analysis of delaminated composite plate using 3D degenerated element. *Journal of Aerospace Engineering*, 32(5), 04019070. Available at: https://doi.org/10.1061/(ASCE)AS.1943-5525.0001053

Tiwari, P., Maiti, D.K. & Maity, D. 2020. Dynamic analysis of composite cylinders using 3-D degenerated shell elements. In *Recent Advances in Theoretical, Applied, Computational and Experimental Mechanics: Proceedings of ICTACEM 2017* (pp. 261-276). Singapore: Springer Singapore. Available at: https://doi.org/10.1007/978-981-15-1189-9_22

Van Long, N., Quoc, T.H. & Tu, T.M. 2016. Bending and free vibration analysis of functionally graded plates using new eight-unknown shear deformation theory by finite-element method. *International journal of advanced structural engineering*, 8(4), pp.391-399. Available at: https://doi.org/10.1007/s40091-016-0140-y

Vasara, D., Khare, S., Sharma, H.K. & Kumar, R. 2022. Free vibration analysis of functionally graded porous circular and annular plates using differential quadrature method. *Forces in Mechanics*, 9, 100126. Available at: https://doi.org/10.1016/j.finmec.2022.100126

Vel, S.S. & Batra, R.C. 2004. Three-dimensional exact solution for the vibration of functionally graded rectangular plates. *Journal of Sound and Vibration*, 272(3-5), pp.703-730. Available at: https://doi.org/10.1016/S0022-460X(03)00412-7

Zhang, D.G. & Zhou, Y.H. 2008. A theoretical analysis of FGM thin plates based on physical neutral surface. *Computational Materials Science*, 44(2), pp.716-720. Available at: https://doi.org/10.1016/j.commatsci.2008.05.016

Zenkour, A.M. 2005. A comprehensive analysis of functionally graded sandwich plates: Part 2—Buckling and free vibration. *International Journal of Solids and Structures*, 42(18-19), pp.5243-5258. Available at: https://doi.org/10.1016/j.ijsolstr.2005.02.016

Zhao, X., Lee, Y.Y. & Liew, K.M. 2009. Free vibration analysis of functionally graded plates using the element-free kp-Ritz method. *Journal of sound and Vibration*, 319(3-5), pp.918-939. Available at: https://doi.org/10.1016/j.jsv.2008.06.025

Analiza slobodnih vibracija poroznih funkcionalno gradiranih ploča primenom nove funkcije oblika

Billel Rebai[a], **autor za prepisku**, *Tidjani* Messas[a], *Mustapha* Meradjah[b], *Mohammed* Benali Amar[c]

[a] Faculty of Sciences & Technology, Civil Eng Department, University Abbes Laghrour, Khenchela, Algeria

[b] Civil Eng Department, Faculty of Technology, University of Sidi Bel Abbes, Algeria +
Joint Research Team "Nano-Biomaterials and Digital Engineering for Pharmaceutical Applications", Thematic Agency for Research in Science and Technology (ATRST), Algeria

[c] Civil Eng Department, Faculty of Technology, University of Sidi Bel Abbes, Algeria

OBLAST: mehanika, materijali, mašinstvo
KATEGORIJA (TIP) ČLANKA: originalni naučni rad

Sažetak:

Uvod/cilj: Ovo istraživanje uvodi novi analitički okvir za sveobuhvatno ispitivanje prirodnih karakteristika vibracija poroznih funkcionalno gradiranih (FG) ploča. Istraživanje ima za cilj kombinovanje inovativne metodologije funkcije oblika sa naprednim modelom poroznosti u okviru teorije smicajne deformacije višeg reda (eng. HSDT).

Metode: Materijalne karakteristike prate raspodelu po zakonu stepena kroz debljinu, pri čemu su šupljine obuhvaćene unapređenim modelom poroznosti. Diferencijalne jednačine za ploče sa prostim oslanjanjem rešene su analitički primenom Navijeove metode. Parametarskom analizom ispituje se uticaj indeksa zakona stepena, geometrijskih odnosa i raspodele poroznosti.

Rezultati: Rezultati pokazuju izuzetno slaganje sa postojećim teorijama i otkrivaju značajne zavisnosti, pri čemu i indeks zakona stepena i raspodela poroznosti imaju ključan uticaj na sopstvene frekvencije. Dobijeni su novi uvidi u njihove međusobne (spregnute) efekte na vibraciono ponašanje.

Zaključak: Rad omogućava fundamentalno razumevanje optimizacije dizajna poroznih FG ploča u naprednim inženjerskim primenama kao što su vazduhoplovni i konstrukcioni sistemi, gde su smanjenje mase i kontrola vibracija od ključnog značaja. Takođe nudi i praktične smernice za inženjerski dizajn i izbor materijala.

Ključne reči: funkcionalno gradirane ploče, poroznost, sopstvene vibracije, funkcija oblika, Hamiltonov princip, analitičko rešenje.

Paper received on: 8 June 2025.
Manuscript corrections submitted on: 3 October 2025.
Paper accepted for publishing on: 21 November 2025.

© 2026 The Authors. Published by Vojnotehnički glasnik / Military Technical Courier (http://vtg.mod.gov.rs). This article is an open access article distributed under the terms and conditions of the Creative Commons Attribution license (http://creativecommons.org/licenses/by/4.0/rs/).

Vibration of the weapon system on an unmanned ground vehicle during movement

Viet Dung Bui[a], *Martin* Macko[b], *Ba Ngoc* Dang[c], *Huu Nguyen* Pham[d]

[a] University of Defence, Faculty of Military Technology, Department of Weapons and Ammunition, Brno, Czech Republic,
e-mail: vietdung.bui@unob.cz,
ORCID iD: https://orcid.org/0009-0004-9752-9054

[b] University of Defence, Faculty of Military Technology, Department of Weapons and Ammunition, Brno, Czech Republic,
e-mail: martin.macko@unob.cz, **corresponding author**,
ORCID iD: https://orcid.org/0000-0002-3896-0803

[c] University of Defence, Faculty of Military Technology, Department of Weapons and Ammunition, Brno, Czech Republic,
e-mail: bangoc.dang@unob.cz,
ORCID iD: https://orcid.org/0009-0006-0481-4572

[d] Tran Dai Nghia University, Faculty of Ammunition, Department of Explosives and Ballistics, Hochiminh, Socialist Republic of Vietnam,
e-mail: huunguyenvhp@gmail.com,
ORCID iD: https://orcid.org/0009-0004-9615-9426

https://doi.org/10.5937/vojtehg74-61289

FIELD: mechanical engineering
ARTICLE TYPE: original scientific paper

Abstract:

Introduction/purpose: The article presents a mathematical model of the vibration of a weapon mount on a small unmanned ground vehicle (UGV) with a total weight of up to 70 kg, including the weapon. The design of these small vehicles is similar to that of larger combat vehicles: a mount is placed on a wheeled or tracked chassis, allowing the weapon to be elevated and azimuthally adjusted, and if it allows firing while moving, the angular position of the barrel is affected by chassis vibration and should be stabilized. The vibration of the chassis and parts of the weapon mount is not desirable, and the results of vibration simulation allow for the design of a solution that will eliminate it.

Methods: A system of differential equations describing the vibrations of the weapon system and a system of equations describing the motion of the vehicle over terrain were created. Subsequently, the vibrations were simulated in Matlab-Simulink software. Further testing was carried out to

measure the deviation of the camera axis from the center of the target. The results of the experiment were compared with the results of the simulation.

Results: The research results indicate that the vibration of the weapon system on unmanned ground vehicles depends on many factors, such as the road surface profile, tire properties, suspension system, and overall dimensions, layout, and weight of components. The experimental results of camera stability measurements during target tracking correspond to the simulation results in Matlab-Simulink software.

Conclusion: The system of mathematical differential equations of an unmanned ground vehicle, together with the road profile model, describes the factors affecting the vibration of the weapon system during vehicle movement. Mathematical models allow for parameter changes and thus enable simulation of changes in the angular position of the barrel for other input conditions.

Key words: unmanned ground vehicle, weapon system, stabilization, vibration analysis.

Introduction

Unmanned Ground Vehicles (UGVs) are vehicles that move on the ground without human presence on board. These vehicles are equipped with weapon systems used to destroy targets such as enemy forces, fortifications on land and water, as well as low-altitude aerial vehicles, etc. Using UGVs helps avoid human losses, dangers on the battlefield, reduce financial losses and at the same time increase combat effectiveness in modern warfare.

The vehicle has a sensor system to observe the environment. These sensors are electronic devices used to measure the angle of deviation of the barrel in range and direction relative to the target, based on changes in physical processes (pressure, temperature, sound, light, etc.) from the surrounding environment emitted by the target and converted into electrical signals used to send information to the controllers. The controller sends control signals to the servo motors. The servo motor is a closed-loop transmission and feedback system used to create control torque quickly and accurately. The UGV uses two servo motors, one motor to control the azimuth angle and one to control the direction of the barrel. The servo motors control the position, regulate the speed accurately, and adjust the torque appropriately to direct the barrel to the target.

There have been many studies on the mathematical modeling and simulation of weapon system vibrations on main battle tanks, however, these studies have not yet specifically calculated the influence of the road surface profile when the vehicle is in motion, nor have they sufficiently

examined unmanned vehicles. Abdeselem et al. (2024) developed a mathematical model and simulated the suspension system of a half vehicle in the roll plane with four degrees of freedom. The study focused on the influence of the suspension system on vehicle performance characteristics such as ride comfort, road holding, and working space. The study by Karayumak (2011) was conducted under experimental conditions at Aberdeen Proving Ground (APG), focusing on a main battle tank moving on a bumpy road surface and during turning maneuvers. The experimental data measured on the computer are the input factors for the simulation problems. Ambarish et al. (2017) focused on developing a mathematical model of the elevation dynamics of a tracked vehicle using a half-vehicle model. Differential equations were developed for the weapon system using the state-space approach, simulating the elevation dynamic on the half-vehicle body. The elevation dynamic model of the weapon system includes three degrees of freedom, generated from the rotational dynamics of the drive, breech section and muzzle section. Then, backstepping, LQR (Linear Quadratic Regulator) and PID control techniques were integrated into the state space matrix for the coupled dynamic model, in which the control parameters were determined through different iterations. David (2001), Hallbeck (2021) developed mathematical equations of motion for the weapon system on a tracked vehicle with a suspension system, based on rotation matrices. The above authors have measured and calculated the actual model and then simulated the vibration system. The unmanned vehicle is a combination of a suspension system, azimuth drive, elevation drive and firing system. These are the parameters that determine the stability of the barrel. The suspension system of the vehicle body helps the vehicle move smoothly, reducing vibrations on uneven terrain. The azimuth drive has the effect of transmitting the rotation of the turret in the horizontal plane, while the elevation drive rotates the barrel in the vertical plane with the help of an electric motor driving the reduction gear. The barrel rotates in the vertical plane created by the electric motor connected to the turret ring, as described by Hallbeck (2021) and Cagil (2016).

This study develops a system of mathematical equations of a vehicle with seven degrees of freedom, combined with a six-degree-of-freedom azimuth dynamics model and five-degree-of-freedom elevation dynamics model. In the experimental section, this paper employs the DJI RoboMaster S1 platform to measure the deviation of the camera center during a human target-tracking task. A gimbal-mounted camera is used to continuously orient the lens toward the moving target. The tracking process is conducted in a real-world environment, with the target being a person moving freely in various directions and at different speeds. The

image coordinates of the target's center are continuously recorded using an object detection algorithm and compared with the center coordinates of the camera frame. The deviation is quantified as the Euclidean distance between the target's center and the frame center and it is collected across multiple time samples for analysis. Experimental results show that the deviation increases significantly when the target moves rapidly or changes direction abruptly, particularly during moments when the gimbal system has not yet fully compensated. The collected data play an important role in evaluating the gimbal controller's performance and optimizing the tracking algorithm to enhance system stability and accuracy. Moreover, these experimental results can also be applied to assess the vibrations of a weapon system mounted on an unmanned ground vehicle, under the influence of terrain conditions, vehicle speed, direction of motion, and dynamic torque disturbances from the actuator.

Mathematical model

Mathematical model of the unmanned vehicle

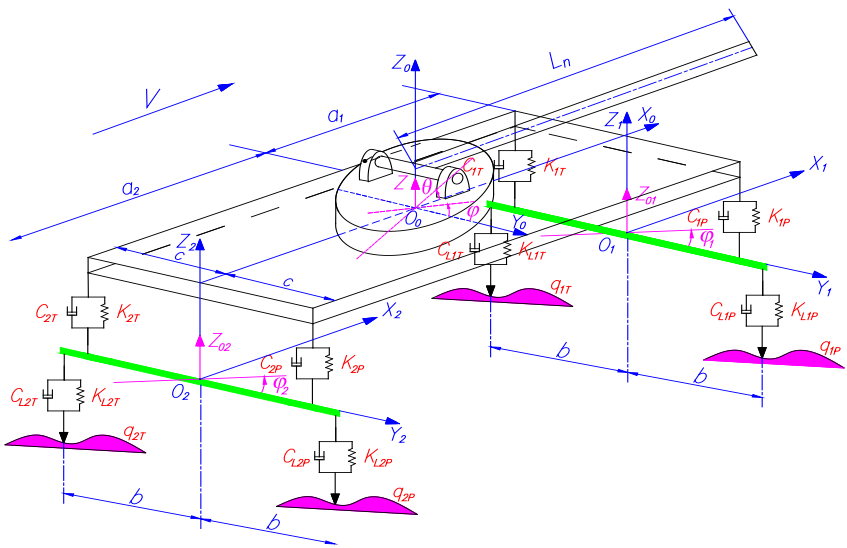

Figure 1 - Unmanned vehicle model

The research model includes the following elements: vehicle body, turret, barrel, front axle, and rear axle (Bui et al, 2024).

The model uses three coordinate systems. The $O_0X_0Y_0Z_0$ coordinate system is located at the center of gravity of the vehicle body, the $O_1X_1Y_1Z_1$

coordinate system is located at the center of gravity of the front axle, whereas the $O_2X_2Y_2Z_2$ coordinate system is located at the center of gravity of the rear axle.

Symbols: q_{1T}, q_{1P}, q_{2T}, q_{2P} denote the roughness of the road surface at the contact points with the front and rear tires on the left and right sides.

C_{L1T}, K_{L1T}, C_{L1P}, K_{L1P}, C_{L2T}, K_{L2T}, C_{L2P}, K_{L2P} denote the damping coefficient and elasticity coefficient of the front and rear tires on the left and right sides.

C_{1T}, K_{1T}, C_{1P}, K_{1P}, C_{2T}, K_{2T}, C_{2P}, K_{2P} denote the coefficient and elasticity coefficient of the front and rear suspension on the left and right sides.

a_1, a_2 denote the distance from the center of gravity of the vehicle body to the front axle and rear axle; $2b$ denotes the average distance between the right and left wheel tracks; $2c$ denotes the average distance between left and right suspension; Z_{01}, φ_1, Z_{02}, φ_2 denote the vertical displacement and roll angle of the front and rear axles; Z_0, φ, θ denote the vertical displacement, roll angle, pitch angle of the vehicle body; L_n denotes the barrel length; $L=a_1+a_2$ denote the standard long; V is the vehicle speed.

$F_{CL1T}, F_{KL1T}, F_{CL1P}, F_{KL1P}, F_{CL2T}, F_{KL2T}, F_{CL2P}, F_{KL2P}$ denote the damping and elastic force of the front and rear tires on the left and right.

$F_{C1T}, F_{K1T}, F_{C1P}, F_{K1P}, F_{C2T}, F_{K2T}, F_{C2P}, F_{K2P}$ denote the damping and elastic force of the front and rear suspension on the left and right.

Road surface function equation

The article uses the Inverse Fourier Transform method based on ISO 8608:2016 to represent the road surface profile over time.

The height of the road surface profile over time is determined by the following formula (Liangkuan et al, 2023; Bui et al, 2025):

$$q_{(t)} = \sum_{i=1}^{n} \sqrt{4 S_q \Delta\Omega \cos\left(\Omega_i t + \gamma_i\right)} \tag{1}$$

where: $q_{(t)}$ is the height of the road surface bump, S_q is the power spectral density of the road surface bump according to ISO 8608:2016, Ω_i is the spatial frequency of the road surface profile, $\Delta\Omega$ is the point distance divided by spatial frequency calculated according to the simulation path length L, γ_i is the initial phase, which is random and usually chosen according to a uniform distribution in the interval [0,2π], n is the upper limit of the sum, representing the number of components taken to approximate the amplitude of the rough pavement surface. It indicates the

number of spatial frequencies considered when calculating the pavement profile. The larger the value of n, the more accurate the model is in representing the actual pavement surface.

The power spectrum of the pavement is determined by the following formula (Liangkuan et al, 2023):

$$S_q(\Omega) = \begin{cases} S_{q(\Omega_0)} \left(\dfrac{\Omega}{\Omega_0} \right)^{-w} & \Omega_1 \le \Omega \le \Omega_2 \\ 0 & \Omega < \Omega_1;\ \Omega > \Omega_2 \end{cases} \quad (2)$$

where: Ω_1, Ω_2 are spatial frequency limits determined from the time-frequency range f_1, f_2 and the vehicle's speed V in the direction X.

$$\Omega_1 = f_1 / V; \qquad \Omega_2 = f_2 / V \quad (3)$$

Ω_0 is the reference spatial frequency, with $\Omega_0 = 0{,}1\ m^{-1}$, w is the exponent index (usually $w = 2$), and $S_{q(\Omega_0)}$ is determined based on the ISO 8608:2016 standard presented in Table 1.

Table 1 - Power spectrum density by road surface levels

Road surface levels	$S_{q(\Omega_0)}(10^{-6} m^2/m^{-1})$ with Ω_0 = 0.1 (m^{-1})			$S_{q(\Omega)}(10^{-6} m^2/m^{-1})$ with 0.011m^{-1}≤Ω≤ 2.83m^{-1}		
	Lower bound	Average	Upper bound	Lower bound	Average	Upper bound
A	8	16	31	2.69	3.81	5.38
B	32	64	128	5.38	7.61	10.77
C	128	256	512	10.77	15.23	21.53
D	512	1024	2048	21.53	30.45	43.06
E	2048	4096	8192	43.06	60.90	86.13
F	8192	16284	32768	86.13	121.80	172.26
G	32768	65536	131072	172.26	243.61	344.52
H	131072	262144	524288	344.52	487.22	689.04

The mathematical equations of the vehicle body

The mathematical model was developed in studies by Bui et al. (2024, 2025), based on previous research by Chen et al. (2012), Yin et al. (2023) and Kim et al. (2024).

$$
\begin{aligned}
&m_1.Z''_{01} = -F_{CL1T} - F_{KL1T} - F_{CL1P} - F_{KL1P} + F_{C1T} + F_{K1T} + F_{C1P} + F_{K1P} \\
&J_{m1}.\varphi''_1 = b\left[\left(F_{CL1T} + F_{KL1T}\right) - \left(F_{CL1P} + F_{KL1P}\right)\right] + c\left[\left(F_{C1P} + F_{K1P}\right) - \left(F_{C1T} + F_{K1T}\right)\right] \\
&m_2 Z''_{02} = -F_{CL2T} - F_{KL2T} - F_{CL2P} - F_{KL2P} + F_{C2T} + F_{K2T} + F_{C2P} + F_{K2P} \\
&J_{m2}.\varphi''_2 = b\left[\left(F_{CL2T} + F_{KL2T}\right) - \left(F_{CL2P} + F_{KL2P}\right)\right] + c\left[\left(F_{C2P} + F_{K2P}\right) - \left(F_{C2T} + F_{K2T}\right)\right] \\
&(M_k + \mathrm{M}_n + \mathrm{M}_t)Z'' = -F_{C1T} - F_{K1T} - F_{C1P} - F_{K1P} - F_{C2T} - F_{K2T} - F_{C2P} - F_{K2P} \\
&(J_{xk} + \mathrm{J}_{xn} + \mathrm{J}_{xt})\varphi'' = c\left[\left(F_{C1T} + F_{K1T}\right) - \left(F_{C1P} + F_{K1P}\right)\right] + c\left[\left(F_{C2T} + F_{K2T}\right) - \left(F_{C2P} + F_{K2P}\right)\right] \\
&(J_{yk} + \mathrm{J}_{yn} + \mathrm{J}_{yt})\theta'' = -a_1\left[\left(F_{C1P} + F_{K1P}\right) + \left(F_{C1T} + F_{K1T}\right)\right] + a_2\left[\left(F_{C2P} + F_{K2P}\right) + \left(F_{C2T} + F_{K2T}\right)\right]
\end{aligned}
\tag{4}
$$

System of equations for elevation dynamics

The kinematic dimensions and diagrams of the forces acting on the elevation dynamics block are given in Figure 2 by Banerjee et al. (2016, 2018), Ambarish et al. (2017), Jitesh (2018) and Bui et al. (2025).

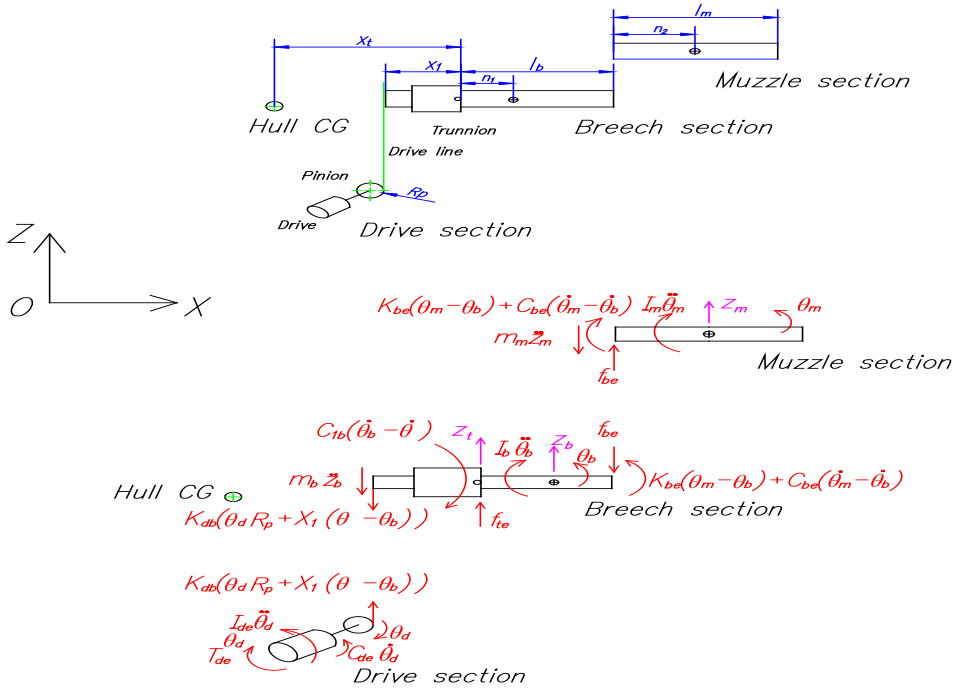

Figure 2 - Diagram of the forces acting on the elevation dynamics

The following symbols are used in the diagram:

$\theta, \theta_d, \theta_b, \theta_m$ represent the roll angle of the vehicle body, the rotation angle of the drive, the rotation angle of the breech section and the muzzle section in the vertical plane;

T_{de}, I_{de}, I_b, I_m are the torsional torque, the mass moment of inertia of the drive, the mass moment of inertia of the breech section and the muzzle section;

K_{db}, K_{be} are the driveline stiffness of rack and pinion arrangement for the elevation and torsional stiffness of the breech section with the muzzle section;

C_{1b}, C_{de}, C_{be} demote the torsional viscous damping coefficient of the trunnion hinge about the OY axis, the torsional viscous damping in the elevation drive, the torsional viscous damping at the connection interface between the breech section and the muzzle section about the OY axis;

m_b, m_m are the mass of the breech section and the muzzle section;

z_b, z_m are the vertical displacement at the center of gravity of the breech section and the muzzle section;

f_{te}, f_{be} denote the reaction force acting at the pivot joint, the reaction force acting at the junction point between the breech section and the muzzle section;

X_t is the distance from the center of gravity of the vehicle body to the axis of rotation of the barrel in the vertical plane;

X_1 is the distance of the transmission line to the axis of rotation;

n_1 is the distance from the axis of rotation to the center of gravity of the breech section;

l_b is the distance from the axis of rotation to the point of junction between the breech section and the muzzle section;

n_2 is the distance from the point of junction of the breech section and the muzzle section to the center of gravity of the muzzle section;

l_m is the length of the muzzle section.

The mathematical model was developed by Bui et al. (2025).

$$
\begin{aligned}
&I_{de}\theta''_d = T_{de} - C_{de}\theta'_d - K_{db}\left[\theta_d R_p + X_1\left(\theta - \theta_b\right)\right]R_p \\
&I_b\theta''_b = -C_{1b}\left(\theta'_d - \theta'\right) - f_{be}\left(l_b - n_1\right) - f_{te}n_1 + K_{be}\left(\theta_m - \theta_b\right) + \\
&\qquad + C_{be}\left(\theta'_m - \theta'_b\right) + K_{db}\left[\theta_d R_p + X_1\left(\theta - \theta_b\right)\right]\left(X_1 + n_1\right) \\
&m_b z''_b = f_{te} - K_{db}\left[\theta_d R_p + X_1\left(\theta - \theta_b\right)\right] - f_{be} \\
&I_m\theta''_m = -f_{be}n_2 - K_{be}\left(\theta_m - \theta_b\right) - C_{be}\left(\theta'_m - \theta'_b\right) \\
&m_m z''_m = f_{be}
\end{aligned}
\tag{5}
$$

System of equations for azimuth dynamics

The force diagram acting on the azimuth dynamics and the symbols used are given in Figure 3, as in Ambarish et al. (2017) and Jitesh (2018).

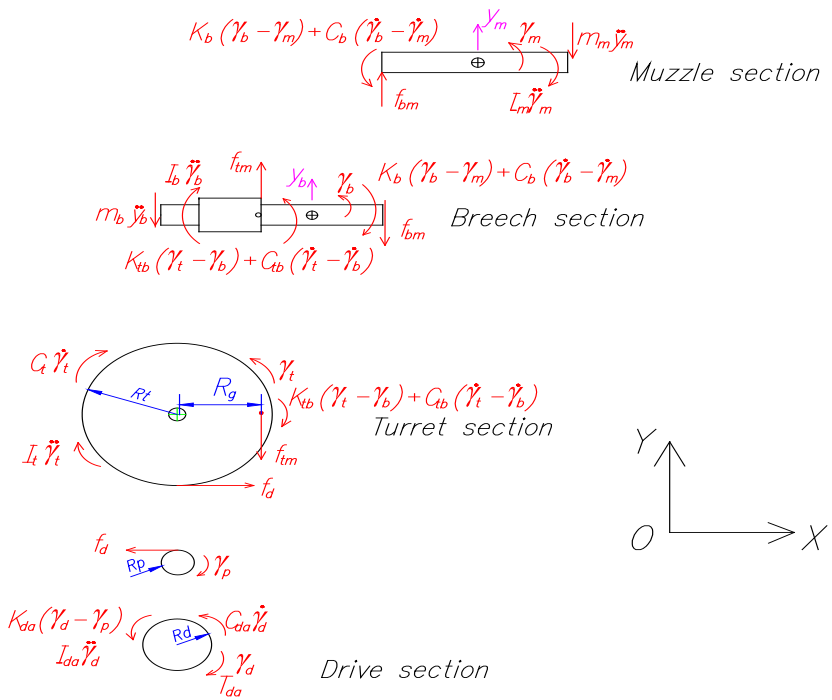

Figure 3 - Diagram of the forces acting on the azimuth dynamics

The symbols used in the figure are as follows:

$\varphi, \gamma_d, \gamma_t, \gamma_b, \gamma_m$ are the pitch angle of the vehicle body, the rotation angle of the drive, the rotation angle of the turret gear ring, the rotation angle of the breech section and the muzzle section in the horizontal plane;

$T_{da}, I_{da}, I_t, I_b, I_m$ are the torsional torque, the mass moment of inertia of the drive, the mass moment of inertia of the turret, the mass moment of inertia of the breech section and the muzzle section;

K_{da} is the torsional stiffness of the azimuth drive, K_{tb} is the torsional stiffness about the OZ axis, at the trunnion interface, connecting the breech section and turret, K_b is the torsional stiffness about the OZ axis at the connection interface between the breech and the muzzle sections;

C_{da} is the torsional viscous damping coefficient in the azimuth drive, C_{tb} is the torsional viscous damping about the OZ axis, at the trunnion interface, connecting the gun breech section and the turret;

C_b is the torsional viscous damping about the OZ axis, at the connection interface between the breech and the muzzle sections;

y_b, y_m are the displacements at the center of gravity of the breech section and the muzzle section, f_d, f_{tm}, f_{bm} are the reaction force at the point of contact between the pinion and the turret ring gear, measured along the OZ direction and the turret roller gear, the reaction force between the turret with the breech and reaction force the breech point of contact between the breech section and the muzzle section;

R_d, R_p, R_t, R_g are the radius of the engine gear, the transmission gear, the turret gear ring and the distance from the center of gravity of the turret to the axis of rotation.

The system of differential equations for azimuth dynamic consists of six equations with six unknowns $\gamma_d, \gamma_t, \gamma_b, y_b, \gamma_m, y_m$, as in Bui et al. (2025).

$$
\begin{aligned}
&I_{da}\gamma''_d = T_{da} - K_{da}\left(\gamma_d - \frac{R_t\gamma_t}{R_p}\right) - C_{da}\gamma'_d \\
&I_t\gamma''_t = K_{da}R_t\left(\frac{R_p\gamma_d - R_t\gamma_t}{R_p^2}\right) - C_t\gamma'_t - K_{tb}\left(\gamma_t - \gamma_b\right) - C_{tb}\left(\gamma'_t - \gamma'_b\right) - R_g\left(m_b y''_b + m_m y''_m\right) \\
&I_b\gamma''_b = -\left(m_b y''_b + m_m y''_m\right)n_1 - m_m y''_m\left(l_b - n_1\right) + K_{tb}\left(\gamma_t - \gamma_b\right) + C_{tb}\left(\gamma'_t - \gamma'_b\right) + K_b\left(\gamma_m - \gamma_b\right) + C_b\left(\gamma'_m - \gamma'_b\right) \\
&y_b = X_t\gamma_t + n_1\gamma_b \\
&I_m\gamma''_m = K_b\left(\gamma_b - \gamma_m\right) + C_b\left(\gamma'_b - \gamma'_m\right) + n_2 m_m y''_m \\
&y_m = X_t\gamma_t + l_b\gamma_b + n_2\gamma_m
\end{aligned}
\tag{6}
$$

Because the barrel and the turret system are mounted on the vehicle body and are directly affected by its motion, the elevation dynamics are

coupled with the vehicle body's roll and pitch angles through an integration equation.

$$z_b = Z + \theta X_t - X_t \varphi \sin\gamma_t + \theta_b n_1 - n_1 \varphi \sin\gamma_t$$
$$z_m = Z + \theta X_t - X_t \varphi \sin\gamma_t + \theta_m n_2 + \theta_b l_b - (l_b + n_2)\varphi \sin\gamma_t \quad (7)$$

Simulation results

Simulation input parameters

The input parameters for simulating vehicle vibration as well as the azimuth and elevation motions are provided in Table 2 and Table 3. The values used in the simulation are based on Ambarish et al. (2017), Banerjee (2018), Bui et al. (2024, 2025).

Table 2 - Parameters for simulating the system of vibration differential equations

Quantities	Values	Quantities	Values	Quantities	Values
Front axle					
m_1	210 kg	K_{L1T}	800000 N/m	C_{L1T}	2000 N.s/m
b	0.75 m	K_{L1P}	800000 N/m	C_{L1P}	2000 N.s/m
Rear axle					
m_2	260 kg	K_{L2T}	800000 N/m	C_{L2T}	2000 N.s/m
b	0.75 m	K_{L2P}	800000 N/m	C_{L2P}	2000 N.s/m
Vehicle body					
M_k	2480 kg	K_{1T}	180000 N/m	K_{2T}	180000 N/m
a_1	1.3 m	K_{1P}	180000 N/m	K_{2P}	180000 N/m
a_2	1.5 m	C_{1T}	9000 N.s/m	C_{2T}	9000 N.s/m
c	0.6 m	C_{1P}	9000 N.s/m	C_{2P}	9000 N.s/m
J_{xk}	4800 kg.m2	J_{yk}	2000 kg.m2		
Turret and barrel					
M_t	1200 kg	J_{yt}	3800 kg.m2	J_{xt}	3500 kg.m2
M_n	500 kg	J_{xn}	600 kg.m2	J_{yn}	450 kg.m2

Table 3 - Parameters for elevation dynamics and azimuth dynamics

Quantities	Values	Quantities	Values	Quantities	Values
Parameters for elevation dynamics					
I_{de}	0.5 kg.m2	K_{db}	3500 N/m	C_{de}	8000 N.m.s/rad
I_b	900 kg.m2	K_{be}	1200 N.m/rad	C_{be}	500 N.m.s/rad
I_m	200 kg.m2	C_{1b}	8000 N.m.s/rad	m_b	400 kg
X_t	0.3 m	X_1	0.15 m	m_m	120 kg
n_1	0.4 m	l_b	1.2 m	n_2	0.3 m
Parameters for azimuth dynamics					
I_{da}	25 kg.m2	R_t	0.45 m	C_{da}	300 N.m.s/rad
I_t	2000 kg.m2	R_p	0.06 m	C_{tb}	250 N.m.s/rad
K_{da}	400 N.m/rad	K_{tb}	300 N.m/rad	C_b	300 N.m.s/rad
K_b	350 N.m/rad	C_t	300 N.m.s/rad	R_g	0.3 m

For the elevation and azimuth motions, small-amplitude torque inputs are applied to investigate the disturbances of the barrel induced by the servo motors. The input torque profiles for the elevation and azimuth axes are illustrated in Figure 4, as shown by Jitesh (2018).

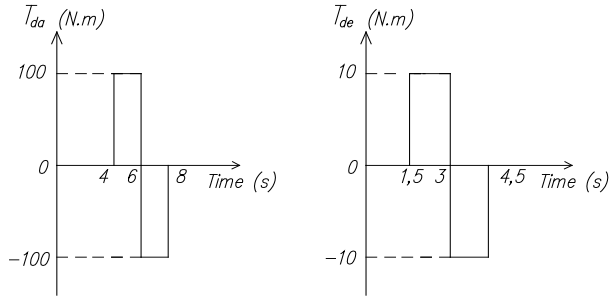

Figure 4 - Applied torque inputs to the servo motors for azimuth and elevation angle control

Road surface profile simulation

The paper simulates different road surface profiles on the left and right sides to generate lateral vibrations for the barrel. The simulation uses a

level B road surface profile, with a speed of 8.33 m/s, $S_{q(\Omega_0)} = 64 \times 10^{-6}\, m^2 / m^{-1}$ and a simulation duration of 20 seconds. The results of the road surface profile simulation are shown in Figure 5 and Figure 6.

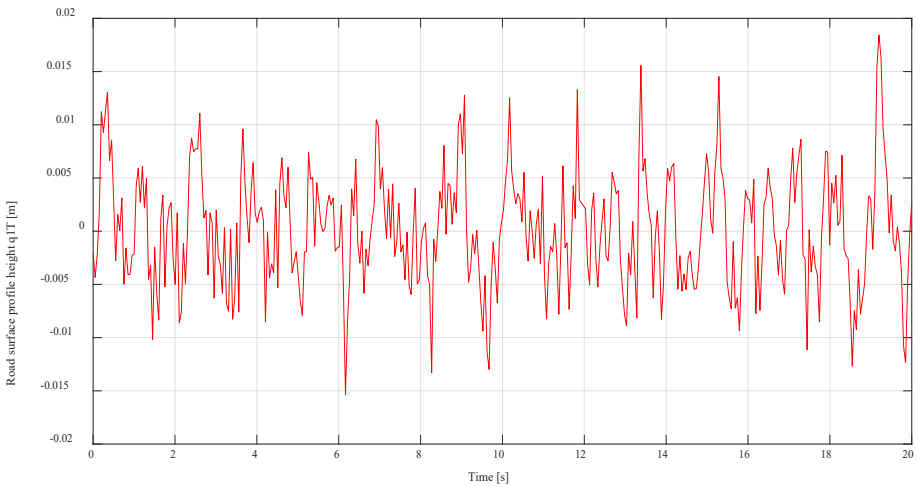

Figure 5 - Road surface profile height on the left side q_T

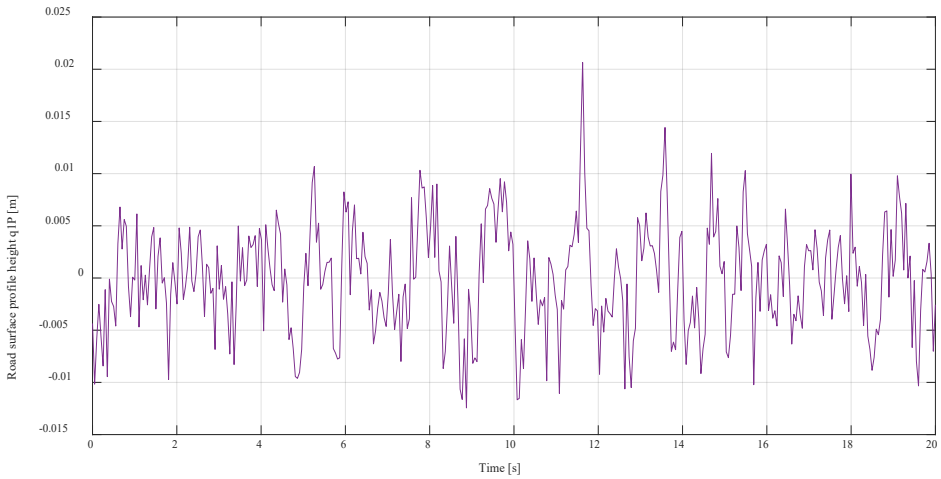

Figure 6 - Road surface profile height on the right side q_P

Simulation of longitudinal and angular vibrations of the barrel

Vibrations in the vertical plane

The simulation results shown in Figure 7 and Figure 8 represent the longitudinal and angular vibrations of the barrel in the vertical plane.

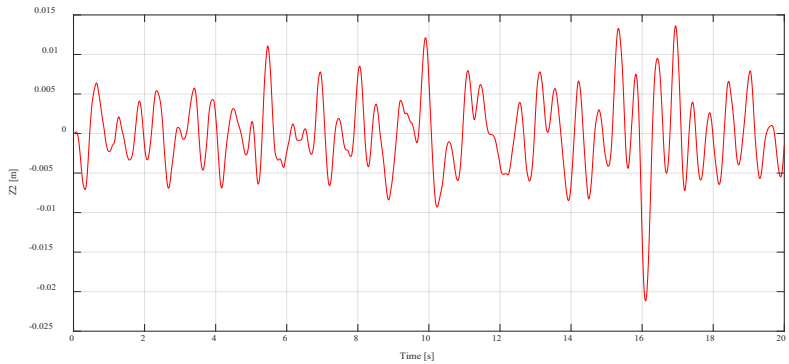

Figure 7 - Graph of the longitudinal vibration amplitude of the barrel in the vertical plane

From the graph shown in Figure 7, the vibration amplitude of the barrel ranges from $-0.021 \div 0.014\ m$, indicating that the barrel operates within a small amplitude with high-frequency vibrations, repeating several cycles per second. However, at approximately 16.1s, the vibration amplitude suddenly decreases, reaching a maximum value of about -0.021 m. Following this, the amplitude gradually decreases and returns to the small vibration level initially observed.

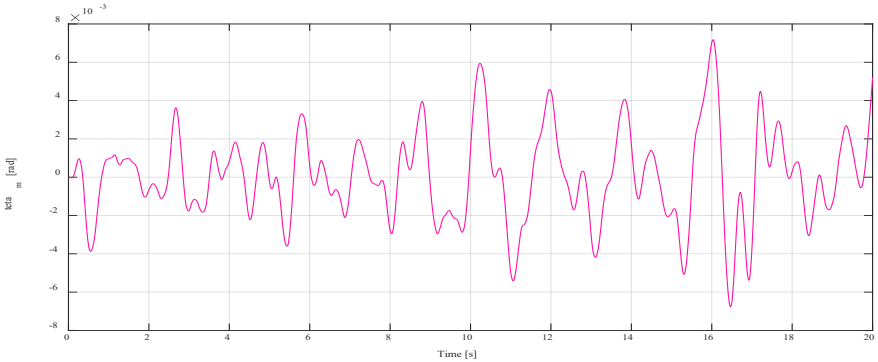

Figure 8 - Angular vibration amplitude of the barrel in the vertical plane

The angular vibration amplitude remains within the range of $-6.5\times10^{-3} \div 7.2\times10^{-3}\ rad$. The amplitude is not entirely uniform but shows slight variations over time, with some segments exhibiting higher amplitudes-particularly in the interval from $15 \div 16.5\ s$, where the amplitude reaches nearly $7.2\times10^{-3}\ rad$.

Vibrations in the horizontal plane

The results of the longitudinal and angular vibrations of the barrel in the horizontal plane are shown in Figure 9 and Figure 10.

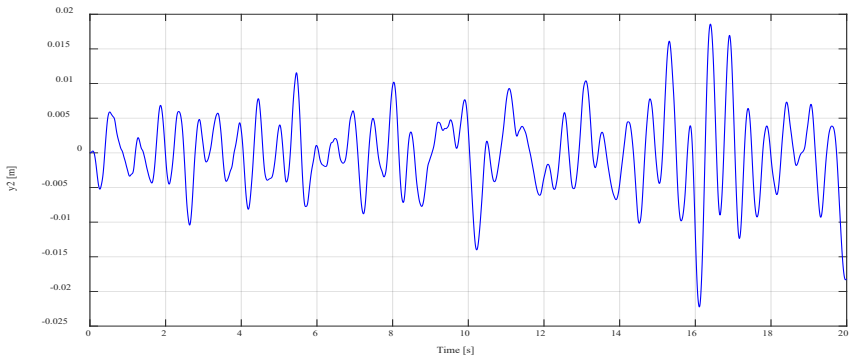

Figure 9 - Longitudinal vibration amplitude of the barrel in the horizontal plane

The graph can be observed that the vibration amplitude remains within a certain range around the equilibrium position.

These large amplitudes occur irregularly, suggesting the presence of abnormal external excitation forces. After each spike, the vibrations tend to decrease back to smaller amplitudes, though they do not fully return to the original steady-state condition.

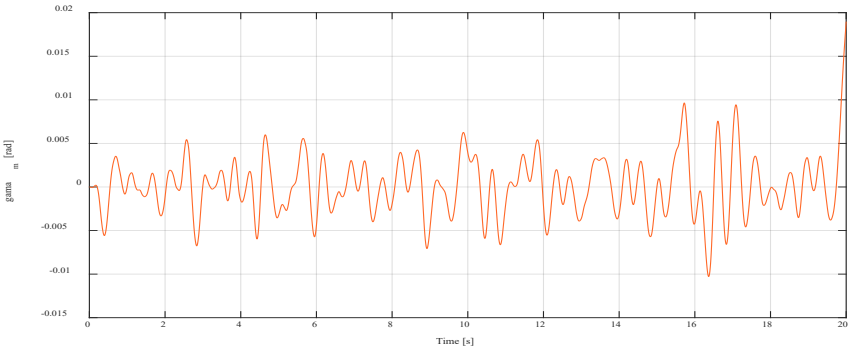

Figure 10 - Angular vibration amplitude of the barrel in the horizontal plane

In the range of 0-15 s, the vibrations of the gun barrel are relatively stable with small amplitudes, and the barrel does not deviate significantly from the equilibrium position. However, the sudden increase in amplitude at the end of the graph indicates that the system may encounter stability issues when subjected to large disturbances from road conditions.

The simulation results for the vibrations of the gun barrel in both the vertical and horizontal planes show a common characteristic: the vibration frequency is lower than the excitation frequency from the road. This can be explained by the damping coefficients and the spring constants of the suspension system and wheels. These factors help reduce the vibrations, contributing to greater stability of the gun barrel during movement and when the control motors are active.

Experimental measurement of barrel vibrations on the DJI RoboMaster S1

Technical specifications of the DJI RoboMaster S1

DJI RoboMaster S1 (Figure 11) is an intelligent robot developed and manufactured by DJI, a company based in China. The S1 is not only a remote-controlled robot but also a powerful educational tool that introduces users-especially beginners-to programming, artificial intelligence (AI), and robotics through its smart features. The robot supports programming in both Scratch 3.0 and Python, making it suitable for learners at all levels.

DJI RoboMaster S1 is equipped with a two-axis gimbal system consisting of a gun barrel and turret. Mounted above the barrel is a camera used for target tracking. The gimbal component is relatively lightweight, allowing for agile and responsive movement.

Figure 11 - DJI RoboMaster S1

The technical specifications of the DJI RoboMaster S1 are provided in Table 4.

Table 4 - Main parameters of DJI RoboMaster S1

Parameters	
Size	0.32 × 0.24 × 0.270 m
Weight	≈ 3.3 kg
2-axis gimbal	Vertical plane $-20 \div 35^0$. Horizontal plane $-235 \div 235^0$
Drivetrain	Four Mecanum wheels (omnidirectional movement), each equipped with 12 angled rollers.
Engine	Brushless M3508I motors with integrated FOC ESC.
Control system	Central controller with a processor that supports Python and Scratch programming.
Camera	1 FPV camera (120° wide-angle), 1080p resolution, supports machine vision.
Movement speed	Maximum: ≈ 3.5 m/s (forward), ≈ 1 m/s (sideways).
Rotation speed	≈ 600°/s
Simulation weapons	Gel bead gun, with a safety limit; integrated with a collision detection system.
Sensor	6 armor sensors, distance sensors, IMU, encoder
Programming	Supports Python 3.6, Scratch 3.0; has extended API
Machine vision	Road, sign, person, gesture, and other robot recognition.
Connect	Wi-Fi Direct, control via mobile app or computer

Experiment on the DJI RoboMaster S1

The paper implements a target tracking and locking mode at a specific position on the human body. When the person moves, the robot follows and controls the turret to track the predetermined position. The target tracking is carried out through the integrated camera and computer vision algorithms. The images captured by the camera are processed directly on the machine or sent to a computer/phone to run computer vision algorithms. Once the person's position is determined, either through the bounding box or pixel coordinates, the system can control the turret's (gimbal's) elevation angle to track the target and simultaneously command the robot to move in follow mode to maintain pursuit. This is achieved by using feedback signals from the vision system to adjust the rotation motors and Mecanum wheels.

The area of the target zone is shown in Figure 12. The robot follows the target at a fixed distance.

Figure 12 - The target bounding box is the back of the person's body

When the target moves to the right or left, the robot will change its direction (Figure 13 and Figure14) and the controller will rotate the turret to follow the target.

Figure 13 - The target moves to the right

Figure *14 - The target moves to the left*

When the robot moves on an uneven road or when the target accelerates and changes direction, it causes vibrations between the camera's center and the target's center. This phenomenon is seen as jittering in the camera in real life when tracking a moving object that continuously changes direction, as clearly shown in Figure 13. The paper records a video of the robot tracking the target, then uses the Python programming language and the VidStab library on the robot to stabilize the video, i.e., to reduce the shaking and jittering in the original video. As we know, a video is a series of continuous frames, and stabilizing the video is equivalent to stabilizing each individual frame. After obtaining the stabilized video, we can calculate the deviations of each frame in both the horizontal and vertical directions, with the unit being radian. The experiment was conducted to measure angular deviations in the horizontal and vertical directions using a video with a duration of 89 seconds. The

distance from the camera center to the target is 2 m. The results are shown in Figures 15 and 16.

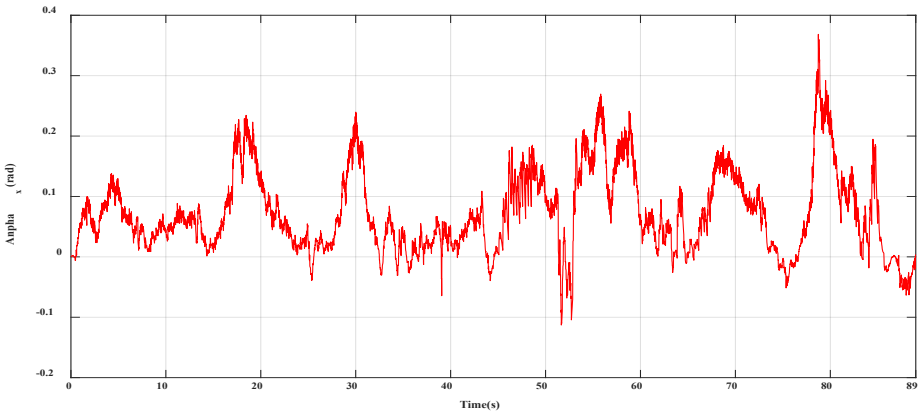

Figure 15 - Angular deviation graph in the horizontal plane

The graph illustrates that the angular deviation fluctuates continuously around a mean value of approximately 0.6 rad, with an amplitude ranging from –0.12 rad to +0.36 rad. During the oscillation process, numerous peaks and troughs can be observed, indicating significant dynamic phases-particularly evident in the time intervals of 18-20 s, 29-31 s, 51-59 s and 78-80 s. These variations reflect continuous changes in the relative position between the camera and the target, primarily caused by the target's directional shifts from left to right or vice versa, resulting in abrupt changes in oscillation amplitude. Additionally, the system is influenced by vehicle body vibrations, road surface conditions, and the response of the suspension system.

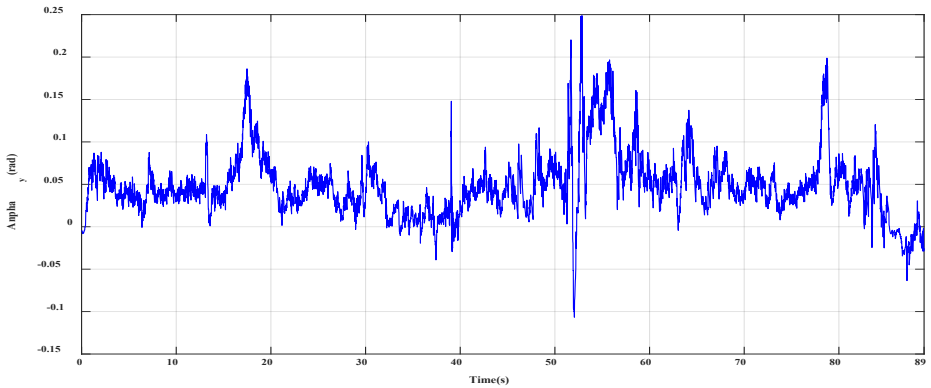

Figure 16 - Angular deviation graph in the vertical plane

The graph in Figure 16 shows that the oscillation amplitude remains relatively small and stable, as there is no significant change in the target's height. The amplitude ranges from -0.11 rad to 0.25 rad, with sudden increases observed during the intervals of 18-20 s, 51-56 s and 77-79 s.

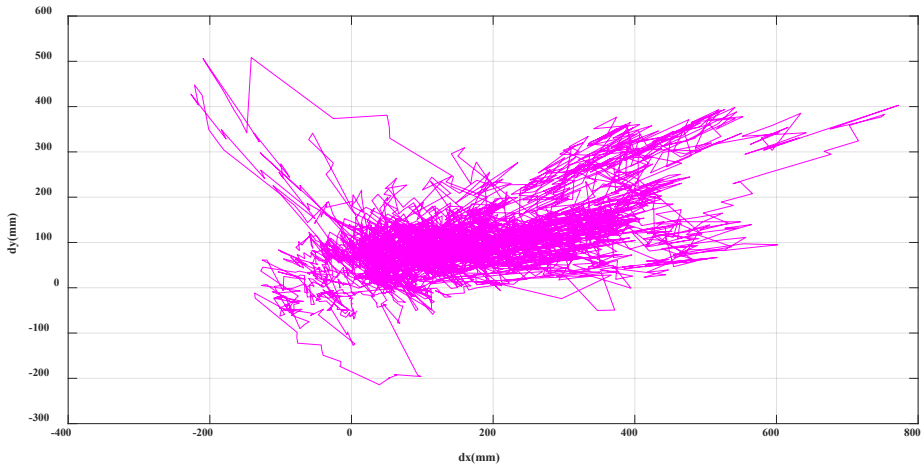

Figure 17 - Barrel deflection position graph on coordinate plane

The graph indicates that the deviation between the camera center and the target is greater in the horizontal direction than in the vertical direction. The horizontal deviation is concentrated within the range of 0-400 mm, while the vertical deviation remains within 0-200 mm. The above results accurately reflect the fact that when the barrel tracks the target, the deviation of the gun barrel depends greatly on the speed and direction of movement of the target.

Conclusion

The experimental and simulation results exhibit similar vibration patterns, which can be interpreted as the vibration behavior of the cannon barrel on an autonomous vehicle. The curves in the simulation results are smooth due to the assumed input conditions and approximated outputs. In contrast, the experimental results reflect real-world conditions where the robot operates on actual terrain, involving directional changes and varying speeds. This distinction highlights the key differences between simulation and real-world testing outcomes.

From both simulation and the experiments conducted on the DJI RoboMaster S1, it is evident that road surface profiles, suspension system parameters, damping and spring characteristics, and torques generated

by control motors are critical factors contributing to cannon barrel vibrations during movement. The simulation model accurately captures the physical characteristics of the system, including terrain profile conditions, suspension stiffness, wheel dynamics, actuator behavior, and the physical properties of the cannon and turret system on the autonomous vehicle.

The barrel on an unmanned ground vehicle is strongly affected by road surface irregularities, directional changes, and torques from the control mechanism. When traversing uneven or rough terrain, the suspension system transmits vibrations to the vehicle body, which in turn propagates to the turret and barrel, producing forced vibrations with amplitudes and frequencies that vary based on terrain conditions. Additionally, during maneuvers such as turning, acceleration or deceleration, inertial torques are generated, leading to temporary misalignment and vibrations in the barrel.

Moreover, torque generated by the turret and elevation actuators, if not accurately controlled or if subject to latency, results in residual oscillations and deviations in aiming accuracy. The combination of these factors causes continuous misalignment in the aiming line, reducing the stability of the weapon system and potentially causing significant targeting errors, especially in scenarios that demand high precision in a short time. Therefore, compensating for these vibrations using sensors, controllers, and stabilization mechanisms plays a crucial role in maintaining targeting and firing accuracy under complex real-world conditions.

This study introduces a basic mathematical model and serves as a preparatory step for developing a comprehensive model to address the stability problem in subsequent studies.

References

Abdeselem, B.B., Momir, M.D., Aleksandar, S.Đ., Sreten, R.P., Aleksandar, G.B. & Abdellah, B.F. 2024. Mathematical modeling and simulation of a half-vehicle suspension system in the roll plane. *Vojnotehnički glasnik/Military Technical Courier*, 72(1), pp.192-208. Available at: https://doi.org/10.5937/vojtehg72-47551.

Ambarish, J., Saayan, B. & Jebaraj, C. 2017. Development of mathematical models, simulating vibration control of tracked vehicle weapon dynamics. *Defence Science Journal*, 67(4), pp.465–475 [online]. Available at: https://www.researchgate.net/publication/318363890_Development_of_Mathematical_Models_Simulating_Vibration_Control_of_Tracked_Vehicle_Weapon_Dynamics [Accessed: 24 July 2025].

Banerjee, S., Balamurugan, V. & Krishnakumar, R. 2016. Ride comfort analysis of math ride dynamics model of full tracked vehicle with trailing arm

suspension. In: *International Conference on Vibration Problems 2015*, pp.1110–1118. Available at: https://doi.org/10.1016/j.proeng.2016.05.074.

Banerjee, S., Balamurugan, V. & Krishnakumar, R. 2018. Effect of integrated ride and cornering dynamics of a military vehicle on the weapon responses. *Proceedings of the Institution of Mechanical Engineers, Part K: Journal of Multi-body Dynamics*, 232(4). Available at: https://doi.org/10.1177/1464419318754647.

Bui, V.D., Martin, M., Zbynek, K., Tranh, D.D., Do, Q.V. & Pham, H.N. 2024. Mathematical model of unmanned ground vehicle. In: *International Conference QUAERE 2024*, Hradec Kralove, Czech Republic, 14, pp.765–771 [online]. Available at: http://www.vedeckekonference.cz/library/proceedings/quaere_2024.pdf [Accessed: 24 July 2025].

Bui, V.D., Martin, M., Tran, D.D., Martin, C. & Zbynek, K. 2025. Research on Vibrations of an Unmanned Vehicle on a Random Road Surface. In: *2025 International Conference on Military Technologies (ICMT)*, Brno, Czech Republic, 27-30 May 2025. Available at: https://doi.org/10.1109/ICMT65201.2025.11061271.

Bui, V.D., Martin, M., Miloš, M., Dejan, J. & Tran, D.D. 2025. Barrel Vibration of an Automatic Weapon on an Unmanned Vehicle. In: *2025 International Conference on Military Technologies (ICMT)*, Brno, Czech Republic, 27-30 May 2025. Available at: https://doi.org/10.1109/ICMT65201.2025.11061266.

Cagil, C. 2016. Dynamic modeling and analysis of gun turret elevation drive system. MSc thesis, Department of Mechanical Engineering, Middle East Technical University [online]. Available at: https://etd.lib.metu.edu.tr/upload/12620067/index.pdf [Accessed: 24 July 2025].

Chen, K., Zhang, M. & Tong, X. 2012. Vibration characteristic analysis of vehicle air suspension based on fuzzy control. In: *2nd International Conference on Electronic & Mechanical Engineering and Information Technology (EMEIT-2012)*, Paris, France, pp.2196–2199. Available at: https://doi.org/10.2991/emeit.2012.486.

David, J.P. 2001. Comparison of balance and out of balance main battle tank armaments. *Shock and Vibration*, 8(3–4), pp.167–174. Available at: https://doi.org/10.1155/2001/326219.

Hallbeck, V. 2021. System modelling and evaluation of main battle tank fire precision. MSc thesis, KTH Royal Institute of Technology, School of Engineering Sciences [online]. Available at: https://www.diva-portal.org/smash/get/diva2:1595629/FULLTEXT01.pdf [Accessed: 24 July 2025].

ISO. 2016. ISO 8608:2016 – Mechanical vibration – Road surface profiles – Reporting of measured data. International standard [online]. Available at: https://cdn.standards.iteh.ai/samples/71202/05b2151f255b44928f80acb897fc0c2c/ISO-8608-2016.pdf [Accessed: 24 July 2025].

Jitesh, S. 2018. Modelling and simulation of main battle tank to stabilize the weapon control system. In: *International Conference on Advances in Design, Materials, Manufacturing and Surface Engineering for Mobility*. Available at: https://doi.org/10.4271/2018-28-0078.

Kim, Y.J., Sohn, Y., Chang, S., Choi, S.B. & Oh, J.S. 2024. Vibration control of car body and wheel motions for in-wheel motor vehicles using road type classification. *Actuators*, 13(2). Available at: https://doi.org/10.3390/act13020080.

Liangkuan, W., Xu, T., Ji, F. & Cheng, H. 2023. Prediction of firing accuracy of self-propelled antiaircraft gun in marching fire based on GA-BP neural network. In: *International Conference on Defence Technology (2022 ICDT), IOP Conference Series: Journal of Physics: Conference Series*, 2478, 092007. Available at: https://doi.org/10.1088/1742-6596/2478/9/092007.

Yin, Z., Su, R. & Ma, X. 2023. Dynamic responses of 8-DoF vehicle with active suspension: Fuzzy-PID control. *World Electric Vehicle Journal*, 14(9), pp.1–23. Available at: https://doi.org/10.3390/wevj14090249.

Vibracije sistema naoružanja na besposadnom kopnenom vozilu tokom kretanja

Viet Dung Bui[a], *Martin* Macko[a], **autor za prepisku**, *Ba Ngoc Dang*[a], *Huu Nguyen* Pham[b]

[a] University of Defence, Faculty of Military Technology, Department of Weapons and Ammunition, Brno, Czech Republic,

[b] Tran Dai Nghia University, Faculty of Ammunition, Department of Explosives and Ballistics, Hochiminh, Socialist Republic of Vietnam

OBLAST: mašinstvo
KATEGORIJA (TIP) ČLANKA: originalni naučni rad

Sažetak:

Uvod/cilj: U radu je predstavljen matematički model vibracija nosača naoružanja na malom besposadnom kopnenom vozilu ukupne mase do 70 kg sa naoružanjem. Konstrukcija ovih malih vozila slična je konstrukciji većih borbenih vozila: nosač je postavljen na gusenično šasijsko postolje ili postolje sa točkovima, što omogućava elevaciju i podešavanje azimuta naoružanja, a ako je omogućeno gađanje u pokretu, vibracije šasije utiču na ugaoni položaj cevi, te je isti potrebno stabilizovati. Vibracije šasije i delova nosača naoružanja nisu poželjna pojava, a rezultati simulacije vibracija pružaju projektovanje rešenja za njihovu eliminaciju.

Metode: U radu su kreirani sistemi diferencijalnih jednačina koji opisuju vibracije sistema naoružanja i kretanje vozila po terenu, nakon čega je urađena simulacija vibracija u softveru u Matlab-Simulink. Dodatna ispitivanja su sprovedena u cilju merenja odstupanja ose kamere od centra mete, a rezultati eksperimenta su upoređeni sa rezultatima simulacije.

Rezultati: Rezultati istraživanja pokazuju da na vibracije sistema naoružanja na besposadnim kopnenim vozilima utiče mnogo faktora, kao što su profil terena, karakteristike guma, sistem vešanja, kao i ukupne dimenzije, raspored i masa komponenti. Eksperimentalni rezultati merenja stabilnosti kamere tokom praćenja mete odgovaraju rezultatima simulacije u softveru Matlab-Simulink.

Zaključak: Sistem matematičkih diferencijalnih jednačina besposadnog kopnenog vozila i model profila terena opisuju faktore koji utiču na vibracije sistema naoružanja tokom kretanja vozila. Matematički modeli omogućavaju promenu parametara, a time i simulaciju promena ugaonog položaja cevi u različitim uslovima unosa.

Ključne reči: besposadno kopneno vozilo, sistem naoružanja, stabilizacija, analiza vibracija.

Paper received on: 5 September 2025.
Manuscript corrections submitted on: 21 November 2025.
Paper accepted for publishing on: 25 November 2025.

© 2026 The Authors. Published by Vojnotehnički glasnik / Military Technical Courier (www.vtg.mod.gov.rs).This article is an open access article distributed under the terms and conditions of the Creative Commons Attribution license (http://creativecommons.org/licenses/by/4.0/rs/

Improving silty sand performance with cement and fiber reinforcement: study of mechanical behavior

Asma Halimi[a], *Souad* Amal Bourokba[b], *Moulay* Smaine Ghembaza[c], *Abdelkader* Hachichi[d]

[a] DjlillaliLiabès University of Sidi Bel-Abbès, Civil Engineering and Environment Laboratory (LGCE),
email: mounsifsiradj20@gmail.com,
ORCID ID: https://orcid.org/0009-0000-0514-3308

[b] Civil Engineering Department, Materials Soil and Thermal Laboratory (LMST), University of Sciences and Technology Mohamed Boudiaf Oran, El Mnaouar, BP 1505, Bir El Djir 31000, Oran, Algeria,
email: souad.bourokba@univ-usto.dz,
ORCID ID: https://orcid.org/0009-0009-3524-9256

[c] DjlillaliLiabès University of Sidi Bel-Abbès, Civil Engineering and Environment Laboratory (LGCE),
email: moulay.ghembaza@univ-sba.dz, **corresponding author**,
ORCID ID: https://orcid.org/0009-0008-6987-7333

[d] Civil Engineering Department, Materials Soil and Thermal Laboratory (LMST), University of Sciences and Technology Mohamed Boudiaf Oran, El Mnaouar, BP 1505, Bir El Djir 31000, Oran, Algeria,
email: abdelkader.hachichi@univ-usto.dz,
ORCID ID: https://orcid.org/0000-0043-0447-0133

https://doi.org/10.5937/vojtehg74-60016

FIELD: geotechnics
ARTICLE TYPE: original scientific paper

Abstract:

Introduction/purpose: This study aims to valorize a local material from the western region of Algeria for potential use in road construction. The main objective is to investigate the effect of incorporating synthetic polypropylene fibers and natural Alfa plant fibers at varying contents (0%, 0.3%, 0.6%, and 0.9%) on the strength of a silty sand stabilized with 4% cement.

Methods: An experimental program was conducted using unconfined compression tests and unconsolidated-undrained triaxial tests. These tests were performed on soil–fiber–cement mixtures compacted statically at the Standard Optimum Proctor (SOP) conditions (γ_{dmax}= 17 kN/m^3 and wopt =16.6%) and cured for 1, 7, and 28 days in open air.

Results: The results revealed a significant improvement in the mechanical strength of the treated soil, with a change in the failure behavior from brittle to ductile. The addition of 0.3% fibers enhanced cohesion while reducing the internal friction angle. Furthermore, fiber-reinforced cemented samples exhibited greater stiffness compared to untreated soil. Moreover, the highest unconfined compressive strength was obtained with the combination of 0.9% fiber reinforcement and 4% cement.

Conclusion: The reinforcement of cemented silty sand with polypropylene and Alfa fibers significantly improves its mechanical strength and stiffness. The addition of 0.9% fiber content yields the highest compressive strength while effectively transitioning the soil's behavior from brittle to ductile. These findings confirm that valorizing local Algerian materials is a technically viable and sustainable solution for road infrastructure development.

Key words: silty sand soil, Alfa plant, polypropylene fibers, shear resistance, friction angle, cohesion, unconfined compressive strength.

Introduction

The stabilization or reinforcement of soils is performed through a set of techniques that aim to improve the soil strength and/or limit its deformation under structures. It is useful to note that the reinforcement of foundation or backfill soils consists of improving their mechanical characteristics. Over the past few years, fiber reinforcement techniques have been widely and successfully used in various applications, such as the stabilization of slopes, road construction, and embankments (Wang et al, 2018).

The first experimental studies conducted on fiber-reinforced soils focused primarily on soil-plant root systems. In this regard, Gray (1978), Waldron (1977), and Wu et al. (1988) indicated that plant roots increase the shear strength of soil as well as the stability of natural slopes. Additionally, it is worth noting that natural fibers have long been used in cementitious composites and earth blocks in developing countries due to their availability and low cost (Ghavami et al, 1999; Savastano et al, 2000). Moreover, natural fibers such as sisal (Mesbah et al, 2004), coconut (Pradani et al, 2017), and jute (Hossain et al, 2015) are potentially environmentally friendly materials that have been recognized in recent years as very important and have been widely used in experimental studies on fiber-reinforced soils.

Furthermore, unconsolidated undrained (UU) triaxial tests have previously been carried out by Dasaka and Sumesh (2011) and AbouDiab et al. (2016). The results obtained could be interpreted only in terms of shear strength because the pore water pressures were not measured

during the tests. The authors reported that the integration of fibers of different lengths helps increase the internal friction angle of the reinforced soil to an optimal value. This angle then begins to decrease. However, the fiber-reinforced soil cohesion decreases to a minimum value and then starts to increase for an inclusion rate of 0.3% fiber. The authors concluded that this is due to the interaction between soil particles and the fibers, without providing a sufficiently detailed explanation of this phenomenon. Jiang et al. (2010) and Pradhan et al. (2012) reported similar findings. Furthermore, Mirzababaei et al. (2017) and Mirzababaei et al. (2018a et b) observed that the effective internal friction angle (ϕ') was not significantly influenced by the fibrous reinforcement but, on the other hand, the effective cohesion (c') of the soil was considerably improved. It was also observed that the effect of fibrous reinforcement on shear strength was evident at low confining pressure (50 kPa).

Furthermore, the results of the triaxial tests performed under low confining pressure (Consoli et al, 1998; 2009) showed that fiber reinforcement has a significant impact on cement-treated sand as it increases the compressive volumetric strain at a specific axial strain, which in turn increases the ductility of the soil. It has also been shown that the presence of fibers can improve strength and ductility. However, the improvement rate decreases as the confining pressure increases (Uddin et al, 2011; Wang et al, 2014; Shen et al, 2021). In 2016, Nguyen and Fatahi found that, under undrained conditions, higher fiber content results in excessive pore pressure, which is consistent with Athanasopoulos' postulate (1994), who suggests that the presence of fibers is in many situations similar to the presence of additional confining pressure. Falorca and Pinto (2011) used low plasticity clay reinforced with polypropylene fibers to study the effects of the fiber texture and normal stress level in direct shear tests. They reported that the shear strength decreases with the increase of the applied normal stress, which means that the fibers contributed more significantly at low normal stress levels. More recently, Araldi et al. (2018) and Imanzadeh et al. (2018) have studied the effect of plant fibers on improving the plastic behavior of soils in order to minimize cracks. The findings showed that, in general, the maximum and residual shear strength due to fiber reinforcement is relatively high, which can considerably improve the cohesion and the internal friction angle of the cement-treated soil.

Furthermore, other studies have been carried out to study the influence of cement treatment on soil ductility using the secant modulus E_{50} at maximum strength (Gray and Al-Refeai, 1986; Al-Refeai, 1991; Lee et al, 2005; Michalowski and Zhao, 1996; Falorca and Pinto, 2011). The

authors concluded that this modulus increases with the percentage of fibers used. However, when the quantity of fibers exceeds an optimal value, the secant modulus begins to decrease due to the balling effect (Silveira et al, 2020).

Other studies on the unconfined compressive strength of cement-treated and fiber-reinforced soil have been conducted by Consoli et al. (2010, 2011, 2012), Xiao et al. (2013), Hamidi et al. (2013), Cristelo et al. (2017), Correia et al. (2015), Festugato et al. (2017), and Shen et al. (2021). The results showed that the increase in the compressive strength of soils due to their reinforcement with fibers is relatively significant. However, this strength remains much lower than that obtained when the cement content is increased (Consoli et al, 2010; Xiao et al, 2013). It is worth noting that the main objective of fiber reinforcement is to increase the ductility of the cement-treated soil. Michalowski and Cermak (2003) showed that the strength of sand can be improved by adding fibers. The present article aims primarily to carry out an experimental study in order to investigate the impact of two types of fibers, natural plant fiber (Alfa) and synthetic fiber (polypropylene), on the shear strength and unconfined compressive strength of silty sand treated with 4% cement.

Unconsolidated undrained (UU) triaxial compression tests were conducted at two confining pressures (100 and 300 kPa) on mixtures of soil with different fiber percentages (0%, 0.3%, 0.6%, and 0.9%). In addition to the triaxial tests, unconfined compressive strength (UCS) tests were also carried out at different curing times in open air on mixtures (soil-fibers) and (soil-cement-fibers) in order to analyze the effect of fiber incorporation on the properties of cemented soil. Moreover, it was observed that adding a certain percentage of fibers to the mixture (soil-cement) caused an increase in cohesion and friction angle. The inclusion of fibers also made it possible to obtain soil that exhibited a ductile behavior. Hence, significant deformations were observed without stress peaks. The UCS results showed that the incorporation of fibers in the mixture (soil-cement) made the material more resistant. The characterization of the behavior of the soil was carried out by considering the secant modulus, which was defined on the basis of the compression curves of the specimens during the UU triaxial tests. The effect of fiber reinforcement on the stiffness increase was analyzed by comparing the evolution of the secant modulus of the reinforced samples with fibers and treated with 4% cement. It was shown that the secant modulus of the soil treated with cement and reinforced with 0.3% polypropylene fibers was significantly improved.

Materials and methods

Location and identification of the studied soil

The material used in this study was collected from a site located in the town of Telagh in the Sidi Bel Abbès region (North-West of Algeria), at a depth of approximately 1 meter. This soil has been subject of previous research (Ghembaza et al, 2023). Several tests were conducted to determine the physical and chemical characteristics of the soil, and the results are summarized in Table 1. The natural soil is predominantly composed of sand and silt, with a natural water content of 14.86% and a plasticity index (Ip) ranging from 6.25% to 8.42% (Ikhlef, 2015). As the organic matter content of the soil is very low (1.35%), it should not interfere with the treatment process.

According to the Unified Soil Classification System (USCS) and the American Association of State Highway and Transportation Officials (AASHTO, 1978), the soil is classified as silty sand (SM) and as a granular material (A-2-4), respectively. Its chemical composition indicates high silica (SiO_2) and lime (CaO) contents, conferring pozzolanic properties (Janz and Johansson, 2002). Additionally, the soil's pH value of 9.06 (higher than 6) makes it suitable for stabilization (Vilenkina, 1956).

Table 1 - The identification parameters of the studied soil

	Parameters	Values
Sieve analysis	Gravel (%)	6.26
	Coarse sand (%)	20.06
	Fine sand (%)	35.42
	Silt (%)	25
	Clay (%)	13.21
Physical parameters	Natural water content (%)	14.85
	Liquidity limit, LL (%) (ASTM D-4318)	25.65- 28.22
	Plasticity limit, PL (%) (ASTM D-4318)	19.4 - 19.8
	Plasticity index (%) (PI = LL – PL)	6.25 – 8.42
Chemical parameters	SiO2 (%)	38.86
	CaO (%)	27
	pH	9,1
Compaction properties	Dry density at SPO (kN/m3) (ASTM D-698)	17
	Optimum water content (%) (ASTM D-698)	16,6

Characteristics of the used cement

The cement used as a stabilizing agent in this study is Portland cement type CEM I 42.5R, produced by Zahana Company (Algeria). Its main characteristics are presented in Table 2. As a hydraulic binder, Portland cement reacts readily with water, producing a significant amount of hydration products in a short time. Its high silica (SiO_2 = 20.71%) and calcium oxide (CaO = 62.07%) contents, present in the clinker, promote pozzolanic reactions that enhance the long-term mechanical properties of treated soils (Taylor, 1997; Janz and Johansson, 2002).

Table 2 - Physico-chemical properties of the cement

Parameters	Physical		Chemical							
Denomination	Specific surface	Setting time	SiO_2 (%)	CaO (%)	Al_2O_3 (%)	Fe_2O_3 (%)	MgO (%)	SO_3 (%)	Perte au feu	CaO libre
Notation	cm^2/g	h								
Values	3500	2h13mn	20,7	62	5,99	3,47	1,12	1,66	5,14	0,7

Characteristics of the used fibers

Two types of fibers were used for soil reinforcement in this study. The first type consists of synthetic polypropylene fibers, whose properties are summarized in Table 1. These fibers act as mechanical links between soil particles, enhancing the overall bearing capacity of the soil–fiber mixture. According to Pakravan et al. (2012), polypropylene is hydrophobic and does not react with moisture from either the cement paste or the soil. Synthetic fibers have been widely used in previous experimental studies (Khattak and Alrashidi, 2006; Yetimoglu et al, 2005; Viswanadham et al, 2009; Olgun, 2013).

The second type consists of natural Alfa fibers obtained from the El-Bayadh region in South-West of Algeria. These plant fibers are primarily composed of cellulose, hemicellulose, lignin, and pectins. They are valued for their low density, thermal insulation properties, mechanical strength, biodegradability, and ecological benefits. The fibers were collected directly from the field, air-dried, cut into 18 mm lengths, and then pretreated and extracted using the traditional seawater retting method, with a salinity

ranging from 37 to 40 g/l (Mediterranean Sea) and a pH value of 8. The main properties of Alfa fibers are listed in Table 3.

Table 3 - Characteristics of the used fibers (Hanana et al, 2015; Dallel, 2012)

Parameters	Unit	Polypropylene	Alfa
Length (l)	mm	18	18
Diameter (d)	µm	26 - 32	10-30
Specific density	g/cm^3	0,91	1,43 - 1,51
Tensile strength	MPa	(400-300)	75 ± 24,09
Young's modulus	MPa	(3,5-3,9)	8000 ± 2700

Sample preparation

The experimental program consists of producing mixtures composed of soil, cement, and fibers. The different tests were carried out on samples that were previously reworked and dried in an oven at a temperature of 60°C for 24 hours in order to avoid any alteration of the particles. The soil was treated with 4% of cement. It should be noted that the choice of the cement percentage was made in accordance with the nature of the material used and its pH, which is 9.1.

Then different percentages (0.3%, 0.6%, 0.9%) of synthetic (polypropylene) or vegetable (Alfa) fibers, 18 mm in length, were added to the natural soil. Afterwards, the dry soil-cement and fibers were mixed homogeneously with water for 15 minutes, according to the NF EN 197-1 standard. Then, the mixture (soil + cement + fibers) was prepared mainly by hand, rather than using a mixer that can cause the fibers to tangle or break. Table 4 presents the symbol sand proportions of the materials used in the composition of the different mixtures tested in this study.

On the other hand, unconsolidated and undrained (UU) triaxial compression tests were carried out on three series of cylindrical samples of 35 mm diameter and 70 mm height, which gives a length-to-diameter ratio of 2. It should be mentioned that this study examines three different samples: an untreated soil, a cement-treated soil, and a cement-treated soil reinforced with fibers. The samples were then compacted at the optimal water content (w_{opt}) and at 95% of the maximum dry density (γ_{dmax}) in a mold with two upper and lower pistons in order to have a homogeneous compaction stress distribution in three equal layers of soil using the static compression method.

Afterwards, the samples were slowly and carefully removed from the mold and were then immediately wrapped in a plastic film for 24 hours in order to avoid or minimize any change in moisture. It should be noted that,

once the samples were prepared, they were subjected to confining pressure values equal to 100 and 300 kPa. Then, a piston was used to apply a vertical stress on the samples until failure. The vertical deformation Δh was measured using a 10-2 precision dial gauge. The testing speed used during the unconsolidated and undrained (uu) triaxial compression tests was set at 0.5 mm/min.

Furthermore, unconfined compression strength tests (UCS) were carried out on two series of cylindrical samples of 50 mm in diameter and 100 mm in height. Three types of samples are considered in this study: an untreated soil, a cement-treated soil, and a cement-treated soil reinforced with fibers. The samples were made at the SOP (Standard Optimum Proctor). Once the compacted specimens were removed from the steel mold, they were stored in a humid room at a temperature of (20± 1)°C for a curing time of 1, 7 and 28 days. The machine used in the tests is a compression press with a capacity of 50 kN, with a crushing speed of 1.27 mm/min. The vertical deformation was measured using a 10-2 mm precision dial gauge. The test was conducted until failure occurred or until the axial deformation reached approximately 10% of the total length of the specimen. In order to guarantee the reliability of the unconfined compressive strength results, the average of two values recorded on two standard samples was taken.

Table 4 - Mixture suggestions

Materials		Name of the mixtures studied
S0	Series 1	Natural Soil
S0 et Fpp 0,3%	Series 2	Soil and 0,3% polypropylene fibers
S0 et Fpp 0,6%		Soil and 0,6% polypropylene fibers
S0 et Fpp 0,9%		Soil and 0,9% polypropylene fibers
S0 et FA 0,3%		Soil and 0,3% Alfa fibers
S0 et FA 0,6%		Soil and 0,6% Alfa fibers
S0 et FA 0,9%		Soil and 0,9% Alfa fibers
S4 et Fpp 0,3%	Series 3	Soil with 4% cement and 0,3% polypropylene fibers
S4 et Fpp 0,6%		Soil with 4% cement and 0,6% polypropylene fibers
S4 et Fpp 0,9%		Soil with 4% cement and 0,9% polypropylene fibers
S4 et FA 0,3%		Soil with 4% cement and 0,3% Alfa fibers
S4 et FA 0,6%		Soil with 4% cement and 0,6% Alfa fibers
S4 et FA 0,9%		Soil with 4% cement and 0,9% Alfa fibers

Results and analyses

Determination of the cement percentage

The measurement of the pH in materials allows the evaluation of the binder treatments necessary to react with the soil over time. The pH was determined using a pH meter equipped with a glass electrode in a soil suspension diluted in distilled water according to ASTM D-4972. The effect of cement content on pH for the treated and untreated samples is presented in Figure 1. The pH value increases with the percentage of cement to reach a value of 11.7 for samples containing 4% and 6% cement, from an initial value of 9.1 for the natural soil. It can be concluded that the amount of cement necessary to react with the soil is about 4%. This result is consistent with those of several researchers (Chew et al, 2004; Tran 2009; Kalkan, 2011; Portelinha et al, 2012).

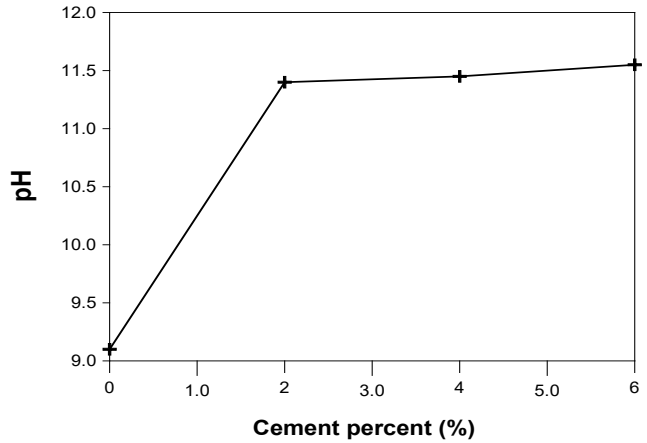

Figure 1 - Effect of the cement on the pH

Effect of fibers and cement on the shear strength

Figures 2a and 2b, and Figures 3a and 3b represent the variations of the deviatoric stress (q) and the axial strain (ε_1) for unreinforced and fiber-reinforced samples, using polypropylene and Alfa fibers at various fiber contents (0%, 0.3%, 0.6%, and 0.9%) under confining pressure values of 100 kPa and 300 kPa. The triaxial tests considered three key variables: fiber inclusion rate (ρf), type of fiber (polypropylene or Alfa), and confinement stress (σ_3), in order to study and analyze the behavior of both unreinforced and fiber-reinforced soils.

From Figure 2a, it can be seen that for the unreinforced samples, the deviatoric stress increases up to approximately 8% axial strain and then

remains constant under a low confining pressure (σ_3 = 100 kPa). When the same confining pressure was applied to soil reinforced with polypropylene fibers at different inclusion rates (i.e., 0.3%, 0.6%, and 0.9%), no peak was observed in the deviator stress–strain curves up to approximately 12% axial strain. Similar findings have been reported by Michalowski and Cermak (2003), Yetimoglu and Salbas (2003), Kumar et al. (2007), Diambra et al. (2010), Li and Zomberg (2012), Maliakal and Thiyyakkandi (2013), Kumar et al. (2018), Diambra and Ibraim (2014), and Shen et al. (2021).

It was nevertheless observed that the presence of polypropylene fibers led to an increase in the deviatoric stress as the fiber content increased under the same confining pressure. For instance, a failure stress of 475 kPa was recorded for unreinforced samples at axial strains between 8% and 11.5% under a confining pressure of 100 kPa. In comparison, deviator stresses of 550, 551, and 575 kPa were obtained for fiber contents of 0.3%, 0.6%, and 0.9%, respectively, indicating a slight improvement ranging from 16% to 21%.

With regard to reinforcement with polypropylene fibers under a confining pressure of 300 kPa (Figure 2b), it was observed that the maximum strength increased as the fiber content in the soil increased (0.3%, 0.6%, and 0.9%). The corresponding deviatoric stresses were 1000, 1150, and 1200 kPa, indicating strength increases of 25%, 44%, and 50%, respectively. This improvement could be explained by the emergence of contact forces leading to particle locking. Similar findings were reported by Shen et al. (2021) based on triaxial tests conducted on low-plasticity clay reinforced with fibers.

On the other hand, in the presence of Alfa fibers, an opposite effect of fiber reinforcement on the maximum shear strength was observed under low confining pressure (Figure 3a). Specifically, for a confining pressure of σ_3 = 100 kPa, the deviatoric stress decreased with the increase in fiber content of 0.3%, 0.6%, and 0.9%, reaching 350, 300, and 250 kPa, respectively. At higher confining pressure (σ_3 = 300 kPa) (Figure 3b), the soil samples were more confined and thus more resistant to deformation, resulting in a higher deviatoric stressat failure compared to samples tested at 100 kPa. In the case of Alfa fiber-reinforced soil, it was noted that under the same confinement (σ_3 = 300 kPa), the deviatoric stressslightly exceeded that of the unreinforced soil, reaching 850 kPa for a fiber content of 0.3%. For higher fiber contents (0.6% and 0.9%), the deviatoric stressvalues were approximately 750 and 790 kPa, respectively. However, a decrease in strength was observed in soil samples reinforced with Alfa

fibers, compared to the resistance of soil samples reinforced with polypropylene fibers.

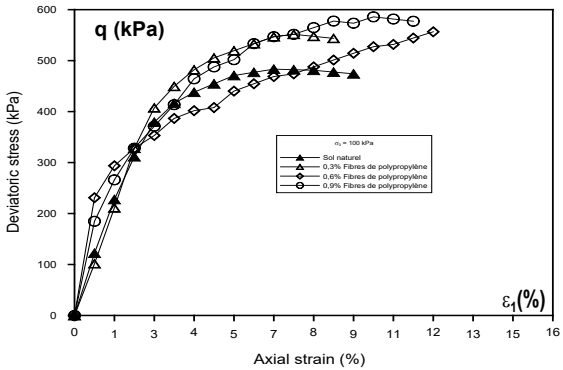

Figure 2a - Relationship between deviatoric stress and axial strain for polypropylene fiber-reinforced and unreinforced soils specimens under a confining pressure of 100 kPa

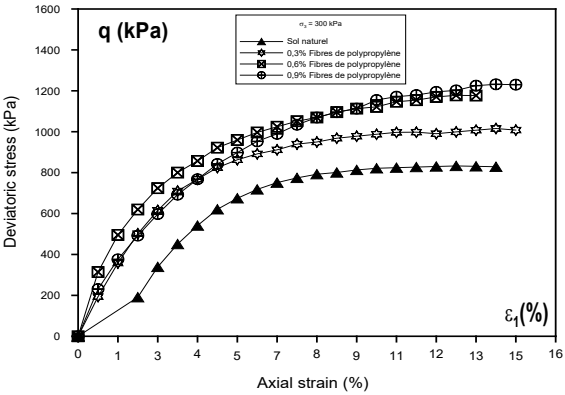

Figure 2b - Relationship between deviatoric stress and axial strain for polypropylene fiber-reinforced and unreinforced soils specimens under a confining pressure of 300 kPa

When the soil was treated with 4% cement and reinforced with fibers (Figures 3a, 3b, 4a and 4b), it was noted that its deviatoric stress became much larger than that of the untreated and unreinforced soil.

However, for a low confining pressure (σ_3 = 100 kPa) (Figure 4a), the Alfa fiber-reinforced and cemented soil presented a deviatoric stress ranging from 525 to 620 kPa corresponding to 0.3% to 0.9% of fibers content. On the other hand, for a high confining pressure (σ_3 = 300 kPa) (Figure 4b), an increase in the maximum shear strength was observed to reach 800, 900 and 1100 kPa for 0.3%, 0.6% and 0.9% of Alfa fibers.

Comparing with the natural sample, a maximum increase of 27% and 38% was obtained for low and high confining pressure, respectively.

Under low confining pressure (σ_3 = 100 kPa), samples reinforced with polypropylene fibers and cemented (Figures 5a), presented a maximum deviatoric stress values of 700, 760, and 850 kPa, corresponding to an increase of 78%, 73%, and 68% with 0.3%, 0.6%, and 0.9% of fibers, respectively. At high confining pressure (σ_3 = 300 kPa) (Figure 5b), the maximum deviatoric stresses were 1170, 1400 and 1430 kPa, corresponding to an increase of 46%, 75% and 79%, respectively.

In general, no peak shear strength was observed in cemented and fiber-reinforced samples, which explains the ductile behavior of the soil. Except for the case of those treated and reinforced with 0.6% and 0.9% Alfa fibers, under a low confining pressure (σ_3 =100 kPa) where a strength peak was observed, followed by a residual strength for a low confining pressure.

It can consequently be asserted that the incorporation of fibers, regardless of their nature, influences the behavior of the soil and enhances its deformation capacity. In other words, the soil becomes more ductile. The studies cited above indicate that the shear strength of the soil can be improved through the addition of reinforcing fibers. Furthermore, it is observed that there is a confining pressure limit which affects the shear strength of the soil. Similar observations were reported by Gray and Ohashi (1983), Estabragh et al. (2011, 2012), and Shen et al. (2021), who noted that below a certain confining pressure, fibers tend to slide or detach.

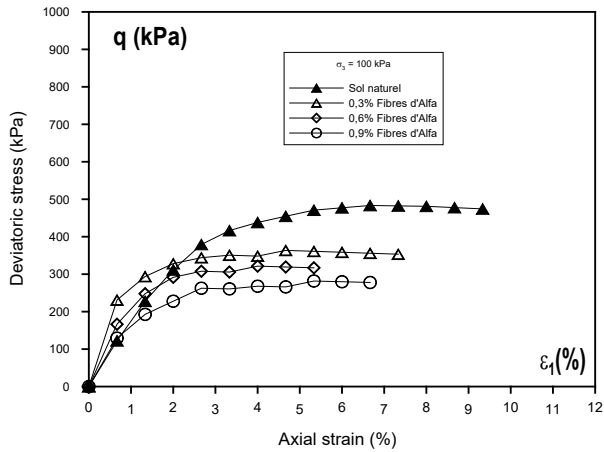

Figure 3a - Relationship between deviatoric stress and axial strain for Alfa fiber-reinforced and unreinforced soils specimens under a confining pressure of 100 kPa

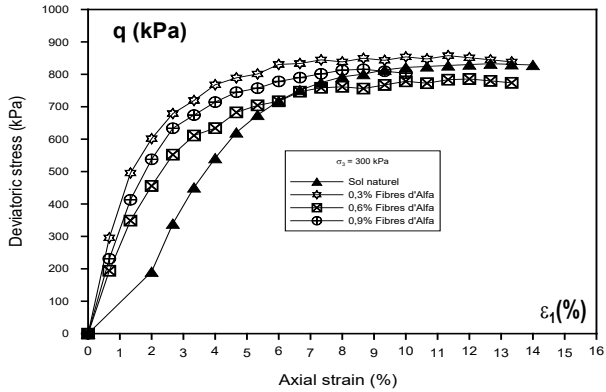

Figure 3b - Relationship between deviatoric stress and axial strain for Alfa fiber-reinforced and unreinforced soils specimens under a confining pressure of 300 kPa

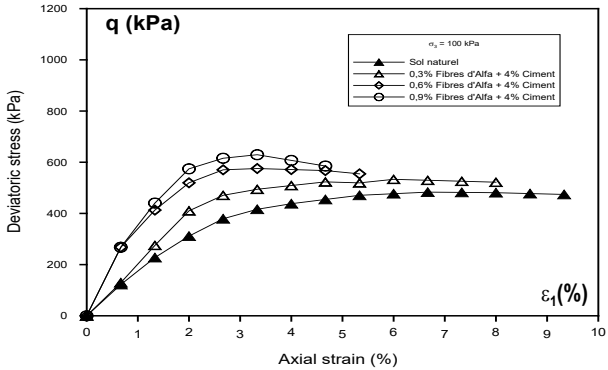

Figure 4a - Relationship between deviatoric stress and axial strain for cement-treated, Alfa fiber-reinforced, and unreinforced soil specimens under a confining pressure of 100 kPa

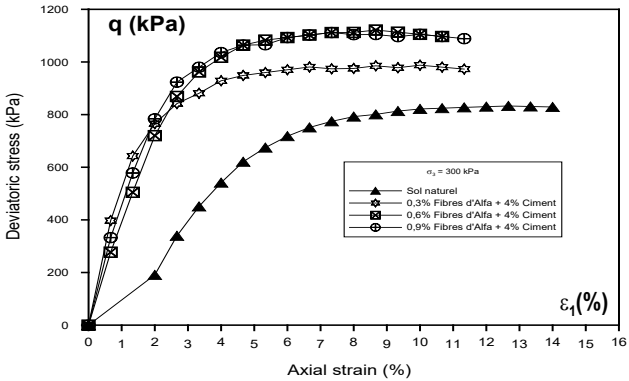

Figure 4b - Relationship between deviatoric stress and axial strain for cement-treated, Alfa fiber-reinforced, and unreinforced soil specimens under a confining pressure of 300 kPa

Figure 5 shows the variation of undrained maximum strength (q_{max}) as a function of fiber content for untreated and treated-reinforced samples. The results indicate that q_{max} of the fiber-reinforced cemented soil is influenced by both the confining pressure (σ_3) and the fiber content.

The q_{max} of the fiber-reinforced soil decreases with the percentage of Afla fibers (Figure 5a) and increases with the percentage of polypropylene fibers for both confining pressure (Figure 6b). In the case of Alfa fibers, the decrease in q_{max} could be due to the absorption of water by the latter, which alters their mechanical behavior and strength capacity. The increase of q_{max} for the polypropylene fibers (Figure 5b) can be attributed to their random distribution within the soil matrix, which forms a reinforcing structure that limits particle displacement and deformation of the soil. Conversely, for the reinforced and cemented samples, qmax increases consistently with fiber content, regardless of their nature. This can be explained by the cementation between particles of the soil and fibers.

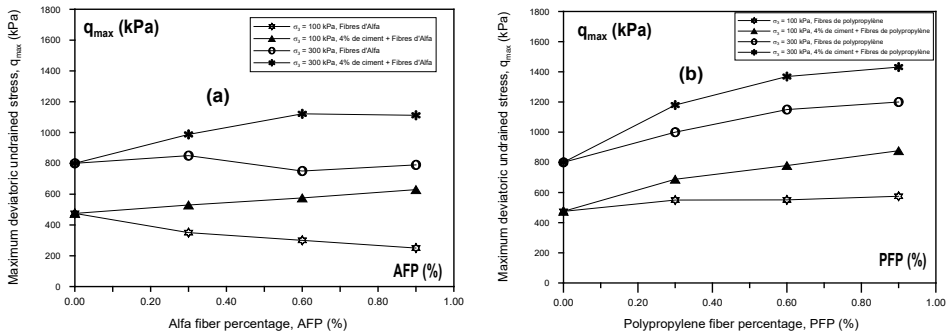

Figure 5 - Variation of undrained shear strength with fiber content at different confining pressures for untreated and cement-treated reinforced soil
(a) Alfa fibers, (b) *p*olypropylene fibers

Furthermore, the effect of cement treatment and reinforcement with two types of fibers on the mechanical strength parameters was examined in detail by analyzing the internal friction angle (ϕ_u) and cohesion (C_u), which were determined using Mohr's circles. Figure 6 illustrates an example of the determination of cohesion and the friction angle for the untreated samples.

It was observed that both parameters are influenced by the fiber content and the amount of cement used. Additionally, the variation of cohesion (C_u) and friction angle (ϕ_u) seems to be different between the samples that are only reinforced and those reinforced and cemented.

Figures 7 and 8 illustrate the effect of fiber reinforcement and treatment with 4% cement on the cohesion and internal friction angle of the soil. The results show a significant reduction in cohesion, for Alfa fiber-

reinforced samples (Figure 7a), decreasing from 100 kPa to 20 kPa as the fiber content increases from 0% to 0.9%, which corresponds to an 80% reduction. In contrast, samples reinforced with polypropylene fibers exhibit only a slight decrease in cohesion, from 100 kPa to 78 kPa (Figure 7b). This reduction in cohesion can be attributed to sliding between fibers, which reduces the interlocking effect and, hence, the cohesive strength. These observations are consistent with the findings of Consoli et al. (1998).

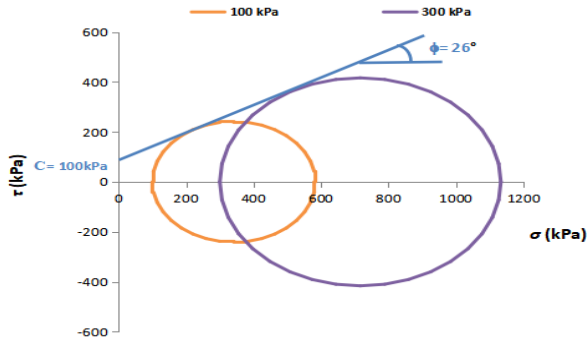

Figure 6 - Determination of shear strength parameters (C_u, ϕ_u) from Mohr's circles for the untreated samples

On the other hand, for samples treated with 4% cement and reinforced with Alfa fibers, the results show a slight increase in cohesion, from 100 kPa to 120 kPa, as the fiber content increases up to 0.9%, as shown in Figure 7a. This increase in cohesion is more pronounced in the case of polypropylene fiber reinforcement, where cohesion rises from 100 kPa to 160 kPa, representing an increase of approximately 60% compared to initial value (Figure 7b). The findings suggest that artificial fibers, in the presence of cement, promote better cementation of the soil matrix, thereby enhancing cohesion. Similar behavior was observed by Sivakumar Babu et al. (2008), Harichane et al. (2011), and Shen et al. (2021). Conversely, the presence of fibers in untreated soil tends to reduce cohesion. This may be due to grain sliding caused by the presence of fibers.

For samples treated with 4% cement and reinforced with Alfa fibers, the friction angle increased from 26° to 31° up to 0.3% fiber content, followed by a decrease of 3° when the fiber content exceeded 0.3%, as shown in Figure 8a. Conversely, in untreated soil samples reinforced with Alfa fibers, the friction angle increased up to 0.3% fiber content and then remained constant up to 0.9%.

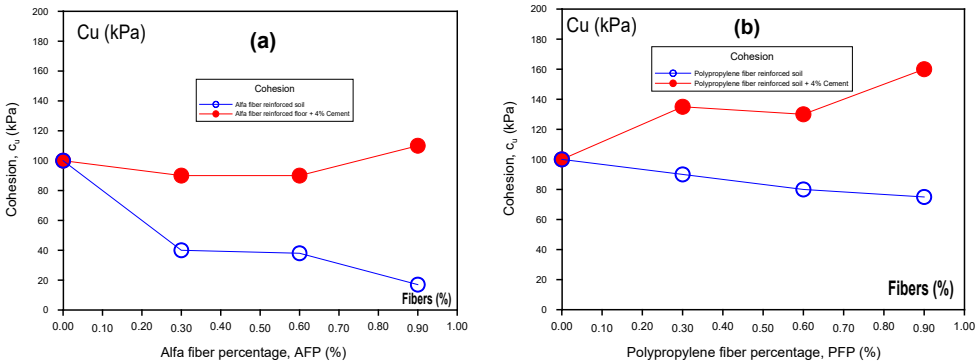

Figure 7 - Effect of fiber reinforcement and 4% cement treatment on soil cohesion: (a) Alfa fibers, (b) polypropylene fibers

With regard to the influence of cement treatment and fiber reinforcement on the friction angle, an increase from 26° to 34° was observed for samples treated with 4% cement and reinforced with 0.3% polypropylene fibers to an optimal content (Figure 8b). However, when the fiber content exceeded 0.3%, a slight angle decrease in the friction angle of about 2° was recorded. In contrast, untreated samples containing polypropylene fibers showed a continuous increase in friction angle with increasing fiber content (Figure 8b).

A simple comparison of the results regarding the influence of fibers on the friction angle and cohesion of samples treated with 4% cement and reinforced with fibers shows a general trend: an increase in cohesion for soils treated with 4% cement and reinforced with fibers (Figures 7a and 7b), as well as an increase in the internal friction angle for fiber-reinforced soils (Figures 8a and 8b).

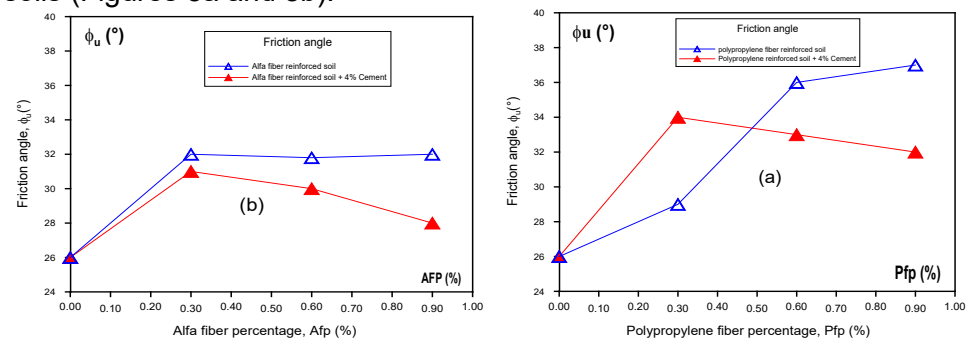

Figure 8 - Effect of fiber reinforcement and 4% cement treatmen on internal friction angle of the soil: (a) Alfa fiber, (b) polypropylene fiber

These findings can be attributed to the improvement of interfacial bonding and interlocking mechanisms between the fibers and soil particles as fiber content increases. It is important to note that fibers have the

potential to generate multiple points of intersection, leading to the formation of a fiber network that enhances the confinement effect within the soil matrix (Wei et al, 2018). However, a general tendency toward reduced cohesion was observed in fiber-reinforced soils, regardless of fiber type (Figures 7a and 7b), along with a decrease in the internal friction angle in cement-treated, fiber-reinforced soils beyond a fiber content of 0.3% (Figures 8a and 8b). This reduction can be attributed to fiber overlapping and fibers wrapping, which may cause the formation of weak interfaces, thereby reducing the friction angle. In addition, no optimum fiber content could be identified in terms of improving the cohesion of reinforced soils, as shown in Figures 7a and 7b.

Effect of fibers on the secant modulus of a cemented soil

Figure 9 illustrates the variation of the secant modulus(E_{50}%) as a function of fiber content determined from the deviator stress–strain curves. Two levels of confining pressure, i.e., 100 kPa and 300 kPa, were applied. For samples treated with 4% cement and reinforced with different percentages of fibers, the secant modulus values increased. However, the inclusion of fibers, regardless of their type, reduces the stiffness of untreated (cement-free) soils under low confining stress (100 kPa) (Figures 9a and 9b). These findings are in agreement with those reported by Ozkul and Baykal (2006), Ekinci and Ferreira (2012), Maliakal and Thiyyakkandi (2013), Ekinci (2016), and Mirzababaei et al. (2017, 2018). It is also worth noting that under higher confining stress (300 kPa), a clear increase in the secant modulus is observed, as illustrated in Figures 9c and 9d. In all cases, specimens treated with cement and reinforced with fibers (either polypropylene or Alfa) exhibited significantly higher stiffness compared to unreinforced samples.

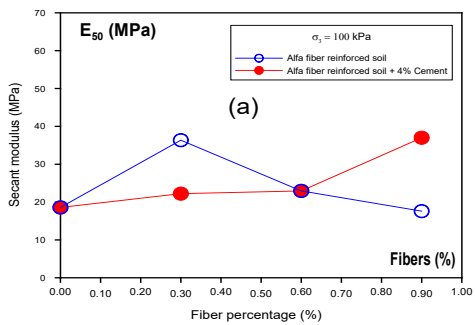

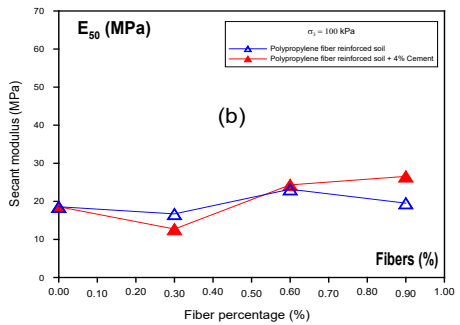

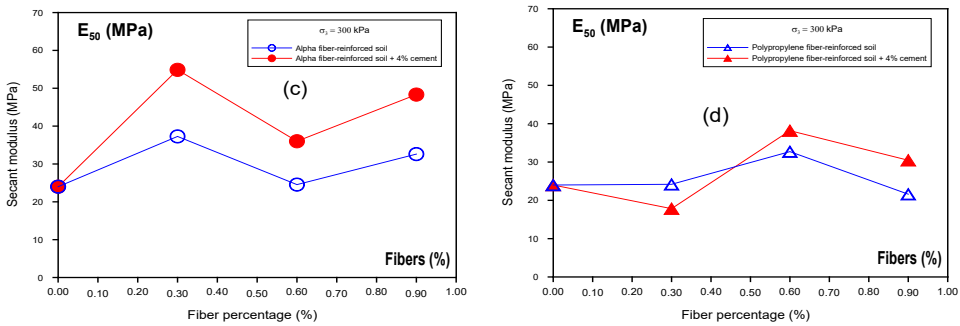

Figure 9 - Effect of fibers reinforcement and treatment at 4% cement on secant modulus of the soi: (a) Alfa and (b) polypropylene at 100 kPa confining pressure, (c) Alfa and (d) polypropylene at 300 kPa confining pressure

Effect of fibers on the unconfined compressive strength

Figures 10a and 10b present the evolution of the maximum unconfined compressive strength over curing time in open air for 1, 7, 14, and 28 days. A large number of tests were conducted in this study; however, only a selection of representative results is presented to illustrate the influence of fiber type and content. The findings clearly indicate that the unconfined compressive strength of specimens treated with 4% cement is significantly affected by both the nature and dosage of the added fibers.

Furthermore, in all cases analyzed, an increase in unconfined compressive strength was observed with the inclusion of polypropylene fibers in the presence of 4% cement, for fiber contents ranging from 0.3% to 0.9% (Figure 10a). This may be due to the entanglement of fibers and the bonding forces between soil particles, which have contributed to improved contact between the fiber surface and the soil matrix. The unconfined compressive strength reached its maximum values after 7 days of curing and remained nearly constant. The maximum UCS values recorded were 1380 kPa, 1510 kPa, and 1575 kPa for 0.3%, 0.6%, and 0.9% of fiber content respectively. Accordingly, an increase in unconfined compressive strength of approximately 47%, 43%, and 41% was observed for fiber contents of 0.3%, 0.6%, and 0.9%, respectively, compared to untreated soil. On the other hand, the compressive strengths of samples treated with 4% cement and reinforced with Alfa fibers after 7 days of curing time were lower than those reinforced with polypropylene fibers. However, at 14 days of curing time, the strength of samples reinforced with 0.9% Alfa fibers reached 1800 kPa, representing a 36% increase compared to the corresponding polypropylene fiber-reinforced samples (Figure 10b). These findings suggest that, overall, the combination of

fibers and cement significantly enhances the compressive strength of silty sand soils.

Similar findings have been reported by other researchers, such as Anggraini et al. (2015), Wei et al. (2018), Choobbasti et al. (2019), Shen et al. (2021), and Xiao et al. (2022), who demonstrated that the compressive strength of soils treated with hydraulic binders can be significantly improved.

It can be observed that the optimal compressive strength was achieved after 7 days of curing for all samples treated with cement and reinforced with polypropylene fibers (FP). Beyond this curing period, the strength values remained nearly constant up to 28 days (Figure 10a). In contrast, for samples treated with cement and reinforced with Alfa fibers (FA), the maximum compressive strength was reached after 14 days of curing (Figure 10b).

To better illustrate the influence of fiber content on the soil matrix, the variation in unconfined compressive strength (Rc) as a function of fiber percentage is presented in Figures 11a and 11b. It can be observed that uniaxial compressive strength increases with the fiber percentage. This is in agreement with several researchers (Kumar et al, 2007; Consoli et al, 2011; Shao et al, 2014; Kumar et al, 2018).

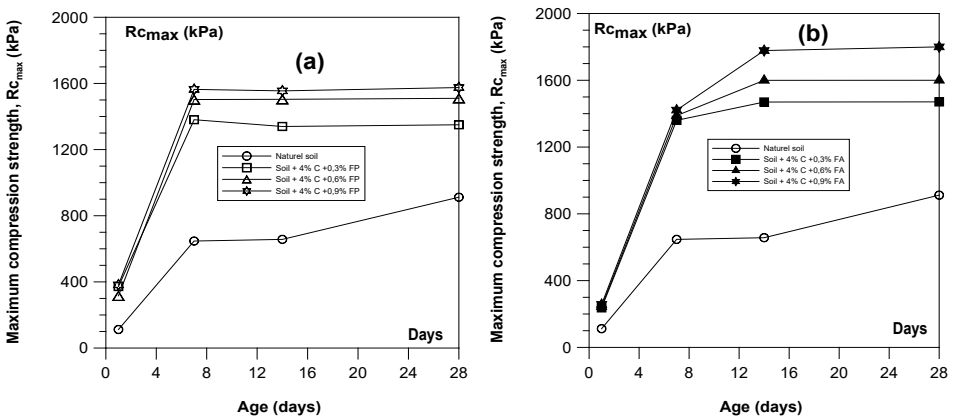

Figure 10 - Effect of curing time on the maximum compressive strength of soil specimens reinforced with fibers and stabilized with 4% cement in open-air condition: (a) polypropylene fibers, (b) Alfa fibers

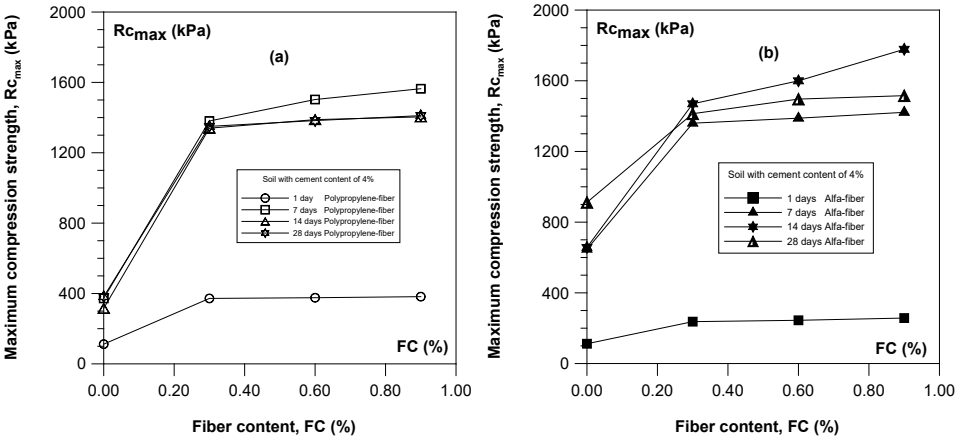

Figure 11 - Effect of fiber type and content on UCS in open-air curing conditions: (a) polypropylene fibers, (b) Alfa fibers

Conclusion

This study investigated the effects of two types of fibers (polypropylene and Alfa) on the mechanical properties of silty sand through unconsolidated undrained triaxial and unconfined compression tests. The results show that fiber reinforcement significantly improved the geotechnical properties of the soil, particularly its shear and compressive strength. The key findings are as follows:

1. Polypropylene fibers (0.9%) significantly increased shear strength, thanks to their high tensile strength and the strong frictional bond between soil particles and fibers. Alfa fibers (0.3%) also improved shear resistance, but to a lesser extent.

2. Soil samples treated with 4% cement and reinforced with polypropylene fibers exhibited ductile behavior across both confining stresses (100 and 300 kPa). In contrast, cement-treated samples reinforced with Alfa fibers were slightly brittle at low confining stress but became more ductile under higher confining stress.

3. The cohesion of the samples treated with 4% cement increased as the fiber content increased. This increase was higher in the case of cement-treated samples reinforced with polypropylene fibers. The cohesion value was equal to 160kPa for samples reinforced with 0.9% polypropylene fibers. However, the samples treated with cement and reinforced with Alfa fibers had a cohesion value of 110 kPa for the same reinforcement percentage.

4. The friction angle for cement-treated samples reinforced with 0.3% polypropylene fibers increased from 26° to 34°. On the other hand, the friction angle for untreated and fiber-reinforced samples also increased with fiber content. In general, the friction angles of the untreated and reinforced samples were higher than those of treated and reinforced samples.

5. The secant modulus (E50%) of the cemented and Alfa fiber-reinforced samples was higher than those reinforced with synthetic fibers. Nevertheless, the stiffness of the reinforced samples with synthetic fiber was greater than the natural samples. The optimal stiffness was achieved with 0.3% Alfa fibers and 0.6% polypropylene fibers.

6. The UCS test showed that both polypropylene and Alfa fibers increased the compressive strength of the soil. The soil reinforced with polypropylene fiber exhibited a higher compressive strength (42%) than the untreated soil. Furthermore, the compressive strength of Alfa fiber-reinforced samples increased by 36% at 14 days of curing. The fiber entanglement and bonding forces between the soil particles contributed to this improvement.

Overall, the combination of cement treatment and fiber reinforcement is highly effective in improving the soil's mechanical properties, offering a cost-effective solution with environmental benefits, particularly with the use of natural fibers like Alfa in civil engineering and road construction projects.

References

Abou Diab, S., Sadek, S., Najjar, M.H. and Abou Daya, M. (2016) 'Undrained shear strength characteristics of compacted clay reinforced with natural hemp fibers', *International Journal of Geotechnical Engineering*, 10(3), pp. 263–270. Available at: https://doi.org/10.1080/19386362.2015.1133758

AFNOR (2012). *Ciment – Partie 1 : composition, spécifications et critères de conformité des ciments courants (*NF EN 197-1). Association Française de Normalisation.

Al-Refeai, T.O. (1991) 'Behavior of granular soils reinforced with discrete randomly oriented inclusions', *Geotextiles and Geomembranes*, 10(4), pp. 319–333. Available at: https://doi:10.1016/0266-1144(91)90009-L.

Anggraini, V., Huat, B.B.K., Asadi, A. and Nahazanan, H. (2015) 'Effect of coir fibers on the tensile and flexural strength of soft marine clay', *Journal of Natural Fibers*, 12(2), pp. 185–200. Available at: https://doi.org/10.1080/15440478.2014.914909

Araldi, E., Vincens, E., Fabbri, A. and Plassiard, J.P. (2018) 'Identification of the mechanical behavior of rammed earth including water content influence',

Materials and Structures, 51, Article no. 88. Available at: https://doi:10.1617/s11527-018-1203-2.

ASTM D4767 (2000) *Standard test method for consolidated undrained triaxial compression test for cohesive soils*. West Conshohocken, PA: ASTM International.

ASTM D4972 (1995) *Standard test method for pH of soils. (ASTM D4972).* West Conshohocken, PA.

ASTM D698-78 (2012) *Standard test methods for laboratory compaction characteristics of soil using standard effort*. West Conshohocken, PA: *American Society for Testing and Materials.*

Athanasopoulos, G.A. (1994) 'On the enhanced confining pressure approach to the mechanics of reinforced soil', *Geotechnical and Geological Engineering*, 12(2), pp. 122–134. Available at: https://doi.org/10.1007/BF00426177

Choobbasti, A.J., Samakoosh, M.A. and Kutanaei, S.S. (2019) 'Mechanical properties of soil stabilized with nano calcium carbonate and reinforced with carpet waste fibers', *Construction and Building Materials*, 211, pp. 1094–1104. Available at: https://doi.org/10.1016/j.conbuildmat.2019.03.306

Consoli, N.C. and Prietto, D.M. (1998) 'Influence of fiber and cement addition in sandy soils', *Journal of Geotechnical and Geoenvironmental Engineering*, 124(12), pp. 1211–1214. Available at: https://doi.org/10.1061/(ASCE)1090-0241(1998)124:12(1211

Consoli, N.C., Bassani, M.A.A. and Festugato, L. (2010) 'Effect of fiber reinforcement on the strength of cemented soils', *Geotextiles and Geomembranes*, 28(4), pp. 344–351. Available at: https://doi.org/10.1016/j.geotexmem.2010.01.005

Consoli, N.C., Nierwinski, H.P., da Silva, A.P. and Sosnoski, J. (2017) 'Durability and strength of fiber-reinforced compacted gold tailings–cement blends', *Geotextiles and Geomembranes*, 45(2), pp. 98–102. Available at: https://doi:10.1016/j.geotexmem.2017.01.001.

Consoli, N.C., Thomé, A., Girardello, V. and Ruver, C.A. (2012) 'Uplift behavior of plates embedded in fiber-reinforced cement stabilized backfill', *Geotextiles and Geomembranes*, 35, pp. 107–111. Available at: https://doi.org/10.1016/j.geotexmem.2012.05.006

Consoli, N.C., Vendruscolo, M.A., Fonini, A. and Rosa, F.D. (2009) 'Fiber reinforcement effects on sand considering a wide cementation range', *Geotextiles and Geomembranes*, 27(3), pp. 196–203. Available at: https://doi.org/10.1016/j.geotexmem.2008.11.005

Consoli, N.C., Zortéa, F., de Souza, M. and Festugato, L. (2011) 'Studies on the dosage of fiber-reinforced cemented soils', *Journal of Materials in Civil Engineering*, 23(12), pp. 1624–1632. Available at: https://doi:10.1061/(ASCE)MT.1943-5533.0000343.

Correia, A.A., Oliveira, P.J.V. and Custódio, D.G. (2015) 'Effect of polypropylene fibres on the compressive and tensile strength of a soft soil, artificially stabilised with binders', *Geotextiles and Geomembranes*, 43(2), pp. 97–106. Available at: https://doi.org/10.1016/j.geotexmem.2015.02.001

Cristelo, N., Cunha, V.M., Gomes, A.T., Araújo, N., Miranda, T. and Lopes, M.L. (2017) 'Influence of fibers reinforcement on the post-cracking behaviour of a cement-stabilised sandy clay subjected to indirect tensile stress', *Construction and Building Materials*, 138, pp. 163–173. Available at: https://doi.org/10.1016/j.conbuildmat.2017.02.010

Dallel, M. (2012) Évaluation du potentiel textile des fibres d'Alfa (Stipa tenacissima L.): caractérisation physico-chimique de la fibre au fil. PhD thesis. Université de Haute-Alsace, France.

Dasaka, S.M. and Sumesh, K.S. (2011) 'Effect of coir fiber on the stress–strain behavior of a reconstituted fine-grained soil', *Journal of Natural Fibers*, 8(3), pp. 189–204. Available at: https://doi.org/10.1080/15440478.2011.601614

Diambra, A. and Ibraim, E. (2014) 'Modelling of fibers–cohesive soil mixtures', *Acta Geotechnica*, 9(6), pp. 1029–1043. Available at: https://doi.org/10.1007/s11440-013-0283-y

Diambra, A., Ibraim, E., Wood, D.M. and Russell, A.R. (2010) 'Fibre reinforced sands: experiments and modelling', *Geotextiles and Geomembranes*, 28(3), pp. 238–250. Available at: https://doi.org/10.1016/j.geotexmem.2009.09.010

Ekinci, A. (2016) The mechanical properties of compacted clay from the Lambeth Group using fiber reinforcement. PhD thesis. University College London.

Ekinci, A. and Ferreira, P.M.V. (2012) 'The undrained mechanical behaviour of a fiber reinforced heavily over-consolidated clay', in: Proceedings of the International Symposium on Ground Improvement (ISSMGE TC 211), Brussels, Belgium.

Estabragh, A.R., Bordbar, A.T. and Javadi, A.A. (2011) 'Mechanical behavior of a clay soil reinforced with nylon fibers', *Geotechnical and Geological Engineering*, 29(5), pp. 899–908. Available at: https://doi.org/10.1007/s10706-011-9424-y

Estabragh, A.R., Namdar, P. and Javadi, A.A. (2012) 'Behavior of cement stabilized clay reinforced with nylon fiber', *Geosynthetics International*, 19(1), pp. 85–92. Available at: https://doi.org/10.1680/gein.2012.19.1.85

Falorca, I.M.C.F.G. and Pinto, M.I.M. (2011) 'Effect of short, randomly distributed polypropylene microfibres on shear strength behaviour of soils', *Geosynthetics International*, 18(1), pp. 2–11. Available at: https://doi.org/10.1680/gein.2011.18.1.2

Festugato, L., Menger, E., Benezra, F., Kipper, E.A. and Consoli, N.C. (2017) 'Fibre-reinforced cemented soils compressive and tensile strength assessment as a function of filament length', *Geotextiles and Geomembranes*, 45(1), pp. 77–82. Available at: https://doi.org/10.1016/j.geotexmem.2016.09.001

Ghavami, K., Toledo Filho, R.D. and Barbosa, N.P. (1999) 'Behaviour of composite soil reinforced with natural fibres', *Cement and Concrete Composites*, 21(1), pp. 39–48. Available at: https://doi.org/10.1016/S0958-9465(98)00033-X

Ghembaza M. S., Bourokba S. A., Hachichi A., Djeloul R. (2023) Influence of the fibers nature on the shear strength of silty sand. *Algeria Equipment*, N° 68,

pp 23-30, e-ISSN: 2716-7801. Available at: https://doi.org/10.5281/zenodo.1000000

Gray, D.H. (1978) 'Role of woody vegetation in reinforcing soils and stabilizing slopes', in: Proceedings of the Symposium on Soil Reinforcing and Stabilising Techniques, Sydney, Australia, pp. 253–306.

Gray, D.H. and Al-Refeai, T. (1986) 'Behavior of fabric-versus fiber-reinforced sand', *Journal of Geotechnical Engineering*, 112(8), pp. 804–820. Available at: https://doi.org/10.1061/(ASCE)0733-9410(1986)112:8(804)

Gray, D.H. and Ohashi, H. (1983) 'Mechanics of fiber reinforcement in sand', *Journal of Geotechnical Engineering*, 109(3), pp. 335–353. Available at: https://doi.org/10.1061/(ASCE)0733-9410(1983)109:3(335)

Hamidi, A. and Hooresfand, M. (2013) 'Effect of fiber reinforcement on triaxial shear behavior of cement treated sand', *Geotextiles and Geomembranes*, 36(1), pp. 1–9. Available at: https://doi.org/10.1016/j.geotexmem.2012.10.005

Hanana, S., Elloumi, A., Placet, V., Tounsi, H., Belghith, H. and Bradai, C. (2015) 'An efficient enzymatic-based process for the extraction of high-mechanical properties alfa fibres', *Industrial Crops and Products*, 70, pp. 190–200. Available at: https://doi.org/10.1016/j.indcrop.2015.03.023

Harichane, K., Ghrici, M., Kenai, S. and Grine, K. (2011) 'Use of natural pozzolana and lime for stabilization of cohesive soils', *Geotechnical and Geological Engineerin*g, 29(5), pp. 759–769. Available at: https://doi.org/10.1007/s10706-011-9415-z

Hossain, M.A., Hossain, M.S. and Hasan, M.K. (2015) 'Application of jute fiber for the improvement of sub grade characteristics', *American Journal of Civil Engineering*, 3(2), pp. 26–30. Available at: https://doi.org/10.11648/j.ajce.20150302.11

Ikhlef, N.S., Ghembaza, M.S. and Dadouch, M. (2015) 'Effect of treatment with cement on the mechanical characteristics of silt from Telagh region of Sidi Belabes, Algeria', *Geotechnical and Geological Engineering*, 33(4), pp. 987–996. Available at: https://doi.org/10.1007/s10706-015-9888-2

Imanzadeh, M., Hibouche, A., Jarno, A. and Taibi, S. (2018) 'Formulating and optimizing the compressive strength of a raw earth concrete by mixture design', *Construction and Building Materials*, 163, pp. 149–159. Available at: https://doi.org/10.1016/j.conbuildmat.2017.12.122

Janz, M. and Johansson, S.E. (2002) The function of different binding agents in deep stabilization. *Report 9, Swedish Deep Stabilization Research Centre*. Available at: https://www.sip-vips.se/deep-stabilization-report-9

Jiang, H., Cai, Y. and Liu, J. (2010) 'Engineering properties of soils reinforced by short discrete polypropylene fiber', *Journal of Materials in Civil Engineering*, 22(12), pp. 1315–1322. Available at: https://doi.org/10.1061/(ASCE)MT.1943-5533.0000129

Khattak, M.J. and Alrashidi, M. (2006) 'Durability and mechanistic characteristics of fiber reinforced soil–cement mixtures', *International Journal of Pavement Engineering*, 7(1), pp. 53–62. Available at: https://doi.org/10.1080/10298430500489121

Kumar, A., Walia, B.S. and Bajaj, A. (2007) 'Influence of fly ash, lime, and polyester fibers on compaction and strength properties of expansive soil', *Journal of Materials in Civil Engineering*, 19(3), pp. 242–248. Available at: https://doi.org/10.1061/(ASCE)0899-1561(2007)19:3(242)

Kumar, J.S. and Sharma, P. (2018) 'Geotechnical properties of pond ash mixed with cement kiln dust and polypropylene fiber', *Journal of Materials in Civil Engineering*, 30(8), Article ID 04018154. Available at: https://doi.org/10.1061/(ASCE)MT.1943-5533.0002360

Lee, F.H., Lee, Y., Chew, S.H. and Yong, K.Y. (2005) 'Strength and modulus of marine clay–cement mixes', *Journal of Geotechnical and Geoenvironmental Engineering,* 131(2), pp. 178–186. Available at: https://doi.org/10.1061/(ASCE)1090-0241(2005)131:2(178)

Li, J. and Zomberg, G. (2013) 'Mobilization of reinforcement forces in fiber-reinforced soil', *Journal of Geotechnical and Geoenvironmental Engineering*, 139(1), pp. 107–115. Available at: https://doi.org/10.1061/(ASCE)GT.1943-5606.0000745

Maliakal, T. and Thiyyakkandi, S. (2013) 'Influence of randomly distributed coir fibers on the shear strength of clay', Geotechnical and Geological Engineering, 31(2), pp. 425–433. Available at: https://doi.org/10.1007/s10706-012-9595-6

Mesbah, A., Morel, J.C., Walker, P. and Ghavami, K. (2004) 'Development of a direct tensile test for compacted earth blocks reinforced with natural fibers', *Journal of Materials in Civil Engineering*, 16(1), pp. 95–98. Available at: https://doi.org/10.1061/(ASCE)0899-1561(2004)16:1(95)

Michalowski, R.L. and Cermak, J. (2003) 'Triaxial compression of sand reinforced with fibers', *Journal of Geotechnical and Geoenvironmental Engineering*, 129(2), pp. 125–136. Available at: https://doi.org/10.1061/(ASCE)1090-0241(2003)129:2(125)

Michalowski, R.L. and Zhao, A. (1996) 'Failure of fiber-reinforced granular soils', *Journal of Geotechnical Engineering*, 122(3), pp. 226–234. Available at: https://doi.org/10.1061/(ASCE)0733-9410(1996)122:3(226)

Mirzababaei, M., Arulrajah, A., Haque, A., Nimbalkar, S. and Mohajerani, A. (2018) 'Effect of fiber reinforcement on shear strength and void ratio of soft clay', *Geosynthetics International*, 25(4), pp. 471–480. Available at: https://doi.org/10.1680/jgein.18.00023

Mirzababaei, M., Arulrajah, A., Horpibulsuk, S. and Aldava, M. (2017) 'Shear strength of a fiber-reinforced clay at large shear displacement under different stress histories', *Geotextiles and Geomembranes*, 45(5), pp. 422–429. Available at: https://doi.org/10.1016/j.geotexmem.2017.06.002

Mirzababaei, M., Arulrajah, A., Horpibulsuk, S., Soltani, A. and Khayat, N. (2018) 'Stabilization of soft clay using short fibers and polyvinyl alcohol', *Geotextiles and Geomembranes*, 46(5), pp. 646–655. Available at: https://doi.org/10.1016/j.geotexmem.2018.05.001

Nguyen, L. and Fatahi, B. (2016) 'Behaviour of clay treated with cement and fibers while capturing cementation degradation and fiber failure – C3F Model',

International Journal of Plasticity, 81, pp. 168–195. Available at: https://doi.org/10.1016/j.ijplas.2016.01.010

Olgun, M. (2013) 'Effects of polypropylene fiber inclusion on strength and volume change characteristics of cement-fly ash stabilized clay soil', *Geosynthetics International*, 20(4), pp. 263–275. Available at: https://doi.org/10.1680/gein.13.00016

Özkul, Z.H. and Baykal, G. (2006) 'Shear strength of clay with rubber fiber inclusions', *Geosynthetics International*, 13(5), pp. 173–180. Available at: https://doi.org/10.1680/gein.2006.13.5.173

Parkavan, H., Jamshidi, M., Latifi, M. and Pacheco-Torgal, F. (2012) 'Evaluation of adhesion in polymeric fiber reinforced cementitious composites', *International Journal of Adhesion and Adhesives*, 32, pp. 53–60. Available at: https://doi.org/10.1016/j.ijadhadh.2011.09.006

Prabakar, J. and Sridhar, R. (2002) 'Effect of random inclusion of sisal fiber on strength behaviour of soil', *Construction and Building Materials*, 16(2), pp. 123–131. Available at: https://doi.org/10.1016/S0950-0618(02)00005-2

Pradani, N., Irdhiani, W. and Wibowo, J. (2017) 'Analysis of local sanded soil with coconut coir fiber reinforcement as subgrade on structural pavement', *International Journal of Civil Engineering and Technology*, 8, pp. 787–795. Available at: https://iaeme.com/Home/article_id/IJCIET_08_11_080

Pradhan, P.K., Kar, R.K. and Naik, A. (2012) 'Effect of random inclusion of polypropylene fibers on strength characteristics of cohesive soil', *Journal of Materials in Civil Engineering*, 24(9), pp. 1216–1220. Available at: https://doi.org/10.1061/(ASCE)MT.1943-5533.0000490

Savastano Jr, H., Warden, P.G. and Coutts, R.S.P. (2000) 'Brazilian waste fibers as reinforcement for cement-based composites', *Cement and Concrete Composites*, 22(5), pp. 379–384. Available at: https://doi.org/10.1016/S0958-9465(00)00034-2

Shao, W., Cetin, B., Li, Y., Li, J. and Li, L. (2014) 'Experimental investigation of mechanical properties of sands reinforced with discrete randomly distributed fiber', *Geotechnical and Geological Engineering*, 32(4), pp. 901–910. Available at: https://doi.org/10.1007/s10706-014-9766-3

Shen, Y.S., Tang, Y.Y., Li, J., Wen, M.P. and Ting, T. (2021) 'An experimental investigation on strength characteristics of fiber-reinforced clayey soil treated with lime or cement', *Construction and Building Materials*, 294, Article ID 123537. Available at: https://doi.org/10.1016/j.conbuildmat.2021.123537

Silveira, J.V.W., Meireles, A.B. and Ferreira, E.P. (2020) 'Biopolymer membranes for dentistry applications', in: Moraes, M.A., da Silva, C.F. and Vieira, R.S. (eds.) *Biopolymer Membranes and Films*. Elsevier, pp. 243–272. Available at: https://doi.org/10.1016/B978-0-12-818134-8.00010-9

Sivakumar Babu, G. and Vasudevan, A. (2008) 'Strength and stiffness response of coir fiber reinforced tropical soil', *Journal of Materials in Civil Engineering*, 20(9), pp. 571–577. Available at: https://doi.org/10.1061/(ASCE)0899-1561(2008)20:9(571)

Taylor, H.F.W. (1997) *Cement Chemistry*. 2nd ed. London: Thomas Telford Publishing. Available at: https://doi.org/10.1680/cc.25929

Uddin, S., Marri, A. and Wanatowski, D. (2011) 'Effect of high confining pressure on the behaviour of fiber reinforced sand', *Geotechnical Engineering Journal of the SEAGS & AGSSEA*, 42(4), pp. 69–76. Available at: https://seags.ait.ac.th/journals

Vilenkina, N. (1956) *Utilisation de matériau sol dans la construction des bâtiments ruraux*. Moscou, URSS

Viswanadham, B.V.S., Phanikumar, B.R. and Mukherjee, R.V. (2009) 'Swelling behaviour of a geofiber-reinforced expansive soil', *Geotextiles and Geomembranes*, 27(1), pp. 73–76. Available at: https://doi.org/10.1016/j.geotexmem.2008.06.002

Waldron, L.J. (1977) 'The shear resistance of root-permeated homogeneous and stratified soil', *Soil Science Society of America Journal*, 41(5), pp. 843–849. Available at: https://doi.org/10.2136/sssaj1977.03615995004100050005x

Wang, J.Q., Zhang, L.L., Xue, J.F. and Tang, Y. (2018) 'Load-settlement response of shallow square footings on geogrid-reinforced sand under cyclic loading', *Geotextiles and Geomembranes*, 46(5), pp. 586–596. Available at: https://doi.org/10.1016/j.geotexmem.2018.04.009

Wang, Q., Tang, R., Cheng, Q., Wang, X. and Liu, F.L. (2014) 'Research on static triaxial mechanical properties of new cement soil reinforced with polypropylene fiber', Advances in Materials Science and Engineering, 8, pp. 1–10. Available at: https://doi.org/10.1155/2014/198730

Wei, L., Chai, S.X., Zhang, H.Y. and Shi, Q. (2018) 'Mechanical properties of soil reinforced with both lime and four kinds of fiber', *Construction and Building Materials*, 172, pp. 300–308. Available at: https://doi.org/10.1016/j.conbuildmat.2018.03.248

Wu, T.H., McOmber, R.M., Erb, R.T. and Beal, P.E. (1988) 'Study of soil–root interaction', *Journal of Geotechnical Engineering*, 114(12), pp. 1351–1375. Available at: https://doi.org/10.1061/(ASCE)0733-9410(1988)114:12(1351)

Xiao, H., Lee, F.H., Zhang, M. and Yeoh, S. (2013) 'Fiber reinforced cement treated clay', *in: Proceedings of the 18th International Conference on Soil Mechanics and Geotechnical Engineering*. Paris, France, pp 1111-1114.

Xiao, Y., Tong, L., Che, H., Guo, Q. and Pan, H. (2022) 'Experimental studies on compressive and tensile strength of cement-stabilized soil reinforced with rice husks and polypropylene fibers', *Construction and Building Materials*, 344, Article ID 128242. Available at: https://doi.org/10.1016/j.conbuildmat.2022.128242

Yetimoglu, T. and Salbas, O. (2003) 'A study on shear strength of sands reinforced with randomly distributed discrete fibers', *Geotextiles and Geomembranes*, 21(2), pp. 103–110. Available at: https://doi.org/10.1016/S0266-1144(03)00003-7

Poboljšanje performansi muljevitog peska primenom cementa i vlaknaste armature: studija mehaničkog ponašanja

Asma Halimi[a], *Souad* Amal Bourokba[b], *Moulay* Smaine Ghembaza[a], **autor za prepisku**, *Abdelkader* Hachichi[b]

[a] DjlillaliLiabès University of Sidi Bel-Abbès, Civil Engineering and Environment Laboratory (LGCE),

[b] Civil Engineering Department, Materials Soil and Thermal Laboratory (LMST), University of Sciences and Technology Mohamed Boudiaf Oran, El Mnaouar, BP 1505, Bir El Djir 31000, Oran, Algeria

OBLAST: geotehnika
KATEGORIJA (TIP) ČLANKA: originalni naučni rad

Sažetak:

Uvod/cilj: Cilj ovog rada je valorizacija lokalnog materijala iz zapadnog regiona Alžira za potencijalnu primenu u izgradnji puteva. Glavni cilj je ispitivanje uticaja dodavanja sintetičkih polipropilenskih vlakana i prirodnih biljnih vlakana Alfa u različitim količinama (0%, 0,3%, 0,6% i 0,9%) na čvrstoću muljevitog peska stabilizovanog sa 4% cementa.

Metode: Ispitivanje se vrši testovima jednoaksijalne (nekonfinovane) čvrstoće i nekonsolidovanim nedreniranim triaksijalnim testovima. Ispitivanja se sprovode na mešavinama sastava tlo–vlakna–cement koje su statički zbijene u uslovima standardnog Proktorovog optimuma (SOP) (γdmax = 17 kN/m³ i wopt = 16,6%) i očvrsle su na otvorenom u vremenskom periodu od jedan, sedam i 28 dana.

Rezultati: Rezultati su pokazali značajno poboljšanje mehaničke čvrstoće tretiranog tla, uz promenu ponašanja pri lomu iz krhkog u duktilno. Dodatak 0,3% vlakana povećao je koheziju uz istovremeno smanjenje ugla unutrašnjeg trenja. Pored toga, uzorci ojačani vlaknima i cementom pokazali su veću krutost u poređenju sa netretiranim tlom. Takođe, najveća jednoaksijalna čvrstoća na pritisak postignuta je kombinacijom 0,9% vlakana i 4% cementa.

Zaključak: Ojačavanje cementiranog muljevitog peska polipropilenskim i Alfa vlaknima značajno poboljšava njegovu mehaničku čvrstoću i krutost. Dodatak od 0,9% vlakana daje najveću čvrstoću na pritisak, uz efikasan prelaz ponašanja tla iz krhkog u duktilno. Ovi rezultati potvrđuju da je valorizacija lokalnih alžirskih materijala tehnički izvodljivo i održivo rešenje za razvoj infrastrukture puteva.

Ključne reči: muljeviti pesak, biljka Alfa, polipropilenska vlakna, otpornost na smicanje, ugao trenja, kohezija, jednoaksijalna čvrstoća na pritisak.

Paper received on: 8 July 2025.
Manuscript corrections submitted on: 16 July 2025.
Paper accepted for publishing on: 28 October 2025.

© 2026 The Authors. Published by Vojnotehnički glasnik / Military Technical Courier (www.vtg.mod.gov.rs).This article is an open access article distributed under the terms and conditions the Creative Commons Attribution license (http://creativecommons.org/licenses/by/4.0/rs/)

Evaluation of the durability performance of roller-compacted concrete incorporating recycled pavement materials

Fadhila Ali Kouadri[a], *Mohamed* Salhi[b], *Toufik* Boubekeur[c], *Amar* Benyahia[d], *Alex* Li[e], *Boussad* Abbès[f]

[a] Ahmed Zabana University, Faculty of Sciences and Technology, Civil Engineering Department, Innovative Materials Laboratory and Renewable Energies,Relizane, Algeria,
e-mail: fadhila.alikouadri@univ-relizane.dz,
ORCID iD: https://orcid.org/0009-0003-5197-8404

[b] Ahmed Zabana University, Faculty of Sciences and Technology, Civil Engineering Department, Innovative Materials Laboratory and Renewable Energies, Relizane, Algeria,
e-mail: mohamed.salhi@univ-relizane.dz, **corresponding author**,
ORCID iD: https://orcid.org/0009-0007-7920-9120

[c] Civil Engineering, Mechanical and Transportation Department, Faculty of Science and Technology, Tissemsilt University, P. O. B. 182, 38000 Tissemsilt, Algeria,
e-mail: t_boubekeur@yahoo.fr,
ORCID iD: https://orcid.org/0000-0003-4947-2300

[d] Saad Dahlab University, Faculty of Sciences and Technology, Department of Civil Engineering, Blida, People's Democratic Republic of Algeria,
e-mail: a.benyahia@univ-chlef.dz,
ORCID iD: https://orcid.org/0000-0001-6404-0173

[e] University of Reims Champagne-Ardenne, MATIM, Reims, France,
e-mail: alex.li@univ-reims.fr,
ORCID iD: https://orcid.org/0000-0003-4291-9595

[f] University of Reims Champagne-Ardenne, MATIM, Reims, France,
e-mail: boussad.abbes@univ-reims.fr,
ORCID iD: https://orcid.org/0000-0003-1192-6549

https://doi.org/10.5937/vojtehg74-60831

FIELD: materials
ARTICLE TYPE: original scientific paper

Abstract:

Introduction/purpose: This research investigates the durability of roller-compacted concrete pavement (RCCP) incorporating reclaimed asphalt pavement (RAP) as a partial or full replacement for natural aggregates (NA). The primary objective is to assess the feasibility of using RAP in pavement concrete from both performance and sustainability perspectives.

ACKNOWLEDGMENT: This research was supported by the Innovative Materials Laboratory and Renewable Energies, Civil Engineering Department, University of Relizane, Algeria, under the authority of the Ministry of Higher Education and Scientific Research.

Methods: Concrete mixtures were prepared with four RAP substitution levels: 25%, 50%, 75%, and 100%. Durability tests were performed to evaluate the resistance of these mixes to acid and sulfate attacks. Additionally, microstructural analyses were conducted using scanning electron microscopy (SEM) and X-ray diffraction (XRD) to examine internal changes resulting from chemical exposure.

Results: The incorporation of RAP improved durability against acid and sulfate attacks, particularly at substitution levels up to 50%. Beyond this threshold, a slight decline in performance was observed, though it remained within acceptable limits. SEM images revealed a denser matrix and stronger bonding between the cement paste and RAP aggregates. XRD analysis confirmed the presence of stable hydration products, even after exposure to aggressive solutions.

Conclusion: The findings support the use of RAP as a viable and sustainable alternative to NA in RCCP. At optimal substitution levels, it enhances durability, contributes to environmental protection, reduces construction waste, and offers cost-effective solutions by utilizing recycled materials.

Key words: roller-compacted concrete, recycled aggregates pavement, microstructure, durability.

Introduction

Pavements form a critical component of global transportation infrastructure, whether constructed as rigid or flexible systems (Paglia et al, 2022; White et al, 2010). They are required to fulfill various performance criteria, including resistance to heavy traffic loads, durability under diverse climatic conditions, and adaptability to specific local environments and traffic patterns. As such, selecting the appropriate paving material is of paramount importance. Rigid pavements, generally composed of concrete, are valued for their strength and capacity to bear significant loads without undergoing deformation. In contrast, flexible pavements, primarily made from asphalt, are characterized by their ability to accommodate variations in traffic and temperature due to their elastic nature.

Both pavement types offer distinct advantages and face specific limitations that are influenced by local variables such as traffic volume, climate, and budgetary constraints (Santero, 2011). For instance, concrete pavements are particularly well-suited for high-traffic zones thanks to their long-term stability and abrasion resistance. However, they come with notable disadvantages, such as higher initial costs and more demanding

maintenance routines, which can result in more frequent and costly repairs compared to asphalt alternatives (Bilodeau et al, 2012).

In contrast, flexible asphalt pavements, although more vulnerable to deterioration caused by temperature fluctuations and heavy traffic loads, are valued for their inherent flexibility. This trait allows them to better accommodate ground shifts and climate changes, offering a cost-effective solution in the short term. Nonetheless, their long-term durability is a concern, as they are more susceptible to cracking and the development of potholes (Modarres et al, 2014).

The RCCP has emerged as an innovative alternative that bridges the gap between rigid and flexible systems. Characterized by a low water-to-cement ratio and minimal water content, RCCP exhibits superior strength and exceptional durability (Boubekeur et al, 2024; Bílý et al, 2015). These properties make it particularly suitable for harsh climates and exposure to aggressive substances such as diesel (Poon et al, 2004). Additionally, RCCP's simplified placement process and reduced dependence on heavy construction machinery can cut project costs by 10–30% compared to traditional concrete (Abut et al, 2022). An added environmental benefit is its compatibility with recycled materials, contributing to lower carbon emissions and more sustainable construction practices (Modarres et al, 2014).

Simultaneously, incorporating RAP into concrete has gained attention as a strategy for promoting circular economy principles in construction (Oss-Emer et al, 2024; Fakhri et al, 2017; Debbarma et al, 2019). The use of RAP allows for the recycling of previously discarded materials, thus reducing the demand for virgin aggregates and lessening the overall environmental footprint of infrastructure development (Aurangzeb et al, 2014). However, the integration of RAP is not without challenges. The residual bitumen present in RAP can hinder the bonding between the recycled aggregates and cement matrix, which may negatively impact the mechanical performance of the resulting concrete (Singh et al, 2020; Shi et al, 2021).

The growing emphasis on sustainability in road infrastructure has led to an increased interest in incorporating recycled materials like RAP. This shift, which gained momentum in Europe following the 1973-oil crisis (Bilodeau et al, 2012), reflects heightened environmental consciousness and the need to reduce industrial waste and carbon emissions (Modarres et al, 2014). Despite these efforts, technical challenges persist in integrating recycled materials into concrete mixes, necessitating further research to ensure both performance and long-term durability in pavement applications (Singh et al, 2018; Debbarma et al, 2021).

In this context, the present study investigates the potential of substituting NA with RAP in roller-compacted concrete (RCC) mixes. The main objective is to determine whether such replacements can be made without compromising mechanical strength and durability, while still meeting the functional requirements of pavement materials (Aghaeipour et al, 2020; Chaikaew et al, 2024). To this end, a series of RCCP mixes were developed by incrementally replacing natural coarse aggregates with RAP at levels of 25%, 50%, 75%, and 100%. Durability-related tests—including capillary water absorption, porosity, and resistance to acid and sulfate attacks—were conducted to assess material performance.

Concrete specimens were prepared following ASTM C267 (ASTM C267-20) and cured for 28 days. To replicate harsh environmental conditions, samples were exposed to 1% hydrochloric acid (HCl) and 3% sulfuric acid (H_2SO_4) solutions. Sulfate resistance was evaluated using 5% sodium sulfate (Na_2SO_4) and 5% magnesium sulfate ($MgSO_4$) solutions in accordance with ASTM C1012-04 (ASTM C1012-04). The tests aimed to evaluate the degradation behavior of the mixes under chemical and physical stress, including crack development and mechanical deterioration (Bassuoni et al, 2007).

The overarching goal of this study is to propose a sustainable alternative for constructing roller-compacted concrete pavements using recycled materials. By reducing reliance on virgin resources, this approach supports environmentally responsible construction practices and emphasizes the critical role of recycled materials in enhancing the durability of modern road infrastructure.

Experimental program

Material used

Aggregates

In this study, several types of aggregates sourced from different regions in Algeria were employed. The natural sand, with a particle size range of 0/4 mm, was collected from the Oued Ras area in the Chlef province. Additionally, two types of gravel were used, namely, 3/8 mm and 8/15 mm, both extracted from a quarry located in the Relizane province. These materials were chosen based on their local availability and favorable physical properties, which made them suitable for the experimental program.

The RAP used in the study was retrieved from a national highway in the Relizane region after 18 years of service.

Figure 1 – Milling of existing asphalt pavements

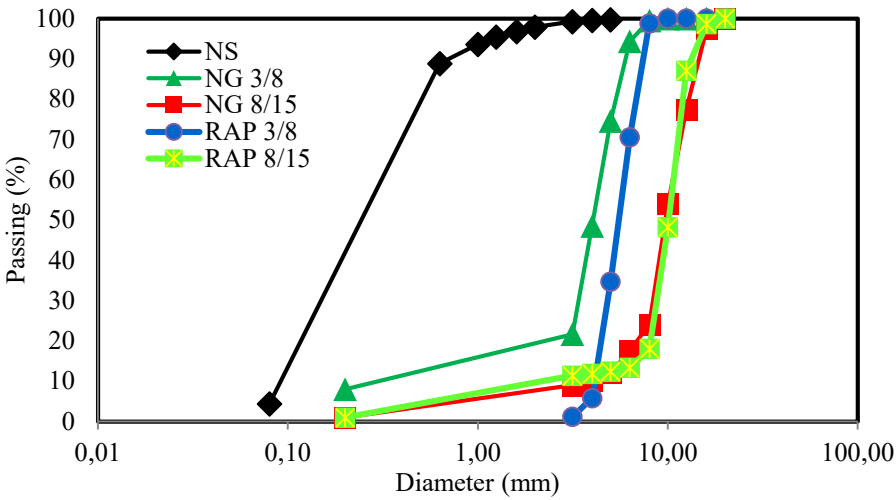

Figure 2 – Granulometric analysis of the aggregates used

The RAP material was carefully collected and then processed through crushing and sieving to obtain usable particles. One notable feature of the RAP aggregates is the presence of a hardened asphalt binder coating the coarse particles, which has a significant impact on their mechanical behavior and their interaction within concrete mixes.

Figure 2 presents the particle size distribution curves for the different aggregates, while Table 2 summarizes the physical properties of both NA and RAP. These data help in understanding the unique characteristics of each type of aggregate and facilitate a comparative analysis of their performance within the concrete mixtures studied.

Cement

The experimental program utilized a single type of cement: Portland cement classified as CEM II/C-M (P-L) 32.5 R. This is a composite cement

that incorporates both limestone and pozzolanic materials, indicating a product containing 21-35% additives and having a relatively low clinker content. It was manufactured by the Oggaz cement plant, located in the Mascara province, and meets the requirements of Algerian standard NA 17092 as well as European standard EN 197-5. The key physical and mechanical properties of the cement, essential for analyzing the concrete mixtures, are presented in Table 1. This cement was chosen for its local availability and full compliance with current standards, ensuring the reliability and consistency of the materials used in the study.

Table 1 – Physicochemical and mineralogical characteristics of the cement used

Chemical composition (%)	
SiO_2	19.12
Al_2O_3	3.55
Fe_2O_3	3.45
CaO	58.7
MgO	1.65
SO_3	2.15
Free lime	—
Na_2O	0.12
K_2O	1.6
Loss of ignition	| 11 ± 1 |
Sulfate content (SO_3, %)	| 2.4 ± 0.5 |
Magnesium oxide content (MgO, %)	| Max 5% |
Mineralogical composition (%)	
C_2S	60.72
C_3S	12.15
C_3A	6.66
C_4AF	9.82

Figure 3 – The different types of aggregates used

Table 2 – Study of RCCP formulation

Materials (Kg/m³)	RCCP0	RCCP25	RCCP50	RCCP75	RCCP100
Cement	250	250	250	250	250
W/C	0.576	0.472	0.49	0.472	0.552
Sand 0/4	631.7	631.7	631.7	631.7	631.7
Gravel 3/8 N	258.5	193,9	129,3	64,6	/
Gravel 8/18N	976.1	732,1	488,1	244	/
Gravel 3/8 RAP	/	64,6	129,3	193,9	258,5
Gravel 8/15 RAP	/	244	488,1	732,1	976,1
W_{opt}	6.9	5.58	5.8	5.57	6.61
Absorption rate of RAP 2.08% Absorption rate of NA 0.97%					

Testing methods

Mixing and compaction

Preparation of specimens

This study evaluates the influence of RAP on the performance of RCCP. Four specimen mixes were prepared with RAP replacements of 25%, 50%, 75%, and 100%, substituting NA in the 3/8 and 8/15 mm fractions. A 0% RAP mix served as the control. Cubic specimens (10×10×10 cm³) were produced by adjusting material proportions to assess fresh and hardened properties. Compaction was carried out using a vibrating hammer in accordance with NF EN 12697-32+A1, as shown in Figure 4.

Figure 4 – HILTI vibrating hammer

Mixing and curing process

The specimens were initially cured under wet conditions at 20°C with 58% relative humidity, and demolded 24 hours after preparation. They were kept under these conditions until testing, after which they were transferred to their respective curing environments and maintained there until the performance testing.

Testing method

Acid and sulfate attack

Acid attack

Concrete surfaces are highly susceptible to physical and chemical deterioration, particularly when exposed to aggressive agents such as sulfate and chloride ions. Evaluating the resistance of these materials to such attacks is therefore essential. In this study, fifty concrete cubes measuring 100 mm were cast in accordance with ASTM C267 standards and cured for 28 days to assess their performance under acidic exposure.

To replicate aggressive environmental conditions in the laboratory, 3% solutions of hydrochloric acid (HCl) and sulfuric acid (H_2SO_4) were prepared. For each RCCP formulation, two sets of ten specimens were submerged in the respective acid solutions.

Additionally, a third group of ten samples was used to monitor mass loss at 15-day intervals. The acid solutions were renewed every 30 days to ensure consistent concentration levels during the testing period. After 45 days of exposure, the specimens were removed, rinsed with tap water, and gently wiped with a cotton cloth before recording their surface-saturated mass. The percentage of mass loss was then calculated using appropriate formulas to evaluate the acid resistance of each RCCP mix.

Sulfate attack

Sulfate attack is another major factor contributing to the deterioration of concrete, particularly when exposed to environments rich in sulfate ions such as sodium sulfate (Na_2SO_4) and magnesium sulfate ($MgSO_4$). Several studies, including (Bassuoni et al, 2007), have investigated the impact of sulfate exposure on concrete, primarily focusing on two aspects: the physical degradation of the material and the quantification of that damage.

In this study, immersion tests were carried out following the procedures outlined in ASTM C267-20, where RCCP specimens were

submerged for 45 days in solutions containing 5% Na_2SO_4 and 5% $MgSO_4$. The objective was to evaluate the influence of incorporating RAP on the sulfate resistance of the concrete.

Chemical analyses were conducted to assess the durability of the specimens and their ability to withstand sulfate-induced deterioration. The samples were carefully observed throughout the testing period to gain insight into the effects of sulfate solutions on both the mechanical and chemical behavior of concrete, particularly when partially or fully composed of recycled aggregates such as RAP (see Figure 5).

Figure 5 – Acid and sulfate attack test

Results and discussion

Durability tests

Sulfate and acid attacks

Figure 6 presents the mass variation of RCCP samples immersed in 5% Na_2SO_4 and $MgSO_4$ solutions. When RAP is incorporated at levels of 25%, 50%, 75%, and 100%, a mass gain is observed after 220 days of immersion in $MgSO_4$, compared to the reference concrete (RCCP0). Conversely, the samples immersed in Na_2SO_4 exhibit an approximate 65% increase in mass loss. Concrete exposed to $MgSO_4$ undergoes more pronounced expansion than that exposed to Na_2SO_4. This mass loss is largely due to the interconnected porosity in the cement matrix, which facilitates sulfate ion ingress and subsequent leaching of calcium compounds into the surrounding acidic solution (Singh et al, 2018; Debbarma et al, 2021; Aghaeipour et al, 2020; Chaikaew et al, 2024).

The results reveal a steady mass gain up to 15 days of immersion, followed by continued increase over time. This phenomenon is linked to the formation of expansive mineral phases such as gypsum and secondary ettringite, which accumulate, causing swelling and microcracking within the cement paste. When these crystals outgrow the available pore space, internal crystallization pressure builds up, leading to surface cracking. The sulfate attack is driven by chemical reactions between sulfate ions in the

solution and tricalcium aluminate (C_3A) in the cement, forming calcium sulfate hydrates.

Among the mixtures tested, RCCP0 (control) exhibits the smallest mass gain (0.5%), while RCCP100 shows the highest (3%). Additionally, the mass loss of RCCP50 is about 50% lower than that of RCCP100 in the most aggressive exposure conditions.

Overall, the findings suggest that replacing 50% of natural coarse aggregates with RAP in RCCP offers promising performance for sidewalk applications in environments containing sulfates and chlorides. Notably, RCCP25 and RCCP50 experienced only 4% and 2% additional mass loss, respectively, compared to the control under sulfate exposure—supporting their suitability for pavement construction near sulfate-rich areas.

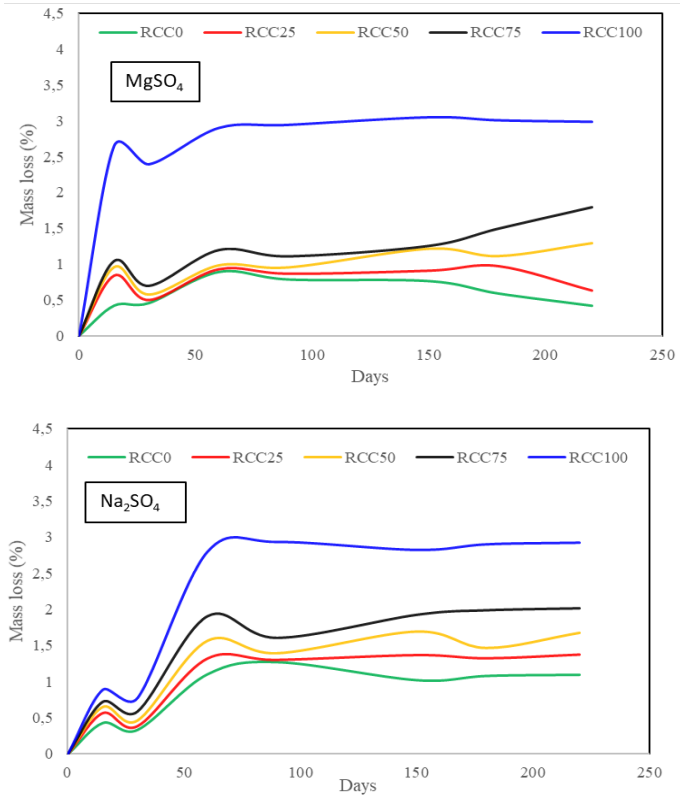

Figure 6 – The mass loss of (RCCP) immersed in both $MgSO_4$ and Na_2SO_4

Figure 7 illustrates the mass loss experienced by RCCP with varying RAP substitution levels (25%, 50%, 75%, and 100%) when exposed to hydrochloric acid (HCl) and sulfuric acid (H_2SO_4) over a period of 0 to 220

days. These data are vital for evaluating the acid resistance of the concrete, as such environments are known to accelerate structural degradation.

Under HCl exposure, the reference mix (0% RAP) demonstrates a gradual increase in mass loss, reaching 1.62% after 220 days. The rate of mass loss is more pronounced in the early stages (between 15 and 60 days) before stabilizing. As the RAP content increases, the degree of mass loss becomes more significant. For instance, the mix with 100% RAP shows a mass loss of 2.83%, nearly twice that of the control. This trend suggests that concretes with higher RAP levels deteriorate faster in acidic environments, likely due to greater porosity and permeability. The residual bitumen on RAP aggregates may facilitate acid and water infiltration, accelerating degradation (Singh et al, 2018).

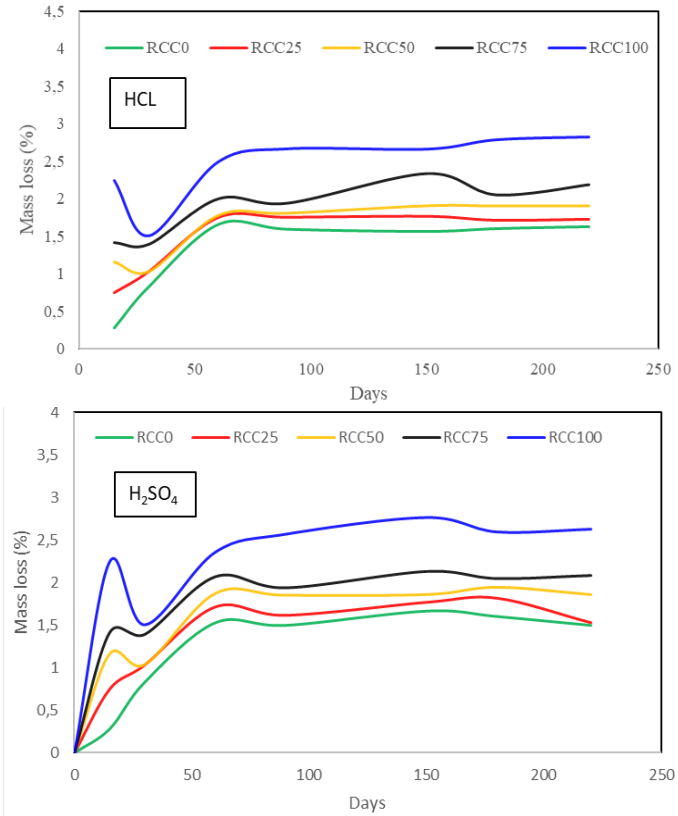

Figure 7 – Comparison of measured and calculated weight loss mortars immersed in H_2SO_4 and HCL solutions

The behavior of concrete under sulfuric acid (H_2SO_4) exposure mirrors the trends observed with hydrochloric acid (HCl). The reference mix (0% RAP) exhibits a gradual increase in mass loss, reaching approximately 1.49% after 220 days. The most significant loss occurs during the early phase (between 15 and 60 days), after which the values begin to level off. As the percentage of RAP increases, mass loss becomes more pronounced. Specifically, the mix containing 100% RAP records a mass loss of 2.63% at 220 days. This trend confirms that higher RAP content leads to greater deterioration, likely due to the aggressive action of sulfuric acid on the cement matrix. The formation of expansive compounds such as gypsum and secondary ettringite byproducts of the acid's reaction with calcium-bearing phases can induce internal stresses, causing cracks and further degradation of the concrete structure (Rahman et al, 2021).

Exposure to both HCl and H_2SO_4 subjects the concrete to intense chemical reactions that progressively compromise its integrity. The correlation between increased RAP content and higher mass loss highlights the critical role of porosity in acid resistance. As RAP content rises, so does the permeability of the concrete, making it more susceptible to acid penetration and subsequent chemical attack (Debieb et al, 2010).

These results support previous research showing that although RAP offers environmental advantages, its incorporation into concrete can compromise durability in acidic environments. The high porosity of RAP and the nature of the residual bitumen can accelerate degradation processes, reducing the long-term performance of concrete under chemically aggressive conditions (Masi et al, 2022).

The data illustrated in Figure 6 show the mass loss experienced by RCCP containing varying proportions of RAP (25%, 50%, 75%, and 100%) after immersion in sodium sulfate (Na_2SO_4) and magnesium sulfate ($MgSO_4$) solutions over a period of 0 to 220 days. These experiments were designed to evaluate the sulfate resistance of the concrete, an essential factor in environments where high sulfate concentrations can accelerate concrete deterioration.

For sodium sulfate (Na_2SO_4) exposure, the reference mixture with 0% RAP shows a steady increase in mass loss, reaching approximately 1.09% by day 220. The greatest mass loss occurs in the early stages (15 to 30 days), after which the values tend to plateau, likely due to the formation of expansive compounds such as ettringite. However, as the RAP content in the concrete increases, so does the mass loss. For instance, the 25% RAP mix records a mass loss of 1.37%, while the 100% RAP mix shows a significant increase to 2.93% after 220 days. This trend suggests that

higher RAP content makes the concrete more vulnerable to sulfate attack. The porous structure of RAP enhances the permeability of the concrete, facilitating the ingress of sulfate ions and promoting the chemical reactions responsible for the formation of expansive products (Uygunoğlu et al, 2024).

In the case of magnesium sulfate ($MgSO_4$), mass loss is generally more pronounced than in the Na_2SO_4 condition. This is attributed to the more aggressive reactions between $MgSO_4$ and calcium aluminates in the cement paste, which result in the formation of expansive minerals such as gypsum and secondary ettringite. These reactions cause internal stress, leading to microcracking and further degradation. The control mix (0% RAP) shows a mass loss of about 0.42% after 220 days, while the 100% RAP mix experiences a significantly higher mass loss of 3%. This outcome underscores the increased susceptibility of RAP-containing concretes to magnesium sulfate attack. The higher porosity and heterogeneity of RAP allow deeper penetration of sulfate ions, amplifying the damage caused by these chemical reactions (Shi et al, 2018).

The observed increase in mass loss with higher levels of RAP substitution suggests that concrete becomes more vulnerable to sulfate-induced degradation as the RAP content rises. This trend aligns with previous research indicating that incorporating RAP modifies the concrete's porosity and chemical makeup, increasing its susceptibility to chemical attacks particularly in environments rich in sulfate ions (Debbarma et al, 2019). The inherent porosity of RAP facilitates deeper ion penetration, accelerating sulfate reactions and promoting expansion and cracking within the concrete matrix. While using RAP in concrete offers clear environmental advantages, these findings emphasize the importance of carefully optimizing RAP content in applications exposed to sulfates. Strategies such as limiting RAP dosage or integrating supplementary cementitious materials (SCMs) including fly ash, slag, or silica fume can significantly enhance sulfate resistance. These SCMs contribute to a denser microstructure, reduce overall porosity, and mitigate the formation of expansive products that cause degradation and mass loss (Bashkoul et al, 2018). Additionally, a thorough analysis of the chemical characteristics and physical properties of RAP could support the development of tailored mix designs to improve the long-term durability of concrete in sulfate-rich environments.

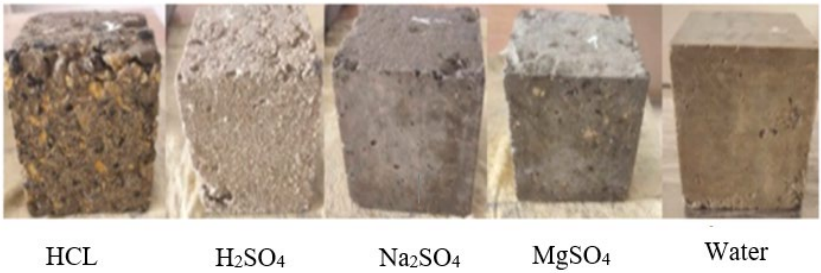

Figure 8 – State of RCCP 50% in various aggressive environments

Microstructure of RCCPs preserved in attack solutions

Scanning Electron Microscope (SEM) analyses of RCC samples incorporating 50% of RAP aggregates reveal notable differences in microstructural behavior depending on the curing environment. Under water-based conditions, the concrete displays a well-developed and hydrated matrix, with a clearly defined interfacial transition zone (ITZ) between the recycled aggregates and the new cement paste. The porosity remains moderate, and no significant deterioration is observed—indicating effective cement hydration and stable structural integrity.

These findings are consistent with previous studies, such as (Rout et al, 2023), who demonstrated the feasibility of using RAP in rigid pavement applications and reported a good bond between recycled aggregates and the cement matrix. Likewise, Fakhri et al. (2017) found that RCC mixtures containing RAP, especially when combined with crumb rubber, can achieve adequate mechanical performance, provided the mix design is carefully controlled.

However, when subjected to aggressive environments, the concrete exhibits marked microstructural degradation. In the presence of magnesium sulfate, there is evident dissolution of portlandite and deterioration of calcium silicate hydrate (C-S-H) gel, along with the formation of secondary products like gypsum and magnesium silicate hydrate (M-S-H). These changes are accompanied by microcracking and increased porosity. Similar degradation patterns were reported by Singh et al. (2017), who emphasized the impact of chemical exposure on the durability of RAP-containing concrete, particularly when mineral admixtures are involved. Exposure to hydrochloric acid (HCl) further compromises the concrete's microstructure. Major hydration products such as portlandite and C-S-H gel are significantly diminished or completely dissolved, the ITZ becomes critically weakened, and calcium chloride deposits are observed—collectively undermining the material's

long-term durability. Abdel-Mohti et al. (2016) reached comparable conclusions, noting that the performance of self-consolidating concrete with RAP is strongly influenced by binder composition and environmental exposure conditions.

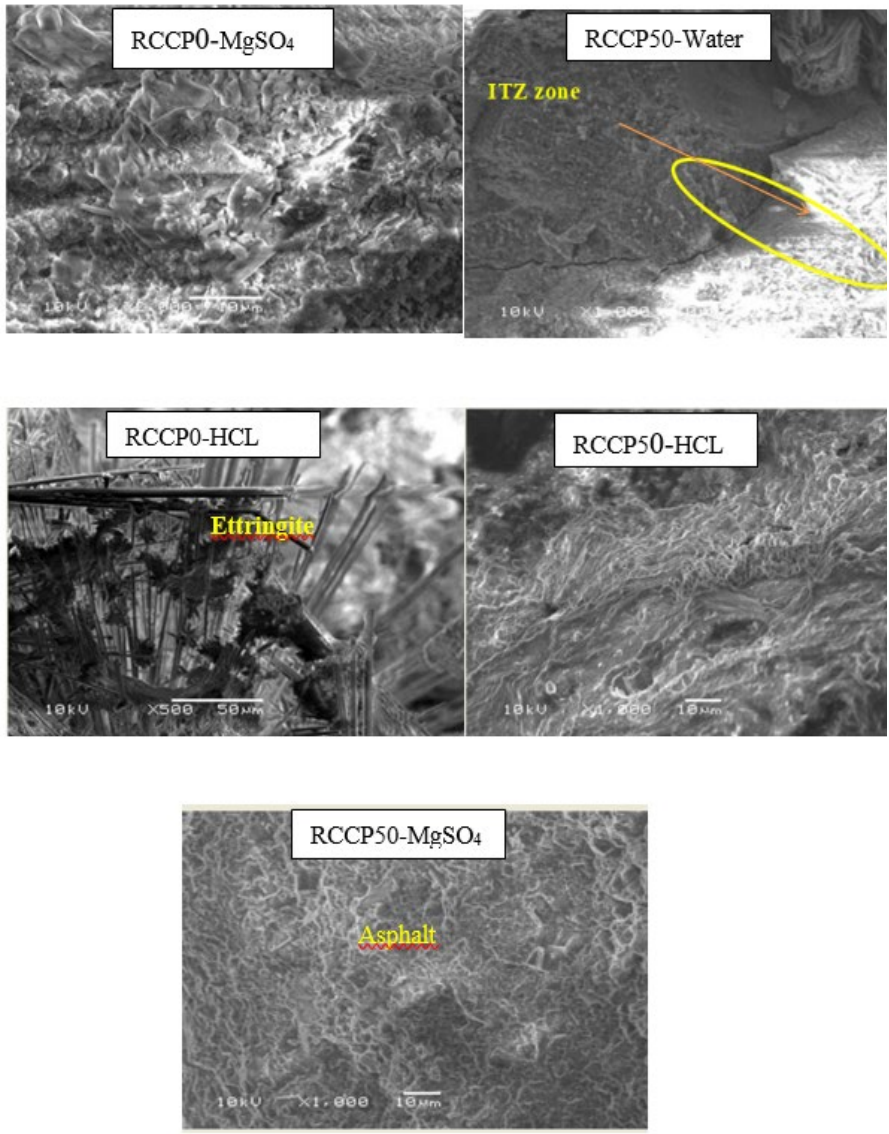

Figure 9 – Microstructure of RCCs preserved in acid and sulfate solutions

Overall, the results of this study are in line with existing literature and reinforce the idea that while RAP is a viable and sustainable alternative in concrete production, its performance is highly dependent on environmental factors and mix design parameters. Proper evaluation of exposure conditions and material compatibility is essential to ensure the durability and reliability of recycled concrete in practical applications.

X-ray diffraction (XRD)

It is essential to analyze the XRD spectrum of a RCC sample containing 50% recycled asphalt concrete aggregates and preserved in a sodium sulfate solution. The interpretation should focus on the mineral phases formed, the possible disappearance of others, and the influence of sodium sulfate on the concrete's microstructure and composition. Accurately identifying each diffraction peak and noting the presence or absence of specific phases is crucial. The XRD analysis of an RCC sample with 50% recycled asphalt aggregates preserved in a magnesium sulfate solution reveals degradation of key cementitious phases. Portlandite peaks are significantly weakened or disappear entirely, indicating its dissolution due to the aggressive attack. Gypsum peaks appear as a result of chemical reactions, and the C-S-H gel is altered—likely transforming into a less stable magnesium silicate hydrate (M-S-H) phase. Inert phases, such as quartz, remain unchanged. Overall, magnesium sulfate exposure leads to microstructural deterioration, compromising the strength and durability of the concrete.

Similarly, the XRD analysis of RCC with 50% recycled asphalt concrete aggregates preserved in a sodium sulfate solution reveals important chemical changes. This environment promotes the formation of gypsum ($CaSO_4 \cdot 2H_2O$) and ettringite ($3CaO \cdot Al_2O_3 \cdot 3CaSO_4 \cdot 32H_2O$), which are characteristic products of sulfate attack and can cause internal expansion and cracking. Peaks for quartz, Portlandite, C-S-H, gypsum, ettringite, and possibly calcite (due to carbonation) are expected. The reduction in portlandite peak intensity confirms its reaction with sodium sulfate and the consequent formation of new expansive phases. The persistence of quartz peaks is attributed to the inert nature of both natural and recycled aggregates.

These results are consistent with findings from Rahman and Khattak (2021) and Rahman et al. (2021), who reported similar microstructural degradation in concrete containing both RCA and RAP. Their study demonstrated that sulfate attacks result in the formation of ettringite and gypsum, negatively affecting mechanical performance and long-term durability.

In the case of HCl exposure, the XRD spectrum of RCC with 50% RAP shows severe microstructural damage. Portlandite and C-S-H are heavily dissolved or altered, significantly weakening the matrix. Calcium chloride ($CaCl_2$) may form as a reaction product, although it may not be easily detected due to its solubility. Quartz remains unaffected. Overall, hydrochloric acid exposure leads to deterioration of the cement matrix and reduced durability.

Likewise, sulfuric acid exposure causes extensive degradation. The XRD analysis reveals dissolution of portlandite, formation of gypsum, and transformation of aluminate phases into secondary ettringite. These reactions generate internal stresses, leading to cracking and mechanical failure. Despite these transformations, quartz remains stable, serving as a reference. Sulfuric acid exposure severely compromises both the strength and durability of the concrete.

Conversely, the XRD spectrum of RCC with 50% RAP preserved in water indicates a healthy hydration process. Well-defined peaks of C-S-H and portlandite suggest complete hydration, while quartz remains stable. Water curing enhances the crystallinity of hydration products and strengthens the matrix. The presence of recycled aggregates does not significantly disrupt the hydration, although it may slightly broaden the peaks due to microstructural variability. These findings support the conclusion that water curing promotes robust microstructure development even with the integration of 50% RAP, aligning with the results of Morales et al. (2020), who emphasized the benefits of water preservation in enhancing hydration in recycled aggregate concrete.

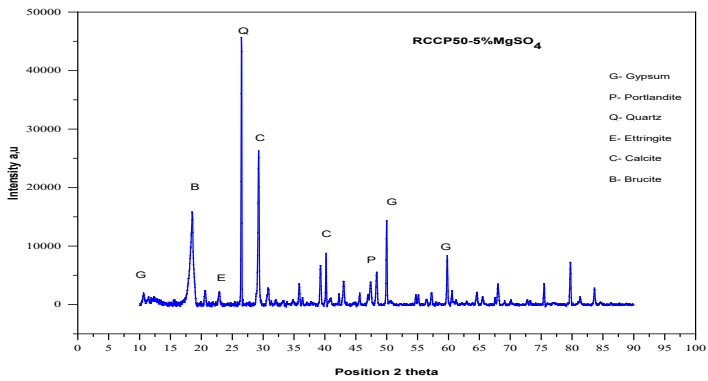

Figure 10 – RCCP50-$MgSO_4$

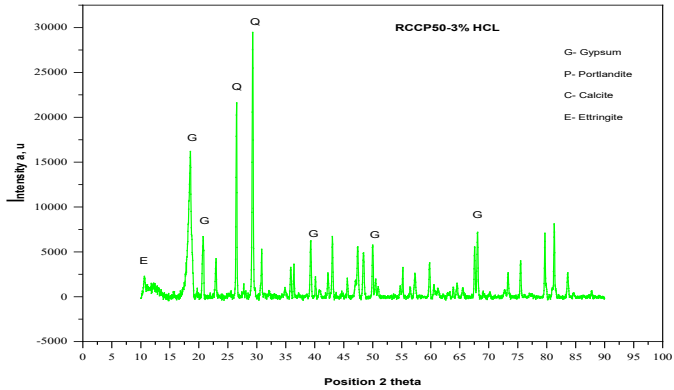

Figure 11 – RCCP50-HCL

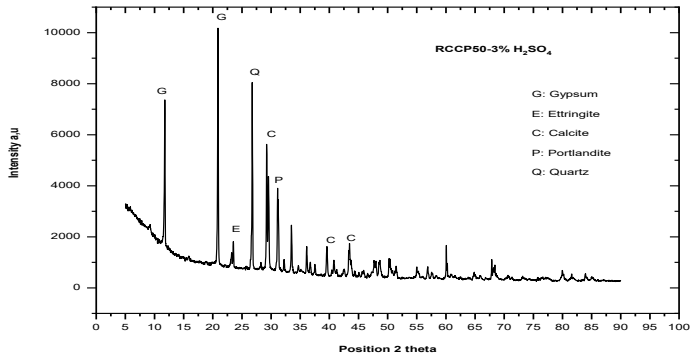

Figure 12 – RCCP50-H_2SO_4

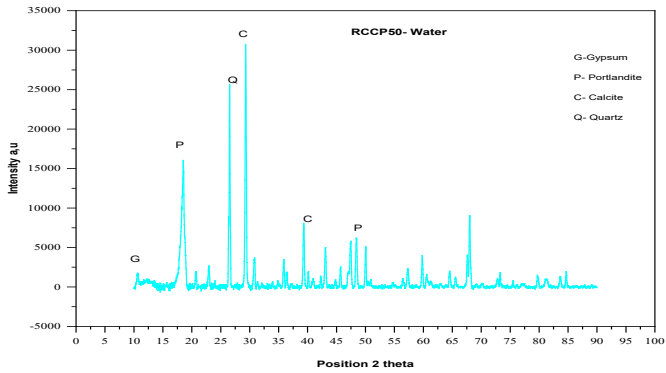

Figure 13 – RCCP50-Water

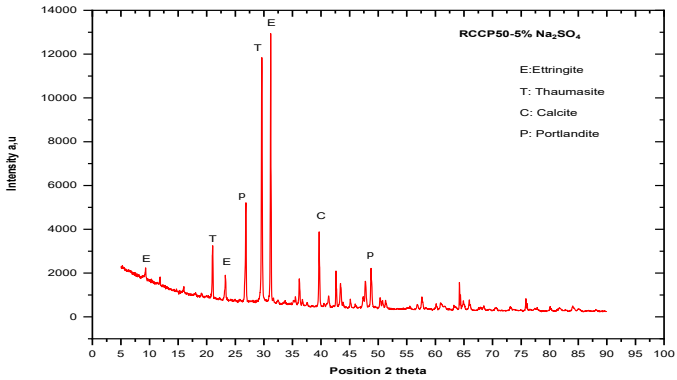

Figure 14 – RCCP50-Na_2SO_4

Conclusion

Incorporating RAP into RCCP influences its properties in significant ways, with effects that can be either advantageous or problematic depending on the RAP proportion and curing conditions.

The resistance of RCCP containing RAP to chemical attacks, such as sulfate (Na_2SO_4) and acid (HCl and H_2SO_4) attacks, is lower compared to conventional RCCP. This is due to the increased porosity, which allows aggressive ions to penetrate more easily. However, mixes with lower RAP content (less than 50%) perform better than those with higher RAP content, indicating that some degree of RAP substitution can still yield acceptable chemical resistance. Proper curing and mix optimization can further enhance the performance of RAP-based RCCP in hard environments.

The overall effect of RAP on RCCP performance represents a trade-off between the environmental benefits of using recycled materials and durability aspects, such as resistance to chemical attacks. However, with proper curing techniques, especially at elevated temperatures, the negative impacts of RAP on the durability of RCCP can be mitigated. Additionally, RAP provides a sustainable solution by reducing the need for virgin aggregates, contributing to more eco-friendly construction practices.

The study analyzes the effects of different preservation environments on the microstructure of roller-compacted concrete containing 50% recycled asphaltconcrete aggregates using XRD and SEM techniques. Water curing enhanceshydration and maintains a dense, stable microstructure. In contrast, exposure tosodium and magnesium sulfate leads to the dissolution of key hydrates (portlandite and C-S-H) and the formation of gypsum, ettringite, or M-S-H,indicating sulfate attack. HCl

exposure causes severe degradation, including microcracking and increased porosity. Overall, aggressive environments deteriorate the concrete's durability, while water curing improves it.

References

Abdel-Mohti, A., Shen, H., & Khodair, Y. 2016. Characteristics of self-consolidating concrete with RAP and SCM. Construction and Building Materials, 102, 564–573. Available at: https://doi.org/10.1016/j.conbuildmat.2015.11.007

Abut, Y., Yildirim, S. T., Ozturk, O., & Ozyurt, N. 2022. A comparative study on the performance of RCC for pavements casted in laboratory and field. International Journal of Pavement Engineering, 23(6), 1777-1790. Available at: https://doi.org/10.1080/10298436.2020.1823391

Aghaeipour, A., & Madhkhan, M. 2020. Mechanical properties and durability of roller compacted concrete pavement (RCCP)–a review. Road Materials and Pavement Design, 21(7), 1775-1798. Available at: https://doi.org/10.1080/14680629.2019.1579754

Algerian Institute of Standardization (IANOR). (Year of publication). NA 17092: Title of the Standard. Algerian Institute of Standardization.

ASTM C267-20 Standard Test Methods for Chemical Resistance of Mortars, Grouts, and Monolithic Surfacings and Polymer Concretes 2012ASTM C267-20

ASTM C1012-04, "Standard Test Method for Length Change of Hydraulic-Cement Mortars Exposed to a Sulfate Solution," American Society for Testing and Materials (ASTM) International, West Conshohocken, 2004.

Aurangzeb, Q., Al-Qadi, IL, Ozer, H., & Yang, R. 2014. Analyse du cycle de vie hybride pour les mélanges bitumineux à forte teneur en RAP. Ressources, conservation et recyclage, 83, 77-86.

Bashkoul, Y., et Divandari, H. (2018). Evaluate the use of Recycled Asphalt Pavement (RAP) in the Construction of Roller Compacted Concret Pavement (RCC). Civil engineering journal, 4 (5), 1157-1164. Available at: https://doi.org/10.28991/cej-0309164

Bassuoni, M.T., Nehdi, M.L., 2007. Resistance of self-consolidating concrete to sul-furic acid attack with consecutive pH reduction. Cem. Concr. Res. 37, 1070-1084. Available at: https://doi.org/10.1016/j.cemconres.2007.04.014

Bilodeau, J. P., & Doré, G. 2012. Estimation of tensile strains at the bottom of asphalt concrete layers under wheel loading using deflection basins from falling weight deflectometer tests. Canadian Journal of Civil Engineering, 39(7), 771-778. Available at: https://doi.org/10.1139/l2012-063

Bílý, P., Fládr, J., & Haase, M. 2015. Experimental Verification of the Properties of Roller Compacted Concrete for Pavements. In Advanced Materials Research, Vol. 1124, pp. 307–312. Trans Tech Publications, Ltd. Available at: https://doi.org/10.4028/www.scientific.net/amr.1124.307

Boubekeur, T., Salhi, M., Benyahia, A., & Benaddi, H. 2024. Experimental Investigation on the Effects of Recycled Pavement Materials on the Performance

of Self-Compacting Concrete: recycled pavement materials & self-compacting concrete. Journal of Scientific & Industrial Research (JSIR), 83(4), 445-452. Available at: https://doi.org/10.56042/jsir.v83i4.2679

Chaikaew, C., Nokkaew, N., Sua-iam, G., & Songkhla, W. N. 2024. Utilizing reclaimed asphalt pavement RAP as a replacement for coarse aggregate in roller compacted concrete. Suranaree Journal of Science and Technology, 31(1). Available at: https://doi.org/10.55766/sujst-2024-01-e02653

CEN. (2011). EN 197-5: Cement – Part 5: Composition, specifications, and conformity criteria for composite cements. European Committee for Standardization.

Debieb, F., Courard, L., Kenai, S., & Degeimbre, R. 2010. Mechanical and durability properties of concrete using contaminated recycled aggregates. Cement and Concrete Composites, 32(6), 421-426. Available at: https://doi.org/10.1016/j.cemconcomp.2010.03.004

Debbarma, S., Ransinchung, G. D., & Singh, S. 2019. Feasibility of roller compacted concrete pavement containing different fractions of reclaimed asphalt pavement. Construction and Building Materials, 199, 508-525. Available at: https://doi.org/10.1016/j.conbuildmat.2018.12.047

Debbarma, S., & Ransinchung, G. D. 2021. Achieving sustainability in roller compacted concrete pavement mixes using reclaimed asphalt pavement aggregates–state of the art review. Journal of Cleaner Production, 287, 125078. Available at: https://doi.org/10.1016/j.jclepro.2020.125078

Fakhri, M., Amoosoltani, E., Farhani, M., & Ahmadi, A. 2017. Determining optimal combination of RCCP mixture containing RAP and crumb rubber using hybrid ANN-GA method considering energy absorbency approach. Can. J. Civil Eng., 44, 945-955. Available at: https://doi.org/10.1139/cjce-2017-0124

Fakhri, M., & Amoosoltani, E. 2017. The effect of reclaimed asphalt pavement and crumb rubber on mechanical properties of roller compacted concrete pavement. Construction and Building Materials, 137, 470–484. Available at: https://doi.org/10.1016/j.conbuildmat.2017.01.150

Masi, G., Michelacci, A., Manzi, S., & Bignozzi, M. C. 2022. Assessment of reclaimed asphalt pavement (RAP) as recycled aggregate for concrete. Construction and Building Materials, 341, 127745. Available at: https://doi.org/10.1016/j.conbuildmat.2022.127745

Modarres, A., & Hosseini, Z. 2014. Mechanical properties of roller compacted concrete containing rice husk ash with original and recycled asphalt pavement material. Materials & Design, 64, 227-236. Available at: https://doi.org/10.1016/j.matdes.2014.07.072

Mohamed, S., Amar, B., Li, A., Boubekeur, T., Ashour, A., & Said, C. 2024. Evaluation of the Performance of Fiber-Reinforced Mortars Based on Dredged Sludge, International Journal of Engineering Research in Africa, 71, 31-44. Available at: https://doi.org/10.4028/p-KiAW2W

Morales Fournier, J., Acosta Álvarez, D., Alonso Aenlle, A., Tenza-Abril, A. J., & Ivorra, S. 2020. Combining reclaimed asphalt pavement (RAP) and recycled

concrete aggregate (RCA) from Cuba to obtain a coarse aggregate fraction. Sustainability, 12(13), 5356. Available at: https://doi.org/10.3390/su12135356

NF EN 12697-32+A1, 2007. Bituminous Mixtures - Test Methods for Hot Mix Hydrocarbons - Part 32: Laboratory Compaction of Bituminous Mixtures by Vibratory Compactor.

Oss-Emer, A. L., & dos Santos, A. G. 2024. Predicting the performance of semi-rigid pavement with partial replacement of RAP in RCC and designed using a mechanistic–empirical method. International Journal of Pavement Research and Technology, 1-15. Available at: https://doi.org/10.1007/s42947-020-0217-7

Paglia, C., Paderi, M., Mosca, C., & Antonietti, S. 2022. The recycling of a concrete with known properties to reproduce a durable material for the civil engineering infrastructure. International meet on civil, structural and environmental engineering, 23-26. Available at: https://www.researchgate.net/profile/C-Paglia

Rahman, S. S., & Khattak, M. J. 2021. Study of tensile properties of roller compacted geopolymer concrete and Portland cement concrete using 100% recycled concrete aggregates (RCA) and reclaimed asphalt pavement (RAP). Reston, VA: American Society of Civil Engineers, In Tran-SET, 212– 222. Available at: https://doi.org/10.1061/9780784483787.022

Rebai, B., Benaddi, H., Messas, T., Salhi, M., Rebai, B., Benaddi, H., & Salhi, M. 2025. Evaluation of self-compacting concrete for concrete repair applications, Res. Eng. Struct. Mater, 11(2), 495-513. Available at: https://jresm.org/archive/resm2024.255st0423rs.html

Rout, M. K. D., Sahdeo, S. K., Biswas, S., Roy, K., & Sinha, A. K. 2023. Feasibility study of reclaimed asphalt pavements (RAP) as recycled aggregates used in rigid pavement construction. Materials, 16(4), 1504. Available at: https://doi.org/10.3390/ma16041504

Salhi, M., Addi, H. B., & Boubekeur, T. 2025. Investigating the performance of self-compacting concrete exposed to hot weather, Periodica Polytechnica Civil Engineering, 69(1), 251-262. Available at: https://pp.bme.hu/ci/article/view/24092

Salhi, M., Boubekeur, T., Li, A., & Ghrici, M. 2022. Effects of cement additions on self-compacting concrete durability indicators, Periodica Polytechnica Civil Engineering, 66(2), 640-652. Available at: https://doi.org/10.3311/PPci.16985

Salhi, M., Ghrici, M., Bilir, T., & Uysal, M. 2020. Combined effect of temperature and time on the flow properties of self-compacting concrete, Construction and Building Materials, 240, 117914. Available at: https://doi.org/10.1016/j.conbuildmat.2019.117914

Santero, N. J., Masanet, E., & Horvath, A. 2011. Life-cycle assessment of pavements. Part I: Critical review. Resources, Conservation and Recycling, 55(9-10), 801-809. Available at: https://doi.org/10.1016/j.resconrec.2011.03.010

Shi, X., Mukhopadhyay, A., & Zollinger, D. 2018. Sustainability assessment for Portland cement concrete pavement containing reclaimed asphalt pavement aggregates. Journal of Cleaner Production, 192, 569-581. Available at: https://doi.org/10.1016/j.jclepro.2018.05.004

Shi, Y .Shen, X., Liu, J., Wang, W., Han, X., Zhang, J., &Li, G. 2021. A physical model demonstrating critical zone structure and flow processes in headwaters. Authorea Preprints.

Singh, S., Monu, K., & Ransinchung Rn, G. D. (2020). Laboratory investigation of RAP for various layers of flexible and concrete pavement. International Journal of Pavement Engineering, 21(14), 1780-1793. Available at: https://doi.org/10.1080/10298436.2019.1567920

Singh, S., Ransinchung RN, G. D., & Kumar, P. 2018. Laboratory investigation of concrete pavements containing fine RAP aggregates. Journal of Materials in Civil Engineering, 30(2), 04017279. Available at: https://doi.org/10.1061/(ASCE)MT.1943-5533.0002124

Singh, S., Ransinchung, G. D., & Kumar, P. 2017. Effect of mineral admixtures on fresh, mechanical and durability properties of RAP inclusive concrete. Construction and Building Materials, 156, 19–27. Available at: https://doi.org/10.1016/j.conbuildmat.2017.08.144

Singh, S., Ransinchung RN, G. D., & Kumar, P. 2018. Performance evaluation of RAP concrete in aggressive environment. Journal of Materials in Civil Engineering, 30(10), 04018231. Available at: https://doi.org/10.1061/(ASCE)MT.1943-5533.0002316.

Uygunoğlu, T., Topçu, İ. L. K. E. R., & Çınar Resuloğulları, E. 2024. Durability effect of reclaimed asphalt aggregate on concrete road pavement. Materiales de Construcción, 74(353). Available at: https://orcid.org/0000-0002-9435-2968

White, P., Golden, J. S., Biligiri, K. P., & Kaloush, K. 2010. Modeling climate change impacts of pavement production and construction. Resources, Conservation and Recycling, 54(11), 776-782. Available at: https://doi.org/10.1016/j.resconrec.2009.12.007

Procena trajnosti valjanog betona sa recikliranim materijalima iz kolovoznih konstrukcija

Fadhila Ali Kouadri[a], *Mohamed* Salhi[a], **autor za prepisku**, *Toufik* Boubekeur[b], *Amar* Benyahia[c], *Alex* Li[d], *Boussad* Abbès[d]

[a] Ahmed Zabana University, Faculty of Sciences and Technology, Civil Engineering Department, Innovative Materials Laboratory and Renewable Energies,Relizane, Algeria

[b] Civil Engineering, Mechanical and Transportation Department, Faculty of Science and Technology, Tissemsilt University, P. O. B. 182, 38000 Tissemsilt, Algeria

[c] Saad Dahlab University, Faculty of Sciences and Technology, Department of Civil Engineering, Blida, People's Democratic Republic of Algeria

[d] University of Reims Champagne-Ardenne, MATIM, Reims, France

OBLAST: materijali
KATEGORIJA (TIP) ČLANKA: originalni naučni rad

Sažetak:

Uvod/cilj: U ovom *istraživanju se ispituje trajnost valjanog betona za kolovoze (eng. RCCP) sa dodatkom recikliranog asfaltnog betona (eng. RAP) kao delimične ili potpune zamene za prirodne agregate (eng. NA). Osnovni cilj je procena mogućnosti primene recikliranog asfaltnog betona u betonu za kolovozne konstrukcije sa stanovišta performansi i održivosti.*

Metode: Betonske mešavine su pripremljene sa četiri nivoa zamene recikliranog asfaltnog betona: 0%, 25%, 50%, 75% u 100%. Vrše se ispitivanja izdržljivosti, a sprovedene su i mikrostrukturne analize upotrebom skenirajuće elektronske mikroskopije (eng. SEM) i rendgenske difrakcije (eng. XRD) u cilju ispitivanja unutrašnjih promena pri hemijskom napadu.

Rezultati: Ugradnja recikliranog asfaltnog betona poboljšala je otpornost na dejstvo kiselina i sulfata, posebno pri nivoima zamene do 50%. Iznad ove granice uočen je blagi pad performansi, iako su one ostale u prihvatljivim okvirima. Snimci skenirajuće elektronske mikroskopije pokazali su gušću matricu i bolje prianjanje između cementne paste i RAP agregata. Rendgenska difrakcija potvrdila je prisustvo stabilnih hidratacionih produkata i nakon izlaganja agresivnim rastvorima.

Zaključak: Rezultati podržavaju upotrebu recikliranog asfaltnog betona kao održive i izvodljive alternative prirodnim agregatima u valjanom betonu za kolovoze. Pri optimalnim nivoima zamene, reciklirani asfaltni beton poboljšava trajnost, doprinosi zaštiti životne sredine, smanjuje građevinski otpad i omogućava ekonomski isplativa rešenja kroz upotrebu recikliranih materijala.

Ključne reči: valjani beton, kolovoz od recikliranog agregata, mikrostruktura, trajnost.

Paper received on: 14 August 2025.
Manuscript corrections submitted on: 20 September 2025.
Paper accepted for publishing on: 20 October 2025.

© 2026 The Authors. Published by Vojnotehnički glasnik / Military Technical Courier (www.vtg.mod.gov.rs).This article is an open access article distributed under the terms and conditions of the Creative Commons Attribution license (http://creativecommons.org/licenses/by/4.0/rs/

Fuzzy algorithms applied to the comparative evaluation of crossroad designs

Oualid Largueche[a], *Mostefa* Lallam[b], *Miloud* Driss[c], *Mohammed Amine* Hamadouche[d]

[a] Department of Civil Engineering, University of Mustapha Stambouli, Mascara, People's Democratic Republic of Algeria + Laboratory of Geomatics, Ecology and Environment Research (LGEO2E), Mascara, Algeria,

e-mail: oualid.largueche@univ-mascara.dz, **corresponding author**, ORCID iD: https://orcid.org/0000-0002-3501-5507

[b] Department of Civil Engineering, University of Mustapha Stambouli, Mascara, People's Democratic Republic of Algeria + Laboratory Mechanics of Structures, University of Tahri Mohamed, Bechar, Algeria,

e-mail: m.lallam@univ-mascara.dz, ORCID iD: https://orcid.org/ 0000-0002-0022-6646

[c] Department of Civil Engineering, University of Mustapha Stambouli, Mascara, People's Democratic Republic of Algeria + Laboratory of Sciences and Technology of Water, University of Mascara, Algeria,

e-mail: miloud.driss@univ-mascara.dz, ORCID iD: https://orcid.org/0000-0001-9727-7353

[d] Department of Economics, University of Mustapha Stambouli, Mascara, People's Democratic Republic of Algeria + Laboratory of Geomatics, Ecology and Environment Research (LGEO2E), Mascara, Algeria,

e-mail: m.hamadouche@univ-mascara.dz, ORCID iD: https://orcid.org/0000-0001-6009-2726

https://doi.org/10.5937/vojtehg74-60076

FIELD: civil engineering, traffic engineering
ARTICLE TYPE: original scientific paper

Abstract:

Introduction/purpose: Urban traffic crossroads represent highly complex nodes within transportation networks due to the convergence of multiple, often conflicting, traffic streams. Managing these competing flows poses significant challenges, leading to issues such as fluctuating delays and backflow, particularly at supersaturated intersections. Given that these crossroads frequently act as bottlenecks, accurate short-term traffic flow predictions are crucial for effective planning and congestion mitigation. This study aims to propose a robust, multi-criteria evaluation framework for

crossroad design to support optimized urban planning and traffic management.

Methods: To address the inherent complexities and uncertainties associated with evaluating such designs, this research employs the Fuzzy Analytic Hierarchy Process (FAHP). This method is particularly suited for contexts in which expert judgments, often involving qualitative criteria such as landscape integration and local economic impact, lack absolute precision. Our approach integrates fuzzy logic to manage the subjective and imprecise nature of these evaluations, alongside quantitative factors such as cost and traffic saturation. Based on an extensive literature review and established disciplinary standards in traffic engineering and urban planning, we developed a comprehensive grid of 32 criteria and sub-criteria. These criteria cover key aspects such as road safety, service level, and traffic flow. Experts then assign weights to these criteria, which are processed through FAHP to produce a global performance indicator. This indicator allows the ranking and comparison of different alternative designs.

Results: The application of this FAHP-based framework yields a global performance indicator that facilitates the objective ranking of alternative crossroad designs. The methodology provides a structured approach to balance multiple, often conflicting, criteria in complex decision environments. The practical relevance of this method is demonstrated through a case study of the Chettia junction, where it successfully identifies the optimal configuration among several proposed alternatives. This underscores FAHP's versatility in evaluating performance within intricate urban systems.

Conclusion: This study successfully situates FAHP within a broader Multi-Criteria Decision Analysis (MCDA) framework, offering an original application to crossroad design. By integrating fuzzy logic, it effectively manages the uncertainty associated with both qualitative and quantitative evaluation criteria, proving particularly valuable when precise expert judgments are diffucult for experts to provide. The proposed framework provides a robust and multidimensional evaluation tool for urban planners and traffic engineers, enabling more informed and optimized infrastructure decisions for complex urban intersections.

Key words: crossroad, fuzzy analytic hierarchy process (FAHP), design alternatives, criteria, level of service, comprehensive performance indicator (CPI).

Introduction

Urban traffic crossroads are among the most complex points in transportation networks due to the convergence of multiple conflicting traffic streams. This complexity arises from managing these competing flows, as shown in extensions of Tanner's work on unsignalized

intersections, where delays in minor streams depend on gaps in major flows (Cowan, 1987). At supersaturated intersections, backflow and fluctuating delays further underscore these challenges (Liu & Wu, 2009). Given that crossroads often act as bottlenecks, short-term traffic flow predictions are essential for effective planning and congestion mitigation (Qu et al., 2020). Models that account for multimodal demand and traffic priority at unsignalized intersections offer structured approaches for delay estimation and flow management (Guler & Menendez, 2016).

Consequently, the growing complexity of traffic problems has driven the shift from cost-benefit analysis (CBA) to Multi-Criteria Analysis (MCA), also known as Multiple-Criteria Decision-Making (MCDM). MCA evaluates alternatives across competing objectives, offering a structured, flexible framework increasingly adopted in transport planning (Dean, 2020).

Furthermore, integrating CBA and MCA combines their strengths, enhancing project prioritization and policy alignment (Gühnemann, Laird & Pearman, 2012; Henke, Cartenì & Di Francesco, 2020). Participatory MCA, involving stakeholders in decision-making, captures diverse perspectives but presents challenges in participant selection and criteria definition (Dean, Hickman & Chen, 2018; Hickman & Dean, 2017). To address these complexities, techniques such as the Analytic Hierarchy Process (AHP) and the Technique for Order Preference by Similarity to Ideal Solution (TOPSIS) structure evaluations based on multiple criteria and uncertainty. They improve objectivity in transport planning by integrating technical, environmental, social, and economic factors (Bandyopadhyay, 2021; Sari & Şen, 2021; Otković et al., 2021; Singh, Singh & Singh, 2024). Indeed, numerous studies confirm the value of MCDM in infrastructure planning. AHP has been used to compare road designs (Barić, Pilko & Županović, 2016), support strategic planning (Barić & Starčević, 2015), and prioritize scenarios in cities such as Baghdad (Abdullah & Asmael, 2023). Hybrid approaches combining AHP with CBA strengthen investment decisions (Barić, Pilko & Dragčević, 2007). Fuzzy AHP (FAHP) further enhances transparency in uncertain contexts such as supplier selection (Ha, Fugate & Kazemi, 2015).Building on this foundation, fuzzy logic, introduced by Zadeh in 1965, enables experts to manage imprecision and subjectivity. FAHP, by integrating fuzzy sets into AHP, is widely applied in energy site selection, sustainable infrastructure, and resource management (Chan, Sun & Chung, 2019; Liu, Eckert & Earl, 2020; Ren et al., 2019). It effectively balances multiple, often conflicting, criteria in complex decision environments. Reflecting its growing importance, since 2008, MCDM research has expanded significantly.

Hybrid models such as FAHP-FTOPSIS demonstrate FAHP's versatility in evaluating performance in complex systems (Chamoli, 2015).

In this context, this study situates FAHP within the broader Multi-Criteria Decision Analysis (MCDA) framework. It applies fuzzy logic to address the uncertainty inherent in evaluating both qualitative criteria such as ecological and local economic impact and quantitative factors such as cost and traffic saturation. FAHP proves particularly suited to contexts where expert judgments lack precision. Specifically, based on the literature and disciplinary standards in traffic engineering and urban planning, this study proposes a grid of 32 criteria and sub-criteria. It offers an original application of FAHP to crossroad design, supporting a multidimensional evaluation framework. Experts assign weights to criteria related to road safety, service level, and traffic flow, producing a global performance indicator to rank the four alternative designs.

To demonstrate its practical application, the case study of Chettia junction illustrates the method's for selecting the optimal configuration among proposed alternatives. Ultimately, the article comprises six sections: an introduction and literature review; the study area and the intersection; explanation of the FAHP methodology; a comparative analysis of alternatives; and conclusions with research perspectives.

Fundamental information

Study area

This study focuses on an unsignalized intersection at Chettia on National Route 19 (NR 19) in Chlef province, Algeria. Because of this problematic intersection, traffic frequently backs up on this vital road, which serves the port of Tenes and connects to the east-west freeway. Due to the discomfort and danger it causes, local authorities are considering ways to address this issue. Consequently, they proposed four development plans to enhance the efficiency and safety (Figure 1).

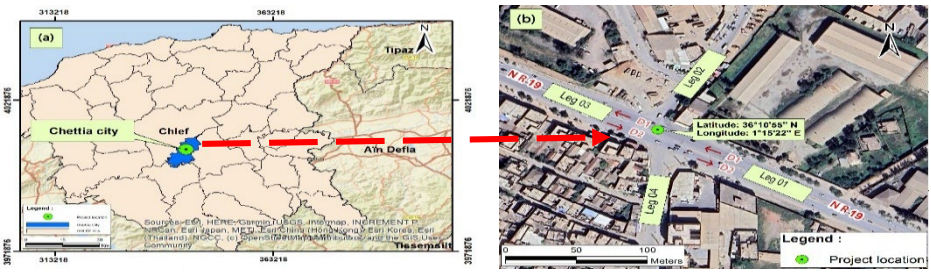

Figure 1 – Global location of the study area, (a) the Chlef province; (b) satellite image of the crossroad in the city of Chettia. Source: authors

The current state and geometric configuration of the crossroad

As shown in Figure 1b, the crossroad under study is located on flat terrain and consists of four distinct legs, each with specific characteristics. The first leg, part of NR19, is a major road in the Chlef province, featuring two lanes in each direction, a 7-meter carriageway on each side, and a 1-meter central reservation. The second leg is a bidirectional 7-meter-wide collector road serving the hospital and post office in Chettia, carrying fairly heavy traffic. The third leg, also on the NR19, leads to Chettia's north exit and Tenes port, with dimensions identical to the first. The fourth leg is a 7-meter-wide bidirectional collector road toward the southern extension of Chettia and the East-West motorway. This crossroad plays an essential role in traffic flow and access to services in the region.

Traffic flow and road safety

The traffic at this crossroad is heterogeneous, consisting mainly of light vehicles but also heavy goods vehicles, motorized two-wheelers, and bicycles. Figure 2 illustrates the crossroad's operational problems, which result in traffic jams that affect road users' comfort and safety.

Figure 2 – Photographs illustrating the operational problems at the studied crossroad. Source: authors

The Technical Studies Company of Sétif reports that traffic data collected at the main intersection in Chettia show significant differences in how vehicles move across the four approaches. The traffic study conducted at the Chettia crossroads on NR19 indicates a daily average volume ranging from 40,000 to 50,000 vehicles. Approach 1 has the

highest traffic, with 24,865 vehicles going to the port of Ténès and 24,738 going to the city centre of Chlef every day. Approach 3 also has a lot of traffic, with 22,463 vehicles going to Chlef and 22,091 vehicles going to Ténès daily. Approach 2, which goes to the hospital, carries 14,424 vehicles daily. Approach 4, which connects to the East-West Highway, on the other hand, has the lowest traffic, with only 2,962 vehicles per day.

These numbers show how important the intersection is for traffic between Chlef's urban centre and the port of Ténès. They also confirm that it is a key node in the regional transport network.

Figure 3 illustrates the distribution of vehicles at the crossroad by transport mode. Light vehicles (LV) account for approximately 65%, utility vehicles (CV) about 18%, and heavy vehicles 12%. Most traffic originates from Leg A with 2189 pcu/hr (47% of total), followed by Leg C with 1758 pcu/hr (37%), Leg B with 632 pcu/hr (13%), and Leg D with 126 pcu/hr (3%).

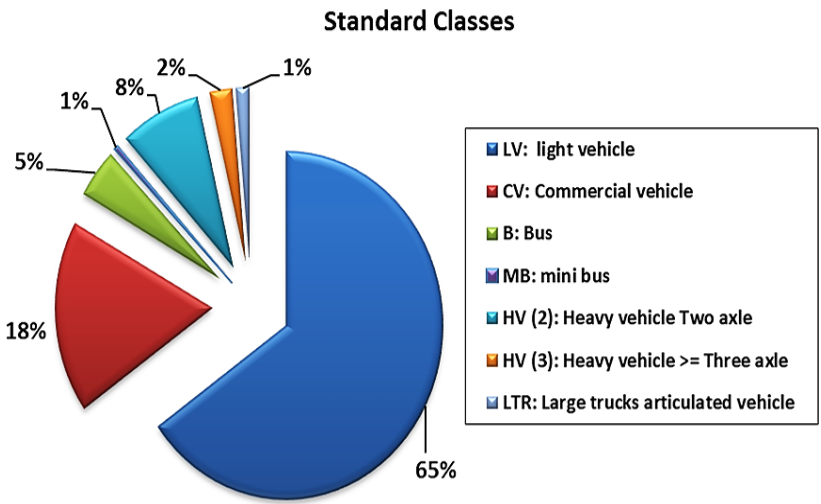

Figure 3 – Standard classes. Source: Technical Studies Company of Sétif

Overview of alternatives

Four design solutions for reconstruction were proposed by the leaders (Department of Public Works of Chlef). We aim to develop a fuzzy algorithm-based technique to control uncertainty and prioritize various criteria for selecting the optimal alternative. The method remains flexible, allowing modification of weights if designs change. Its adaptability and the generalization of criteria and sub-criteria are advantages for responding to design changes.

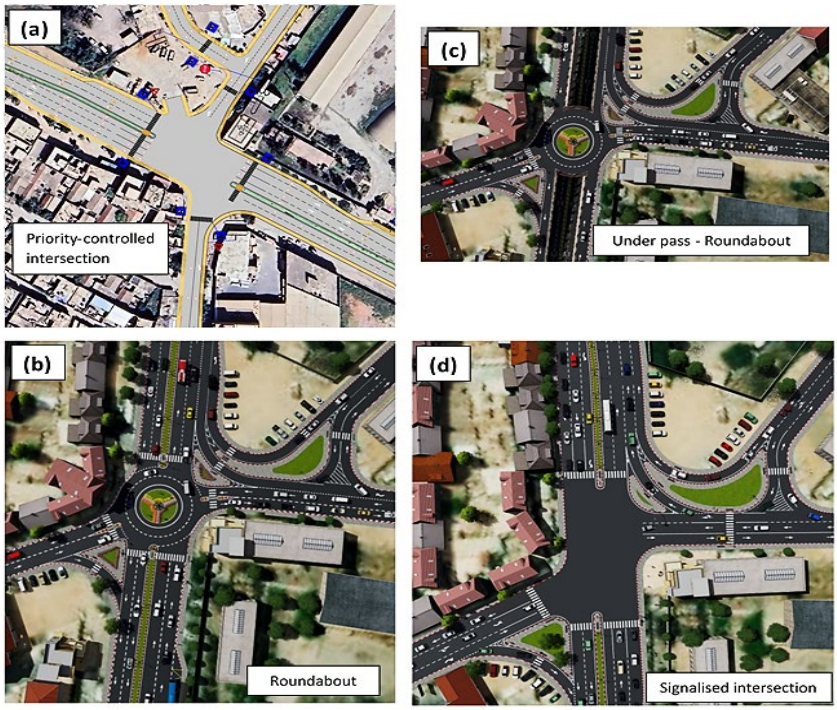

Figure 4 – Suggested alternatives for the reconstruction of Chettia Crossroad: (a) alternative 1 (priority-controlled intersection), (b) alternative 2 (roundabout), (c) alternative 3 (under pass - roundabout), (d) alternative 4 (signalised intersection). Source: authors

Alternative 1: Current state (priority-controlled intersection)

Alternative 1 (Scenario 1) involves preserving the current design while improving the visibility and understanding of horizontal and vertical signage. Horizontally, it includes redefining road markings such as stop lines, pedestrian crossings, and directional arrows. Vertically, it is advisable to install highly visible traffic signs at optimal heights with LED lighting. This would aid decision-making for drivers and pedestrians, enhancing safety and promoting smooth traffic flow (Figure 4a).

Alternative 2: Roundabout

This entails creating a circular crossroad with four arms, each with a 15 m turning radius. The circulatory carriageway has two 3.5 m lanes plus a 1.5 m overrun strip. NR19 consists of two two-lane roads (7 m each) with a 2 m central reservation. The entering radius is 12 m and the exit radius

is 20 m. The two other arms have two 3.5 m lanes in both directions, a 4.5 m entering lane, and a 5.5 m departure lane. A 4 m-wide slip lane with a 23.5 m inner radius is proposed to eliminate overlap and improve safety and flow. Figure 4b shows a proposal for two 33 m-long, 3.5 m-wide bus stops on the main road in each direction.

Alternative 3: Underpass – roundabout

The third alternative proposes an underpass-roundabout design, with a four-legged roundabout at the upper level and an underpass (covered trench) at the lower level (-1) on NR19 to facilitate linear traffic flow. The roundabout has a 20 m turning radius and two 4 m-wide lanes. The underpass includes two 7 m-wide lanes in each direction with a 1.5% gradient and 1 m sidewalks on both sides; the clearance height is 5.25 m. The open section (Figure 4c) also features two 7 m lanes per direction, a 2 m central median, a 6% longitudinal slope, and 1 m sidewalks. The design aims to enhance safety, improve service, and increase intersection capacity.

Alternative 4: Signalized intersection

The rehabilitation plan includes synchronized traffic signal cycles (red, yellow, green) for three 3.5 m-wide lanes, with a 2 m central median on the circulatory route to manage peak traffic. Dedicated signal phases for pedestrians and cyclists will ensure safe crossing and reduce conflicts with vehicles. LED lighting and additional signage will enhance night visibility, indicate phase changes, improve intersection management, reduce accidents, and enhance traffic flow (Figure 4d).

Integration of fuzzy logic in multi-criteria decision-making methods

Advantages and limitations

The integration of fuzzy logic into established multi-criteria decision-making methods such as the Analytic Hierarchy Process (AHP) and the Technique for Order of Preference by Similarity to Ideal Solution (TOPSIS) represents a significant methodological advancement in managing uncertainty and imprecision inherent in expert judgments (Pilevar et al., 2020; Yucesan & Gul, 2020). This hybridization substantially enhances the reliability and robustness of alternative rankings while effectively mitigating the risk of subjective errors that commonly plague conventional crisp approaches (Bouamrane et al., 2020). The fuzzy paradigm provides

unprecedented methodological flexibility and enables the seamless incorporation of qualitative criteria that are traditionally challenging to quantify precisely, constituting a notable competitive advantage over conventional deterministic methods (Pilevar et al., 2020; Yucesan & Gul, 2020).

Fuzzy set theory has emerged as a powerful framework for addressing vagueness and epistemic uncertainty across diverse decision-making contexts, from risk assessment to strategic planning (Yucesan & Gul, 2020; Lyu et al., 2019). The Fuzzy Analytical Hierarchy Process (FAHP), in particular, has proven to be an exceptionally effective methodology for comprehensive risk assessment scenarios where expert knowledge is systematically captured through structured questionnaires and linguistic evaluations (Lyu et al., 2019). This approach significantly enhances assessment precision by employing flexible linguistic scales through sophisticated fuzzy membership functions and intuitive linguistic variables that better capture the nuanced nature of human judgment (Sayyaadi et al., 2021).

However, the literature also acknowledges several inherent limitations and implementation challenges associated with fuzzy approaches. The increased computational complexity represents a significant barrier, requiring specialized algorithms and extended processing times compared to traditional methods (Garg et al., 2020). Furthermore, the critical dependence on expert judgment for model calibration and the strong need for reliable, contextually appropriate data constitute substantial methodological challenges that can compromise result validity (Lyu et al., 2019; Sayyaadi et al., 2021). The determination of appropriate fuzzy numbers and reliable parameter estimations can prove particularly challenging in FAHP implementations, especially in data-scarce environments (Lyu et al., 2019). Ultimately, the effectiveness of fuzzy approaches remains highly contingent on the quality of the calibration process and the appropriateness of the selected membership functions for the specific context (Sayyaadi et al., 2021). While FAHP demonstrates clear potential for improving decision precision through flexible scaling mechanisms, the acquisition of reliable empirical data and adequate resources for location-specific implementations continues to present significant practical challenges (Sayyaadi et al., 2021).

FAHP-based assessment of intersection efficiency

The objective of this work is to develop a computerized modeling system based on the FAHP approach to assess and determine the optimal crossroad configuration. The methodology, illustrated in Fig. 5, follows five

essential stages. The first stage identifies key factors that influence the intersection's operational effectiveness. The second stage establishes a hierarchical framework for the model. In the third stage, the FAHP technique evaluates the relative importance of identified elements and sub-elements. The fourth stage calculates the Comprehensive Performance Indicator (CPI). Finally, the CPI categorizes the intersection's level of operational efficiency.

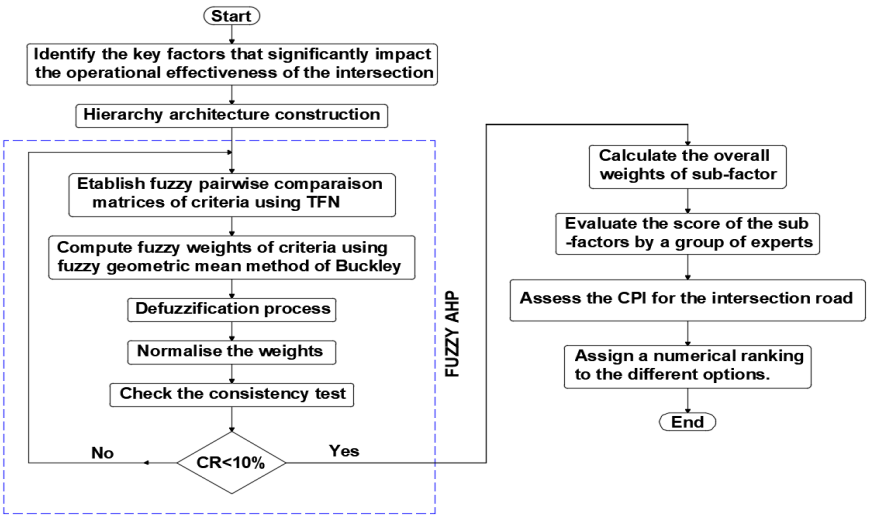

Figure 5 – A flowchart depicting the process of assessing the crossroad. Source: authors

Identifying the critical elements and establishing a hierarchical structure to select the optimal crossroad design

The first step of the model's calculation technique involves identifying crucial attributes that directly influence the performance of the optimal junction configuration (Figure 5). A rigorous elimination process removed less significant elements that did not contribute to operational efficiency. This selection draws from specialized literature and input from traffic engineering experts. The hierarchical structure, shown in Fig. 6, includes thirty-two criteria and sub-criteria.

The fuzzy analytic hierarchy process (FAHP) approach selects the optimal design among four alternatives using 32 economic, technical, and service-level criteria. Criterion C3 (level of service) divides into C3.1 (safety-related) and C3.2 (traffic-related), which includes C3.2.1 (traffic homogeneity), C3.2.2 (theoretical capacity), C3.2.3 (speed limit), and C3.2.4 (average waiting time).

The study incorporates human factors through C2.1 (mobility of pedestrians and cyclists), which evaluates the pedestrian experience based on comfort and safety, from absence of facilities to well-signposted, secure crossings. This criterion integrates vulnerable users' perception, often neglected in technical approaches.

Criteria linked to level of service (e.g., C3.2.1, C3.2.2) reflect driving conditions, fluidity, traffic light wait times, and congestion risks, all influencing pedestrian safety. Vehicle-pedestrian interaction is addressed through C3.1.3 (pedestrian and cyclist safety), C4.1 (visibility), and C4.2 (readability), assessing visual and cognitive clarity in the urban space. These criteria highlight the need for understandable, safe designs: poor visibility increases accident risk, while signalized crossroads enhance structure and visibility. Roundabouts can provide dynamic visibility when the central island is properly designed.

The FAHP model criteria quantify design impacts on human behavior and account for perceptual, safety, and operational urban dimensions, strengthening evaluation relevance and robustness. A group of seven experts evaluated each alternative, assigning scores from 0 to 10 per criterion based on their influence on overall performance. This impartial evaluation method identifies the solution best aligned with project requirements. The hierarchical structure plays a key role in ensuring th operational efficiency of the proposed junction.

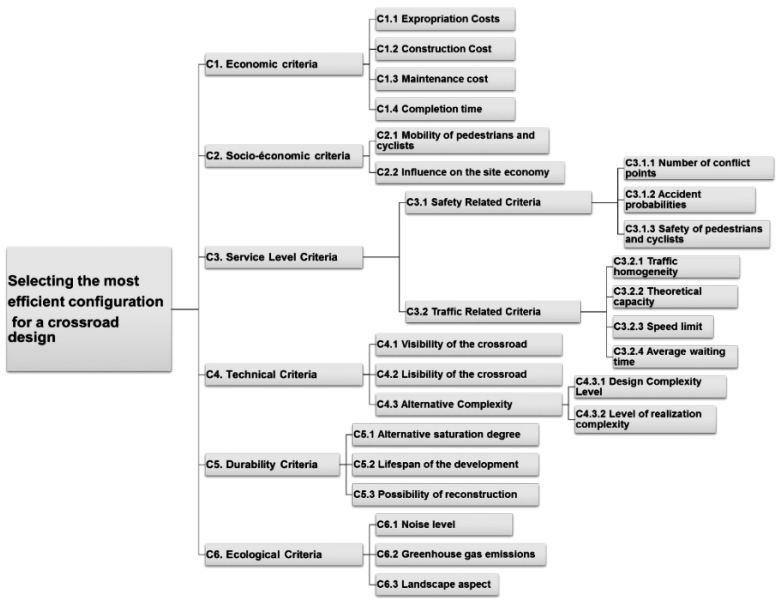

Figure 6 – The hierarchical structure of the adopted assessment criteria. Source: authors

Weight calculation using the FAHP method

Choice of membership functions and methodological implications

The choice between triangular, trapezoidal, and Gaussian membership functions constitutes a fundamental methodological decision whose impact on result quality is now well documented in the scientific literature. Several studies emphasize the crucial importance of this selection (Ameljanczyk, 2021), particularly through recent sensitivity analyses that demonstrate how the shape of the selected function can significantly modify the final ranking of alternatives, especially when differences between options are slight (Shukla & Muhuri, 2024; Faizi et al., 2020). Triangular functions, characterized by their conceptual simplicity and ease of interpretation, prove particularly suitable for situations where methodological transparency constitutes an essential prerequisite for stakeholder acceptance (Khokhar & Peng, 2022; Raval & Tailor, 2020). In contrast, trapezoidal functions offer better consideration of tolerance zones by enabling the modeling of maximum membership plateaus, while Gaussian functions prove particularly appropriate for representing naturally distributed data following a normal distribution, although they require more complex calibration and increased technical expertise. This selection invariably involves a delicate trade-off between methodological simplicity (promoting appropriation by decision-makers and operational robustness) and representational precision (enabling more faithful modeling of the uncertainty and variability inherent in the studied phenomena), necessitating a contextualized analysis of the specific requirements of the considered decision problem.

The TFNs, or triangular fuzzy numbers:

To solve the inherent imprecision and ambivalence in our study, we have opted to utilize the triangular fuzzy number (TFN) within the context of the FAHP approach. Many researchers prefer using TFN since they are easy to implement computationally. A triangular fuzzy number (TFN) is defined by a set of three numbers (l, m, u), where 'l' represents the lower bound, 'm' represents the middle value, and 'u' represents the upper bound of the TFN. Fig. 7 illustrates the visual representation of a TFN's membership function. This methodology enables the accurate representation of imprecise or ambiguous data, thereby providing increased adaptability in the analysis of intricate variables in our research. Utilizing TFNs in the FAHP procedure allows us to effectively collect and

measure subtle intricacies and deviations that may go unnoticed in a traditional study.

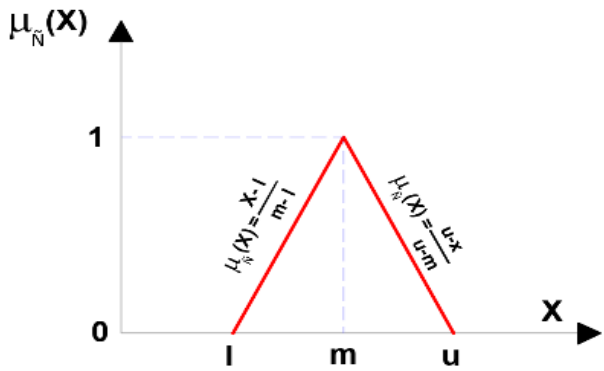

Figure 7 – Graphical illustration of TFNs. Source: Lallam & Mammeri, 2023

The conventional comparative scale

The selection of an appropriate triangular fuzzy number (TFN) requires a meticulous evaluation. This process necessitates a concurrent assessment of two critical parameters, the relative importance of which varies according to the specific objectives of the study. Figure 8 provides a detailed graphical representation of this complex decision-making process. Experts must exercise considerable judgment to balance these two criteria, each of which significantly impacts the suitability of the chosen TFN. This two-dimensional approach ensures that the selected TFN optimally meets the unique requirements of our research project.

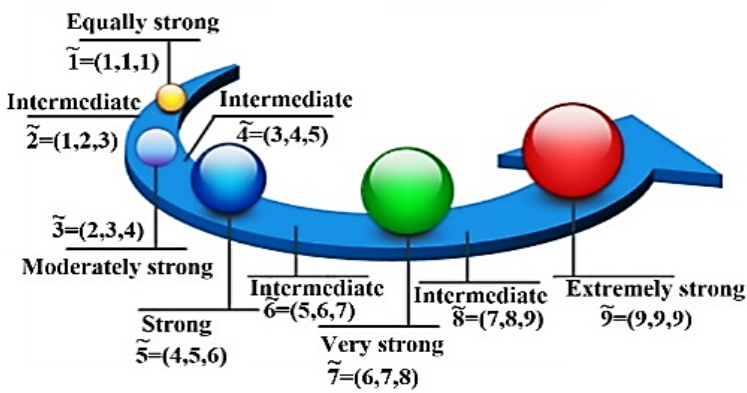

Figure 8 – Evaluation scale for criteria in terms of TFNs. Source: Lallam, Mammeri & Djebli, 2021

Fuzzy geometric mean method (FGMM)

Figure 9 presents a flowchart illustrating the fuzzy analytic hierarchy process (FAHP). The method starts by constructing pairwise comparison matrices using triangular fuzzy numbers to express uncertain judgments. These fuzzy values are then converted into crisp numbers to ease the computation. A consistency check follows to ensure the reliability of comparisons. The process continues with the calculation of fuzzy geometric means and weights, which are then defuzzified and normalized. The FAHP method provides a structured framework for handling uncertainty and ranking alternatives across multiple criteria. Table 1 complements the flowchart.

Table 1 – Random coherence index (RI). Source: Lallam, Mammeri & Djebli (2021, pp.1933–1946)

n	3	4	5	6	7	8	9	10
RI	0.525	0.882	1.109	1.248	1.342	1.406	1.450	1.485

This paper applies the proposed methodology to determine the weights of the primary criteria using the FAHP at level one of the hierarchical structure. This application demonstrates the approach's feasibility and applicability.

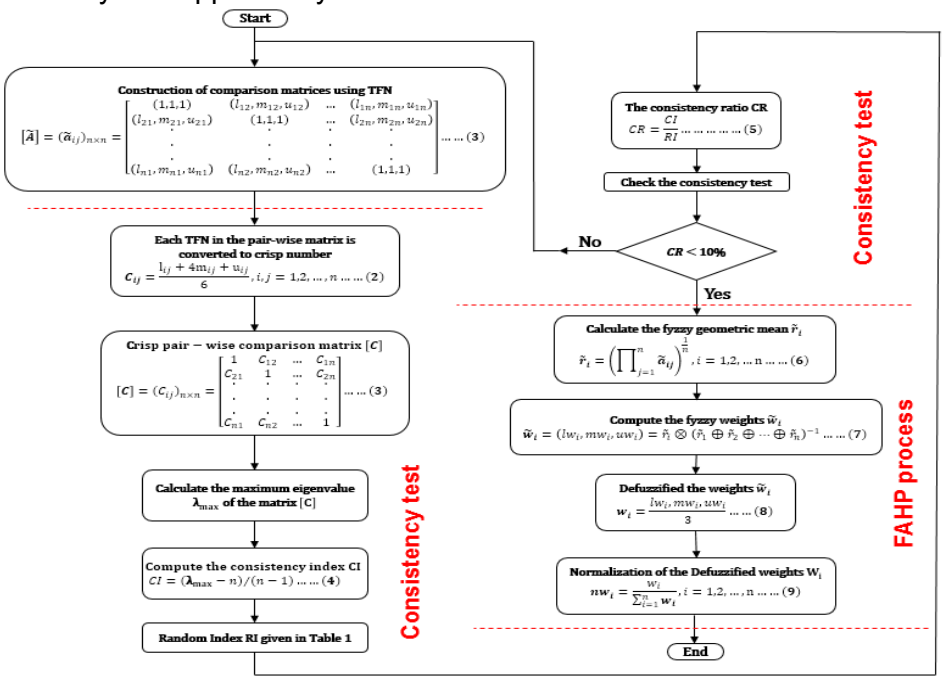

Figure 9 – A flowchart of the process of calculating weight using the fuzzy geometric mean method. Source: authors

Assessment of expert rating (ER)

In this section of the study, the relative weights of each element are determined using the FAHP method. Afterwards, experts award an intersectional functioning index (ER) to each element, ranging from 0 to 10. This index represents the comparative significance of each component in assessing the efficient operation of a crossroad. Table 2 displays the relationship between 'ER' and its equivalent scale.

Table 2 – Status of grading. Source: Lallam, Djebli & Mammeri, 2023

ER	State condition of scaling
[0,2]	super high
]2,4]	high
]4,6]	moderate
]6,8]	low- grade
]8,10]	grade noticed

The collective expert assessment (CEA) is derived using the following equation:

$$CEA_i = \frac{\sum_{j=1}^{m} ER_j}{m} \quad (1)$$

The number *m* represents the total number of specialists involved in the evaluation process. To conclude, the Comprehensive Performance Indicator (CPI), which represents the overall operational effectiveness of the intersection under scrutiny, is mathematically expressed as

$$CPI = \sum_{i=1}^{k} W_i \times CEA_i \quad (2)$$

In this formula, *i* ranges from 1 to *k*, where *k* denotes the number of the sub-factors chosen for analysis.

Comparative assessment

The evaluation process is based on the pairwise comparison method. It offers the possibility to analyze the criteria, sub-criteria, and their descriptions in depth. During these comparisons, the criteria are evaluated based on their relative weight with respect to each other. Experts are encouraged to evaluate the criteria and sub-criteria two by two, detailing their importance, definition, and justification, as presented in the case of the criterion Completion Time (C1.4) in Table 3. Experts can consult this information to better understand the evaluation process.

Table 3 – Intensity of the importance of the completion time criteria C1.4 (adapted to Saaty's scale). Source: authors

Criteria Score	Description	Interpretation
[0,2]	Very long	The completion time is very long (>6 months).
[2,4]	Long	The completion time is long (4 to 6 months).
[4,6]	Medium	The completion time is Medium (2 to 4
[6,8]	Short	The completion time is short (1 to 2 months).
[8,10]	Very short	The completion time is very short (<1 month).

Analysis of the results

The algorithm's numerical calculations, illustrated in Figure 5, were executed in Excel to enhance simplicity. Table 4 includes all the comparisons made between the different criteria. The evaluation of the judgment matrices' consistency, indicated by the CRs, demonstrates a high level of coherence, with all CRs below the 10% threshold.

Table 4 – Pairwise comparison matrices and their consistency tests. Source: authors

Factors	C1	C2	C3	C4	C5	C6	Consistency test
C1	$\tilde{1}$	$\tilde{4}$	$\tilde{2}$	$\tilde{2}$	$\tilde{4}$	$\tilde{5}$	λmax=6.077, CI=0.015, RI=1.240, CR=1.24%< 10%
C2	$\tilde{4}^{-1}$	$\tilde{1}$	$\tilde{2}^{-1}$	$\tilde{2}^{-1}$	$\tilde{1}$	$\tilde{1}$	
C3	$\tilde{2}^{-1}$	$\tilde{2}$	$\tilde{1}$	$\tilde{1}$	$\tilde{3}$	$\tilde{3}$	
C4	$\tilde{2}^{-1}$	$\tilde{2}$	$\tilde{1}$	$\tilde{1}$	$\tilde{2}$	$\tilde{3}$	
C5	$\tilde{4}^{-1}$	$\tilde{1}$	$\tilde{3}^{-1}$	$\tilde{2}^{-1}$	$\tilde{1}$	$\tilde{2}$	
C6	$\tilde{5}^{-1}$	$\tilde{1}$	$\tilde{3}^{-1}$	$\tilde{3}^{-1}$	$\tilde{2}^{-1}$	$\tilde{1}$	
	C1.1	C1.2	C1.3	C1.4			Consistency test
C1.1	$\tilde{1}$	$\tilde{4}^{-1}$	$\tilde{2}$	$\tilde{2}$			λmax=4.165, CI=0.055, RI=0.900, CR=6.12%< 10%
C1.2	$\tilde{4}$	$\tilde{1}$	$\tilde{6}$	$\tilde{3}$			
C1.3	$\tilde{2}^{-1}$	$\tilde{6}^{-1}$	$\tilde{1}$	$\tilde{3}^{-1}$			
C1.4	$\tilde{2}^{-1}$	$\tilde{3}^{-1}$	$\tilde{3}$	$\tilde{1}$			
	C2.1	C2.2					Consistency test
C2.1	$\tilde{1}$	$\tilde{2}$					CR not verified for comparison between two criteria
C2.2	$\tilde{2}^{-1}$	$\tilde{1}$					
	C3.1	C3.2					Consistency test
C3.1	$\tilde{1}$	$\tilde{2}^{-1}$					CR not verified for comparison between two criteria
C3.2	$\tilde{2}$	$\tilde{1}$					
	C3.1.1	C3.1.2	C3.1.3				Consistency test
C3.1.1	$\tilde{1}$	$\tilde{2}^{-1}$	$\tilde{2}^{-1}$				λmax=3.042, CI=0.021, RI=0.580, CR=3.64%< 10%
C3.1.2	$\tilde{2}$	$\tilde{1}$	$\tilde{2}^{-1}$				
C3.1.3	$\tilde{2}$	$\tilde{2}$	$\tilde{1}$				
	C3.2.1	C3.2.2	C3.2.3	C3.2.4			Consistency test
C3.2.1	$\tilde{1}$	$\tilde{2}^{-1}$	$\tilde{1}$	$\tilde{1}$			λmax=4.054, CI=0.018, RI=0.900, CR=2.01%< 10%
C3.2.2	$\tilde{2}$	$\tilde{1}$	$\tilde{2}$	$\tilde{1}$			
C3.2.3	$\tilde{1}$	$\tilde{2}^{-1}$	$\tilde{1}$	$\tilde{1}$			
C3.2.4	$\tilde{1}$	$\tilde{1}$	$\tilde{1}$	$\tilde{1}$			

Factors	C1	C2	C3	C4	C5	C6	Consistency test
	C4.1	C4.2					Consistency test
C4.1	$\tilde{1}$	$\tilde{2}$					CR not verified for comparison between two criteria
C4.2	$\tilde{2}^{-1}$	$\tilde{1}$					
	C4.1	C4.2	C4.3				Consistency test
C4.1	$\tilde{1}$	$\tilde{1}$	$\tilde{3}^{-1}$				λmax=3.000, CI=0.000, RI=0.580, CR=0.00%< 10%
C4.2	$\tilde{1}$	$\tilde{1}$	$\tilde{3}^{-1}$				
C4.3	$\tilde{3}$	$\tilde{3}$	$\tilde{1}$				
	C4.3.1	C4.3.2					Consistency test
C4.3.1	$\tilde{1}$	$\tilde{2}$					CR not verified for comparison between two criteria
C4.3.2	$\tilde{2}^{-1}$	$\tilde{1}$					
	C5.1	C5.2	C5.3				
C5.1	$\tilde{1}$	$\tilde{2}$	$\tilde{2}$				λmax=3.061, CI=0.030, RI=0.580, CR=5.23%< 10%
C5.2	$\tilde{2}^{-1}$	$\tilde{1}$	$\tilde{2}$				
C5.3	$\tilde{2}^{-1}$	$\tilde{2}^{-1}$	$\tilde{1}$				
	C6.1	C6.2	C6.3				
C6.1	$\tilde{1}$	$\tilde{1}$	$\tilde{2}$				λmax=3.056, CI=0.028, RI=0.580, CR=4.79%< 10%
C6.2	$\tilde{1}$	$\tilde{1}$	$\tilde{1}$				
C6.3	$\tilde{2}^{-1}$	$\tilde{1}$	$\tilde{1}$				

Figure 10 presents a sunburst chart illustrating the local weights acquired following consistency tests.

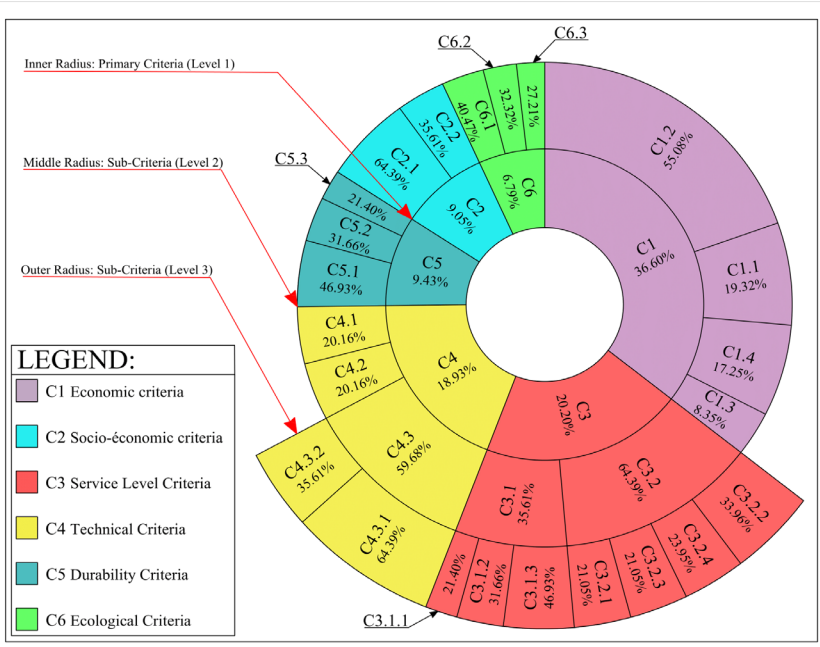

Figure 10 – Sunburst chart for local weightings. Source: authors

The hierarchical sunburst chart offers an effective visualization of hierarchical data. It consists of a central circle surrounded by concentric rings, each representing a different level. Segment sizes are proportional to their values, allowing a clear distribution display and facilitating detection of the relationships between categories. This layered structure also supports interactive exploration.

At level 1 of Figure 10, economic criteria dominate with a weight of 35.60%, followed by level of service (20.20%) and technical factors (18.93%). Sustainability and socio-economic elements weigh 9.43% and 9.05%, respectively, while environmental criteria hold the lowest weight at 6.79%. These weightings reflect a prioritization of economic, technical, and service-related factors.

The hierarchical model calculates the global weights of sub-criteria by multiplying local weights of their parent criteria at lower levels (Lallam, Djebli & Mammeri, 2023, pp.1–20; Bandyopadhyay, 2021).

Categorization of the optimal design from the four different alternatives

The approach adopted in this article, known for managing uncertainty through fuzzy numbers, relies heavily on the quality and representativeness of expert evaluations. To ensure methodological robustness and practical applicability, a rigorous expert selection process was implemented, emphasizing a balance between academic and professional profiles.

In the first phase, the theoretical foundations of the criteria grid were established through academic research and comparison with similar studies, identifying converging trends and ensuring scientific and geographical relevance. This led to a structured initial set of criteria classified by intervention area, serving as the basis for expert selection.

In the second phase, seven experts from diverse professional backgrounds were selected, including a transportation economist, two design engineers, a traffic engineer, two project managers, and a business engineer, each with over ten years of experience. This balanced panel ensured reliable and consistent evaluations.

A synthesis of 32 criteria and sub-criteria was then consolidated as a structured foundation for FAHP analysis. This method streamlines the comparison of alternatives. Unlike traditional AHP, it avoids recalculating judgment matrices for each alternative. Once criteria scores are assigned (Table 4), calculating the Comprehensive Performance Indicator (CPI) and ranking alternatives becomes straightforward. This simplifies the numerical implementation of the methodology.

The study applies the FAHP method to a real case involving a crossroad in Chettia, Chlef province, Algeria. The method offers a structured framework to synthesize expert opinions and establish a clear hierarchy of alternatives, providing practical value while maintaining scientific rigor.

A panel of seven specialists evaluated the four project alternatives. Each expert assigned a score from 0 to 10 to each criterion per variant, based on its impact on overall performance. This ensured impartial assessment and selection of the most suitable solution. Table 5 presents the complete evaluation results.

Table 5 – Full results of the evaluation by experts. Source: authors

N°	Factors	W_i	CEA_i			
			Alternative1	Alternative2	Alternative3	Alternative4
1	C1.1	0,069	9,214	6,714	2,429	8,500
2	C1.2	0,196	9,250	7,214	3,071	6,429
3	C1.3	0,030	8,250	7,714	4,536	5,000
4	C1.4	0,061	9,214	7,286	2,643	6,786
5	C2.1	0,058	1,571	4,143	7,571	8,786
6	C2.2	0,032	5,000	5,000	3,000	5,000
7	C3.1.1	0,015	1,000	7,000	10,000	9,000
8	C3.1.2	0,023	1,286	4,714	7,571	7,000
9	C3.1.3	0,034	1,000	4,857	8,286	8,357
10	C3.2.1	0,027	1,000	3,429	8,714	2,714
11	C3.2.2	0,044	1,000	5,143	9,214	6,857
12	C3.2.3	0,027	1,286	5,714	9,214	4,000
13	C3.2.4	0,031	1,000	6,429	9,000	3,429
14	C4.1	0,038	2,714	6,143	9,000	7,857
15	C4.2	0,038	3,857	7,643	7,714	7,929
16	C4.3.1	0,040	9,000	7,286	2,857	7,571
17	C4.3.2	0,073	9,000	7,143	3,000	7,429
18	C5.1	0,044	1,000	3,000	9,071	5,000
19	C5.2	0,030	2,286	4,500	8,714	2,571
20	C5.3	0,020	9,071	7,000	2,000	7,714
21	C6.1	0,027	1,571	5,000	8,286	2,714
22	C6.2	0,022	1,286	4,714	8,857	2,143
23	C6.3	0,018	1,071	6,571	8,643	3,571
$CPI = \sum_{i=1}^{23} W_i \times CEA_i$			5.382	6.122	5.643	6.346
Rank			4	2	3	1

According to the comprehensive performance indicator (CPI), Table 5 shows how the four choices performed in comparison. Alternative 4

ranks first with a CPI of 6.346, followed by Alternative 2 (6.12), Alternative 3 (5.643), and Alternative 1 (5.382). A CPI of 6.346 positions Alternative 4 as the most effective solution, reflecting a balance between economic criteria, service level, technical aspects, sustainability, and environmental factors.

For expropriation costs (C1.1), Alternative 4 scores 8.500, indicating a moderate land footprint and minimal implementation constraints. Alternative 1 scores higher (9.214), but its overall weaknesses outweigh this advantage. In construction cost (C1.2), Alternative 1 scores highest (9.25), offering the lowest expense, yet it has the shortest lifespan (C5.2 = 2.286). Alternative 4, with a C1.2 score of 6.429, presents an "appropriate" cost (200–400 MDA).

On pedestrian and cyclist safety (C3.1.3), Alternative 4 scores 8.357, classified as "optimal," predicting lower accident risks. It also ranks highest in conflict point reduction (C3.1.1 = 9.000), reflecting an effective geometric design. In terms of mobility (C2.1), it scores 8.786, described as "pleasant," improving accessibility.

Operationally, Alternative 3 achieves the highest theoretical capacity (C3.2.2 = 9.214), manages congestion and traffic imbalance effectively (C3.2.1 = 8.714), offers minimal waiting time (C3.2.4 = 7.429), and maintains a smooth flow (C5.1 = 9.071). However, it has low scores in expropriation (C1.1 = 2.429), construction cost (C1.2 = 3.071), and requires a longer completion time.

Alternative 3 shows strong environmental performance with high scores for emissions (C6.2 = 8.857) and noise (C6.1 = 8.286), but its complexity of implementation (C4.3.2 = 3.0) limits its feasibility in constrained areas. In contrast, Alternative 4 offers low complexity (7.429), easier implementation, and maintains strong service-level performance.

Conclusion

This study presents an application of the Fuzzy Analytic Hierarchy Process (FAHP) for optimizing urban crossroad design, addressing a critical challenge in contemporary traffic engineering. Our comprehensive evaluation framework, incorporating 32 criteria across six dimensions, demonstrates the method's effectiveness in managing the inherent uncertainty and complexity of multi-criteria decision-making in urban infrastructure planning.

The primary contribution of this research lies in developing a holistic evaluation framework that significantly extends beyond traditional approaches. Our hierarchical model revealed that economic criteria

dominate decision-making (35.60%), followed by level of service (20.20%) and technical considerations (18.93%), while sustainability (9.43%), socio-economic factors (9.05%), and environmental criteria (6.79%) play complementary roles. The application to the Chettia crossroad case study validated the framework's practical utility, with Alternative 4 emerging as the optimal solution through its integration of synchronized traffic light cycles and dedicated phases for vulnerable road users.

The methodological innovation resides in the streamlined implementation of FAHP, which eliminates the computational burden of recalculating judgment matrices for each alternative—a significant limitation of traditional AHP approaches. The Comprehensive Performance Indicator (CPI) introduced here enables straightforward ranking through simple score sorting, enhancing the method's scalability and practical applicability. This computational efficiency, combined with the flexibility to incorporate qualitative criteria through fuzzy membership functions and linguistic variables, represents a substantial advancement over conventional deterministic methods.

The framework's societal implications extend beyond technical optimization. By prioritizing safety through dedicated pedestrian and cyclist infrastructure while maintaining economic viability, the approach directly addresses the Sustainable Development Goals related to sustainable cities and communities. The potential reduction in road accidents and improvement in quality of life demonstrate the method's alignment with contemporary urban planning priorities.

While the FAHP approach successfully manages uncertainty, several limitations warrant consideration. The method's effectiveness remains contingent upon expert judgment quality and appropriate membership function calibration. The increased computational complexity compared to deterministic methods, though mitigated by our streamlined approach, may still present challenges for practitioners lacking specialized expertise. Additionally, data acquisition for location-specific parameters continues to pose practical constraints.

Future research should focus on three critical areas. First, applying the framework to diverse intersection typologies across different urban contexts will test its generalizability and robustness. Second, integrating FAHP with real-time traffic simulation tools could enhance predictive accuracy and enable dynamic optimization. Finally, developing automated calibration procedures using machine learning techniques could reduce dependency on expert judgment while maintaining decision quality.

This research establishes a reproducible, adaptable framework for urban crossroad design that balances technical rigor with practical

applicability. The proposed 32-criteria evaluation grid, coupled with the flexible weighting system, provides urban planners and traffic engineers with a robust decision-support tool capable of addressing the multifaceted challenges of modern urban mobility. As cities worldwide grapple with increasing traffic complexity and sustainability imperatives, this FAHP-based approach offers a structured pathway toward evidence-based infrastructure decisions that optimize safety, efficiency, and societal benefit.

References

Abdullah, M.S. & Asmael, B.M. 2023. Application of AHP to prioritize urban road scenarios in Baghdad. Journal of Engineering and Sustainable Development, 27(1), pp.15–24.

Ameljańczyk, A. 2021. The role of properties of the membership function in construction of fuzzy sets ranking. Computer Science and Mathematical Modelling, 11–12, pp.5–12. Available at: https://doi.org/10.5604/01.3001.0015.2732.

Bandyopadhyay, S. 2021. A novel multi-criteria decision analysis technique incorporating demanding essential characteristics of existing MCDA techniques. Research Square. Available at: https://doi.org/10.21203/rs.3.rs-1163422/v1.

Barić, D. & Starčević, D. 2015. Strategic planning of road infrastructure using multi-criteria analysis. Promet – Traffic & Transportation, 27(1), pp.37–45. Available at: https://doi.org/10.7307/ptt.v27i1.1514.

Barić, D., Pilko, H. & Dragčević, V. 2007. The use of multi-criteria decision-making methods in traffic infrastructure investment planning. Promet – Traffic & Transportation, 19(5), pp.305–311.

Barić, D., Pilko, H. & Županović, D. 2016. Application of the AHP method in traffic planning for the purpose of comparing road design alternatives. Tehnički vjesnik – Technical Gazette, 23(6), pp.1717–1723. Available at: https://doi.org/10.17559/TV-20140716141532.

Bouamrane, A., Derdous, O., Dahri, N., Tachi, S.-E., Boutebba, K. & Bouziane, M.T. 2020. A comparison of the analytical hierarchy process and the fuzzy logic approach for flood susceptibility mapping in a semi-arid ungauged basin (Biskra basin: Algeria). International Journal of River Basin Management, 20(2), pp.203–213. Available at: https://doi.org/10.1080/15715124.2020.1830786.

Chamoli, S. 2015. Hybrid FAHP–FTOPSIS approach for performance evaluation of the V down perforated baffle roughened rectangular channel. Energy, 84, pp.432–442. Available at: https://doi.org/10.1016/j.energy.2015.03.007.

Chan, H.K., Sun, X. & Chung, S. 2019. When should fuzzy analytic hierarchy process be used instead of analytic hierarchy process? Decision Support Systems, 125, p.113114. Available at: https://doi.org/10.1016/j.dss.2019.113114.

Cowan, R. 1987. An extension of Tanner's results on uncontrolled intersections. Queueing Systems.

Dean, M. 2020. Multi-criteria analysis. In: Advances in Transport Policy and Planning, pp.165–224. Available at: https://doi.org/10.1016/bs.atpp.2020.07.001.

Dean, M. 2021. Participatory multi-criteria analysis methods: comprehensive, inclusive, transparent and user-friendly? Research in Transportation Economics, 88, p.100887. Available at: https://doi.org/10.1016/j.retrec.2020.100887.

Dean, M., Hickman, R. & Chen, C. 2018. Testing the application of participatory MCA. Transport Policy, 73, pp.62–70. Available at: https://doi.org/10.1016/j.tranpol.2018.10.007.

Faizi, S., Sałabun, W., Rashid, T., Zafar, S. & Wątróbski, J. 2020. Intuitionistic fuzzy sets in multi-criteria group decision making. Symmetry, 12(9), p.1382. Available at: https://doi.org/10.3390/sym12091382.

Garg, H., Ali, Z. & Mahmood, T. 2020. Algorithms for complex interval-valued q-rung orthopair fuzzy sets. Expert Systems, 38(1). Available at: https://doi.org/10.1111/exsy.12609.

Gühnemann, A., Laird, J.J. & Pearman, A.D. 2012. Combining cost-benefit and multi-criteria analysis. Transport Policy, 23, pp.15–24. Available at: https://doi.org/10.1016/j.tranpol.2012.05.005.

Guler, S.I. & Menendez, M. 2016. Estimating capacity and vehicle delays at unsignalized intersections. International Journal of Transportation Science and Technology, 5(4), pp.257–267. Available at: https://doi.org/10.1016/j.ijtst.2017.03.002.

Ha, Q.M., Fugate, B.S. & Kazemi, H. 2015. Supplier selection using Fuzzy AHP and Fuzzy TOPSIS. International Journal of Advanced Manufacturing Technology, 76(1–4), pp.432–442. Available at: https://doi.org/10.1007/s00170-014-6265-3.

Henke, I., Cartenì, A. & Di Francesco, L. 2020. Sustainable evaluation processes in transport. Sustainability, 12(23), p.9854. Available at: https://doi.org/10.3390/su12239854.

Hickman, R. & Dean, M. 2017. Incomplete cost–benefit analysis in transport appraisal. Transport Reviews, 38(6), pp.689–709. Available at: https://doi.org/10.1080/01441647.2017.1407377.

Khokhar, S.U.D. & Peng, Q. 2022. Enhancing membership functions in fuzzy systems. Applied Intelligence, 53(7), pp.7818–7832. Available at: https://doi.org/10.1007/s10489-022-03799-4.

Lallam, M. & Mammeri, A. 2023. Fuzzy analytical hierarchy damage assessment. Building Structures & Structural Mechanics, 23(2), pp.20–26. Available at: https://doi.org/10.35181/tces-2023-0010.

Lallam, M., Djebli, A. & Mammeri, A. 2023. Damage assessment in masonry buildings. International Journal of Architectural Heritage, pp.1–20. Available at: https://doi.org/10.1080/15583058.2023.2295885.

Lallam, M., Mammeri, A. & Djebli, A. 2021. Damage state assessment of arch masonry bridges. Civil Engineering Journal, 7(11), pp.1933–1946. Available at: https://doi.org/10.28991/cej-2021-03091770.

Liu, Y. & Wu, Y. 2009. Traffic capacity impairment mechanism. In: Proceedings of ICICTA 2009, pp.728–731. Available at: https://doi.org/10.1109/ICICTA.2009.641.

Liu, Y., Eckert, C.M. & Earl, C. 2020. Review of fuzzy AHP methods. Expert Systems With Applications, 161, p.113738. Available at: https://doi.org/10.1016/j.eswa.2020.113738.

Lyu, H.M., Sun, W.J., Shen, S.L. & Zhou, A.N. 2019. Risk assessment using fuzzy AHP. Journal of Construction Engineering and Management, 146(3). Available at: https://doi.org/10.1061/(asce)co.1943-7862.0001757.

Otković, I.I., Karleuša, B., Deluka-Tibljaš, A., Šurdonja, S. & Marušić, M. 2021. Combining traffic microsimulation modeling and multi-criteria analysis for sustainable spatial-traffic planning. Land, 10(7), p.666. Available at: https://doi.org/10.3390/land10070666.

Pilevar, A.R., Matinfar, H.R., Sohrabi, A. & Sarmadian, F. 2019. Integrated fuzzy, AHP and GIS techniques for land suitability assessment in semi-arid regions. Ecological Indicators, p.105887. Available at: https://doi.org/10.1016/j.ecolind.2019.105887.

Qu, W., Li, J., Yang, L., Li, D., Liu, S., Zhao, Q. & Qi, Y. 2020. Short-term intersection traffic flow forecasting. Sustainability, 12(19), p.8158. Available at: https://doi.org/10.3390/su12198158.

Raval, S. & Tailor, B. 2020. Mathematical modelling of students' academic performance evaluation using fuzzy logic. International Journal of Statistics and Reliability Engineering, 7(1), pp.149–159.

Ren, J., Manzardo, A., Toniolo, S. & Scipioni, A. 2019. Sustainability evaluation of urban energy systems: a hybrid multi-criteria decision-making approach. Renewable and Sustainable Energy Reviews, 112, pp.117–129. Available at: https://doi.org/10.1016/j.rser.2019.05.041.

Sari, F. & Şen, M. 2021. Highway route planning via least cost path algorithm and multi-criteria decision analysis integration. International Journal of Environment and Geoinformatics, 9(2), pp.27–38. Available at: https://doi.org/10.30897/ijegeo.900200.

Singh, M.P., Singh, P. & Singh, P. 2024. Multi-criteria decision analysis for route alignment planning using GIS and AHP. Chinese Journal of Urban and Environmental Studies, 12(1). Available at: https://doi.org/10.1142/s2345748124500064.

Shukla, A.K. & Muhuri, P.K. 2024. Deep belief network with fuzzy parameters and membership function sensitivity analysis. Neurocomputing. Available at: https://doi.org/10.1016/j.neucom.2024.128716.

Yucesan, M. & Gul, M. 2019. Hospital service quality evaluation based on fuzzy AHP and fuzzy TOPSIS. Soft Computing, 24(5), pp.3237–3255. Available at: https://doi.org/10.1007/s00500-019-04084-2.

Zalhaf, A.S., Elboshy, B., Kotb, K.M., Han, Y., Almaliki, A.H., Aly, R.M.H. & Elkadeem, M.R. 2021. High-resolution wind farm suitability mapping using GIS and fuzzy AHP. Sustainability, 14(1), p.358. Available at: https://doi.org/10.3390/su14010358.

Primena fazi algoritama u komparativnoj evaluaciji projektovanja raskrsnica

Oualid Largueche[a], **autor za prepisku**, *Mostefa* Lallam[b], *Miloud* Driss[c], *Mohammed* Amine Hamadouche[d],
[a] Department of Civil Engineering, University of Mustapha Stambouli, Mascara, People's Democratic Republic of Algeria +
Laboratory of Geomatics, Ecology and Environment Research (LGEO2E), Mascara, Algeria,
[b] Department of Civil Engineering, University of Mustapha Stambouli, Mascara, People's Democratic Republic of Algeria +
Laboratory Mechanics of Structures, University of Tahri Mohamed, Bechar, Algeria
[c] Department of Civil Engineering, University of Mustapha Stambouli, Mascara, People's Democratic Republic of Algeria +
Laboratory of Sciences and Technology of Water, University of Mascara, Algeria
[d] Department of Economics, University of Mustapha Stambouli, Mascara, People's Democratic Republic of Algeria +
Laboratory of Geomatics, Ecology and Environment Research (LGEO2E), Mascara, Algeria

OBLAST: građevinarstvo, saobraćajno inženjerstvo
KATEGORIJA (TIP) ČLANKA: originalni naučni rad

Sažetak:

Uvod/cilj: Urbane saobraćajne raskrsnice su izuzetno složeni čvorovi u transportnim mrežama zbog ukrštanja više, često međusobno konfliktnih, saobraćajnih tokova. Upravljanje takvim tokovima predstavlja značajan izazov, što dovodi do problema poput promenljivih vremena zadržavanja i vraćanja saobraćaja, naročito kod preopterećenih raskrsnica. Budući da ovakve raskrsnice često deluju kao uska grla, tačne kratkoročne prognoze saobraćajnih tokova su ključne za efikasno planiranje i ublažavanje zagušenja. Cilj ove studije je da predloži robustan okvir za višekriterijumsku evaluaciju projektovanja raskrsnica kako bi se podržalo optimizovano urbano planiranje i upravljanje saobraćajem.

Metode: Da bi se odgovorilo na inherentne složenosti i neizvesnosti u vezi sa evaluacijom ovakvih rešenja, u ovom istraživanju se primenjuje fazi analitički hijerarhijski proces (FAHP). Ova metoda je posebno pogodna za kontekste u kojima se stručne evaluacije, koje često uključuju kvalitativne kriterijume poput uklapanja u pejzaž ili uticaja na lokalnu ekonomiju, ne mogu izraziti sa apsolutnom preciznošću. Naš pristup integriše fazi logiku radi upravljanja subjektivnošću i neodređenošću u evaluacijama, kao i

kvantitativnim faktorima poput troškova i zasićenosti saobraćaja. Na osnovu opsežnog pregleda literature i utvrđenih standarda u oblasti saobraćajnog inženjeringa i urbanog planiranja, razvijena je sveobuhvatna mreža od 32 kriterijuma i potkriterijuma koji obuhvataju ključne aspekte kao što su bezbednost saobraćaja, nivo usluge i protok saobraćaja. Eksperti dodeljuju težinske vrednosti ovim kriterijumima, a one se zatim obrađuju pomoću FAHP metode kako bi se dobio globalni pokazatelj performansi. Ovaj pokazatelj omogućava rangiranje i poređenje različitih projektnih rešenja.

Rezultati: Primena FAHP okvira dovodi do izračunavanja globalnog pokazatelja performansi koji omogućava objektivno rangiranje alternativnih rešenja za raskrsnice. Metodologija pruža strukturiran pristup za balansiranje više, često konfliktnih, kriterijuma u složenim okruženjima odlučivanja. Praktična primenljivost metode prikazana je kroz studiju slučaja raskrsnice Šetija, u kojoj je uspešno identifikovana optimalna konfiguracija od više predloženih varijanti. Ovo potvrđuje svestranost FAHP metode u evaluaciji performansi unutar složenih urbanih sistema.

Zaključak: Ova studija uspešno pozicionira FAHP unutar šireg okvira višekriterijumske analize odlučivanja (MCDA) i nudi originalnu primenu u oblasti projektovanja raskrsnica. Integracijom fazi logike, metodologija efikasno upravlja neizvesnošću u vezi sa kvalitativnim i kvantitativnim kriterijumima evaluacije, što je posebno korisno kada je teško doći do preciznih stručnih procena. Predloženi okvir predstavlja robustan i višedimenzionalan alat za urbaniste i saobraćajne inženjere, i omogućava informisanije i optimizovanije odluke o infrastrukturi u složenim urbanim raskrsnicama.

Ključne reči: raskrsnica, fazi analitički hijerarhijski proces (FAHP), alternativna projektna rešenja, kriterijumi, nivo usluge, složeni pokazatelj performansi (CPI).

Paper received on: 12 July 2025.
Manuscript corrections submitted on: 12 September 2025.
Paper accepted for publishing on: 28 October 2025.

© 2026 The Authors. Published by Vojnotehnički glasnik / Military Technical Courier (www.vtg.mod.gov.rs).This article is an open access article distributed under the terms and conditions of the Creative Commons Attribution license (http://creativecommons.org/licenses/by/4.0/rs/)

Experimental determination of surface emissivity for military equipment components and comparison with reference data

Lazar Z. Lazarević[a], *Nebojša* P. Hristov[b], *Damir* D. Jerković[c], *Darko* R. Latinkić[d], *Mihael* M. Bučko[e]

University of Defence, Military Academy, Belgrade, Republic of Serbia

[a] e-mail: llazarevic995@gmail.com,
ORCID iD: https://orcid.org/0000-0003-1949-2685

[b] e-mail: nebojsa.hristov@va.mod.gov.rs,
ORCID iD: https://orcid.org/0000-0002-8163-2223

[c] e-mail: damir.jerkovic@va.mod.gov.rs,
ORCID iD: https://orcid.org/0000-0001-5182-7057

[d] e-mail: darkolatinkic@gmail.com,
ORCID iD: https://orcid.org/0000-0003-4952-123X

[e] e-mail: mihael.bucko@va.mod.gov.rs, **corresponding author**,
ORCID iD: https://orcid.org/0000-0001-6992-8841

https://doi.org/10.5937/vojtehg74-61524

FIELD: materials
ARTICLE TYPE: original scientific paper

Abstract:

Introduction/purpose: The aim of this paper was to investigate the emissivity of materials relevant to the Serbian Armed Forces and to assess their role in infrared signature management and camouflage performance. Emissivity is a critical parameter influencing the thermal detectability of objects, as surfaces with higher emissivity emit more infrared radiation and thus become more visible to thermal imaging systems.

Methods: In this study, emissivity values of textiles, wood, metals, and polymeric components were measured using a FLIR-based thermographic method. The applied approach proved to be fast and reliable, with results consistent with established reference data.

Results: Differences between material classes were evident: textiles and polymers generally showed high emissivity, metals displayed lower values strongly affected by surface treatments, while wooden elements

ACKNOWLEDGMENT: The authors would like to acknowledge support from the scientific projects of the Military Academy, University of Defense in Serbia: “Research on influence of characteristics of explosive ordnance on safety in Ministry of Defense and Army of Serbia” (VA-TT/1/22-24), and “Improvement of ballistic testing in the design phase of weapon systems and ballistic protection” (VA/TT/1/24-26).

remained highly emissive and therefore more exposed to detection. These findings confirm that emissivity is highly dependent on material type, surface finish, and applied coatings.

Conclusion: The results provide a comprehensive dataset for military-relevant materials and highlight the practical importance of emissivity characterization in the development of effective camouflage strategies. By integrating accurate emissivity data into infrared signature modeling, it becomes possible to optimize camouflage design and improve operational survivability by reducing the probability of detection on the battlefield.

Key words: emissivity, infrared thermography, FLIR measurement, military equipment.

Introduction

Thermal radiation plays an important role in the performance and survivability of military systems, and material emissivity is a critical parameter in controlling radiative heat transfer. Emissivity determines the thermal signature visible to infrared sensors. Its accurate characterization is essential not only for conventional engineering applications but also for military technologies, where thermal management and signature control are crucial for operational effectiveness (Modest, 2013).

The emissivity of a material surface is defined as the ratio between the radiant energy emitted by the material at temperature T and that emitted by an ideal blackbody at the same temperature. Thermal radiation represents electromagnetic radiation, typically comprising both visible radiation (light) and infrared radiation, the latter being invisible to the human eye. A fraction of thermal radiation originating from very hot objects is, however, easily detectable by sight (López et al., 2013).

The emissivity of a surface is strongly influenced by its chemical composition as well as its geometric structure. The emissivity coefficient ranges from 0 to 1.0 (King et al., 2017). A perfect blackbody (with emissivity equal to 1.0) emits thermal radiation of approximately 448 W/m² at a room temperature of 25 °C (298 K). Real surfaces with emissivity values lower than unity radiate proportionally less energy under identical thermal conditions (Liu et al., 2024).

The military significance of emissivity is primarily associated with the detectability of vehicles, aircraft, and naval vessels. Low-emissivity coatings are applied to reduce infrared signatures and enhance stealth capabilities, while high-emissivity surfaces are used to improve heat dissipation in critical systems (Ateia et al., 2021). For instance, armored vehicles employ specialized coatings to manage heat from engines and exhaust systems, reducing the probability of detection by enemy infrared

reconnaissance systems. Similarly, missile casings and radar components utilize materials with tailored emissive properties to optimize thermal performance while minimizing detectability (Kim et al., 2017).

Emissivity also has direct implications for the thermal regulation of sensitive military components. Engineered surfaces with selective emissive properties, such as oxide layers, ceramic coatings, and nanostructured films, allow precise control over radiative heat transfer. These surfaces enable efficient heat dissipation from electronic housings, missile structures, and radar components while simultaneously minimizing thermal signatures (Králík et al., 2019).

Infrared thermography is a fundamental tool for analyzing surface temperature distribution and estimating material emissivity under realistic conditions. It allows for non-contact evaluation of thermal performance, which is essential for operational military systems (Salihoglu et al., 2018). Using high-resolution thermal imaging, engineers can identify hotspots, evaluate the effectiveness of thermal coatings, and monitor structural components subjected to variable thermal loads. For example, infrared imaging has been applied to monitor the thermal footprint of armored personnel carriers during field exercises, providing data critical for reducing detection risk and improving crew safety (Tran et al., 2021).

Modern FLIR (Forward-Looking Infrared) cameras provide practical methods for measuring emissivity in situ. These devices combine radiometric measurements with high-resolution imaging, allowing the determination of surface emissivity even on heterogeneous or non-uniform materials. By calibrating against reference surfaces, FLIR systems can correct apparent temperatures and yield accurate emissivity values, a process essential when evaluating complex coatings on metals, composites, or polymers used in military equipment (Lafargue-Tall et al., 2022).

The integration of infrared thermography and FLIR-based emissivity measurement has expanded the ability to quantify and model thermal behavior under field conditions. Real-time thermographic assessment of military systems improves maintenance, the identification of insulation failures, and the evaluation of coating degradation. Moreover, these techniques are applied during experimental trials to optimize material selection and surface treatments, balancing thermal efficiency with stealth requirements (Samolov et al., 2021).

This research focuses on the systematic characterization of the emissive properties of selected military-relevant materials using infrared thermography and FLIR measurement techniques. The investigation includes materials with varying surface treatments, such as metallic

coatings, composite laminates, and polymeric films, reflecting the diversity of contemporary military hardware. This approach ensures a comprehensive evaluation, providing engineers with actionable data for the design of systems with enhanced operational performance under thermal and detection constraints. Using collected emissivity data, engineers can optimize material selection, surface treatments, and coating strategies, ultimately improving the survivability, efficiency, and stealth of critical military assets (Modest, 2013).

Several challenges complicate the reliable measurement of emissivity. First, emissivity is strongly angle-dependent, requiring integration over all emission angles or measurement at the most relevant ones. Second, it exhibits spectral selectivity, as infrared cameras detect only specific wavelength ranges (e.g., 8 – 12 μm), leaving emissivity outside those bands unaccounted for. Third, surface texture plays a major role: rough, oxidized, or contaminated surfaces often radiate differently compared to polished laboratory samples. Fourth, some materials display a pronounced temperature dependence of emissivity, as in the case of VO_2 and other phase-transition compounds. Finally, ambient reflections of infrared radiation can distort measurement results, particularly on metallic or low-emissivity surfaces. These challenges are especially critical in military applications, where accurate emissivity data are essential for camouflage optimization, thermal signature reduction, and infrared detection countermeasures (Salihoglu et al., 2018).

Materials and methods

Experimental setup

The measurement of emissivity was performed using a FLIR E40 infrared camera, which enables non-contact temperature determination by detecting infrared radiation from a material surface. Technical characteristics of the FLIR E40 camera may be found in our previous report (Boukera et al., 2022).

The procedure consisted of heating each sample uniformly in a drying oven (VIMS Elektrik, model VSSW-53, Figure 1a) until it reached a surface temperature of approximately 60 °C. The sample was then placed inside a high-emissivity cardboard protective enclosure, and its temperature was measured as it cooled spontaneously. The infrared camera was positioned at a distance of 1.0 m and oriented at a 45° angle relative to the sample surface in order to reduce reflection and minimize measurement errors (Figure 1b). The temperature measurements of the samples were

conducted under controlled laboratory conditions, with an ambient temperature at 22 ± 1 °C and relative humidity below 50%.

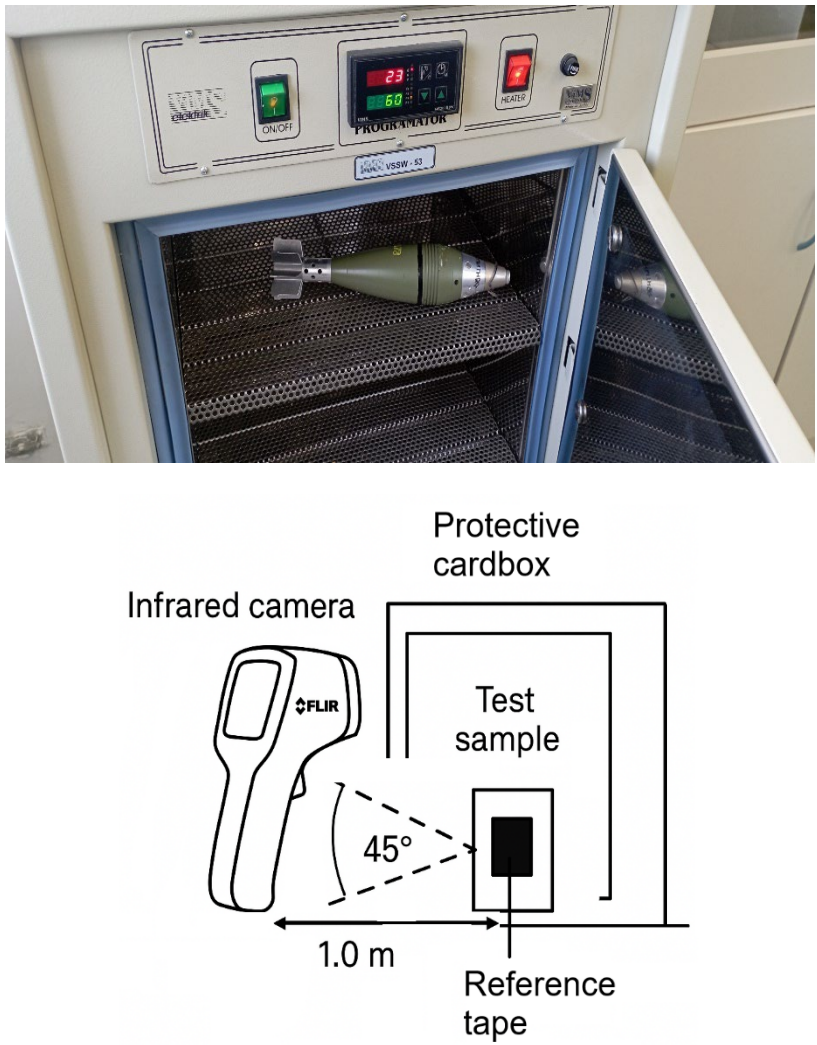

Figure 1 – Sample heating in the laboratory oven and the experimental setup scheme

The samples included metallic and polymeric surfaces with different surface treatments: bare steel, blued steel, wood, textile, polymers, and coatings. Each sample was cleaned with ethanol prior to measurement to remove dust and grease, since contaminants may significantly affect emissivity values (Liu et al., 2024).

Measurement procedure

Emissivity was determined using the direct method implemented in the FLIR software package. Namely, a matte black reference tape with a known emissivity coefficient of 0.95 (Boukera et al., 2022) was mounted onto the test specimens used for emissivity measurements, thereby ensuring thermal equilibrium between the plate and the specimen surface. In the first stage, the apparent temperature of the reference black tape was recorded by the FLIR camera, assuming a default emissivity value of 0.95. Then, the camera was pointed at the surface of the specimen, and the emissivity parameter in the software was iteratively adjusted until the measured infrared temperature matched the temperature of the reference tape. The resulting value was taken as the true emissivity of the sample surface (Boukera and Bouhidel, 2022).

The data collected by the FLIR camera were exported into FLIR Tools+ software for further processing. Emissivity maps were generated in order to visualize spatial variations across the surface. Statistical analysis was performed on three independent measurements for each sample to ensure repeatability, and the mean values were reported. The standard deviation (SD) was also calculated for each material and was found to be less than 0.050 in all cases, as shown in the tables below, which is acceptable for military applications where detection thresholds depend on relative rather than absolute differences (Liu et al., 2024).

Calibration of the FLIR camera was performed at the beginning of each measurement day using the black reference plate. To minimize reflections, the experiments were carried out in a darkened environment with no direct sunlight or artificial infrared sources.

Results and discussion

Tables 1 – 4 present both our experimentally obtained emissivity values and the reference values reported by Fluke and ThermoWorks databases (instrument manufacturer guidelines for emissivity adjustment) (Fluke Process Instruments, 2025; ThermoWorks, 2025) and other relevant literature sources. Representative infrared images are shown for different sample materials, where the attached plate appears as a distinct area of contrasting color, serving as a visual indicator of emissivity differences between the surfaces.

Table 1 - Emissivity of textile-based military equipment

Material	Average measured emissivity (ε)	Standard Deviation (ε)	Literature emissivity range (ε)
Serbian Armed Forces uniform, M10	0.87	0.034	0.90 – 0.98
Serbian Armed Forces uniform, M93 (Figure 2)	0.83	0.043	
Hook-and-loop insignia fastener (M10 uniform)	0.81	0.025	
Serbian Armed Forces insignia (Figure 2)	0.71	0.018	

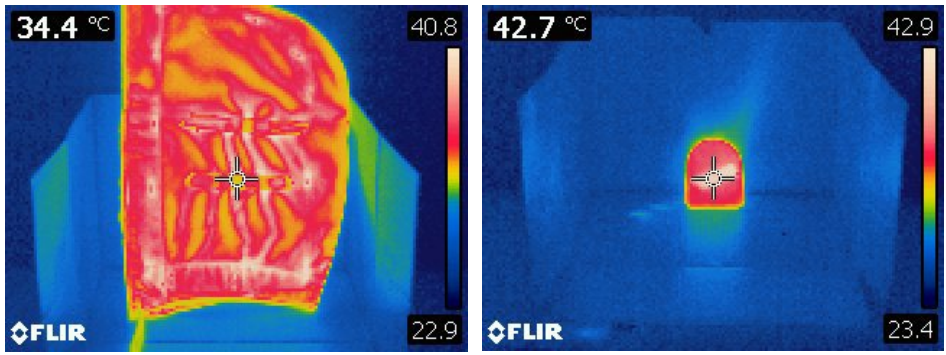

Figure 2 - Infrared images of the M93 uniform component and the insignia at the M10 uniform

The known emissivity values for cloth fabric range between 0.90 and 0.98, for black rubber are in the range of 0.94 – 0.95, and for leather are in the range of 0.95 – 0.98. Therefore, the measured emissivity values for military uniforms in our experiment (M10, M93) (0.83 – 0.87) are consistently lower than the reference emissivity range for generic fabrics. This discrepancy can be attributed to the presence of hydrophobic or flame-retardant coatings, specific dyeing processes (olive drab shade vs. black fabrics in literature), and surface wear and field use, which alter infrared reflectivity.

Hook-and-loop fasteners and insignia both show reduced emissivity (0.71 – 0.81) compared to textile standards, reflecting their plastic-based and partially reflective surfaces. This confirms that uniform accessories should be treated as distinct categories from fabric itself.

To achieve effective camouflage in the infrared region of the electromagnetic spectrum, the emissivity of a fabric must be engineered

to approximate the thermal radiation characteristics of its surrounding environment. In natural terrains, vegetation represents the dominant background, and its emissivity is typically around 0.95, indicating the emissive behavior that camouflage textiles must replicate to minimize thermal contrast.

A variety of strategies may be employed to modify the emissivity of textile substrates. These include the incorporation of tailored pigments or nanostructured additives capable of altering the radiative properties of the surface, as demonstrated in the work on enhancing VIS and IR camouflage performance through PVB/IF-WS_2 impregnation of cotton fabrics (Samolov et al., 2021). Furthermore, emissivity can be adjusted by integrating metallic or other highly reflective layers into the textile architecture; however, such approaches often introduce undesirable reflections in the visible spectrum (Degenstein et al., 2021).

Table 2 - Emissivity of wooden components of military equipment

Material	Average measured emissivity (ε)	Standard Deviation (ε)	Literature emissivity range (ε)
Wooden ammunition box	0.85	0.024	
Wooden handguard for M70 assault rifle (Figure 3)	0.93	0.018	
Softwoods (spruce, pine)			0.80 – 0.90
Hardwoods (oak, redwood)			0.83 – 0.92
Processed wood (planed / varnished)			0.85 – 0.93
Plywood (smooth, commercial)			0.82 – 0.98

Measured emissivity values for wooden ammunition boxes and weapon handguards range from 0.85 to 0.93, which falls within the literature range for natural and processed wood (0.80 – 0.93) (López et al., 2013). This indicates that our measurements for wood are more consistent with reference values than those of the textile group. One may conclude that wooden components of military equipment are highly emissive and therefore are easily detectable in thermal imaging, which is important for assessing camouflage effectiveness in the field.

The measured emissivity values for metallic components generally fall within or slightly below the range reported in the literature. The measured emissivity of the M70 bolt carrier ($\varepsilon = 0.51$) is consistent with literature values for unpolished/rough steel ($\varepsilon \approx 0.30 – 0.60$), indicating a machined or lightly oxidized surface finish rather than a mirror-polished treatment

(Howell et al., 2010). Brass components show intermediate values that correlate well with literature data.

Table 3 - Emissivity of metallic parts of military equipment

Material	Average measured emissivity (ε)	Standard Deviation (ε)	Reference ε (Fluke)	Reference ε (ThermoWorks)
Bolt carrier with bolt, M70 assault rifle (alloy steel, polished finish) (Figure 3)	0.51	0.034	0.30 – 0.60 for unpolished steel	
Brass 76 mm M58 shell (Figure 3)	0.73	0.008	0.69	0.61
Brass 20 mm M69 cartridge (Figure 3)	0.61	0.016	0.69	0.61
Blued (burnished) steel components				
Slide assembly with bolt for M57 pistol (Figure 3)	0.54	0.016	0.60 – 0.95	
Slide cover for CZ99 pistol	0.67	0.005		
Receiver cover for M70 assault rifle	0.75	0.042		
Detachable box magazine, 30-round, for M70 assault rifle (Figure 4)	0.64	0.029		
Detachable box magazine, 9-round, for M57 pistol	0.67	0.016		
Detachable box magazine, 15-round, for CZ99 pistol	0.72	0.017		

The measured emissivity values for the burnished components of Serbian small arms, including the slide assembly with bolt for the M57 pistol (ε = 0.54), slide cover for the CZ99 pistol (ε = 0.67), receiver cover for the M70 assault rifle (ε = 0.75), and various detachable box magazines (ε = 0.64 – 0.72), are generally lower than the emissivity reported in literature for similarly treated steel surfaces. According to Fluke Process Instruments, oxidized steel surfaces exhibit emissivity values near 0.95, while for polished steel it can be as low as 0.07 (Fluke Process Instruments, 2025). Similarly, Omega Engineering reports an emissivity of

blued steel around 0.79, depending on the thickness of the oxide layer and surface roughness (Omega Engineering, 2025). These reference values suggest that our measured results are systematically lower, likely due to experimental factors such as ambient reflections, the finite angle of infrared detection, and possible local variations in the oxide layer.

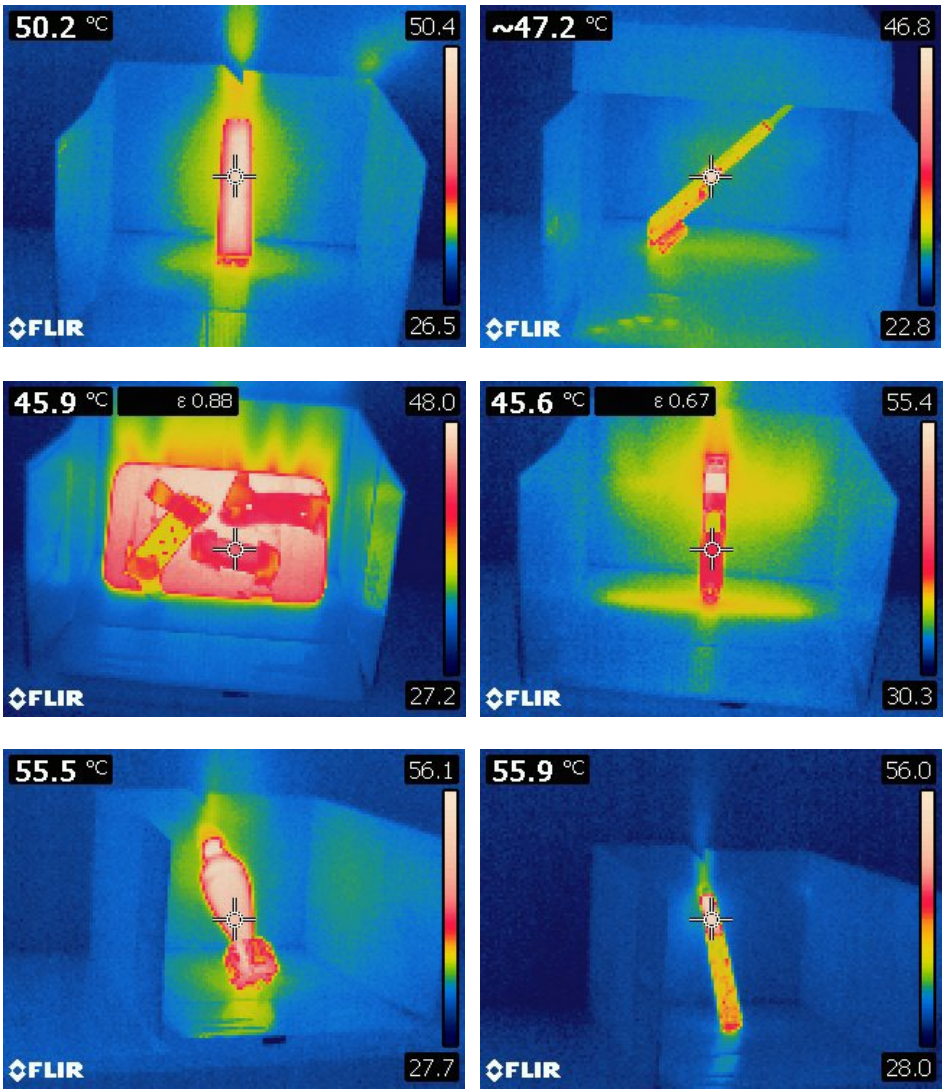

Figure 3 - Infrared images of the weapons and ammunition parts: wooden handguard for the M70 assault rifle; bolt carrier for the M70 rifle; the M57 pistol components; slide assembly for pistol M57 pistol; brass 76 mm M58 shell; and brass 20 mm M69 cartridge

The variation observed among the measured parts: ε = 0.54 for the M57 slide versus ε = 0.75 for the M70 receiver cover—may reflect differences in surface finish, machining, or oxidation procedures. Surface characteristics of metals, including sandblasting, increased roughness and oxide layer thickness, strongly influence emissivity. Increased roughness enhances surface–radiation interaction by creating more microfacets and trapping emitted radiation, typically increasing emissivity by 0.05–0.15 for steels, whereas oxidation can raise emissivity more substantially, from ~0.3–0.5 up to ~0.6–0.8, depending on material and treatment conditions, because the oxide layer is less reflective and more absorptive in the infrared, efficiently emitting thermal radiation (King et al., 2017).

Burnishing, also known as bluing or black oxide coating, is a conversion treatment that forms a thin magnetite (Fe_3O_4) layer on steel, enhancing corrosion resistance and yielding a characteristic dark appearance (Oberg & Green, 2004). Importantly, the thermal radiative properties of such coated metals are highly dependent on surface condition. Oxidized or black-oxide-treated surfaces exhibit markedly higher emissivity compared to their polished or untreated counterparts, primarily due to increased surface roughness and absorption characteristics. This relationship is well-documented in studies exploring the influence of surface treatments on metal emissivity (Králík et al., 2016).

Overall, these measurements highlight that while burnished steel significantly increases thermal emission compared to polished steel, our results suggest a moderate underestimation relative to literature values. For future measurements, consideration of angle-dependent emissivity corrections and accounting for ambient infrared reflections could improve accuracy (Modest, 2013). Despite these limitations, the measured emissivity values remain consistent with expected behavior for darkened steel surfaces and can inform infrared-based detection or thermal analysis of similar military equipment.

Plastics, polymers and dark-colored organic coatings exhibit generally high emissivity values, typically ranging between 0.80 and 0.95 (Fluke, 2025; ThermoWorks, 2025), and our results fall within this range. Interestingly, the emissivity measured for the polymer of the M19 rifle was even higher than that of the black insulating tape employed as a reference standard in our experiments. A plausible explanation for this observation lies in surface texture: the insulating tape has a smooth finish, whereas the black polymer on the rifle exhibits a slightly roughened surface. It is well-established that microscale surface roughness increases the effective emissivity by enhancing absorption and scattering of thermal radiation, thereby reducing reflection (Modest, 2013).

Table 4 - Emissivity of polymeric materials and coated surfaces of military equipment

Material	Measured ε	Standard Deviation (ε)	Reference ε (ThermoWorks)
VMRUD anti-personnel mine, olive drab plastic casing	0.92	0.000	0.93 – 0.95 (for dark plastic)
60 mm M57 mortar shell, olive drab coating	0.93	0.005	
Pistol grip (carved section) for M57 pistol	0.86	0.005	
Receiver cover for M19 assault rifle, polymer (Figure 4)	0.99	0.000	
Detachable box magazine, 30-round, for M19 assault rifle, polymer (Figure 4)	0.99	0.000	

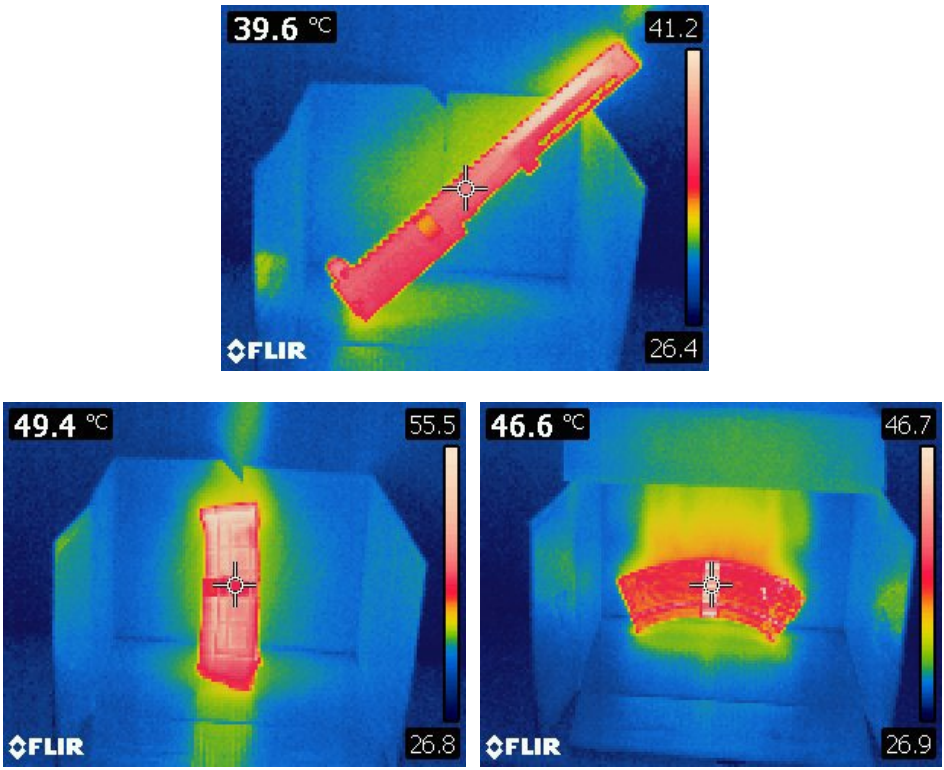

Figure 4 - Infrared images of the receiver cover for the M19 rifle; box magazine for the M19 rifle (left), and the M70 rifle (right)

For visual comparison, Figure 4 presents thermal images of the two box magazines with different emissivity values (ε = 0.99 for the M19 rifle and ε = 0.64 for the M70 rifle), each covered with a high-emissivity black tape (ε = 0.95). It can be visually observed, even without numerical analysis, that the tape appears darker than the high-emissivity substrate and brighter than the low-emissivity substrate. This occurs because high-emissivity surfaces emit thermal radiation more efficiently and therefore appear closer to their true temperature in infrared images, while low-emissivity surfaces emit less radiation and reflect more of the cooler surroundings, causing them to appear artificially colder compared to the tape.

From a practical perspective, this high emissivity has implications for thermal signature and infrared detectability. Surfaces with emissivity closer to a perfect black body emit thermal radiation more efficiently, which can make them more conspicuous under infrared observation, as these components would appear relatively “hot” under infrared observation. Therefore, while the polymer's mechanical and protective properties may be advantageous, its elevated emissivity could be a limiting factor for thermal camouflage in operational environments. This highlights a trade-off in material selection between durability, aesthetics, and infrared signature management in military applications.

Conclusion

The comprehensive emissivity measurements of military-relevant materials conducted in this study confirm both the reliability and rapidity of the FLIR-based method, which demonstrated consistent agreement with tabulated emissivity values. The deviations observed were minor for most classes of materials, although metallic surfaces systematically exhibited slightly lower emissivity compared to literature data, primarily due to surface finish and ambient reflection effects. Military textiles such as M10 and M93 uniforms showed emissivity values in the range of 0.83–0.87, notably lower than the generic fabric range (0.90–0.98), indicating the influence of coatings and treatments. Wooden components of weapons and ammunition boxes yielded emissivity values of 0.85–0.93, which are in close alignment with literature ranges for natural and processed wood (0.80–0.93), confirming their highly emissive and thus easily detectable nature. Metallic weapon parts, such as the M70 bolt carrier (ε = 0.51) and blued steel magazines (ε = 0.64–0.75), fell within expected ranges but slightly underestimated compared to standard references, underlining the importance of accounting for oxidation layers and surface preparation. In

contrast, polymeric and coated surfaces exhibited high emissivity values (0.86–0.99), in full agreement with ThermoWorks and Fluke data, with polymer magazines and M19 rifle components approaching blackbody-like behavior ($\varepsilon \approx 0.99$).

Overall, this work provides a robust dataset of emissivity values across textiles, wood, metals, and polymers commonly used in Serbian military equipment, with results directly comparable to established databases. Building on the work of Samolov et al. (2021), our study addresses the continuous need within the Serbian Armed Forces for materials that enhance infrared camouflage capabilities. Importantly, the applied FLIR thermography method proved to be a fast, practical, and reliable approach for emissivity characterization, enabling rapid measurement in both field and laboratory conditions. This research equips engineers of the Serbian Armed Forces with a practical tool for evaluating and improving IR camouflage strategies, ultimately enhancing operational survivability and reducing the probability of detection.

References

Ateia, E. E., Metwaly, M. A. & Tantawy, H. R., 2021. Low thermal emissivity coating based on aluminium/acrylic composite coatings. IOP Conference Series: Materials Science and Engineering, 1172(1), 012027. https://doi.org/10.1088/1757-899X/1172/1/012027

Boukera Abaci, W., Hristov, N., Ziane Ahmed, N., Jerkovic, D. & Drakulic, M., 2022. Determination of the gun barrel walls temperature distribution and its experimental validation during multiple-shots firing process. International Journal of Thermal Sciences, 179, 107667. https://doi.org/10.1016/j.ijthermalsci.2022.107667

Degenstein, L., Sameoto, D., Hogan, J., Asad, A., Dolez, P., Smart Textiles for Visible and IR Camouflage Application: State-of-the-Art and Microfabrication Path Forward. Micromachines, 2021 12(7):773. https://doi.org/10.3390/mi12070773

Fluke Process Instruments, 2025. Emissivity Values for Common Materials. Available at: https://www.fluke.com

Howell, J., Siegel, R. & Mengüç, M. P., 2010. Thermal Radiation Heat Transfer. Fifth Edition. CRC Press. ISBN: 1439805334. https://doi.org/10.1201/9781439894552

Kim, T., Kim, T., Bae, J.-Y., Jung, D., & Cho, H.-H. (2017). Infrared Signature Analysis on Armored Vehicle Applied with Emissivity Controlled Structure. Journal of the Computational Structural Engineering Institute of Korea, 30(2), 179–184. https://doi.org/10.7734/COSEIK.2017.30.2.179

King, J. L., Jo, H., Tirawat, R., Blomstrand, K. & Sridharan, K., 2017. Effects of surface roughness, oxidation, and temperature on the emissivity of reactor

pressure vessel alloys. Nuclear Technology, 199(3), 329–343. https://doi.org/10.1080/00295450.2017.1353869

Králík, T., Hanzelka, P., Musilova, V. & Srnka, A., 2014. Factors influencing thermal radiative properties of metals. Refrigeration Science and Technology, 239–247. https://doi.org/10.48550/arXiv.1610.00915

Lafargue-Tallet, T., Vaucelle, R., Caliot, C., Aouali, A., Abisset-Chavanne, E., Sommier, A., Peiffer, R. & Pradere, C., 2022. Active thermo-reflectometry for absolute temperature measurement by infrared thermography on specular materials. Scientific Reports, 12, 11616. https://doi.org/10.1038/s41598-022-11616-8

Liu, Y., Long, L., Gao, Y., Li, W., Tang, Z. & Ye, H., 2024. Influence of emissivity on infrared camouflage performance. Infrared Physics & Technology, 141, 105509. https://doi.org/10.1016/j.infrared.2024.105509

López, G., Basterra, L. A., Acuña, L. & Casado, M., 2013. Determination of the emissivity of wood for inspection by infrared thermography. Journal of Nondestructive Evaluation, 32(2), 172–176. https://doi.org/10.1007/s10921-013-0170-3

Modest, M. F., 2013. Radiative Heat Transfer, 3rd Edition. Academic Press. https://doi.org/10.1016/C2010-0-65874-3

Omega Engineering, Inc., 2025. Table of Total Emissivity – Metals, Technical Reference Z-88/Z-89. Available at: https://www.omega.com

Salihoglu, O., Uzlu, H. B., Yakar, O., Aas, S., Balci, O., Kakenov, N., Balci, S., Olcum, S., Süzer, S. & Kocabas, C., 2018. Graphene-based adaptive thermal camouflage. Nano Letters, 18(7), 4541–4548. https://doi.org/10.1021/acs.nanolett.8b01746

Samolov, A. D., Simić, D. M., Fidanovski, B. Z., Obradović, V. M., Tomić, L. D., & Knežević, D. M. 2021. Improvement of VIS and IR camouflage properties by impregnating cotton fabric with PVB/IF-WS_2. Defence Technology, 17(6), 2050–2056. https://doi.org/10.1016/j.dt.2020.10.008

ThermoWorks, 2025. Material Emissivity Table. Available at: https://www.thermoworks.com

Tran, T. B. & Hoa, T. M. 2025. Experimental research and evaluation of thermal camouflage effectiveness of advanced materials for mobile vehicles. Journal of Military Science & Technology, 102, 109–117. https://doi.org/10.54939/1859-1043.j.mst.102.2025.109-117

Oberg, E., Jones, F. D., Horton, H. L. & Ryffel, H. H., 2004. Machinery's Handbook. Industrial Press, New York

Eksperimentalno određivanje površinske emisivnosti za komponente vojne opreme i poređenje sa referentnim podacima

Lazar Z. Lazarević, *Nebojša* P. Hristov, *Damir* D. Jerković, *Darko* R. Latinkić, *Mihael* M. Bučko, **autor za prepisku**
Univerzitet odbrane u Beogradu, Vojna akademija, Beograd, Republika Srbija

OBLAST: mašinstvo, materijali
KATEGORIJA (TIP) ČLANKA: originalni naučni rad

Sažetak:

Uvod/cilj: Cilj ovog rada bio je da se ispita emisivnost materijala relevantnih za Vojsku Srbije i oceni njihova uloga u upravljanju infracrvenim potpisom i efektivnosti kamuflaže. Emisivnost je kritičan parametar koji utiče na termičku detektabilnost objekata, jer površine sa većom emisivnošću emituju više infracrvenog zračenja i samim tim postaju vidljivije za termovizijske sisteme.

Metode: U ovoj studiji, vrednosti emisivnosti tekstila, drveta, metala i polimernih komponenti izmerene su termografskom metodom FLIR. Primenjeni pristup se pokazao brzim i pouzdanim, sa rezultatima koji su u skladu sa utvrđenim referentnim podacima.

Rezultati: Razlike između klasa materijala bile su očigledne: tekstil i polimeri generalno pokazuju visoku emisivnost, metali imaju niže vrednosti jako zavisne od obrade površine, dok drvene komponente ostaju visoko emitivne i samim tim više izložene detekciji. Ovi rezultati potvrđuju da emisivnost zavisi od tipa materijala, završne obrade površine i premaza.

Zaključak: Rezultati pružaju sveobuhvatan skup podataka za materijale relevantne za vojnu upotrebu i naglašavaju praktičnu važnost karakterizacije emisivnosti u razvoju efektivnih kamuflažnih strategija. Integrisanjem preciznih podataka o emisivnosti u modelovanje infracrvenog potpisa, postaje moguće optimizovati dizajn kamuflaže i produžiti operativnu upotrebu smanjenjem verovatnoće detekcije na bojnom polju.

Ključne reči: emisivnost, infracrvena termografija, FLIR merenje, vojna oprema.

Paper received on: 3 September 2025.
Manuscript corrections submitted on: 17 November 2025.
Paper accepted for publishing on: 24 November 2025.

© 2026 The Authors. Published by Vojnotehnički glasnik / Military Technical Courier (www.vtg.mod.gov.rs).This article is an open access article distributed under the terms and conditions of the Creative Commons Attribution license (http://creativecommons.org/licenses/by/4.0/rs/

Experimental assessment of acoustic effects of cannon fire on crew

Dragan R. Stojadinović[a], *Snezana B*. Jovanović[b],
Aleksandar S. Đurić[c], *Aleksandar B*. Bukvić[d], *Sreten* R. Perić[e]

[a] Technical Test Center, Sector for mototechnical and means of river units, Department for vehicles and superstructures, Belgrade, Republic of Serbia,
e-mail: dragan.stojadinovic@vs.rs, dragan.stojadinovic90@gmail.com, **corresponding author**,
ORCID iD: https://orcid.org/0009-0004-6534-8443

[b] Technical Test Center, Sector for mototechnical and means of river units, Department for vehicles and superstructures, Belgrade, Republic of Serbia,
e-mail: sneza.jovanovic.toc@gmail.com,
ORCID iD: https://orcid.org/0009-0004-6468-7726

[c] University of Defence in Belgrade, Military Academy, Department of Military Mechanical Engeneering, Belgrade, Republic of Serbia,
e-mail: aleksandar_djrc@yahoo.com,
ORCID iD: https://orcid.org/0000-0002-2165-528X

[d] University of Defence in Belgrade, Military Academy, Department of Military Mechanical Engeneering, Belgrade, Republic of Serbia,
e-mail: aleksandar.bukvic@mod.gov.rs,
ORCID iD: https://orcid.org/0000-0002-3025-8446

[e] University of Defence in Belgrade, Military Academy, Department of Military Mechanical Engeneering, Belgrade, Republic of Serbia,
e-mail: sretenperic@yahoo.com,
ORCID iD: https://orcid.org/0000-0002-7270-5187

https://doi.org/10.5937/vojtehg74-62152

FIELD: mechanical engineering
ARTICLE TYPE: review article

Abstract:

Introduction/purpose: The noise generated by artillery firing can have an extremely harmful effect on the people using it, namely the crew. The subject of this paper is the measurement and analysis of noise levels on artillery weapons used in the Serbian Army.

Methods: The analysis and comparison of the results were carried out during operation of weapons of different calibers. Also, the aspect of impact and risk on the crew exposed to the mentioned physical phenomena was considered.

Results: The results of the examination of the acoustic parameters in relation to the available criteria show that the crew on certain vehicles is exposed to a higher level of noise than allowed.

Conclusion: It is concluded that all measured noise levels exceed the prescribed limit value. Based on the obtained results, further work can be done on reducing negative physical phenomena, as well as providing adequate equipment for the protection of the crew.

Key words: noise, measurement, assessment, risks, crew.

Introduction

Artillery weapons, which are integrated on various combat platforms, produce extremely high noise levels when firing missiles. When adopting and introducing new assets into the military system, the satisfaction of "humane" characteristics is checked: the requirements of ergonomics, human engineering, and the suitability of the asset to the user, so that it can operate and work efficiently, successfully, and effectively (Jovanović et al., 2024).

By measuring and analyzing noise levels generated by artillery fire, information is obtained about the noise intensity. The quality of the measurement depends on several factors: the correct choice of the measurement location (measuring places), the use of adequate tesing and measuring equipment, and experience in processing the obtained data (Jovanović, 2010).

The literature that clearly defines all tolerance thresholds and permissible limits of exposure of the military equipment crew to risks when firing missiles, as well as the criteria for evaluating the risks, is not fully defined in the Republic of Serbia, or many countries worldwide. Only certain aspects of noise have been defined in the literature and can be used for the purpose of assessing the impact on system crews.

In the Republic of Serbia, the Rulebook on preventive measures for safe and healthy work under conditions of noise exposure ("Official Gazette of RS", No. 96/2011, 78/2015, and 93/2019) which defines general provisions in accordance with the requirements of European directives and standards (Directive 2003/10/EC of the European Parliament and the Council on the minimum health and safety requirements regarding the exposure of workers to risks arising from physical agents - noise) is used. In addition, the Regulation on noise indicators, limit values, methods for evaluating noise indicators, disturbance and harmful effects of noise in the environment ("Official Gazette of RS", No. 75/2010), prescribes limit values for industrial and traffic noise. The Law on Protection from Noise in the Environment ("Official Gazette of the RS, No. 96/2021") defines mandatory noise

measurements in the environment, as well as other legal issues of importance for the protection of the environment and human health.

The number of works by authors who have dealt with these problems is low (Ylikoski, 1994; Duvdevany et al., 2006; Biočanin, 2009; Mlynski et al., 2018; Živaljević, 2018, Blevins et al., 2021), so research in this field is certainly a challenge.

This paper aims to present a comparative analysis and evaluation of the acoustic parameters produced by cannons of different calibers on different platforms. The noise measurement data at the appropriate measuring points during firing are presented, and the risks to the crew are analyzed based on the mentioned regulations, standards, and laws.

The measurements were carried out in real field conditions on platforms with integrated 122 mm, 125 mm, 130 mm, and 152 mm cannons. In order to reduce the measurement error, repetitions were carried out at the same measurement point several times.

Methodology and noise measurement procedure

The measurement of the acoustic parameters of military combat systems is of great importance for analyzing the crew's exposure to noise, and it is classified as a priority measurement during all tests of assets under development.

The method for calculating the acoustic energy of the impulse sound above the barrel (muzzle blast) for calibers less than 20 mm or equivalent explosive mass is described in "ISO 17201-1 (First edition 2005, Acoustics, Noise from shooting ranges. Determination of muzzle blast by measurement). This document defines the following quantities:

p [Pa] - current sound pressure, represents the total current pressure at a point when a sound wave is present, minus the atmospheric pressure at that point;

p_0 - reference sound pressure (in air, usually 20 μPa);

Lp [dB] - sound pressure level calculated according to the formula

$$L_p = 10 \cdot \log_{10}\left(\frac{p^2}{{p_0}^2}\right); \qquad (1)$$

p_{peak} [Pa] - peak sound pressure, represents the maximum absolute value of the current sound pressure during a certain time interval;

L_{peak} [dB] - the peak sound pressure level is calculated according to the formula

$$L_{peak} = 10 \cdot log_{10}\left(\frac{{p_{peak}}^2}{{p_0}^2}\right); \qquad (2)$$

T [s] - the duration of the phenomenon, a time interval that is long enough to include all the significant sounds of the phenomenon;

E [Pa^2s] - exposure to sound, the time integral of the frequency-weighted square of the current sound pressure calculated by the formula

$$E = \int_T p^2(t)dt \quad (3)$$

and it represents the energy (E) of one pulse;

L_E (dB) - the sound exposure level is defined by a formula

$$L_E = 10 \cdot log_{10}\left(\frac{E}{E_0}\right), \quad (4)$$

where E_0 is equal to the square of the reference sound pressure of 20 μPa multiplied by a time interval of 1 s (400 $\mu Pa^2 \cdot 1$ s).

In the Republic of Serbia, the Rulebook on Preventive Measures for Safe and Healthy Work with Exposure to Noise ("Official Gazette of RS", No. 96/2011, 78/2015, and 93/2019) prescribes the following physical parameters that are used in assessing the risk of exposure to noise:

1. peak sound pressure value p_{peak} [Pa];
2. daily noise exposure level $L_{A,EX,8h}$ [dB] in relation to the reference value of 20μPa;
3. level of weekly exposure to noise $L_{A,EX,8h}$ [dB].

The same Rulebook defines the peak value of the sound pressure as the maximum value "C" of the frequency-weighted current sound pressure in the measurement interval and is used primarily in the assessment of impulse noise, while the other two parameters are used in the assessment of continuously variable or intermittent noise. The defined physical quantities are in accordance with the European directive that defines the minimum requirements for safe and healthy work when personnel are exposed to noise (Directive 2003/10/EC of the European Parliament and the Council on the minimum health and safety requirements regarding the exposure of workers to the risks arising from physical agents - noise). Moreover, these quantities coincide with the 2005 document "ISO 17201-1".

In any case, cannon fire is characterized by impulse noise, so the peak value of the sound pressure was considered - the peak noise level, that is, the maximum measured sound pressure value (peak) expressed in decibels [dB].

For the purposes of acoustic measurements, a measuring chain (Figure 1) consisting of a NetdB12 measuring system (manufactured by 01dB Metravib) in a chain with two 1/4" "free-field" microphones (type 46AE, manufactured by G.R.A.S) was formed.

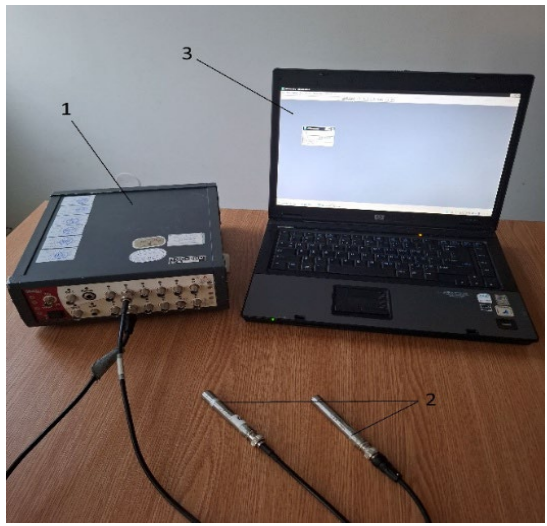

Figure 1 - Elements of the measuring chain: 1 - NetdB12, 2 – microphones, 3 – computer with appropriate software

In the closed dome of the tested vehicle with a 125 mm cannon, the microphone measuring point was at the position of the commander (c) and the gunner (g), at ear level, as well as outside (on the dome, above the gunner's place), which was directed towards the noise source. 125 mm ammunition, instantaneous high-explosive projectile (IHEP) was used for firing. The noise level curve resulting from the firing of the 125 mm cannon is given in Diagrams 1 and 2, where the noise level is presented on the y-axis [dB] depending on the duration of the event itself on the x-axis [s].

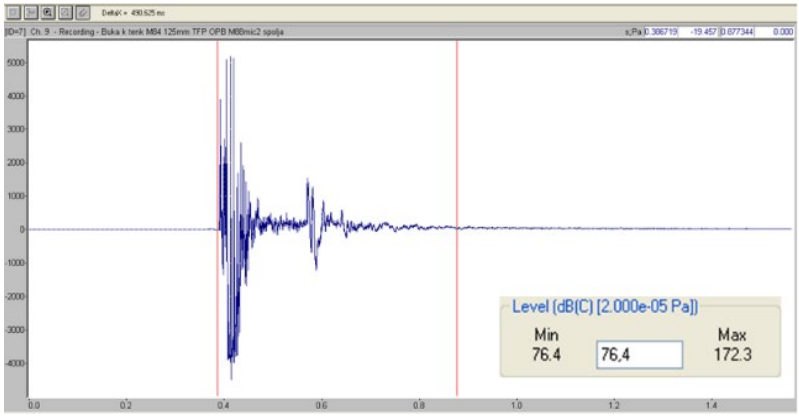

Diagram 1 - Noise curve produced by the 125 mm cannon on a turret

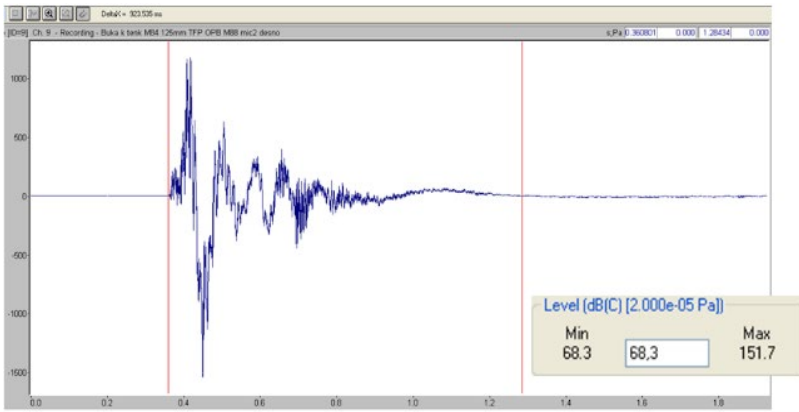

Diagram 2 - Noise curve produced by the 125 mm cannon at the commander's place

In the closed turret of the 122 mm howitzer gun, the measuring point of the microphone was at the position of the commander (c) and the gunner (g), at ear level. Two types of ammunition were used for firing, the 122 mm instantaneous high-explosive projectile (IHEP) and the 122 mm reduced powder charge projectile (RPCP).

The measuring points on the 130 mm and 152 mm cannons were also in a closed turret, but at the position of the gunner (g) and his assistant (a), at a height of 1.2 m, directed towards the muzzle and the direction of firing. Instantaneous high-explosive projectiles (IHEP) were used for both calibers. The presentation of the noise curve resulting form the firing of the 130 mm cannon is given in Diagram 3, where the noise level is presented on the y-axis [dB] depending on the duration of the event itself on the x-axis [s].

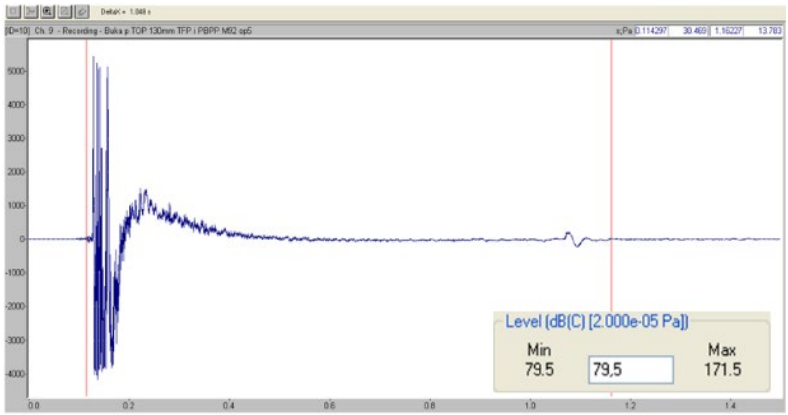

Diagram 3 - Presentation of the noise produced by the 130 mm cannon at the position of the gunner's assistant

Diagram 4 presents an overview of the noise signal (L_{peak}) of all cannons as a function of time (t), in order to compare the amplitude and duration of signals each signal at the marksman's position.

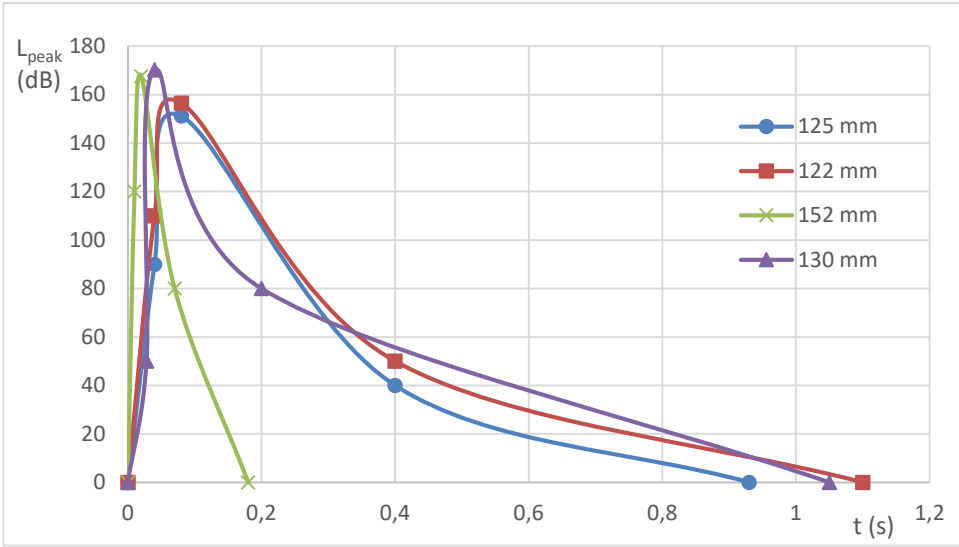

Diagram 4 - Overview of the noise signals produced by all cannons as a function of time at the marksman's position

The results of measuring the noise level on the equipment on which cannons of different calibers are integrated are shown in Table 1.

Table 1 - Noise measurement results

Firing number	Object of examination	Measuring point	Peak noise level **dB(peak)**	
			peak	medium
1.	Cannon 125 mm	marksman	151,2	
2.		commander	151,7	
3.		on the dome	172,3	170
4.			169	
5.			168,8	
1.	Howitzer 122 mm	m (IHEP)	156,5	marksman / commander 155,9 / 156,3
2.		c (IHEP)	157,1	

Firing number	Object of examination	Measuring point	Peak noise level **dB(peak)**	
			peak	medium
3.		m (RPCP)	156,4	
4.		c (RPCP)	156,4	
1.	Gun - howitzer 152 mm	m	167,6	marksman / assistant 166,9 / 168,3
2.		a	169,1	
3.		m	165,9	
4.		a	169,8	
1.	Cannon 130 mm	m	168,7	marksman / assistant 169,9 / 171,2
2.		a	171,5	
3.		m	170,2	
4.		a	170,1	

Criteria for noise assessment and analysis of measurement results

The criterion of exposure of a person to the effects of noise, according to the Rulebook on preventive measures for safe and healthy work when exposed to noise (Official Gazette of RS, No. 96/2011, 78/2015, 93/2019), defines the following classes:

- class A (up to 140 dB) - the permitted daily number of exposures is unlimited,
- class B (from 140 dB to 162 dB) - the permitted number of exposures is:
  - 0, no protection,
  - up to 2000 firings per day, with earplugs or ear defenders,
- class C (from 162 dB to 167 dB) - the permitted number of exposures is:
  - 0, no protection,
  - up to 100 firings per day, with earplugs or ear defenders,
- class D (from 167 dB to 173 dB) - the permitted number of exposures is:

- 0, no protection,
- up to 5 burns per day, with earplugs or ear defenders,
- from 5 to 100 firings per day, earwith plugs and ear defenders.

By analyzing the results of the measured values of the peak noise level for the mentioned devices, which are shown in Table 1, it is stated that the devices fall into:

- class B, for gunners and commanders at the 125 mm cannon, which means that the use of earplugs or ear defenders is mandatory for exposure up to 2000 shots per day;
- class C, for the gunner's position of the 152 mm howitzer gun, which means that the use of earplugs or ear defenders is mandatory for exposure up to 100 shots per day;
- class D, on the turret above the gunner for the 125 mm cannon, for the position of assistant gunner of the 152 mm howitzer, and for the position of the gunner and gunner's assistant for the 130 mm cannon, which means that for persons who are in those zones during firing, it is mandatory to use earplugs or ear defenders for exposure to up to 5 shots per day, i.e. earplugs and ear defenders for exposure from 5 to 100 shots per day.

Graphical representation of the peak noise levels for the examined objects and the relation to the limit value is given in Diagram 5.

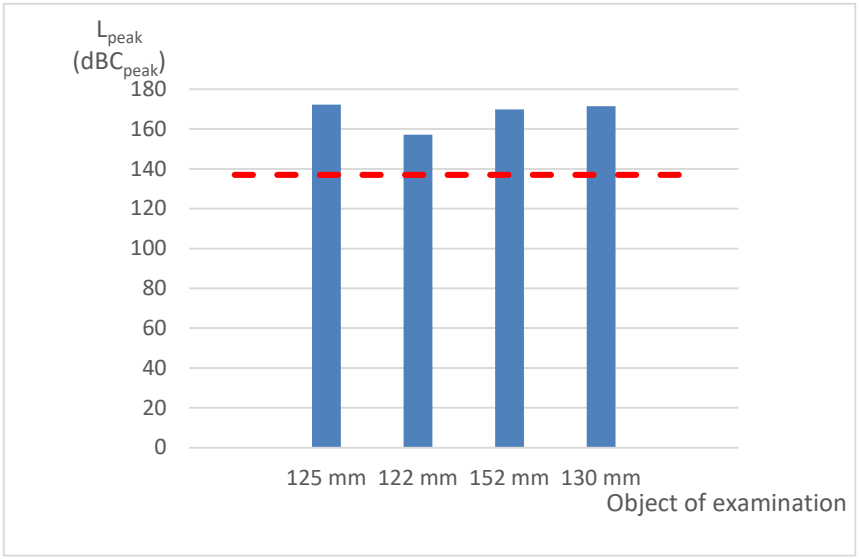

Diagram 5 - Summary of the peak noise level for all cannons in relation to the limit value

According to the Rulebook on preventive measures for safe and healthy work when exposed to noise ("Official Gazette of the RS No. 96/2011, 78/2015, and 93/2019"), the limit value of exposure to impulse noise is 137 dB(peak), which means that all noise measurement results from Table 1 exceed the limit value.

Conclusion

Assessments of the crew's exposure to noise due to cannon fire were carried out according to the criteria of the Rulebook of the Republic of Serbia on preventive measures for safe and healthy work when exposed to noise (which relies on the requirements of Directive 2003/10/EC of the European Parliament and the Council on minimum health and safety requirements regarding the exposure of workers to the risks arising from physical agents - noise).

Based on the noise measurement results, it can be concluded that all measured levels exceed the prescribed limit value. This requires additional crew protection measures. This means that the use of protective ear defenders with a high noise reduction rating above 30 dB is mandatory, which would reduce the noise level below the prescribed warning value of 137 dB (peak) according to the Rulebook on preventive measures for safe and healthy work when exposed to noise ("Official Gazette of the RS, No. 96/2011, 78/2015, and 93/2019").

By using adequate measuring equipment to examine the acoustic effects on the crew and by comparing the results with current standards, European directives and existing research, concrete indicators in the domain of safety and protection of human health from the effects of physical phenomena are obtained, which was the goal of this work.

The described measurement methodology can also be applied to other types of military equipment, the ultimate goal of which is to meet European standards in terms of occupational safety, health protection, and comfort. Considering that this work does not include all factors that can influence the measurement results, there is room for improvement, especially regarding the different conditions under which the tests are conducted. In future research, it is recommended to extend the analysis to the effects of different types of ammunition and variations in loading. Such measurements enable a more precise analysis, which would lead to the creation of a document which could lead to the creation of the criteria for assessing acoustic effects on the crew, for the specific equipment and calibers used in the army.

References

Biočanin R., Amidžić B., Bektašević S., 2009. Noise and vibration: Physical polluters and disorders of work and human environment. Časopis IMK-14 „Istrazivanje i razvoj“, ISSN 0354-6829.

Blevins M., Lyons G., Hart C., White M. 2021., Optical and Acoustical Measurement of Ballistic Noise Signatures. Available at: https://dx.doi.org/10.21079/11681/39501.

Duvdevany A., Furst M., 2006., Immediate and long-term effect of rifle blast noise on transient-evoked otoacoustic emissions. Available at: https://doi/10.1515/JBCPP.2006.17.3.173.

Jovanović, B.S., Stojadinović, R.D., Jovanović, M., Djurić, S.A., 2024. Assessment of exposure to physical hazards in the working environment during testing of prototypes. Zbornik 11. Internacionalne konferencije odbrambenih tehnologija - OTEH 2024, pp.186-190. Available at: https://doi.org/10.5937/OTEH24034J.

Jovanović, M.M., 2010. Analiza niskofrekventnog spektra vibracija na elementima strukture helikoptera „Gazela“, *Vojnotehnički glasnik/Military Technical Courier*, 10(4), pp.17-36. Available at: https://doi.org/10.5937/vojtehg1004017J.

Mlynski R., Kozlowski E., Usowski J., Jurkiewicz D., 2018., Evaluation of Exposure to Impulse Noise at Personnel OccupiedAreas During Military Field Exercises. Available at: https://doi.org/10.24425/122367.

Ylikoski M., 1994., Prolonged exposure to gunfire noise among professional soldiers. Available at: https://doi.org/10.5271/sjweh.1416

Živaljević Z., Živić Lj, Bukumirić Z., Nikolić I., Vorkapić B., Baletić N., 2018. Uticaj bojevog gađanja iz automatske puške na čulo sluha kod profesionalnih vojnih lica. Vojnosanitetski pregled, 2018; 75(7): 710–715. Available at: https://doi.org/10.2298/VSP160528366Z

Directive 2003/10/EC of the European parliament and the council – Minimum health and safety requirements regarding the exposure of workers to the risks arising from physical agents (noise).

ISO 17201-1 First edition 2005., Acoustics, Noise from shooting ranges. Determination of muzzle blast by measurement.

Uredba o indikatorima buke, graničnim vrednostima, metodama za ocenjivanje indikatora buke, uznemiravanja i štetnih efekata buke u životnoj sredini ("Sl. glasnik RS", br. 75/2010).

Zakon o zaštiti od buke u životnoj sredini („Sl. Glasnik RS broj 96/2021“).

Eksperimentalna procena akustičnih uticaja topovske paljbe na posadu

Dragan R. Stojadinović[a], **autor za prepisku**, *Snezana B*. Jovanović[a], *Aleksandar* S. Đurić[b], *Aleksandar B*. Bukvić[b], *Sreten* R. Perić[b]
[a] Tehnički opitni centar, Sektor za mototehnička i sredstva rečnih jedinica, Odeljenje za vozila i nadgradnje, Beograd, Republika Srbija
[b] Univerzitet Odbrane u Beogradu, Vojna Akademija, Odsek za vojnomašinsko inženjerstvo, Beograd, Republika Srbija

OBLAST: mašinsko inženjerstvo
KATEGORIJA (TIP) ČLANKA: pregledni rad

Sažetak:

Uvod/cilj: Buka koja nastaje kao posledica opaljenja iz artiljerijskog naoružanja može imati izuzetno štetno dejstvo na korisnike - posadu. Predmet ovog rada je merenje i analiza izmerenih nivoa buke na pojedinom naoružanju koje se koristi u Vojsci Srbije.

Metode: Analiza i poređenje rezultata su izvršeni prilikom dejstva iz sredstava sa različitim kalibrima naoružanja. Takodje, razmatran je i aspekt uticaja i rizika na posadu koja je izložena navedenim fizičkim pojavama.

Rezultati: Rezultati ispitivanja akustičnih parametara u odnosu na dostupne kriterijume pokazuju da je posada na pojedinim vozilima izložena većem nivou buke od dozvoljenog.

Zaključak: Svi izmereni nivoi buke prelaze propisanu graničnu vrednost. Na osnovu dobijenih rezultata može se dalje raditi na smanjenju negativnih fizičkih pojava kao i na obezbeđenju adekvatne opreme za zaštitu posade.

Ključne reči: buka, merenja, procena, rizici, posada.

Paper received on: 16 October 2025.
Manuscript corrections submitted on: 19 November 2025.
Paper accepted for publishing on: 25 November 2025.

© 2026 The Authors. Published by Vojnotehnički glasnik / Military Technical Courier (www.vtg.mod.gov.rs).This article is an open access article distributed under the terms and conditions of the Creative Commons Attribution license (http://creativecommons.org/licenses/by/4.0/rs/)

CALL FOR PAPERS AND ARTICLE FORMATTING INSTRUCTIONS

The instructions to authors about the article preparation for publication in *Military Technical Courier* are based on the Regulations on categorization and ranking of scientific journals of the Ministry of Education, Science and Technological Development of the Republic of Serbia (Official Gazette of the Republic of Serbia, No 159/20). This Regulations aims at improving the quality of national journals and raising the level of their compliance with the international system of scientific information exchange.

Military Technical Courier / Vojnotehnički glasnik (www.vtg.mod.gov.rs/index-e.html, ISSN 0042-8469 – print issue, e-ISSN 2217-4753 – online, UDC 623+355/359, DOI: 10.5937/VojnotehnickiGlasnik; https://doi.org/10.5937/VojnotehnickiGlasnik), is a peer-reviewed scientific journal.

The owners of the journal are the Ministry of Defence of the Republic of Serbia and the Serbian Armed Forces. The publisher and financier of *Military Technical Courier* is the University of Defence in Belgrade (Military Academy).

The program of the journal is based on the annual classification of journals performed by a relevant Ministry as well as on its indexing in international indexing databases.

The journal covers scientific and professional fields within the educational-scientific field of **Natural-Mathematical Sciences**, as well as within the educational-scientific field of **Technical-Technological Sciences**, and especially the field of **defense sciences and technologies**. It publishes theoretical and practical achievements leading to professional development of all members of Serbian, regional and international academic communities as well as members of the military and ministries of defence in particular. It publishes papers with balanced coverage of analytical, experimental, and applied research as well as numerical simulations from various disciplines. The material published is of high quality and relevance, written in a manner that makes it accessible to a wider readership. The journal welcomes papers reporting original theoretical and/or practice-oriented research as well as extended versions of already published conference papers. Manuscripts for publication are selected through a double-blind peer-review process to validate their originality, relevance, and readability. This being so, the objective is not only to keep the quality of published papers high but also to provide a timely, thorough, and balanced review process.

The editorial policy of *Military Technical Courier* is based on the COPE Core Practices, common COPE, DOAJ, OASPA and WAME Principles of Transparency and Best Practice in Scholarly Publishing as well as on the best accepted practices in scientific publishing. Military Technical Courier has been a COPE (Committee on Publication Ethics) member since 2nd May 2018 and a member of OASPA (Open Access Scholarly Publishers Association) since 27th November 2015.

The Ministry of Science, Technological Development and Innovation of the Republic of Serbia classified *Military Technical Courier* for the year 2025, on December, 2025:

- **on the list of periodicals for computer sciences,**
  category: reputed national journal **(M51)**,
- **on the list of periodicals for electronics, telecommunications and IT,**
  category: reputed national journal **(M51)**,
- **on the list of periodicals for mechanical engineering,**
  category: reputed national journal **(M51)**,
- **on the list of periodicals for materials and chemical technology,**
  category: national journal of international importance **(M24)**.

The approved lists of national periodicals for the year 2025 can be viewed on the website of *Military Technical Courier*, page *Journal categorization*.

More detailed information can be found on the website of the Ministry of Education, Science and Technological Development of the Republic of Serbia.

The information on the categorization can be also found on the website of KOBSON (Consortium of Libraries of Serbia for Unified Acquisition).

The periodical is categorized in compliance with the Regulations on categorization and ranking of scientific journals of the Ministry of Education, Science and Technological Development of the Republic of Serbia (Official Gazette of the Republic of Serbia, No 159/20). More detailed information can be found on the website of the Ministry of Education, Science and Technological Development.

The journal is in the Serbian Citation Index – SCIndex (data base of national scientific journals), in the Scientific Information System Redalyc, and in the Russian Index of Science Citation/Российский индекс научного цитирования (RINC/РИНЦ) and is constantly monitored depending on the impact within the bases themselves. More detailed information can be viewed on the website of *Military Technical Courier*, page *Journal indexing*.

Military Technical Courier, in terms of its content, offers the possibility of open access (DIAMOND OPEN ACCESS) and applies the Creative Commons Attribution (CC BY) licence on copyright. The copyright details can be found on the *Copyright notice and Self-archiving policy* page of the journal's website.

Manuscripts are submitted online, through the electronic editing system ASSISTANT, developed by the Center for Evaluation in Education and Science – CEON.

The access and the registration are through *Military Technical Courier* site http://www.vtg.mod.gov.rs/index-e.html, on the page *ASSISTANT* or the page *SCINDEKS* or directly through the link (aseestant.ceon.rs/index.php/vtg).

The detailed instructions about the registration for the service are on the website http://www.vtg.mod.gov.rs/index-e.html, on the page *Instructions for ASSISTANT*.

All authors submitting a manuscript for publishing in *Military Technical Courier* should register for an ORCID ID following the instructions on the web page *Registration for an ORCID identifier*.

Military Technical Courier publishes articles in English, using Arial and a font size of 11pt with Single Spacing.

The procedures of article preparation, writing and editing should be in accordance with the *Publication ethics statement* (http://www.vtg.mod.gov.rs/publication-ethics-statement.html).

The article should contain an abstract with keywords, introduction (motivation for the work), body (adequate overview of the representative work in the field, a clear statement of the novelty in the presented research, suitable theoretical background, one or more examples to demonstrate and discuss the presented ideas), conclusion, and references (without heading and subheading enumeration). The article length should not normally exceed 16 pages of the A4 paper format with single spacing, up to a maximum of 24 pages with references and supplementary material included.

The article should be formatted following the instructions in the Article Form which can be downloaded from website page *Article form*.

Title

The title should be informative. It is in both Journal's and author's best interest to use terms suitable for indexing and word search. If there are no such terms in the title, the author is strongly advised to add a subtitle.

Letterhead title

The letterhead title is given at a top of each page for easier identification of article copies in an electronic form in particular. It contains the author's surname and first name initial (for multiple authors add "et al"), article title, journal title and collation (year, volume, issue, first and last page). The journal and article titles can be given in a shortened form.

Author's name

Full name(s) of author(s) should be used. It is advisable to give the middle initial. Names are given in their original form (with diacritic signs if in Serbian).

Author's affiliation

The full official name and seat of the author's affiliation is given, possibly with the name of the institution where the research was carried out. For organizations with complex structures, give the whole hierarchy (for example, University of Defence in Belgrade, Military Academy, Department for Military Electronic Systems). At least one organization in the hierarchy must be a legal entity. When some of multiple authors have the same affiliation, it must be clearly stated, by special signs or in other way, which department exactly they are affiliated with. The affiliation follows the author's name. The function and title are not given.

Contact details

The postal addresses or the e-mail addresses of the authors are given in the first page.

Type of articles

Classification of articles is a duty of the editorial staff and is of special importance. Referees and the members of the editorial staff, or section editors, can propose a category, but the editor-in-chief has the sole responsibility for their classification.

Military Technical Courier publishes scientific articles.

Scientific articles:

– Original scientific papers (giving the previously unpublished results of the author's own research based on scientific methods);

– Review papers (giving an original, detailed and critical view of a research problem or an area to which the author has made a contribution demonstrated by self-citation);

– Short communications or Preliminary communications (original scientific full papers but shorter or of a preliminary character);

– Scientific commentaries or discussions (discussions on a particular scientific topic, based exclusively on scientific argumentation) and opinion pieces.

Exceptionally, in particular areas, a scientific paper in the Journal can be in a form of a monograph or a critical edition of scientific data (historical, archival, lexicographic, bibliographic, data survey, etc.) which were unknown or hardly accessible for scientific research.

Papers classified as scientific must have at least two positive reviews.

If the journal contains non-scientific contributions as well, the section with scientific papers should be clearly denoted in the first part of the Journal.

Short communications are usually 4-7 pages long, research articles and case studies 10-14 pages, while reviews can be longer. Page number limits are not strict and, with

appropriate reasoning, submitted manuscripts can also be longer or shorter. If extended versions of previously published conference papers are submitted, Editors will check if sufficient new material has been added to meet the journal standards and to qualify such manuscripts for the review process. The added material must not have been previously published. New results are desired but not necessarily required; however, submissions should contain expansions of key ideas, examples, elaborations, etc. of conference papers.

Language

The language of the article should be English. The grammar and style of the article should be of good quality. The systematized text should be without abbreviations (except standard ones). All measurements must be in SI units. The sequence of formulae is denoted in Arabic numerals in parentheses on the right-hand side.

Abstract and summary

An abstract is a concise informative presentation of the article content for fast and accurate evaluation of its relevance. It contains the terms often used for indexing and article search. A 100- to 250-word abstract has the following parts: introduction/purpose of the research, methods, results and conclusion.

Keywords

Keywords are terms or phrases showing adequately the article content for indexing and search purposes. They should be allocated having in mind widely accepted international sources (index, dictionary or thesaurus), such as the Web of Science keyword list for science in general. The higher their usage frequency is, the better. Up to 10 keywords immediately follow the abstract and the summary, in respective languages. For this purpose, the ASSISTANT system uses a special tool KWASS for the automatic extraction of key words from disciplinary thesauruses/dictionaries by choice and the routine for their selection, i.e. acceptance or rejection by author and/or editor.

Article acceptance date

The date of the reception of the article, the dates of submitted corrections in the manuscript (optional) and the date when the Editorial Board accepted the article for publication are all given in a chronological order at the end of the article.

Acknowledgements

The name and the number of the project or programme within which the article was realised is given in a separate note at the bottom of the first page together with the name of the institution which financially supported the project or programme.

Article preliminary version

If an article preliminary version has appeared previously at a meeting in a form of an oral presentation (under the same or similar title), this should be stated in a separate note at the bottom of the first page. An article published previously cannot be published in *Military Technical Courier* even under a similar title or in a changed form.

Tables and illustrations

All the captions should be in the original language as well as in English, together with the texts in illustrations if possible. Tables are typed in the same style as the text and are denoted by Arabic numerals at the top. Photographs and drawings, placed

appropriately in the text, should be clear, precise and suitable for reproduction. Drawings should be created in Word or Corel.

For figures and graphs, proper data plot is recommended i.e. using a data analysis program such as Excel, Matlab, Origin, SigmaPlot, etc. It is not recommended to use a screen capture of a data acquisition program as a figure or a graph.

Citation in the text

Citation in the text must be uniform. *Military Technical Courier* applies the Harvard Referencing System given in the Harvard Style Manual. When citing sources within your paper, i.e. for in-text references of the works listed at the end of the paper, place the year of publication of the work in parentheses and optionally the number of the page(s) after the author's name, e.g. (Petrovic, 2012, pp.10-12). A detailed guide on citing, with examples, can be found on *Military Technical Courier* website on the page *Instructions for Harvard Style Manual*. In-text citations should follow its guidelines. For checking in-text citations, the ASSISTANT system uses a special tool CiteMatcher to find out quotes left out within papers and in reference lists.

Footnotes

Footnotes are given at the bottom of the page with the text they refer to. They can contain less relevant details, additional explanations or used sources (e.g. scientific material, manuals). They cannot replace the cited literature.

Reference list (Literature)

The cited literature encompasses bibliographic sources such as articles and monographs and is given in a separate section in a form of a reference list. References are not translated to the language of the article.

In compiling the reference list and bibliography, *Military Technical Courier* applies the Harvard System – Harvard Style Manual. All bibliography items should be listed alphabetically by author's name, without numeration. A detailed guide for listing references, with examples, can be found on *Military Technical Courier* website on the page *Instructions for Harvard Style Manual*. Reference lists at the end of papers should follow its guidelines. In journal evaluation systems, non-standard, insufficient or inconsequent citation is considered to be a sufficient cause for denying the scientific status to a journal.

Authorship Statement

The Authorship statement, submitted together with the paper, states authors' individual contributions to the creation of the paper. In this statement, the authors also confirm that they followed the guidelines given in *Call for papers* and *Publication ethics and malpractice statement of the journal*.

All articles are peer reviewed.

The list of referees of *Military Technical Courier* can be viewed at website page *List of referees*. The article review process is described on the *Peer Review Process* page of the website.

Editorial Team

Address of the Editorial Office:
Vojnotehnički glasnik / Military Technical Courier
Veljka Lukića Kurjaka 33
11042 Belgrade, Republic of Serbia
e-mail: vojnotehnicki.glasnik@mod.gov.rs,
tel.: +381 11 3603 260

POZIV I UPUTSTVO AUTORIMA O NAČINU PRIPREME ČLANKA

Uputstvo autorima o načinu pripreme članka za objavljivanje u *Vojnotehničkom glasniku* urađeno je na osnovu Pravilnika o kategorizaciji i rangiranju naučnih časopisa Ministarstva prosvete, nauke i tehnološkog razvoja Republike Srbije („Službeni glasnik RS“, broj 159/20). Primena ovog Pravilnika prvenstveno služi unapređenju kvaliteta domaćih časopisa i njihovog potpunijeg uključivanja u međunarodni sistem razmene naučnih informacija.

Vojnotehnički glasnik / Military Technical Courier (www.vtg.mod.gov.rs, ISSN 0042-8469 – štampano izdanje, e-ISSN 2217-4753 – online, UDC 623+355/359, DOI: 10.5937/VojnotehnickiGlasnik; https://doi.org/10.5937/VojnotehnickiGlasnik), jeste recenzirani naučni časopis.

Vlasnici časopisa su Ministarstvo odbrane Republike Srbije i Vojska Srbije. Izdavač i finansijer časopisa je Univerzitet odbrane u Beogradu (Vojna akademija).

Programska orijentacija časopisa zasniva se na godišnjoj kategorizaciji časopisa, koju vrši nadležno državno ministarstvo u određenim oblastima, kao i na njegovom indeksiranju u međunarodnim indeksnim bazama.

Časopis obuhvata naučne, odnosno stručne oblasti u okviru obrazovno-naučnog polja **prirodno-matematičkih nauka**, kao i u okviru obrazovno-naučnog polja **tehničko-tehnoloških nauka**, a naročito oblasti **odbrambenih nauka i tehnologija**. Objavljuje teorijska i praktična dostignuća koja doprinose usavršavanju svih pripadnika srpske, regionalne i međunarodne akademske zajednice, a posebno pripadnika vojski i ministarstava odbrane. Publikuje radove sa uravnoteženim izveštavanjem o analitičkim, eksperimentalnim i primenjenim istraživanjima, kao i numeričkim simulacijama, obuhvatajući različite discipline. Objavljeni materijali su visokog kvaliteta i relevantnosti, napisani na način koji ih čini dostupnim širokoj čitalačkoj publici. Svi radovi koji izveštavaju o originalnim teorijskim i/ili praktično orijentisanim istraživanjima ili proširenim verzijama već objavljenih radova sa konferencija su dobrodošli. Radovi za objavljivanje odabiru se dvostruko slepim postupkom recenzije kako bi se osigurala originalnost, relevantnost i čitljivost. Pritom cilj nije samo da se kvalitet objavljenih radova održi visokim već i da se obezbedi pravovremeni, temeljni i uravnoteženi postupak recenzije.

Uređivačka politika *Vojnotehničkog glasnika zasniva* se na preporukama Odbora za etičnost u izdavaštvu (COPE Core Practices) i zajedničkim principima transparentnosti i najbolje prakse u izdavaštvu COPE, DOAJ, OASPA i WAME, kao i na najboljim prihvaćenim praksama u naučnom izdavaštvu. Vojnotehnički glasnik je član COPE (Committee on Publication Ethics) od 2. maja 2018. godine i član OASPA (Open Access Scholarly Publishers Association) od od 27. novembra 2015. godine.

Ministarstvo nauke, tehnološkog razvoja i inovacija Republike Srbije utvrdilo je decembra 2025. godine kategorizaciju Vojnotehničkog glasnika, za 2025. godinu:

- **na listi časopisa za računarske nauke:**
  kategorija vrhunski časopis nacionalnog značaja **(M51),**
- **na listi časopisa za elektroniku, telekomunikacije i informacione tehnologije:**
  kategorija vrhunski časopis nacionalnog značaja (**M51),**
- **na listi časopisa za mašinstvo:**
  kategorija vrhunski časopis nacionalnog značaja **(M51),**
- **na listi časopisa za materijale i hemijske tehnologije:**
  kategorija nacionalni časopis međunarodnog značaja (**M24).**

Usvojene liste domaćih časopisa za 2025. godinu mogu se videti na sajtu *Vojnotehničkog glasnika*, stranica *Kategorizacija časopisa*.

Detaljnije informacije mogu se pronaći i na sajtu Ministarstva prosvete, nauke i tehnološkog razvoja Republike Srbije.

Podaci o kategorizaciji mogu se pratiti i na sajtu KOBSON-a (Konzorcijum biblioteka Srbije za objedinjenu nabavku).

Kategorizacija časopisa izvršena je prema Pravilniku o kategorizaciji i rangiranju naučnih časopisa Ministarstva prosvete, nauke i tehnološkog razvoja Republike Srbije („Službeni glasnik RS", broj 159/20).

Časopis se prati u kontekstu Srpskog citatnog indeksa – SCindeks (baza podataka domaćih naučnih časopisa), Naučno-informacionog sistema Redalyc i Ruskog indeksa naučnog citiranja (RINC). Podvrgnut je stalnom vrednovanju (monitoringu) u zavisnosti od uticajnosti (impakta) u samim bazama. Detalji o indeksiranju mogu se videti na sajtu *Vojnotehničkog glasnika*, stranica *Indeksiranje časopisa*.

Vojnotehnički glasnik, u pogledu svog sadržaja, pruža mogućnost otvorenog pristupa (DIAMOND OPEN ACCESS) i primenjuje Creative Commons (CC BY) odredbe o autorskim pravima. Detalji o autorskim pravima mogu se videti na sajtu časopisa, stranica *Autorska prava i politika samoarhiviranja*.

Radovi se predaju putem onlajn sistema za elektronsko uređivanje ASISTENT, koji je razvio Centar za evaluaciju u obrazovanju i nauci (CEON).

Приступ и регистрација за сервис врше се на сајту www.vtg.mod.gov.rs, преко странице *АСИСТЕНТ* или *СЦИНДЕКС*, односно директно на линку aseestant.ceon.rs/index.php/vtg.

Detaljno uputstvo o registraciji i prijavi za servis nalazi se na sajtu www.vtg.mod.gov.rs, stranica *Uputstvo za ASISTENT*.

Potrebno je da se svi autori koji podnose rukopis za objavljivanje u *Vojnotehničkom glasniku* registruju u registar ORCID (Open Researcher and Contributor ID), prema uputstvu na stranici sajta *Registracija za dobijanje ORCID identifikacione šifre*.

Vojnotehnički glasnik objavljuje članke na engleskom jeziku (arial, veličina slova 11 pt, prored Single).

Postupak pripreme, pisanja i uređivanja članka treba da bude u saglasnosti sa *Izjavom o etičkom postupanju* (http://www.vtg.mod.gov.rs/izjava-o-etickom-postupanju.html).

Članak treba da sadrži sažetak sa ključnim rečima, uvod (motivaciju za rad), razradu (adekvatan pregled reprezentativnosti rada u njegovoj oblasti, jasnu izjavu o novini u predstavljenom istraživanju, odgovarajuću teorijsku pozadinu, jedan ili više primera za demonstriranje i diskusiju o predstavljenim idejama), zaključak i literaturu (bez numeracije naslova i podnaslova). Obim članka treba da bude do jednog autorskog tabaka (16 stranica formata A4 sa proredom Single), a najviše 24 stranice.

Članak treba da bude napisan na obrascu za pisanje članka, koji se u elektronskoj formi može preuzeti sa sajta na stranici *Obrazac za pisanje članka*.

Naslov

Naslov treba da odražava temu članka. U interesu je časopisa i autora da se koriste reči prikladne za indeksiranje i pretraživanje. Ako takvih reči nema u naslovu, poželjno je da se pridoda i podnaslov.

Tekući naslov

Tekući naslov se ispisuje sa strane svake stranice članka radi lakše identifikacije, posebno kopija članaka u elektronskom obliku. Sadrži prezime i inicijal imena autora (ako autora ima više, preostali se označavaju sa „et al." ili „i dr."), naslove rada i časopisa i

kolaciju (godina, volumen, sveska, početna i završna stranica). Naslovi časopisa i članka mogu se dati u skraćenom obliku.

Ime autora

Navodi se puno ime i prezime (svih) autora. Veoma je poželjno da se navedu i srednja slova autora. Imena i prezimena domaćih autora uvek se ispisuju u originalnom obliku (sa srpskim dijakritičkim znakovima), nezavisno od jezika na kojem je napisan rad.

Naziv ustanove autora (afilijacija)

Navodi se pun (zvanični) naziv i sedište ustanove u kojoj je autor zaposlen, a eventualno i naziv ustanove u kojoj je autor obavio istraživanje. U složenim organizacijama navodi se ukupna hijerarhija (npr. Univerzitet odbrane u Beogradu, Vojna akademija, Katedra prirodno-matematičkih nauka). Bar jedna organizacija u hijerarhiji mora biti pravno lice. Ako autora ima više, a neki potiču iz iste ustanove, mora se, posebnim oznakama ili na drugi način, naznačiti iz koje od navedenih ustanova potiče svaki od navedenih autora. Afilijacija se ispisuje neposredno nakon imena autora. Funkcija i zvanje autora se ne navode.

Kontakt podaci

Adresa ili e-adresa svih autora daje se pored imena i prezimena autora.

Kategorija (tip) članka

Kategorizacija članaka obaveza je uredništva i od posebne je važnosti. Kategoriju članka mogu predlagati recenzenti i članovi uredništva, odnosno urednici rubrika, ali odgovornost za kategorizaciju snosi isključivo glavni urednik.

Vojnotehnički glasnik objavljuje naučne članke.

Naučni članak je:

– originalan naučni rad (rad u kojem se iznose prethodno neobjavljeni rezultati sopstvenih istraživanja naučnim metodom);

– pregledni rad (rad koji sadrži originalan, detaljan i kritički prikaz istraživačkog problema ili područja u kojem je autor ostvario određeni doprinos, vidljiv na osnovu autocitata);

– kratko ili prethodno saopštenje (originalni naučni rad punog formata, ali manjeg obima ili preliminarnog karaktera);

– naučna kritika, odnosno polemika (rasprava na određenu naučnu temu, zasnovana isključivo na naučnoj argumentaciji) i osvrti.

Izuzetno, u nekim oblastima, naučni rad u časopisu može imati oblik monografske studije, kao i kritičkog izdanja naučne građe (istorijsko-arhivske, leksikografske, bibliografske, pregleda podataka i sl.), dotad nepoznate ili nedovoljno pristupačne za naučna istraživanja.

Radovi klasifikovani kao naučni moraju imati bar dve pozitivne recenzije.

Ako se u časopisu objavljuju i prilozi vannaučnog karaktera, naučni članci treba da budu grupisani i jasno izdvojeni u prvom delu sveske.

Poželjno je da obim kratkih saopštenja bude 4 do 7 stranica, naučnih članaka i studija slučaja 10 do 14 stranica, dok pregledni radovi mogu biti i duži. Broj stranica nije strogo ograničen i, uz odgovarajuće obrazloženje, prijavljeni članci takođe mogu biti duži ili kraći.

Ako su radovi koji su prethodno objavljeni na konferenciji prošireni, urednici će proveriti da li je dodato dovoljno novog materijala koji ispunjava standarde časopisa i kvalifikuje podnesak za postupak recenzije. Dodati materijal ne sme biti prethodno objavljen. Novi rezultati nisu nužno potrebni, ali su poželjni. Međutim, podnesak treba da sadrži proširene

ključne ideje, primere, razrade, itd., koji su prethodno bili sadržani u podnesku sa konferencije.

Jezik rada

Jezik rada treba da bude engleski.

Tekst mora biti jezički i stilski doteran, sistematizovan, bez skraćenica (osim standardnih). Sve fizičke veličine moraju biti izražene u Međunarodnom sistemu mernih jedinica – SI. Redosled obrazaca (formula) označava se rednim brojevima, sa desne strane u okruglim zagradama.

Sažetak

Sažetak jeste kratak informativan prikaz sadržaja članka koji čitaocu omogućava da brzo i tačno oceni njegovu relevantnost. U interesu je uredništava i autora da sažetak sadrži termine koji se često koriste za indeksiranje i pretragu članaka. Sastavni delovi sažetka su uvod/cilj istraživanja, metodi, rezultati i zaključak. Sažetak treba da ima od 100 do 250 reči i treba da se nalazi između zaglavlja (naslov, imena autora i dr.) i ključnih reči, nakon kojih sledi tekst članka.

Ključne reči

Ključne reči su termini ili fraze koje adekvatno predstavljaju sadržaj članka za potrebe indeksiranja i pretraživanja. Treba ih dodeljivati oslanjajući se na neki međunarodni izvor (popis, rečnik ili tezaurus) koji je najšire prihvaćen ili unutar date naučne oblasti. Za npr. nauku uopšte, to je lista ključnih reči Web of Science. Broj ključnih reči ne može biti veći od 10, a u interesu je uredništva i autora da učestalost njihove upotrebe bude što veća. U članku se pišu neposredno nakon sažetka.

Sistem ASISTENT u tu svrhu koristi specijalnu alatku KWASS: automatsko ekstrahovanje ključnih reči iz disciplinarnih tezaurusa/rečnika po izboru i rutine za njihov odabir, tj. prihvatanje odnosno odbacivanje od strane autora i/ili urednika.

Datum prihvatanja članka

Datum kada je uredništvo primilo članak, datum kada je uredništvo konačno prihvatilo članak za objavljivanje, kao i datumi kada su u međuvremenu dostavljene eventualne ispravke rukopisa navode se hronološkim redosledom, na stalnom mestu, po pravilu na kraju članka.

Zahvalnica

Naziv i broj projekta, odnosno naziv programa u okviru kojeg je članak nastao, kao i naziv institucije koja je finansirala projekat ili program, navodi se u posebnoj napomeni na stalnom mestu, po pravilu pri dnu prve strane članka.

Prethodne verzije rada

Ako je članak u prethodnoj verziji bio izložen na skupu u vidu usmenog saopštenja (pod istim ili sličnim naslovom), podatak o tome treba da bude naveden u posebnoj napomeni, po pravilu pri dnu prve strane članka. Rad koji je već objavljen u nekom časopisu ne može se objaviti u *Vojnotehničkom glasniku* (preštampati), ni pod sličnim naslovom i izmenjenom obliku.

Tabelarni i grafički prikazi

Poželjno je da naslovi svih prikaza, a po mogućstvu i tekstualni sadržaj, budu dati dvojezično, na jeziku rada i na engleskom jeziku.

Tabele se pišu na isti način kao i tekst, a označavaju se rednim brojevima sa gornje strane. Fotografije i crteži treba da budu jasni, pregledni i pogodni za reprodukciju. Crteže treba raditi u programu word ili corel. Fotografije i crteže treba postaviti na željeno mesto u tekstu.

Za slike i grafikone ne sme se koristiti snimak sa ekrana računara programa za prikupljanje podataka. U samom tekstu članka preporučuje se upotreba slika i grafikona neposredno iz programa za analizu podataka (kao što su Excel, Matlab, Origin, SigmaPlot i drugi).

Navođenje (citiranje) u tekstu

Način pozivanja na izvore u okviru članka mora biti jednoobrazan.

Vojnotehnički glasnik za referenciranje (citiranje i navođenje literature) primenjuje Harvardski sistem referenci, odnosno Harvardski priručnik za stil (Harvard Referencing System, Harvard Style Manual). U samom tekstu, u običnim zagradama, na mestu na kojem se vrši pozivanje, odnosno citiranje literature nabrojane na kraju članka, obavezno u običnoj zagradi napisati prezime citiranog autora, godinu izdanja publikacije iz koje citirate i, eventualno, broj stranica. Npr. (Petrović, 2012, pp.10–12).

Detaljno uputstvo o načinu citiranja, sa primerima, dato je na stranici sajta *Uputstvo za Harvardski priručnik za stil*. Potrebno je da se pozivanje na literaturu u tekstu uradi u skladu sa pomenutim uputstvom.

Sistem ASISTENT u svrhu kontrole navođenja (citiranja) u tekstu koristi specijalnu alatku CiteMatcher: otkrivanje izostavljenih citata u tekstu rada i u popisu referenci.

Napomene (fusnote)

Napomene se daju pri dnu strane na kojoj se nalazi tekst na koji se odnose. Mogu sadržati manje važne detalje, dopunska objašnjenja, naznake o korišćenim izvorima (na primer, naučnoj građi, priručnicima), ali ne mogu biti zamena za citiranu literaturu.

Lista referenci (literatura)

Citirana literatura obuhvata, po pravilu, bibliografske izvore (članke, monografije i sl.) i daje se isključivo u zasebnom odeljku članka, u vidu liste referenci. Reference se ne prevode na jezik rada i nabrajaju se u posebnom odeljku na kraju članka.

Vojnotehnički glasnik, kao način ispisa literature, primenjuje Harvardski sistem referenci, odnosno Harvardski priručnik za stil (Harvard Referencing System, Harvard Style Manual).

Literatura se obavezno piše na latiničnom pismu i nabraja po abecednom redosledu, navodeći najpre prezimena autora, bez numeracije.

Detaljno uputstvo o načinu popisa referenci, sa primerima, dato je na stranici sajta *Uputstvo za Harvardski priručnik za stil.* Potrebno je da se popis literature na kraju članka uradi u skladu sa pomenutim uputstvom..

Nestandardno, nepotpuno ili nedosledno navođenje literature u sistemima vrednovanja časopisa smatra se dovoljnim razlogom za osporavanje naučnog statusa časopisa.

Sistem ASISTENT u svrhu kontrole pravilnog ispisa liste referenci koristi specijalnu alatku RefFormatter: kontrola oblikovanja referenci u skladu sa Harvardskim priručnikom za stil.

Izjava o autorstvu

Pored članka dostavlja se Izjava o autorstvu u kojoj autori navode svoj pojedinačni doprinos u izradi članka. Takođe, u toj izjavi potvrđuju da su članak uradili u skladu sa Pozivom i uputstvom autorima i Izjavom o etičkom postupanju časopisa.

Svi radovi podležu stručnoj recenziji.

Spisak recenzenata *Vojnotehničkog glasnika* može se videti na stranici sajta *Spisak recenzenata*. Proces recenziranja objašnjen je na stranici sajta *Recenzentski postupak*.

Uredništvo

Adresa redakcije:
Vojnotehnički glasnik
Veljka Lukića Kurjaka 33
11042 Beograd
e-mail: vojnotehnicki.glasnik@mod.gov.rs
telefon: 011/3603-260

Graphic design editor
Marija Marić, e-mail: marija.maric@mod.gov.rs

Proofreading, English language editing and translation
Maja Hristić, e-mail: maja.hristic@hotmail.com

CIP – Cataloguing in the publication
National Library of Serbia, Belgrade

623+355/359

VOJNOTEHNIČKI glasnik : naučni časopis Ministarstva odbrane i Vojske Srbije = Military Technical Courier : Scientific Journal of the Ministry of Defence and Serbian Armed Forces / glavni i odgovorni urednik Dragan Trifković. - God. 1, br. 1 (1953)- . - Beograd : Univerzitet odbrane u Beogradu, Vojna akademija, 1953- (Beograd : Vojna štamparija). - 23 cm

Tromesečno. - Glavni stvarni naslov od br. 1 (2026)
Military Technical Courier. - Tekst na engl. jeziku. -
Drugo izdanje na drugom medijumu:
Vojnotehnički glasnik (Online) = ISSN 2217-4753
ISSN 0042-8469 = Војнотехнички гласник
COBISS.SR-ID 4423938

Price: 600.00 RSD

Printed in 100 copies

According to the Opinion of the Ministry of Science and Technological Development No. 413-00-1201/2001-01 of 12 September 2001, *Military Technical Courier* is a publication of special interest for science.

UDC: National Library of Serbia, Belgrade

Address: Vojnotehnički glasnik/Military Technical Courier,
Veljka Lukića Kurjaka 33, 11042 Belgrade, Republic of Serbia

https://www.scopus.com/sourceid/21101207440
http://www.vtg.mod.gov.rs/index-e.html
http://aseestant.ceon.rs/index.php/vtg/issue/current
http://scindeks.nb.rs/journaldetails.aspx?issn=0042-8469
https://www.redalyc.org/revista.oa?id=6617
http://elibrary.ru/title_about.asp?id=53280
https://doaj.org/toc/2217-4753

Military Technical Courier has entered into an electronic licensing agreement with EBSCO Publishing. The full text of *Military Technical Courier* can be found in EBSCO Publishing databases.

e-mail: vojnotehnicki.glasnik@mod.gov.rs, X: @MilTechCourier
Subscription to print edition: e-mail: vojnotehnicki.glasnik@mod.gov.rs;

The journal is published quarterly.

The first printed issue of the *Military Technical Courier* was published on 1 January 1953.
The first electronic edition of the *Military Technical Courier* was published online on 1 January 2011.

Printed by Vojna štamparija, Belgrade, Ratka Resanovica 1,
e-mail: vojna.stamparija@mod.gov.rs

Likovno-grafički urednik
Marija Marić, e-mail: marija.maric@mod.gov.rs

Prevodilac i lektor za engleski jezik
Maja Hristić, e-mail: maja.hristic@hotmail.com

CIP – Katalogizacija u publikaciji
Narodna biblioteka Srbije, Beograd

6623+355/359

VOJNOTEHNIČKI glasnik : naučni časopis Ministarstva odbrane i Vojske Srbije = Military Technical Courier : Scientific Journal of the Ministry of Defence and Serbian Armed Forces / glavni i odgovorni urednik Dragan Trifković. - God. 1, br. 1 (1953)- . - Beograd : Univerzitet odbrane u Beogradu, Vojna akademija, 1953- (Beograd : Vojna štamparija). - 23 cm

Tromesečno. - Glavni stvarni naslov od br. 1 (2026)
Military Technical Courier. - Tekst na engl. jeziku. -
Drugo izdanje na drugom medijumu:
Vojnotehnički glasnik (Online) = ISSN 2217-4753
ISSN 0042-8469 = Војнотехнички гласник
COBISS.SR-ID 4423938

Cena: 600,00 dinara

Tiraž: 100 primeraka

Na osnovu mišljenja Ministarstva za nauku, tehnologiju i razvoj Republike Srbije, broj 413-00-1201/2001-01 od 12. 9. 2001. godine, časopis „Vojnotehnički glasnik" je publikacija od posebnog interesa za nauku.

UDK: Narodna biblioteka Srbije, Beograd

Adresa redakcije: Vojnotehnički glasnik,
Veljka Lukića Kurjaka 33,11042 Beograd

https://www.scopus.com/sourceid/21101207440
http://www.vtg.mod.gov.rs
http://aseestant.ceon.rs/index.php/vtg/issue/current
http://scindeks.nb.rs/journaldetails.aspx?issn=0042-8469
https://www.redalyc.org/revista.oa?id=6617
http://elibrary.ru/title_about.asp?id=53280
https://doaj.org/toc/2217-4753

Vojnotehnički glasnik je licenciran kod EBSCO Publishing-a.

Kompletan tekst *Vojnotehničkog glasnika* dostupan je u bazama podataka EBSCO Publishing-a.

e-mail: vojnotehnicki.glasnik@mod.gov.rs; X: @MilTechCourier

Pretplata na štampano izdanje: e-mail: vojnotehnicki.glasnik@mod.gov.rs;

Časopis izlazi tromesečno.

Prvi štampani broj Vojnotehničkog glasnika objavljen je 1.1.1953. godine.

Prvo elektronsko izdanje Vojnotehničkog glasnika na Internetu objavljeno je 1.1.2011. godine

Štampa: Vojna štamparija, Beograd, Ratka Resanovica 1,
e-mail: vojna.stamparija@mod.gov.rs

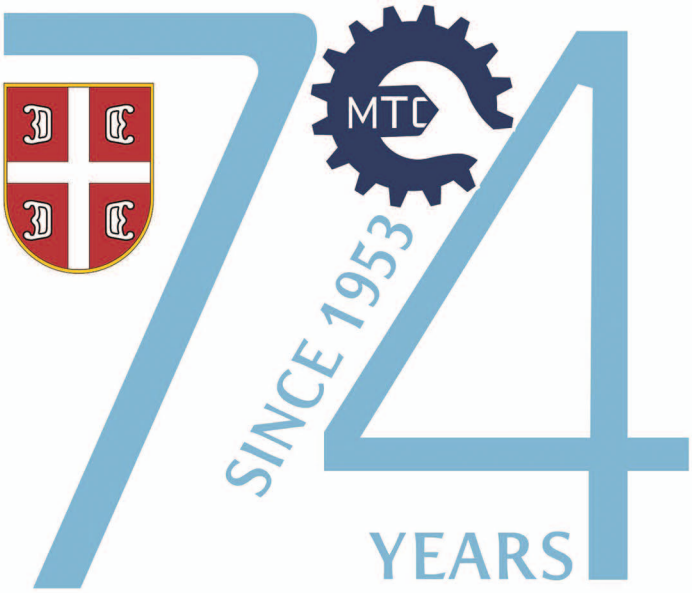
MTC
SINCE 1953
74
YEARS

VTC
OD 1953.
74
GODINA

ISSN 0042-8469
e-ISSN 2217-4753
UDC 623 + 355/359

SCIENTIFIC JOURNAL OF THE MINISTRY OF DEFENCE AND SERBIAN ARMED FORCES

MILITARY TECHNICAL COURIER

VOLUME 74 • NUMBER 2 • APRIL – JUNE 2026.

NAUČNI ČASOPIS MINISTARSTVA ODBRANE I VOJSKE SRBIJE

VOJNOTEHNIČKI GLASNIK

VOLUMEN 74 • BROJ 2 • APRIL – JUN 2026.

www.vtg.mod.gov.rs
COBISS.SR-ID 4423938
DOI: 10.5937/VojnotehnickiGlasnik